UNIVERSITY OF LIVERPOOL

Doctoral Thesis

Characterising the Triassic palaeomagnetic field: Implications for geomagnetic field evolution

Author:
Benjamin T. Handford

Supervisors:
Andrew J. Biggin
Greig A. Paterson
Mimi J. Hill

Examiners:
Silvio de Angelis
Anthony Morris

Declaration of Authorship

I, Benjamin T. **Handford**, declare that this thesis titled, "Characterising the Triassic palaeomagnetic field: Implications for geomagnetic field evolution" and the work presented in it are my own. I confirm that:

- This work was done wholly or mainly while in candidature for a research degree at this University.
- Where any part of this thesis has previously been submitted for a degree or any other qualification at this University or any other institution, this has been clearly stated.
- Where I have consulted the published work of others, this is always clearly attributed.
- Where I have quoted from the work of others, the source is always given. With the exception of such quotations, this thesis is entirely my own work.
- I have acknowledged all main sources of help.
- Where the thesis is based on work done by myself jointly with others, I have made clear exactly what was done by others and what I have contributed myself.

Signed: Benjamin Handford

Date: 28/11/2022

Acknowledgements

Many thanks to my supervisors for their knowledge and guidance that helped to shape this research project, and provided direction when most needed. In particular, I would like to thank Andy Biggin for providing me with the opportunity to conduct this research. It could be perceived as somewhat of a risk to enrol somebody from undergraduate study but in doing so I believe that Andy demonstrated belief in my potential, and for this I am most grateful. It allowed me to experience a role through which I have developed and improved, in a manner that would be difficult to replicate through other experiences. Additionally, completion of this research would not have been possible without the support of the Leverhulme Trust, as this PhD was funded through the grant awarded to Andy Biggin, RL-2016-080.

I wish to acknowledge the wider support of everybody associated with the Geomagnetism Laboratory throughout the time in which this study was completed. In some way, this thesis has benefited from the expertise of each individual, through thoughtful discussions and assistance in understanding processes and procedures. In addition, this project would not have been possible without the help of everybody who was involved in the fieldwork aspects and a particular mention should be given to Augusto Rapalini, who was instrumental in the organisation and implementation of the fieldwork that was conducted in Argentina. Thanks, should also go to Courtney Sprain who co-supervised my undergraduate project, which provided me with an appreciation for palaeomagnetism and its applications.

I would like to express my deepest gratitude to my family, my parents and grandparents, who nurtured my thirst for knowledge and learning. I am under no doubt that I would not have taken the path that I have without their encouragement and the countless visits to libraries and museums that they took me on throughout my childhood. In more general terms, I would like to take this opportunity to acknowledge the impact that such institutions had in developing my interest in the sciences and wider learning. Seemingly under constant financial threat, these services are unique in their potential as socio-economic levellers and it is my hope that the quality of these services is maintained for the benefit of future generations. Finally, a huge thanks to my partner, Naomi. Thank you for staying in Liverpool for another four plus years. Your support throughout this process has been invaluable and one thing is for certain, I cannot wait for whatever comes next.

Abstract

Records of the palaeomagnetic field are unique in their potential to provide insight into the evolution of the Earth's interior. The geomagnetic field is a product of a dynamo process, and certain variations in the geomagnetic field at the Earth's surface are reflective of variations in the Earth's internal dynamics. Across time scales of tens of millions of years, such variations are proposed to reflect changes in core-mantle boundary conditions. Typically, variations in long-term geomagnetic field behaviour are expressed in terms of the frequency at which the geomagnetic field was experiencing polarity reversals, its average strength, and its stability. Of these measurable characteristics, it is changes in average polarity reversal frequency that are most well-defined. In particular, a relatively well-developed, continuous understanding of variations in average polarity reversal frequency has been established for the last 320 million years. Knowledge of average palaeointensity and palaeosecular variation (PSV) of the geomagnetic field, are less well established, with obvious shortcomings for the Triassic (ca. 251.9-201.3 Ma). This study aims to address these gaps by investigating the distribution of virtual geomagnetic pole dispersion, a common measure of PSV, during the Triassic, and conducting palaeointensity experiments on geological units that have previously been assigned Triassic dates. The study on PSV revealed a near-invariant latitudinal dependence of VGP dispersion for a time interval encompassing the Triassic, that was near-identical to that of the preceding time interval, as defined by average polarity reversal frequency. In contrast, the Permo-Carboniferous Reversed Superchron (PCRS), one of two such events during the last 320 million years in which polarity reversals were essentially absent, displayed an extreme example of VGP dispersion pattern that in part suggested that the PCRS was a time interval of enhanced axial dipole dominance. Successful palaeointensity estimates were deemed to be reliable from specimens of pillow lavas of the Fernazza Formation (Italy) and ignimbrites and sills of the Puesto Viejo Group (Argentina). Estimates of virtual (axial) dipole moment ranged between 0.9 and 4.8 x 10^{22} Am^2. These results represent a significant improvement in attempts to define the strength of the geomagnetic field during the middle-late Triassic. Finally, taking advantage of these results, and the resulting improved continuity of palaeomagnetic records across the last 320 million years, statistical models were generated for time intervals of distinct reversal frequency. The resulting models represent a viable description of the palaeomagnetic field across each studied time interval. Exploring a range of different statistical models that aimed to describe the palaeomagnetic field during the PCRS, suggested that the more extreme PSV behaviour observed in the earlier study is likely representative of field behaviour across this time. Comparing preferred models that were representative of the different studied time intervals, suggested that the somewhat unique palaeomagnetic observations for the PCRS might be due to a difference in the relationship between antisymmetric and symmetric terms. Overall, the process deployed throughout this study has demonstrated the effectiveness of analysing palaeomagnetic records alongside statistical models, simultaneously utilising data that describes different characteristics of the palaeomagnetic field. Better constraining the

assumptions associated with statistical models, for example through the use of geodynamo simulations, would better facilitate their use as a method to test the reliability of palaeomagnetic datasets. More refined datasets would in turn provide a more accurate description of the palaeomagnetic field.

Contents

1. Introduction & Background 1
Introduction 1
Background 4
Long-term Variations in Geomagnetic Field Behaviour 4
Acquisition of Palaeomagnetic Data 7
Demagnetisation Processes & Palaeodirectional Data 9
Palaeointensity Determination 10
Introduction to Magnetic Domains 11
Thellier-style Methods 13
Shaw Method 15
Calibrated pseudo-Thellier Method 17
Sample Selection & Ideal Recorders 17
Records of the Palaeomagnetic Field 19
Geomagnetic Polarity Timescale 19
Palaeointensity Record 21
Directional PSV 22
Triassic & Permian Palaeomagnetic Field Behaviour 22
Overall Study Aims & Approach 24
2. Analysing Triassic and Permian geomagnetic palaeosecular variation and the implications for ancient field morphology 27
Abstract 27
Introduction 28
Method 30
Sourcing Data 30
Investigating Robustness with Additional Criteria 31
Measuring PSV 32
Modelling VGP Dispersion 33
Results 33
Datasets 33
Post-PCRS 42
PCRS 44
Discussion 45

Assessing the Robustness of VGP Dispersion 45
Comparison with Other Time Intervals 46
Implications for Field Morphology 49
Conclusions 51
Acknowledgements 52
Data Availability Statement 52
3. Palaeointensity estimates from Triassic pillow basalts of the western Dolomites: implications for geomagnetic field evolution 53
Abstract 53
Introduction 54
Geological Setting & Sampling 55
Method 58
Rock Magnetic Experiments & Microscopy 58
Absolute Palaeointensity Techniques 59
Thermal Thellier 59
Shaw 60
Pseudo-Thellier 61
Results 61
Rock Magnetism & Microscopy 61
Palaeomagnetic Directions & Conglomerate Test 64
Palaeointensity Estimates 65
Discussion 70
Reliability of Palaeointensity Estimates 70
Comparison with Palaeointensity Record 74
Conclusions 77
Acknowledgements 78
4. Triassic palaeointensity estimates from Argentina: investigating the viability of ignimbrites as palaeointensity recorders of the ancient geomagnetic field 79
Abstract 79
Introduction 80
Geological Setting & Sampling 82
Los Menucos Complex 83
Puesto Viejo Group 85
Method 85
Results 86
Los Menucos Results 86

Palaeomagnetic Directions 86
Rock Magnetism & Microscopy 89
Palaeointensity Estimates 92
Reliability of Palaeointensity Estimates 95
Puesto Viejo Results 97
Palaeomagnetic Directions 97
Rock Magnetism & Microscopy 100
Palaeointensity Estimates 104
Reliability of Palaeointensity Estimates 108
Discussion 110
Suitability of Ancient Ignimbrites as Palaeointensity Recorders 110
Implications of Palaeointensity Estimates for the Strength of the Post-PCRS 112
Conclusions 114
Acknowledgments 115
5. Evolution of long-term geomagnetic field behaviour since the Permo-Carboniferous Reversed Superchron 117
Abstract 117
Introduction 118
Background 120
The Introduction of GGP Models – CP88 120
A Major Refinement on GGP Models – TK03 121
Covariant-style GGP Models – BB18 & BB18.Z3 121
GGP Models of More Ancient Time Intervals – KRSM & KRSCovM 122
This Study 123
Method 124
Data Selection 124
Model Construction 125
Comparing Models with Observations 126
Results 127
Preferred Model Construction 127
Comparison Between Time intervals 135
Discussion 137
Combined Analysis of Pre-CNS & Post-PCRS 137
PCRS GGP Model & KRSCovM 138
Effects of Palaeointensity Filtering For the PCRS 141
Geomagnetic Field Evolution 143
Conclusions 147

Acknowledgements **149**
6. Summary & Implications **151**
Summary of Results **151**
Implications & Future Work **154**
Geodynamics 154
Palaeointensity Methods & Recorders 157
Evaluating the Potential of Statistical Models 158
A. Supporting information for Chapter 2 ..... **161**
Introduction **161**
Serial correlation & VGP dispersion **161**
Great Circle Analysis & VGP Dispersion **161**
Supporting Figures **162**
Supporting Datasets **163**
Supporting Tables **163**
B. Supporting information for Chapter 3 ..... **171**
Introduction **171**
Magnetic properties of amygdales **171**
Supporting Figures **172**
Supporting Tables **176**
C. Supporting information for Chapter 4 ..... **193**
Introduction **193**
Supporting Figures **194**
Supporting Tables **201**
D. Supporting information for Chapter 5 ..... **219**
Introduction **219**
Supporting Figures **220**
Supporting Tables **222**
References **225**

Chapter 1. Introduction & Background

Introduction

Ubiquitous throughout the known universe, magnetic fields are observed wherever there is movement of charge (Radi & Rasmussen, 2013; Purcell & Morin, 2013). This fundamental phenomenon is occurring across the smallest and grandest of scales. Electrons generate a magnetic field as they spin intrinsically and orbit across the vast void between themselves and the atomic nucleus to which they are bound (Radi & Rasmussen, 2013). Modern methods and equipment have confirmed hypothesised intergalactic magnetic fields stretching across the voids between galaxies (Arlen et al., 2014; Govoni et al., 2019; Klein & Fletcher, 2015), though their origin presents a mystery to be uncovered, for now. Somewhere in between these scales, are the magnetic fields associated with celestial bodies (Breuer et al., 2021). A manifestation of their internal workings and a guide to unlocking their secrets.

The very presence of a magnetic field, associated with a celestial body, reveals a turbulent dynamo (Jones, 2011), amplifying some pre-existing seed field. Such is the case for the gas giants, Mercury, Ganymede, and Earth (Breuer et al., 2021 and references therein). Considering this within the context of their composition provides further insight into the nature of the convecting fluids, this being a liquid, metallic core in the case of the terrestrial planets (Anderson et al., 2012; Schubert et al., 1996). Crustal magnetisation alongside the absence of an intrinsic magnetic field, tells the story of an exhausted dynamo within Mars and a single-state liquid core (Spohn et al., 1998; Breuer, & Spohn, 2006). The absence of both in the case of Venus (O'Rourke et al., 2018) also suggests a single state core, though its state is still to be constrained (Dumoulin et al., 2017). In these examples, direct measurements of magnetic fields provide insight into planetary interiors. To better understand the temporal evolution of these internal systems, a record of the ancient magnetic field is required.

Such records are preserved because of those smallest of magnetic fields, present at the sub-atomic level. When magnetic moments associated with electrons within an atom do not cancel one another out, an atom is said to have an atomic magnetic moment. Such atoms become aligned parallel to any applied, external magnetic field. In ferromagnetic materials, exchange interactions between adjacent atomic moments order one another, forming magnetic domains (Purcell & Morin, 2013). Domains parallel to an applied field are energetically favourable and exchange interactions between them facilitate some memory of this after the removal of the external magnetic field (Purcell & Morin, 2013). Until the material reaches a temperature at which thermal energy exceeds exchange energy, this ordering of magnetic domains is maintained (Butler, 1992; Purcell & Morin, 2013).

Iron is one such ferromagnetic substance and it is of high abundance throughout the Earth's crust, being the 4th most common element at 5% of its mass (Bernát, 1983).

Primarily distributed as iron oxides and iron sulphides (Bernát, 1983), these minerals record a remanent magnetisation, during the formation of rocks, that reflects the nature of the external magnetic field to which they were exposed during this time (Butler, 1992). This ancient magnetic field is what is referred to as the palaeomagnetic field. The direction of the palaeomagnetic field is relatively straightforward to determine, as the magnetic domains align themselves parallel. Determining the strength of the palaeomagnetic field, its palaeointensity, is more complex, but achievable, as remanent magnetisations obtained during rock formation are typically linearly related to the strength of the palaeomagnetic field (Tauxe et al., 2018). By studying rocks whose dates of formation are reasonably well determined, it is possible to build a record of how the strength and direction of the Earth's magnetic field has varied throughout its geological past. Through this process, it is known that the polarity of the Earth's magnetic field has changed throughout geological time (Brunhes, 1906; Matuyama, 1929), that this is a relatively common occurrence, and the frequency at which it has occurred has varied across different geological time intervals (Ogg, 2012). Likewise, records of palaeointensity are suggestive of long-term variations (Biggin et al., 2012; Biggin et al., 2015; Kulakov et al., 2019), with suggestions that this demonstrates a relationship with geomagnetic polarity reversal frequency (Eid et al., 2022; Gubbins, 1987; Kulakov et al., 2019; Tauxe & Staudigel, 2004).

Such observations provide constraints for geodynamo models that attempt to simulate processes representative of those generating the geomagnetic field (Aubert et al., 2010; Landeau et al., 2022; Olson et al., 2013). Agreement between simulated geomagnetic behaviour and observed palaeomagnetic behaviour across a geologic time interval, provides support for the proposed internal structure of the Earth across that part of its history (Meduri et al., 2021). This combined approach is used to investigate potential timings of inner core nucleation (Biggin et al., 2015; Davies et al., 2022), the evolving influence of compositional convection driving movement of the conductive outer core, and the nature of chemical stratification at the top of the Earth's core (Bouffard et al., 2019; Buffett et al., 2010; Greenwood et al., 2021).

Evolution of the geomagnetic field not only provides information on the state of the core, but also provides insight into the greater internal Earth structure. The longest timescale interactions between the core and mantle involve the transfer of heat and mass across the core-mantle boundary (CMB; Olson, 2016). Of the effects that make up these interactions, it is the transfer of heat from the core to the mantle that is most prominent. In places, the convective heat engine within the mantle draws heat directly from the CMB, in others this heat transfer is mediated by the formation of mantle plumes (Olson, 2016). This cooling process is thought to extend to the rest of the core through outer core convection, a process that likely resulted in the solidification of the inner core and the releasing of lightening elements that is thought to contribute significantly to this process today (Meduri et al., 2021; Nimmo, 2015). As it is convection of the outer core that generates the magnetic field, the power available to the geodynamo is proportional to CMB heat flux (Labrosse & Macouin, 2003; Lay et al., 2008; Olson, 2016). It follows then, that variations in the geomagnetic field can provide insight into the core and mantle processes that govern the temperature gradient across the CMB. Mantle forcing has been proposed as the cause of a 200 million-year cyclicity in geomagnetic field behaviour (Driscoll & Olson, 2011; Biggin et al., 2012). Such a relationship would indicate a cyclic evolution of the state of the CMB, associated with the upwelling and downwelling of

material. Superchrons, tens of millions of years during which polarity reversals are effectively absent, form a major part of the proposed 200 million-year cyclicity in geomagnetic field behaviour (Biggin et al., 2012; Driscoll & Olson, 2011). Within this framework they are preceded by shorter intervals of rapid reversal rates (Biggin et al., 2012). The strength of the geomagnetic field is also considered; it is proposed that superchrons correspond with increased intensity and that this is preceded by a significantly reduced geomagnetic field strength persistent for tens of millions of years (Biggin et al., 2012; Hawkins et al., 2021).

Apparent reversal frequency is sufficiently well-documented from present day back to approximately 320 Myr to allow distinct time intervals of different geomagnetic behaviour to be identified. Amongst them are two superchron events. Such a well-documented record across a timescale of this length is not replicated further back in geological time, due to the more sparsely populated nature of the data (Ogg, 2012; Hawkins et al., 2021). The record across the last ca. 320 Myr presents the best opportunity to investigate proposed relationships between average reversal frequency and other aspects of the palaeomagnetic field such as its average strength, stability, and morphology. The latter characteristics are less well-documented over the last 320 Myr than apparent average reversal rate, with significant gaps in current records (Anwar et al., 2016; Doubrovine et al., 2019; Hulot & Gallet, 2003; Kulakov et al., 2019). Improvements to these records would facilitate a comparison between observable characteristics of the palaeomagnetic field across a time interval that covers a complete cycle in the proposed 200 Myr cyclicity.

The least-well documented time interval within the palaeointensity record, across the past 320 Myr, is between approximately 250 and 200 Myr (Anwar et al., 2016; Biggin & Thomas, 2003; Doubrovine et al., 2019), approximately aligning itself with the Triassic period (ca. 251.9–201.3 Ma; Ogg, 2012). Better characterising the strength of the palaeomagnetic field throughout this time, could be crucial in better assessing the nature of the proposed 200 Myr cyclicity and the relationship between palaeointensity and apparent reversal frequency. Previously, it has been proposed that the palaeomagnetic field was anomalously weak during a time interval following the Triassic (McElhinny & Larson, 2003; Perrin & Shcherbakov, 1997; Prévot et al., 1990). Such an interval has been incorporated into the 200 Myr cyclicity hypothesis (Hawkins et al., 2021), and is suggestive of a decoupling between processes governing polarity reversal frequency and geomagnetic field strength (Prévot et al., 1990). It has recently been suggested that this weak interval was initiated prior to the Triassic and was sustained throughout (Anwar et al., 2016). This would have further implications regarding the evolution and behaviour of the geomagnetic field. Additionally, there has been no previous assessment of the stability of the geomagnetic across this time interval (Doubrovine et al., 2019). Such an assessment provides information on geomagnetic field morphology (Biggin et al., 2020), elements of which have also been proposed to demonstrate a relationship with apparent reversal frequency and palaeointensity (Doubrovine et al., 2019; Hulot & Gallet, 2003).

This thesis is focused on improving our understanding of the behaviour of the geomagnetic field throughout the Triassic, and in doing so, better defining how the geomagnetic field was behaving in between the two most well understood superchron events. This is achieved by utilising existing palaeodirectional data, from published literature, to assess the stability and morphology of the geomagnetic field, and by obtaining much needed palaeointensity estimates through a range of experimental

methods. The stability and morphology of the geomagnetic field during the older of the two superchrons is also reassessed, in an attempt to better constrain palaeomagnetic field behaviour and address some of the uncertainties that surround it. These new results are viewed within the wider context of geomagnetic field behaviour across the last 320 Myr, by comparing geomagnetic field behaviour during the distinct time intervals identified by the apparent reversal frequency record. By utilising this approach, it is possible to investigate proposed relationships between average polarity reversal frequency, geomagnetic field strength, and stability. Finally, optimised statistical models are generated for each distinct time interval that provide a plausible description of the geomagnetic field that best reproduces the observed morphology and strength of the palaeomagnetic field. Such models are described by a suite of plausible Gauss coefficients. From these, predictions of palaeomagnetic distributions can be generated and compared against those generated by geodynamo simulations. This process can provide further evidence to suggest that the compared models may accurately represent the internal structure and interactions of the Earth across the studied time interval.

Background

Long-term Variations in Geomagnetic Field Behaviour

In its entirety, the geomagnetic field is a superposition of magnetic fields from sources internal and external to the Earth. Variations in the geomagnetic field on the shortest timescales (< 1 year) typically occur in response to changes in the nature of external sources. This facilitates isolation of the internally generated contribution to the geomagnetic field, in other words that which is a result of the geodynamo. The contribution from the geodynamo dominates large scale structures of the geomagnetic field and accounts for around 90% of that detected at Earth's surface (Korte & Mandea, 2019). The magnetic field at any point outside of the source can be described by the gradient of a scalar potential (Merrill et al., 1998). As the geomagnetic field is generated in the core, this description is applicable to any point lying outside of it. This position is given by the spherical coordinates: radius (r), colatitude (θ), and longitude (φ). On the Earth's surface, this point lies a distance equivalent to the Earth's radius away from the source (a). Traditionally, the resulting spherical harmonic expansion is represented in Gauss' form which utilises Gauss coefficients (g_l^m, h_l^m). The solution can be solved for a given degree (l), with the full description, the magnetic potential (Ψ), a combination of the contributions from an infinite number of degrees (m).

$$\Psi = \frac{a}{\mu_0} \sum_{l=1}^{\infty} \sum_{m=0}^{l} \left(\frac{a}{r}\right)^{l+1} p_l^m(cos\theta)(g_l^m cosm\phi + h_l^m sinm\phi) \qquad (1.1)$$

The solution of degree 1 is that of the dipole field (Figure 1.1) and its magnetic potential falls of at a rate of r^{-2}, with increasing distance from the source (i.e. the core-mantle boundary (CMB)). With increasing degree, the exponent describing the rate at which magnetic potential falls off, decreases by 1. This results in reduced relative contribution from the non-dipole at the Earth's surface, estimated to be on the order of 10-20% (Korte & Mandea, 2019). Changes in the relative contribution of the different degree harmonics are observed at the Earth's surface as secular variation of the geomagnetic field. These changes occur on timescales greater than a year, with current trends seeing a decrease in

the dipole component and a westward drift in the non-dipole. The rapid rate at which secular variation is observed, points to dynamo action in the outer core as the controlling factor (Loper, 2003). Averaging the geomagnetic field across timescales on the order of 10^4 to 10^5 years sufficiently averages out the effects of secular variation (Tauxe et al., 2018). This time-averaged field (TAF) can be described by a geocentric axial dipole (GAD), corresponding the degree 1, order 0 Gauss coefficient (Figure 1.1).

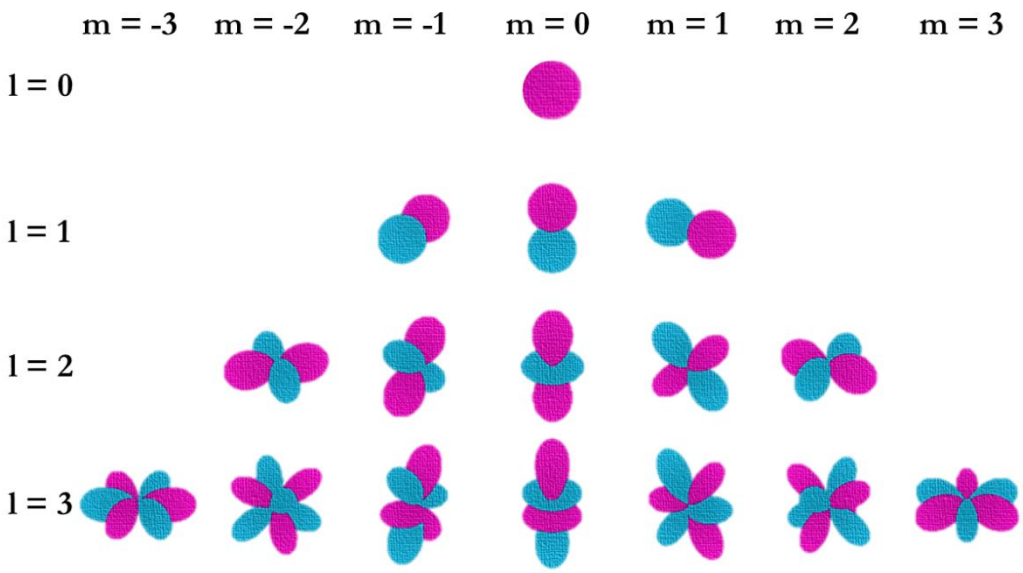

Figure 1.1: Spherical harmonic basis functions up to degree (l) = 3, order (m) = 3. Pink portions represent regions where the function is positive, blue portions where the function is negative. Modified from Xiang, & Landschoot, (2019).

Secular variation experienced during ancient time is referred to as palaeosecular variation (PSV). By this definition, reversals and excursions are examples of PSV. During a reversal, it appears that the strength of the dipole decays before becoming entirely diminished. Throughout this decay, its polarity is maintained but as it grows in strength from its minima, it does so with the opposite polarity. All the while, the non-dipole component of the internally generated geomagnetic field appears to persist (McPheron et al., 2022). During excursional events, the geomagnetic field also exhibits a great departure from GAD, again suggestive of a diminishing dipole whilst the non-dipole is more greatly maintained. The distinction from reversal events is that the geomagnetic field is not re-established in the opposite orientation (McPheron et al., 2022). The definition of established reversed orientation is somewhat arbitrary as an event that achieves a reversed state for a short period of time is viewed as an excursion and not a pair of reversal events. Although there is no formal definition, the reversed state must have existed for sufficient time that it can be described by a TAF to be categorised as a reversal (Gubbins, 1999).

Ordinarily, PSV refers to the characterisation of variations in the geomagnetic field during stable polarity chrons (Johnson & McFadden, 2015). Additional variations in the strength of the geomagnetic field are observed outside of that associated with reversals and excursions. To analyse this variation, palaeomagnetic field intensity (B) is typically expressed as a virtual (axial) dipole moment V(A)DM (Constable, 2007).

$$VDM = \frac{4\pi a^3}{\mu_0} \frac{B}{\sqrt{1+3cos^2\theta_m}} \quad (1.2)$$

This process utilises the dipole formula (Equation 1.3) to determine magnetic colatitude (θ_m) from the measured magnetic inclination (I). When geographic colatitude is used in its place, the calculated dipole moment is a VADM (Constable, 2007).

$$tanI = 2cot\theta_m \quad (1.3)$$

A VDM describes the theoretical geocentric dipole that would result in the observed field strength at a given geographical locality. Through this process, it is possible to directly compare estimates of palaeomagnetic field strength, accounting for the latitudinal variation that arises due to the dipole nature of the field (Constable, 2007). For a given description of the palaeomagnetic field across a sufficiently long time to characterise secular variation, the average intensity can be estimated alongside its variance. When descriptions representative of different time intervals throughout the geological record are compared, differences arise between the average intensities and associated variances that describe them. These variances are also technically a measure of PSV.

Traditionally, studies of PSV have not included variations in the intensity of the field, due to the historical availability of palaeointensity data, which is at a premium when compared with data regarding palaeodirections (Johnson & McFadden, 2015). For this reason, the typical definition of PSV is further narrowed to variations in the direction of the palaeomagnetic field alone, during stable chrons (Johnson & McFadden, 2015). A common way in which PSV, by its traditional definition, is estimated is through the dispersion of virtual geomagnetic poles (VGPs). By a similar rationale to that which sees palaeointensity values converted to V(A)DMs, reported declination and inclination values are generally transformed into VGPs to facilitate a comparison of palaeodirections

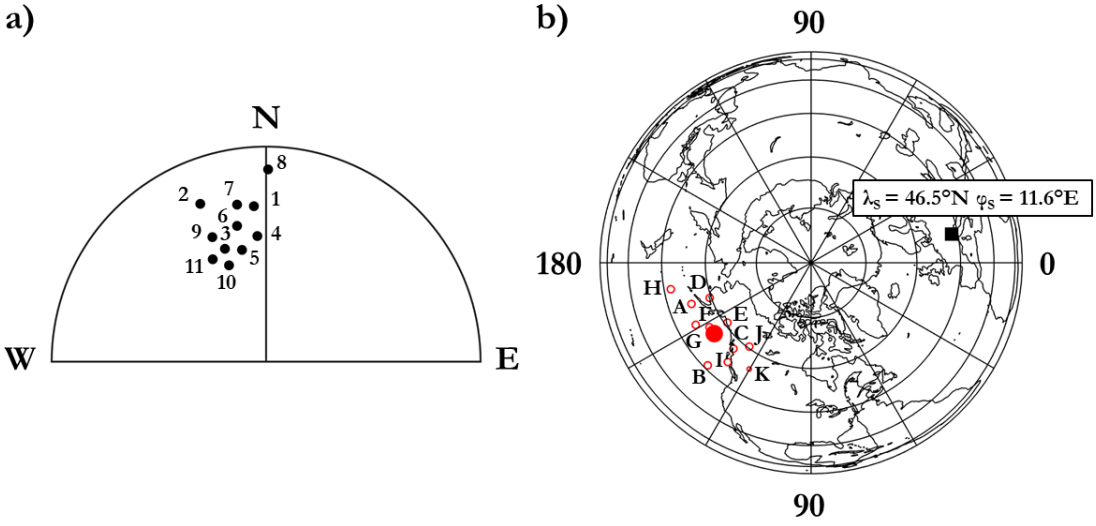

Figure 1.2: a) Stereoplot showing site-mean palaeomagnetic directions from specimens analysed in ***Chapter 3****. b) Black square represents the sampling area of the studied sites with co-ordinates displayed (λ_S, φ_S). Open red circles represent virtual geomagnetic poles (VGPs) corresponding to the site mean directions in Figure 1.2a (e.g. 1-A, 2-B, etc.). The solid red circle represents the position of the mean of the VGPs, referred to as the palaeomagnetic pole.*

obtained at different geographical locations (Figure 1.2). The position of a magnetic pole is defined as the projection of the negative end of the dipole at the surface at which the field is observed (Butler, 1992). Using spherical trigonometry, this pole position can be determined from the magnetic direction (I, D) observed at a given point (λ_s, φ_s). Assuming a geocentric dipole for the geomagnetic field, this allows the same principles to be applied

at the Earth's surface. This gives rise to the VGP, the pole position calculated from a single observation of the geomagnetic field (Butler, 1992). The latitudinal position of this pole (λ_p) is determined by Equation 1.4, once again utilising the dipole formula to determine θ_m (Equation 1.3).

$$\lambda_p = sin^{-1}(sin\lambda_s\, cos\theta_m + cos\lambda_s\, sin\theta_m\, cosD) \tag{1.4}$$

This estimated pole latitude can then be used to determine the longitudinal position of the pole (φ_p) by calculating the longitudinal difference between the pole and the site (β).

$$\beta = sin^{-1}\left(\frac{sin\theta_m\, sinD}{cos\lambda_p}\right) \tag{1.5}$$

A VGP describes the position of a geocentric dipole that can account for the observed magnetic field direction at one location and at one point in time (Butler, 1992). A VGP can be calculated from palaeomagnetic data (Figure 1.2) which, assuming the remanent magnetisation was acquired over sufficiently short time, provides a spot-reading of the palaeomagnetic field.

A spot-reading will contain contributions from the non-dipole field (Butler, 1992). Palaeomagnetic poles are determined, in an attempt to evaluate the extent of these non-dipole contributions. Typically, a set of spot-readings are analysed whose individual magnetisations were acquired over a time scale of 10^4 to 10^5 years (Butler, 1992). The average of these spot-readings should average out the effects of secular variation (Tauxe al., 2018). By the definition of the GAD assumption, the resulting average VGP should lie at the position of the rotation axis (Butler, 1992). This average VGP is what is referred to as a palaeomagnetic pole (Figure 1.2). The variance of the set of VGPs is known as VGP dispersion and can be viewed as a measure of PSV. By this process, times during which spot-readings have captured the field undergoing a polarity reversal or excursion can be identified, as they will display greater deviation from the palaeomagnetic pole (Watkins, 1973; Wilson et al., 1972; Vandamme, 1994). As this behaviour is not traditionally considered as being representative of typical PSV, VGPs from such spot-readings are removed from the analysis so as not to artificially inflate the measure of PSV (Johnson & McFadden, 2015). It should be noted that this approach is not universally supported, with arguments that reversals and excursions are natural outgrowths of the same processes governing PSV (e.g. Johnson & McFadden, 2015).

Acquisition of Palaeomagnetic Data

Reference has been made to palaeomagnetic data, in the form of palaeodirections and palaeointensity, and there will now be an explanation given of how this information is obtained. The fact that there is any record of the palaeomagnetic field can be attributed to the phenomenom of ferromagnetism (Figure 1.3), that results in a material acquiring a remanent magnetisation, and the many processes by which remanent magnetisation is acquired naturally by rocks during their formation. Ferromagnetism occurs in materials that contain strongly interacting atoms that each have a permanent magnetic moment. This interaction is termed exchange energy. The magnetostatic energy of grains is minimised parallel, or anti-parallel, to an externally applied magnetic field (Purcell & Morin, 2013). Crucially, for ferromagnetic materials, some memory of this preferred alignment remains after the external magnetic field is removed. As a consequence of exchange energy, individual atomic magnetic moments attempt to align all other atomic

magnetic moments with itself (Purcell & Morin, 2013). As the atomic magnetic moment was determined by the externally applied magnetic field, the direction of this is the same as that of the applied field. If the system were to increase in thermal energy, the interactions between atoms would weaken, until thermal energy exceeds exchange energy and the remanent magnetisation is reset (Bertotti, 1998; Purcell & Morin, 2013). The temperature at which this occurs is known as the Curie temperature (T_C, Butler, 1992).

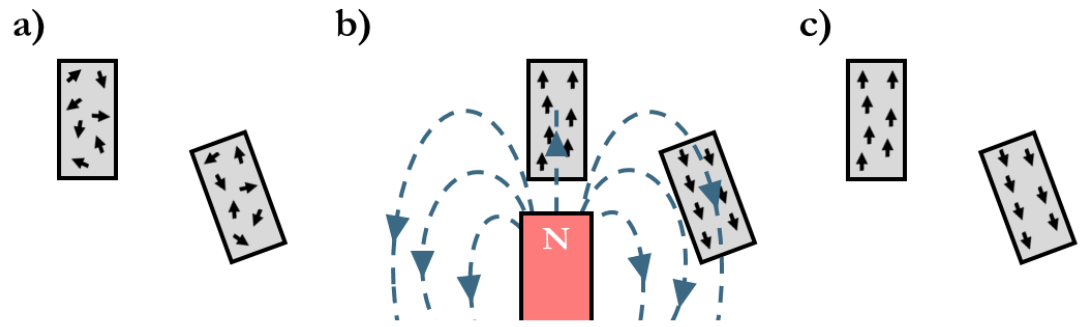

Figure 1.3: Basic schematic outlining the principle of ferromagnetism. a) Unmagnetised bulk material with randomly oriented mangetic moments cancelling eachother out. b) Magnetic moments align with the direction of an applied external magnetic field, resulting in induced magnetism of the bulk material. c) The preferred alignment of the magnetic moments remains after the removal of the external magnetic field; the resulting magnetism of the bulk specimen is referred to as being 'remanent'.

Ferromagnetic materials are of relatively high natural abundance, with ferromagnetic minerals widespread in the geological record. Therefore, during its formation, a bulk rock acquires a remanent magnetisation, as the magnetic moments of ferromagnetic grains align parallel to the geomagnetic field present during that time and at that formation location (Figure 1.3). The process by which this remanent magnetisation is acquired is dependent on the formation process of the bulk rock.

Magnetic grains acquire a thermal remanent magnetisation (TRM) when cooled from above their T_C to some ambient temperature, in the presence of a weak magnetic field, such as the geomagnetic field (Moskowitz et al., 2015). Originally defined by Louis Néel, the time taken for a remanent magnetisation to decay to 1/e of its initial value was termed the relaxation time (τ; Néel, 1949; Smart, 1955). For a material at its T_C, this is very small and so magnetic moments quickly become aligned with the ambient magnetic field. As the temperature of the material decreases, this relaxation time increases until it becomes so long to as effectively 'block' in the remanent magnetisation. The temperature at which this occurs is referred to as the blocking temperature (Barbara, 2019). By means of a similar process, chemical remanent magnetisations (CRMs) can also be acquired. CRMs may occur due to new grain growth or mineral alteration of an existing grain (Stokking & Tauxe, 1987). At some diameter, dependent on the mineralogy, new grains become ferromagnetic. At some critical diameter that is also dependent on mineralogy, τ increases very rapidly, blocking in the remanent magnetisation. This diameter is known as the blocking diameter (Stokking & Tauxe, 1987). If this process occurs during the initial cooling from above T_C, then the grain is said to have acquired a thermochemical remanent magnetisation (TCRM). This term can also be applied to remanence that has been acquired from later thermal events, with reheating resulting in grain growth, remanence unblocking and later blocking during cooling.

Magnetic grains can also acquire an isothermal remanent magnetisation (IRM) in the presence of a strong direct current (DC) magnetic field (Moskowitz et al., 2015). Remanence acquisition by this process is rare in nature, due to the relatively weak strength of the geomagnetic field, with natural occurrences most commonly associated with lightning strikes (Butler, 1992). The application of a strong enough magnetic field opposing the magnetisation of a material will result in its demagnetisation. The field strength at which this occurs is known as the coercivity of a material (Moskowitz et al., 2015). This phenomenon is utilised in a commonly used laboratory technique referred to as anhysteretic remanent magnetisation (ARM; Moskowitz et al., 2015). Applying an AF that linearly decreases at each cycle, in the presence of a weak DC field, systematically imparts a magnetisation parallel to the direction of the DC field in grains with progressively decreasing coercivity. Weak magnetic fields, such as the geomagnetic field, can impart a remanence but only after long exposure. This process, known as viscous remanent magnetisation (VRM), affects ferromagnetic grains with short relaxation times (Butler, 1992). If VRM acquisition occurs as the material is heated to some temperature between T_C and ambient temperature, the remanence is known as thermo-VRM.

Demagnetisation Processes & Palaeodirectional Data

Since their initial formation, most rocks will have acquired some additional magnetisation. This is known as secondary magnetisation, with that acquired during initial rock formation known as primary magnetisation. Blocking temperature is dependent on factors such as mineralogy, grain size, and grain shape (Butler, 1992). As a result, bulk rock samples typically display a range of blocking temperatures. A TRM acquired during a specific blocking temperature interval is known as a partial TRM (pTRM), and subsequent heating of a rock can impart secondary pTRMs. Likewise, new grain growth or alteration can result in secondary CRMs and/or TCRMs (Fabian, 2009; Kellog et al., 1970; Stokking & Tauxe, 1987), and almost all bulk rock specimens will have acquired a secondary VRM (Dunlop & Özdemir, 1997). When the magnetisation of rocks affected in this way is measured, the resulting declination and inclination will be a result of the sum of these pTRM components (Butler, 1992). To reveal information relating to the geomagnetic field at the time of the rock's formation, the primary remanence must be isolated. Stepwise demagnetisation techniques facilitate the removal of overprinting directions (Zijderveld, 1967), though further information is required on the rock's history to ascertain the likelihood of the remaining direction being primary and not simply an older secondary magnetisation. Until there is evidence to suggest that it is primary, it is instead referred to as the characteristic remanent magnetisation (ChRM; Butler, 1992).

The process of thermal demagnetisation relies on the theory of TRM acquisition proposed by Louis Néel in 1949. A bulk rock specimen is heated to a temperature below its Curie temperature, instantaneously randomising the magnetisation of all grains within the unblocking range and demagnetising a pTRM. If the specimen then cools in the absence of a magnetic field, the randomised magnetisations are maintained and the contribution from the associated pTRM to the original remanence has been removed (Butler, 1992). The specimen has been partially demagnetised. Repeating this procedure but heating the specimen to a temperature greater than T_C would completely demagnetise the specimen.

Similarly, the effects of strong applied magnetic fields on magnetised grains can be utilised to demagnetise bulk rock specimens. Such as is the case when imparting an ARM, a strong alternating field is applied that linearly decreases in strength with each cycle. To demagnetise a specimen, this process is conducted in the absence of an applied DC field, however. Magnetic grains whose coercivity is less than the applied field, align themselves parallel to the applied field. The amplitude of the applied field decays with each half cycle, and so for any grains whose coercivity was less than the previous amplitude of the applied field but greater than the new amplitude, their magnetisation remains in the direction of the previously applied field. This highlights the importance of the alternating field, as the magnetisation of the grains with coercivity less than that of the new applied field is now aligned anti-parallel to that of the newly fixed grains. By continuing to gradually reduce the amplitude of the AF with each half-cycle, the magnetisations of grains with a coercivity less than that of the maximum amplitude of the AF field become magnetised in opposite directions in equal proportions (Butler, 1992). The net effect is partial demagnetisation of the bulk specimen, or complete demagnetisation if the maximum amplitude of the AF field exceeds the maximum coercivity fraction within the bulk specimen. To ensure that all three axes of the bulk specimen are affected simultaneously, this process can occur whilst tumbling the bulk specimen (Tauxe et al., 2018).

Palaeointensity Determination

The stepwise demagnetisation procedures outlined, alongside principal component analysis (Kirschvink, 1980), allow the direction of a ChRM component to be relatively easily determined. For a complete description of the geomagnetic field at a given point in time and space, information is required regarding the strength of the magnetic field. The basis for any determination of palaeointensity is that the strength of the remanent magnetisation is proportional to the strength of the magnetising field (Néel, 1949, 1955). The first requirement for this to hold, and to be able to accurately estimate absolute palaeointensity, is that the remanence must have been acquired in the form of a TRM (Dunlop, 2011). By this reckoning, the magnitude of the remanent magnetisation (M_{NRM}) can be expressed as some proportionality constant multiplied by the palaeomagnetic field strength (B_{anc}). In the same vein, the specimen can be given an artificial TRM by heating above the T_C and cooling in an applied field, and the magnitude of the resulting magnetisation (M_{lab}) can be expressed as some proportionality constant multiplied by the applied laboratory field (B_{lab}). Assuming that the proportionality constant remains unchanged, then the two expressions can be set equal to one another (Dunlop, 2011). If the magnetisation of the specimen is measured before and after the heating process, this leaves just one unknown to solve for, the palaeomagnetic field strength.

$$B_{anc} = \frac{M_{NRM}}{M_{lab}} B_{lab} \tag{1.6}$$

This simple process would be sufficient in determining palaeointensity if the original remanence of the bulk specimen, the natural remanent magnetisation (NRM), was a single component, primary TRM. In reality, as has been discussed, secondary magnetisations are common place and contribute to the NRM (Zijderveld, 1967; Dunlop & Özdemir, 1997). One other caveat is the assumption that the proportionality constants relating magnetisation to the ancient geomagnetic field and the applied laboratory magnetic field, respectively, are equivalent (Perrin, 1998). Again, such a finding is unlikely as there are a wealth of properties that determine the proportionality constant for a bulk rock specimen.

These include, but are not limited to, ferromagnetic grain size distribution and ferromagnetic mineralogy (Perrin, 1998). Ferromagnetic grains carrying the primary TRM have often undergone alteration after prolonged exposure to oxidising and/or reducing environments (Dunlop & Özdemir, 1997), and further alteration and/or grain growth is common place during laboratory heating (Perrin, 1998; Tarduno et al., 2007).

Further assumptions are made in an attempt to overcome the issues of applying Néel's model of TRM to obtain palaeointensity estimates in real-world scenarios. These assumptions require that the TRM of a specimen is viewed as a spectrum of pTRMs, and they are known as the Thellier laws (Thellier, 1938; Thellier & Thellier, 1959). The first of these is the law of additivity. It, quite simply, states that the vector sum of all pTRMs is equal to the total TRM. The second law, the law of independence, requires that the direction and intensity of a pTRM associated with a given temperature range are fully independent of any other pTRM associated with an entirely different, non-overlapping, temperature range. Finally, for the first two laws to hold true, the temperatures at which the pTRMs were blocked and subsequently unblock have to be identical. This is known as the law of reciprocity.

Introduction to Magnetic Domains

All theoretical understanding described up until this point, relies on one fundamental assumption. That bulk rock specimens are an assemblage of non-interacting, single domain (SD) grains. In reality, this is not the case with rocks containing grains of a wide range of domain states with the end-member scenarios of SD and multi-domain (MD). A magnetic domain is a region in which all atomic magnetic moments are aligned in the same direction, resulting in a net moment (Dunlop & Özdemir, 1997). In the absence of an applied field, or a previously applied field that resulted in remanence, there is no preferred orientation of these domains relative to one another (Young, 1992). Separating these domains are domain walls.

Domains form where it is energetically favourable to do so. All magnetic grains have surface charges that are present at each pole. These surface charges have an associated demagnetising magnetic field that acts to reduce the magnetic field of the grain. The energy of the surface charges is referred to as magnetostatic energy and it is the potential energy of the magnetic moments in the field they have created (Bertotti, 1998). The formation of a domain wall, and so the separation into two magnetic domains, reduces the magnetostatic energy. The second domain becomes magnetised anti-parallel (Figure 1.4a) (Hummel, 2011). Producing and maintaining a domain wall requires energy, and so domain walls are only generated where it is energetically favourable to do so. That is to say the energy required to maintain a given number of domain walls is equal to the resulting magnetostatic energy (Hummel, 2011). The effects of an applied field are somewhat different for MD grains, as instead of orienting parallel to the applied field, as is the case for magnetic moments of SD grains, in MD grains the domains that align with the applied field grow at the expense of those pointing in other directions (Hummel, 2011). In this respect, ferromagnetic MD grains are also capable of acquiring a remanence but the magnetic properties and behaviours differ to those of SD grains.

For a given composition, increased grain size makes it energetically favourable for domain walls to form, as magnetostatic energy increases. There is no sharp transition observed from an SD to MD state as grain size increases, however. Instead there is a gradual

transition, the size range over which it occurs being dependent on spontaneous magnetisation, shape, and the state of internal stress of a grain (Roberts et al., 2017). Traditionally, these transitional states have been termed pseudo-single domain (PSD). With advances in micromagnetic modelling, greater understanding has been developed on these transitional states, allowing the identification of distinct evolutionary states (Roberts et al., 2017). This makes PSD more of a catch-all term in our modern understanding. At the limit of an SD diameter, a magnetisation state known as the flower state develops (Figure 1.4b). In this state, magnetic moments spread outwards at the edge of a grain (Schabes & Bertram, 1988). Within this flower state, magnetisation remains essentially uniform at the centre of the grain, in a similar manner to the magnetisation held within an SD grain (Roberts et al., 2017). With a diameter above that of a stable SD grain, the reversal response of the magnetic moment to an applied field occurs as curling around a central axis (Williams & Dunlop, 1989). This is commonly referred to as a vortex state (Figure 1.4c) (e.g. Roberts et al., 2017). Nucleation of vortex states has been demonstrated as the cause of stable magnetisations within PSD grains (Roberts et al., 2017; and references therein). So unlike MD grains, it is assumed that PSD grains, both flower and vortex state, are able to preserve remanent magnetisations as well as SD grains (e.g., Nagy et al., 2017).

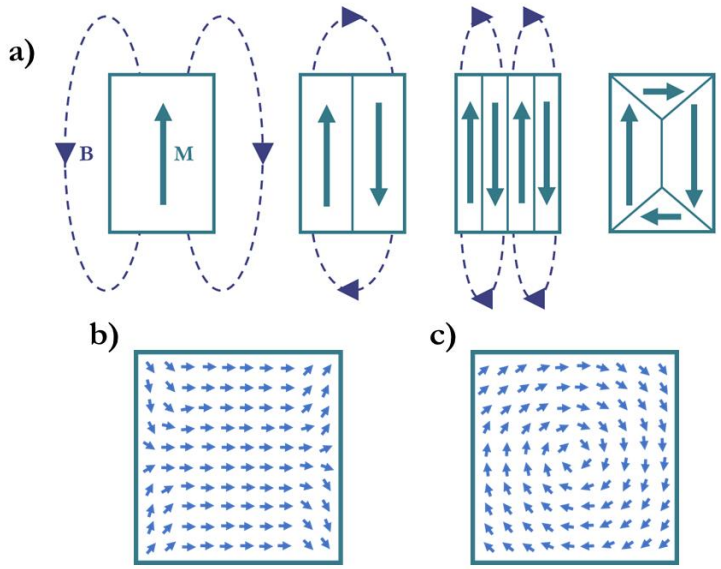

Figure 1.4: Schematics of MD and PSD grain structures. a) Cross-section of alternative grain structures for the same grain. (L-R) A single domain structure; two-domain structure; four-domain (MD) state; two-domain state with closure domains. Reduction of magnetostatic energy achieved by reducing the demagnetising field (B), associated with surface charges, through increasing the length-diameter ratio. Figure is modified from Dunlop & Özdemir (1997). b) In-plane configurations of electron-spin within flower-state domain, c) vortex-state domain. Modified from Zhao et al. (2015).

As MD grains are still capable of recording a remanent magnetisation that retains some memory of the external magnetic field to which they have been exposed, stepwise demagnetisation techniques still isolate a ChRM that is representative of the palaeomagnetic field. The greater issue is the effects that MD grains can have on palaeointensity experiments. Although the effects are not fully understood, it appears likely that MD grains can result in failure of the law of reciprocity (Tauxe et al., 2020). This has been attributed to changes in domain wall structure during the multiple heating events associated with traditional palaeointensity methods (Tauxe et al., 2020). In

addition, elongated SD grains, and PSD and MD grains have all been demonstrated to have the potential to violate the linear relationship between magnetisation and applied field strength (Dunlop & Argyle, 1997; Selkin et al., 2007). To increase the likelihood of obtaining reliable palaeointensity estimates, a variety of experimental methods have been developed that attempt to minimise and/or detect MD effects as well as reduce the likelihood of laboratory induced alteration that invalidates the assumption of equivalent proportionality constants. The following section provides a summary of the palaeointensity techniques utilised within this study, and the steps that are taken to mitigate the impact of non-ideal effects.

Thellier-style Methods

Formalised by Émile & Odette Thellier (1959), the Thellier-Thellier method, referred to hereinafter as simply the Thellier method, was the culmination of over two decades of work that attempted to devise a method to successfully obtain palaeointensity estimates from baked material (e.g. Thellier, 1937a; 1937b; 1937c; 1941a; 1941b; 1946; Roquet & Thellier, 1946). The final method (Thellier & Thellier, 1959), involved double stepwise heating events that replace natural pTRMs with laboratory induced pTRMs across progressively increasing blocking temperature ranges. During the first heating of each step, the specimen is heated to a given temperature in the presence of a known laboratory field then cooled whilst maintaining the same external field. The same specimen is then subject to an identical process, but the specimen is now orientated in the opposite

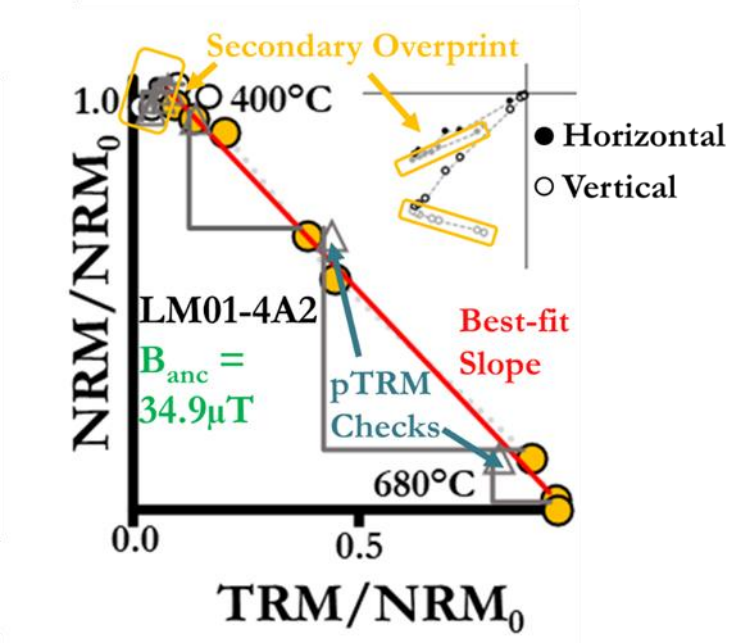

Figure 1.5: Example Arai diagram (Nagata et al., 1963), typically used in analysis of Thellier-style experiments. Data in this example comes from results of a specimen analysed in ***Chapter 4****. Associated palaeomagnetic direction displayed in a Zijderveld plot (top right). Best-fit line (red) determined from selected points (yellow) of the ChRM, and used in determination of* B_{anc}*. Second in-field step at lower blocking range (pTRM check, grey triangle).*

direction. Specimen magnetisation is measured after each of these steps, and from this, the remaining magnetisation ($NRM_{remaining}$) and gained magnetisation ($pTRM_{gained}$) can be determined. The double heating process is then repeated at progressively higher temperature steps. Subsequent adoptions of the Thellier method analysed this data with

an Arai plot (Figure 1.5), in which $pTRM_{gained}$ is plotted against $NRM_{remaining}$ (Nagata et al., 1963). Idealised experiments result in a linear relationship between the two (Nagata et al., 1963). With this approach, the slope of the best-fit line represents the ratio of natural magnetisation to laboratory magnetisation (Figure 1.5). Making use of the proportionality between magnetisation and the applied field, discussed earlier, palaeointensity can then be estimated (Equation 1.6).

To understand the limitations of the Thellier method, and factors for consideration, it is important to develop an understanding of how the method was developed. The double heating technique present in the original Thellier method had previously been developed by Johann Koenigsberger, with little success in obtaining palaeointensity estimates (Dunlop, 2011; Koenigsberger, 1938). Koenigsberger had been conducting experiments on a variety of volcanic rocks that had resulted in complex behaviour, now known to be caused by combinations of MD and alteration effects (Dunlop, 2011). In an attempt to avoid this undesirable behaviour, Thellier conducted experiments on baked clay. Through the development of the Thellier method, a better understanding was developed regarding how a specimen should behave in order to produce successful results. This process resulted in the previously discussed Thellier's laws, which were later provided with a quantitative physical basis in the form of Néel theory (Néel, 1949). As Néel theory describes behaviour exhibited by non-interacting SD assemblages, this would suggest that the baked materials studied by Thellier could be represented by such. A high concentration of SD grains is now a well-established property of baked clays, and so by its development, the Thellier method only strictly holds for these ideal recorders.

Subsequent modifications to the Thellier method have attempted to identify MD effects and reduce the effects of MD contamination. Identifying MD effects provides grounds on which to reject any results, on the basis that they violate the assumptions on which the method is based. It can also provide an opportunity to cease experiments prematurely, as the multiple heating and cooling steps make the Thellier method a time-consuming process. An easily identified, and early discovered (Levi, 1977), effect of MD grains is a sagging of the resulting Arai plot. Such behaviour is observed in the re-analysed results of Koenigsberger (Dunlop, 2011), and it has been proposed to arise due to violation of the law of reciprocity (Tauxe et al., 2020). Another consequence of the violation of this law are pTRM tails (Bol'shakov & Shcherbakova, 1979; Shashkanov & Metallova, 1972). These occur when the demagnetisation of a specimen across a given blocking range, does not remove the pTRM acquired across the same blocking range. In an effort to detect this effect, modern Thellier methods have replaced one of the steps within the double heating with a heating to the same temperature but in the absence of any magnetic field (Aitken, 1988; Coe, 1967; Tauxe & Staudigel, 2004). In the IZZI protocol (Tauxe & Staudigel, 2004), which is utilised in this thesis, the so called 'in-field' and 'zero-field' steps are conducted in an alternating order. Low-temperature pTRM tails can be detected through this method by a zigzagging appearance of the Arai plot. In experiments using other protocols, an additional zero-field step can be performed after in-field steps of the same temperature, to identify pTRM tails (Riisager & Riisager, 2001). Methods utilising a zero-field step can also check that the specimen's ability to acquire a pTRM across a given blocking range has not altered, after subsequent heating to a higher temperature, by including a second in-field step at the lower blocking range (Tauxe et al., 2018). This is

known as a pTRM check (Figure 1.5) and it will be used throughout Thellier experiments presented in this study.

Additional treatment steps have also been developed that attempt to remove a large proportion of the NRM of a specimen that is held by MD grains (Schmidt, 1993; Yamamoto et al., 2003). The most commonly used of these is an AF cleaning step prior to each step of the palaeointensity experiment. This procedure looks to make use of the low coercivity of MD grains by demagnetising them through exposure to a weak AF treatment (Schmidt, 1993).

Despite best efforts to improve traditional thermal Thellier methods, specimens often prove unsuitable and so experiments are associated with high failure rates (Carvallo et al., 2006; Paterson et al., 2010). Additional Thellier-style methods have been developed in an attempt to address this, primarily focusing on reducing laboratory alteration. Two such methods are the microwave method (Hill & Shaw, 1999; 2000; Shaw et al., 1996) and single crystal analysis (Cottrell & Tarduno, 1999; 2000). Microwave heating aims to reduce bulk specimen temperatures, and thus thermochemical alteration, by directly targeting ferromagnetic particles. Through this direct excitation, bulk temperatures remain relatively low throughout the duration of an experiment (Hill & Shaw, 2000; Gratton et al., 2005). In single crystal analysis, plagioclase crystals are isolated that contain titanomagnetite inclusions (Cottrell & Tarduno 1999; 2000). This approach aims to take advantage of the greater resistance of plagioclase to thermochemical alteration, than that of clays that are often common throughout bulk specimens. Neither method is without its limitations (Borlina et al., 2020; Grappone et al., 2020), providing no guarantee of improved success. In addition, specialist equipment is required for both of the outlined methods. The Geomagnetism Laboratory at the University of Liverpool houses the 'Tristan' 14 GHz microwave system, but operational difficulties encountered across the time in which this study was conducted resulted in no palaeointensity experiments being conducted via this method.

Shaw Method

The Shaw method (Shaw, 1974; Kono, 1978; Rolph & Shaw, 1985) aims to overcome the violation of the equivalent proportionality constants that occurs as a consequence of laboratory-induced alteration, by correcting for the effect. In addition, single step TRMs are imparted to reduce the amount of heating and cooling cycles that a specimen is exposed to. In theory, this approach reduces the likelihood of laboratory induced alteration occurring when compared with exposing a specimen to a stepwise heating protocol.

The palaeointensity estimate is determined by comparing the AF demagnetisation spectra with that of subsequent laboratory-imparted TRM (Figure 1.6). This is essentially equivalent to the Arai plot slope described for Thellier experiments. The degree of alteration experienced during laboratory heating is estimated by comparing the demagnetisation spectra of an ARM imparted prior to and after the acquiring and demagnetisation of the TRM (Figure 1.6). The theory is, that if no alteration has occurred during the heating process, the two ARM spectra should be identical as the remanence carriers are unchanged. The difference in the two ARM spectra is determined for each AF demagnetisation step and applied as the correction to the TRM. Final palaeointensity estimates are determined using the slope of the NRM spectra versus the corrected TRM

spectra (Figure 1.6). The application of this correction relies on the assumption that ARM is equivalent to TRM, and that any change in the specimen's ability to record an ARM will be reciprocated in the TRM acquisition.

The double heating technique (DHT) was developed as a validity check for the ARM correction (Tsunakawa & Shaw, 1994), and is now a part of the standardised method when conducting a Shaw experiment (e.g. Lloyd et al., 2021a). The process involves a repeat of the previous process with a second TRM and subsequent ARM imparted and AF demagnetised. The check is said to pass, and the alteration correction to have worked, if application of the second alteration correction results in linearity between the now corrected second TRM with the first imparted TRM (Tsunakawa & Shaw, 1994).

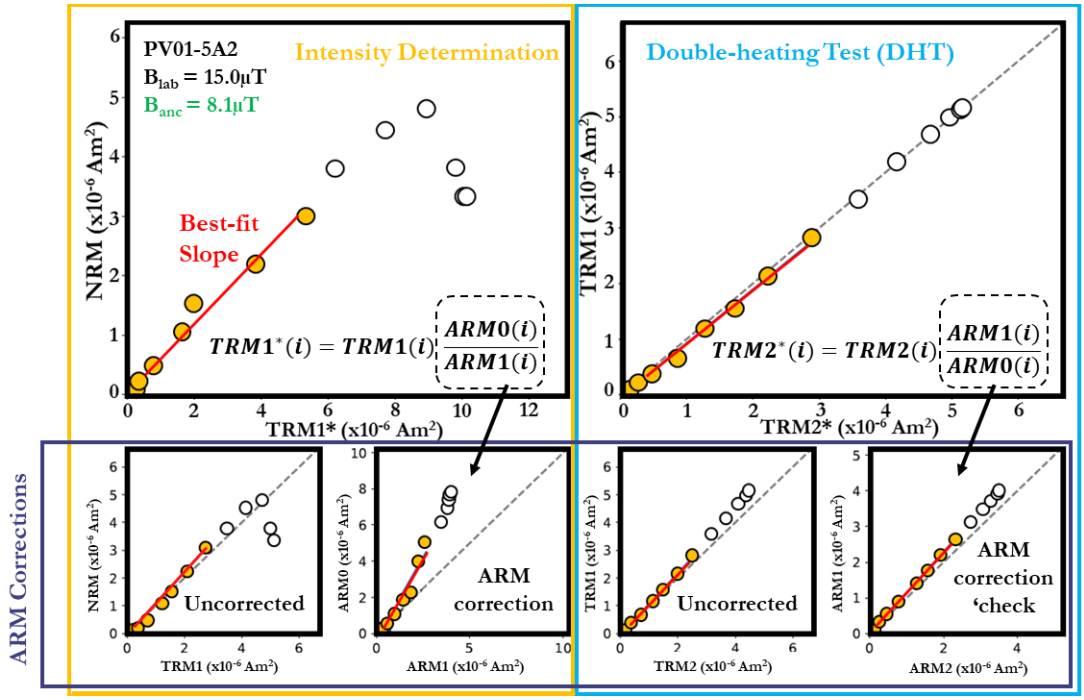

Figure 1.6: Example analysis plots used in a Shaw-DHT experiment. Data in this example comes from results of a specimen analysed in ***Chapter 4****. Left column (yellow) displays the corrected M_{NRM}/M_{lab} plot, from which the palaeointensity estimate is determined (Equation 1.6), and the associated ARM correction (purple row). Right column (blue) displays results of the second heating step after the application of the ARM correction, and the correction itself (purple row).*

Pre-treatment of specimens, through low-temperature demagnetisation (LTD), has been proposed as an additional step to minimise MD contributions (Yamamoto et al., 2003). This approach could also be applied to specimens subjected to a Thellier style experiment, but as treatment must be applied prior to each step this further increases the experiment time associated with the already time-consuming Thellier method (e.g. Fukuma & Kono, 2016). As the Shaw method imparts full TRMs, less steps are involved but the process is still time-consuming. With conflicting findings on the improvements this has made to palaeointensity estimates (Lloyd et al., 2021b; Thallner et al., 2021; Mochizuki et al., 2004; Oishi et al., 2005; Yamamoto et al., 2007) and an effectiveness only for magnetite bearing rocks (Smirnov et al., 2017), it is beneficial to assess the nature of the specimens prior to starting the experiment to determine the likelihood of a need to reduce MD effects.

Calibrated pseudo-Thellier Method

The most effective way to mitigate the effects of laboratory induced alteration is to utilise a palaeointensity method that does not rely on imparting the specimen with a suite of pTRMs or a TRM. These methods are known as non-heating methods and the most commonly used of these is the pseudo-Thellier method (de Groot et al., 2013; Tauxe et al., 1995), a variation on the traditionally used Thellier method. In the absence of TRMs, the method imparts ARMs, utilising the coercivity range present within bulk specimens as an alternative to the blocking spectra. The process is relatively simple. It involves the step-wise AF demagnetisation of the NRM, followed by progressive ARM acquisition at the same AF steps, followed by a final step-wise AF demagnetisation (Paterson et al., 2016; Tauxe et al., 1995). In an analogous manner to the analysis of Thellier data, $NRM_{remaining}$ is plotted against ARM_{gained}, this time referred to as a pseudo-Arai plot.

Estimates from the pseudo-Thellier method only provide a relative palaeointensity value (Tauxe et al., 1995). This is due to the use of an ARM when imparting a laboratory field and the fact that the natural remanence being studied was acquired as a TRM. In order to obtain an absolute palaeointensity estimate, a calibration factor is required that accounts for this difference in remanence acquisition (e.g. de Groot et al., 2013; Paterson et al., 2016). This is not an intuitive issue, as the relationship between ARM acquisition and TRM cquisition is complex and has been shown to be grain size dependent (Yu et al., 2003). As such, best estimates of a suitable calibration factor have been determined empirically (e.g. de Groot et al., 2015; de Groot et al., 2016; Paterson et al., 2016). For this process, palaeointensity estimates are determined through the pseudo-Thellier method, on natural specimens where the strength of the geomagnetic field to which they were exposed during their formation is known. For this reason, historical or archaeological material is studied with expected field strengths determined from the international geomagnetic reference field (IGRF). Perhaps unsurprisingly, calibration factors determined by different authors display differences (de Groot et al., 2013; Paterson et al., 2016; Yu, 2010). As such, consideration should be given to the choice of calibration factor when taking advantage of the calibrated pseudo-Thellier method.

The main drawback of pseudo-Thellier methods comes back to the use of an ARM in the place of a TRM. ARM acquisition displays a strong dependence on grain size (Maher, 1988). As such, the relationship between the laboratory imparted ARM and the natural TRM will vary between specimens, depending on the grain size distribution of the specimen. The resulting uncertainty in final palaeointensity estimates is demonstrated by the large uncertainty associated with the most recently derived calibration factor (3.280 ± 0.828, Paterson et al., 2016). When this error is propagated through, it results in an uncertainty in the final palaeointensity estimate of ~25%. For this reason, it is inadvisable to obtain palaeointensity estimates via the pseudo-Thellier method in isolation (Thallner et al., 2021).

Sample Selection & Ideal Recorders

Comparing the experiences of Koenigsberger and Thellier, when first attempting to obtain estimates of ancient geomagnetic field strength, it is evident that obtaining successful results from geological material is highly challenging. Koenigsberger conducted experiments on a wide range of rock types including basalts, andesites, granites, granodiorites, gabbros, and diabases (Dunlop, 2011), but ultimately produced no

successful palaeointensity estimates. Conversely, by being selective with the studied material, Thellier achieved much greater success that ultimately resulted in an understanding of the properties and behaviours that a material must exhibit to achieve results. Despite efforts to overcome difficulties in obtaining palaeointensity estimates from non-ideal recorders, some of which have been discussed, the most effective way to ensure the success for a palaeointensity experiment is to conduct them on the type of specimens around which they were developed. Such specimens contain a high concentration of SD grains that are unlikely to have changed in such a manner to have altered their associated constant of proportionality and are unlikely to experience such changes during laboratory heating.

Such material is rare geologically speaking, but by considering the range of processes involved in rock formation, and the effects of depositional environments, the likelihood of observing more idealised behaviour can be increased. Igneous rocks that experienced a faster rate of cooling are more likely to contain ferromagnetic grains whose size falls within typical SD size ranges (Özdemir, 2007). In this respect, lava flows are generally more favourable than intrusive bodies, though the thickness of the igneous body is also a factor for consideration. Composition of an igneous body can also be important. Mafic rocks contain a greater proportion of iron bearing minerals, and iron-oxides and iron-sulphides are known to be the most dominant ferromagnetic minerals found in the geological record (Bernát, 1983). Increased iron content increases the likelihood of specimens exhibiting strong magnetisations, and so changes during demagnetisation are more distinguishable at the resolution of magnetometers.

Consideration of the environment to which an outcrop has been exposed to since its formation can provide insight into the likelihood of rocks in their current state having at least a similar constant of proportionality to that possessed at the time of their formation. Alteration affects the chemical composition, size, and shape of grains, all of which will affect their ability to acquire a remanence (Dunlop & Özdemir, 1997). For this reason, specimens acquired from submarine environments, areas of intense deformation, or regions subjected to prolonged hydrothermal activity associated with volcanic processes are more likely to result in non-ideal behaviour. This is without the added complication of considering that alteration can affect primary TRMs so that remanence is then held by a TCRM (Draeger et al., 2006; Dunlop & Özdemir, 1997; Fabian, 2009; Shcherbakov et al., 2019). Reducing the likelihood of variation in the proportionality constant during laboratory heating is more difficult but selecting specimens more likely to contain end-member states of a solid solution series could reduce laboratory induced changes. For example, the common iron-oxide magnetite is the end member of the solid solution series of the iron-titanium oxide, titanomagnetite (Dunlop & Özdemir, 1997). During initial cooling, titanomagnetites commonly experience high-temperature oxidation that pushes their composition closer to pure magnetite. Once cooled sufficiently, this oxidation process stops and the titanomagnetite composition at this point remains (Dunlop & Özdemir, 1997). When heated further under laboratory conditions, titanomagnetite can experience further high-temperature oxidation that would ultimately result in magnetite (Draeger et al., 2006). In igneous rocks that have cooled sufficiently slowly, this effect is less likely. The caveat is that increased grain sizes, and thus MD grains, are also likely to be more common.

When these factors are considered in unison, sub-aerial, basaltic lava flows appear a favourable lithology that may result in successful palaeointensity determinations. The palaeointensity record reflects this, with sub-aerial basalts the most common combination of rock-unit and lithology from which palaeointensity results have previously been obtained (PINT v8.0.0, Bono et al., 2021).

Records of the Palaeomagnetic Field

Average polarity reversal frequency, palaeointensity, and directional PSV are the most commonly described characteristics of the palaeomagnetic field (Butler, 1992; Tauxe et al., 2018). Of these, the evolution of average reversal frequency throughout geological time is the most well-defined (Bono et al., 2021; Doubrovine et al., 2019; Ogg, 2012). As discussed, obtaining palaeointensity estimates is complicated by MD effects and alteration. Reliable palaeomagnetic directions can still often be acquired from similarly affected rocks (Dunlop & Özdemir, 1997). The other central reasoning behind a substantially more greatly populated directional record is that palaeomagnetic directions can be obtained from both sedimentary and igneous records. The fundamental requirement in determining absolute palaeointensity estimates, that rock remanence was acquired as a TRM, makes sedimentary rocks unsuitable for such experiments. This is of great impact to potential palaeointensity targets, as sedimentary rocks are the most common rock type exposed at Earth's surface. Similarly, sedimentary rocks present difficulties in assessing directional PSV due to issues of age calibration and remanence smoothing (Johnson & McFadden, 2015), and an inability to account for measurement error (Biggin et al., 2008). Igneous units are often preferred, and are in fact required to analyse directional PSV in the manner previously outlined (Johnson & McFadden, 2015). Being an analysis of palaeomagnetic directions, MD effects and alteration are less of an issue than in palaeointensity experiments but, crucially, igneous units must have cooled sufficiently quickly so to have not averaged out secular variation (Johnson & McFadden, 2015). For these reasons, far fewer rocks are suitable for palaeointensity and PSV analysis than is the case for palaeomagnetic experiments.

Geomagnetic Polarity Timescale

Magnetostratigraphy is the study of the geomagnetic polarity reversals registered within a stratigraphic section (Ogg, 2012). Correlation of magnetostratigraphic sections with those from other localities, marine magnetic anomalies, and biostratigraphy has resulted in the Geomagnetic Polarity Timescale (GPTS, Ogg, 2012). Complemented with additional dating techniques, it provides the most comprehensive record of the changes in geomagnetic polarity throughout geological history. It is from this record, that the average polarity reversal rate can be estimated, commonly expressed as the number of reversals per million year (Myr^{-1}).

The GPTS is well documented, and constrained, back to the middle Jurassic (~160 Ma), due to the present-day occurrence of oceanic crust that formed back to this time (Figure 1.7). The detailed records of magnetic stripes either side of ocean ridges provide a template against which magnetostratigraphic sections can be compared. Much progress has been made in recent years to better define the GPTS during the Triassic (Haque et al., 2021; Kent et al., 2017, 2018, 2019; Li et al., 2016; Maron et al., 2019; Zhang et al., 2020). This work built upon an already well-developed polarity timescale, that arose due to the concerted efforts of palaeomagnetists, biostratigraphers, and cyclostratigraphers

(Ogg, 2012). Further back in geological time, the GPTS is dominated by the predominantly reversed polarity of the Permo-Carboniferous Reversed superchron (PCRS; ~318-265 Ma; Haldan et al., 2009; Opdyke & Channell., 1996). It is prior to the PCRS that the GPTS becomes much more uncertain (Figure 1.7; Hawkins et al., 2021; Hounslow, 2021; Ogg, 2012; van der Boon et al., 2022). Recent reviews of Carboniferous (358.9-298.9 Ma; Ogg, 2012; Hounslow, 2021) and Devonian (419.2-358.9 Ma; van der Boon et al., 2022) magnetostratigraphy concluded that, with the currently available data, it is impossible to construct full, detailed polarity timescales. Reversal records then further deteriorate with minimal magnetostratigraphy available for the Silurian (Hounslow et al., 2021). Recent progress has been made to Ordovician and Cambrian records, but polarity timescale construction is still very much in its infancy (Hounslow et al., 2021; Pavlov & Gallet, 2020).

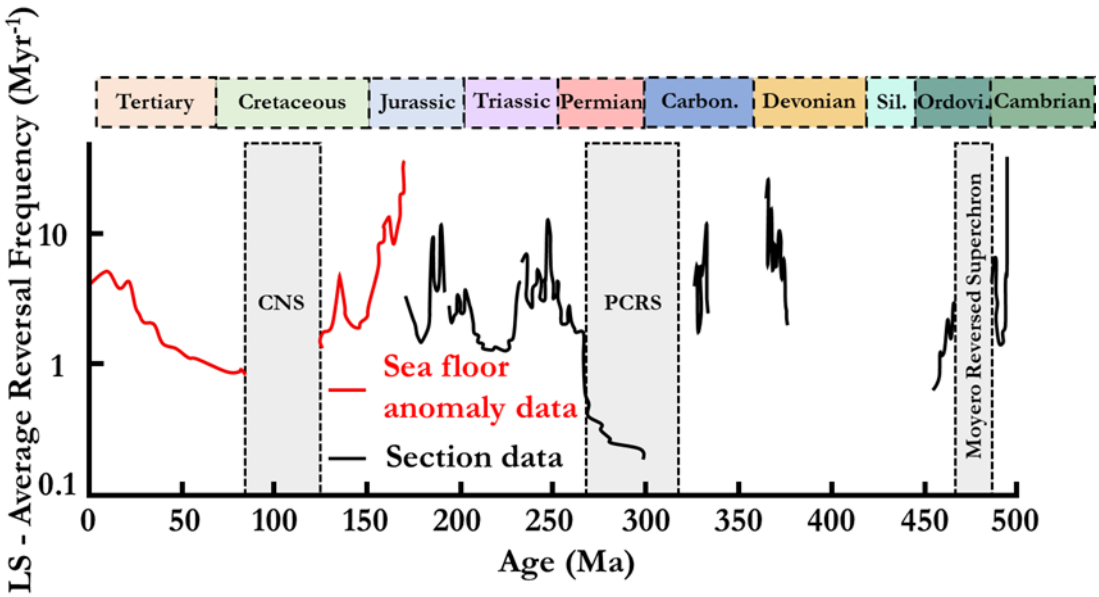

Figure 1.7: Average polarity reversal rate for the last 500 Ma. Rates presented on a log scale with the source of data highlighted, sea-floor (red) or terrestrial stratigraphic sections (black). Geological periods from across this time highlighted (Ogg, 2012). Figure modified from Hounslow et al. (2018), who utilised LOCFIT estimating procedures (Loader, 1999) to construct reversal frequency model.

As all characteristics of the geomagnetic field fundamentally result from the geodynamo process, it has long been postulated that relationships may exist between them (e.g. Biggin et al., 2008; Gubbins, 1987; McFadden et al., 1991; Pal, 1991; Sprain et al., 2015; Tarduno et al., 2001). Average polarity reversal frequency has been hypothesised to be correlated with equatorial VGP dispersion, and inversely correlated with average palaeointensity (Doubrovine et al., 2019; Gubbins, 1987; McFadden et al., 1991). Observing such relationships in the palaeomagnetic records, would provide crucial evidence to support such hypotheses. With the GPTS lacking detail and clarity prior to the onset of the PCRS (Figure 1.7; Ogg, 2012), constraining such relationships through the use of palaeomagnetic records further back in geological time becomes difficult. Therefore, this study focuses solely on the evolution of the geomagnetic field across the last ~320 Ma. By identifying and addressing gaps in our understanding of the evolution of palaeointensity and PSV across this time, direct comparisons between the global records of the different palaeomagnetic characteristics will become more feasible and insightful.

Palaeointensity Record

Databases documenting palaeointensity data have been constructed separately for the last 50 Kyr (GEOMAGIA50, Brown et al., 2015), and the rest of geological time (PINT, Biggin et al., 2009; 2015; Bono et al., 2021; BOROKPINT WDB, e.g. Perrin et al., 1998), due to the relative abundance of data describing the more recent geomagnetic field. The data contained within the Palaeointensity (PINT) database and the World Paleointensity Database from Borok Geophysical Observatory, can be used to assess long-term variations and trends in geomagnetic field strength. There is huge overlap in the data contained within the two databases, but the PINT database has been updated most recently (Bono et al., 2021). The major update also resulted in changes aimed at addressing data quality. Superseded data were highlighted, demonstrably unreliable data were removed, and the quality of each palaeointensity estimate was assessed (Bono et al., 2021). The latter was achieved, by assigning each estimate a quality of palaeointensity (Q_{PI}) score (Biggin & Paterson, 2014). This is a qualitative assessment, with criteria that aim to ensure that assumptions of palaeointensity experiments are fulfilled. For these reasons the PINT database is preferred throughout this study.

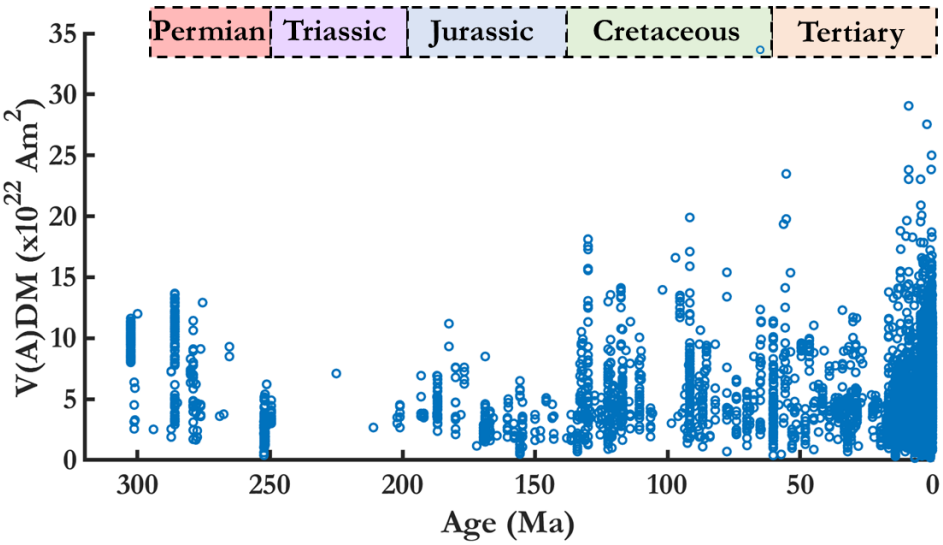

Figure 1.8: Palaeointensity record for the last 320 Ma. V(A)DM data from PINT v8.0.0 with a Q_{PI} score ≥ 1. Geological periods from across this time highlighted (Ogg, 2012).

Within PINT v8.0.0, there is a general decrease in the density of available palaeointensity data, going back across geological time (Bono et al., 2021). In the recent review of the database, a total of 1,572 estimates were available from 66-10 Ma. In comparison, the significantly longer Mesozoic (252-66 Ma) contained just 688 entries. Of these, just 3 palaeointensity estimates described the strength of the geomagnetic field between ca. 250 Ma and 202 Ma (Figure 1.8). This highlights the Triassic as a uniquely poorly understood time period with regards to palaeointensity behaviour since the PCRS, despite previous suggestions to populate the palaeointensity record across this time (e.g. Anwar et al., 2016; Biggin & Thomas, 2003). The availability of palaeointensity data improves going back to 320 Ma, with the PCRS described by 232 entries (Figure 1.8). Crucially behaviour is unaccounted for ca. 318-305 Ma, however (PINT v8.0.0, Bono et al., 2021).

Directional PSV

In an attempt to describe, and explain, the latitudinal dependence observed in the angular dispersion of the palaeomagnetic field (Cox, 1962; Creer, 1962a, 1962b), McFadden et al. (1988) developed a statistical model termed Model G. It was proposed that the parameters defining this model (*a* and *b*) would correlate with the average reversal frequency across the time interval that was being described. A higher Model G *a* parameter and a reduced *b*/*a* ratio were suggested to be characteristic of superchrons, when compared with those of frequently reversing time intervals. These relationships were broadly supported by a subsequent study that estimated such model parameters for discrete time intervals, based on the differences in their apparent average polarity reversal frequency, that were continuous between 180 Ma and present-day (McFadden et al., 1991).

Subsequent studies have reassessed PSV during many of the time intervals studied by McFadden et al. (1991), utilising more greatly populated, and higher quality databases (Biggin et al., 2008; Cromwell et al., 2018; de Oliveira et al., 2021; Doubrovine et al., 2019; Engbers et al., 2022; Franco et al., 2019; Opdyke et al., 2015). With the addition of a PSV study for the PCRS (de Oliveira et al., 2018), and the slight extension of some studies back in geological time (Doubrovine et al., 2019), the only time interval during the last ca. 320 Ma for which PSV has yet to be assessed is between 265 Ma and 198 Ma.

Triassic & Permian Palaeomagnetic Field Behaviour

Evaluation of the palaeomagnetic records representing the last 320 Myr, highlights just how little is understood about geomagnetic field behaviour during the Triassic. The lack of previous focus in addressing the significant gap in the palaeointensity record is particularly surprising considering the potentially significant consequences of palaeointensity across this time. Recent estimates of a weak palaeomagnetic field around the Permo-Triassic Boundary (PTB; ca. 251.9 Ma; Ogg, 2012) (Anwar et al., 2016), led to the suggestion that the Mesozoic Dipole Low (MDL) may have been a consistent feature from the PTB to the early Jurassic (201.3-174.1 Ma; Ogg, 2012). The MDL was originally proposed by Prévot et al. (1990), as an interval of anomalously weak palaeointensity between ~180 Ma-135 Ma, during which the VDM was 1/3 of its present-day value. Such a feature would be suggestive of a decoupling of the processes governing average reversal frequency, and the intensity of the field. This is because there are many distinct intervals, as defined by their average reversal frequency, across this time. This includes the time interval of Jurassic hyperactivity (~171-155 Ma; Ogg, 2012), during which apparent average reversal frequency was over twice that of any other comparably sized time interval over the last 320 Myr. The MDL is not a universally accepted feature of the palaeointensity record, however. Previous studies have suggested that palaeointensity across this time was in keeping with the long-term average (Selkin & Tauxe, 2000), or that the interval of weak intensity is restricted to the Jurassic hyperactivity, supporting the hypothesis of an inverse correlation between reversal frequency and palaeointensity (Kulakov et al., 2019).

A better definition of Triassic palaeointensity also has the potential to influence our understanding of long-term trends in geomagnetic field behaviour, and possible links with plate tectonic and mantle processes (Biggin & Thomas, 2003; Biggin et al., 2012; Driscoll & Olson, 2011). It was previously suggested that long-term variations in the V(A)DM record could be attributed to a chain of geodynamic processes, beginning with plate

reorganisation, that go on to influence convection in the outer core (Biggin & Thomas, 2003). Within this, palaeointensity variations since the Devonian were interpreted within the context of the supercontinent cycle of Pangaea. With the Triassic representing a significant portion of the lifetime of Pangaea, there was a shortage of palaeointensity data against which the modelled could be tested during the climax of the supercontinent cycle.

In a similar fashion, new Triassic palaeointensity estimates could help to better define the proposed 200 Myr cycle of palaeomagnetic behaviour. The original proposal (Driscoll & Olson, 2011) was based on the knowledge that the middle of the two most well-established superchrons, the CNS and the PCRS, are separated by approximately 200 Myr (Figure 1.7), comparable to the timescale on which mantle convection occurs (Biggin et al., 2012; Driscoll & Olson, 2011; Courtillot & Olson, 2007; McFadden & Merrill, 1984). This hypothesis was tested by comparing palaeomagnetic observations with the outputs of a geodynamo model whose CMB conditions were varied, in an attempt to simulate mantle forcing (Driscoll & Olson, 2011). The model simulated behaviour moving out of one superchron and into another, comparable to the behaviour occurring from the middle of the PCRS to the middle of the CNS. A more complete understanding of the evolution of the strength of the geomagnetic field throughout this time, would provide a more direct comparison against which the modelled behaviour could be compared.

The originally proposed relationship between PSV and reversal frequency (McFadden et al., 1991) becomes less clear when evaluating the findings of the most recent PSV studies (Biggin et al., 2008; Cromwell et al., 2018; de Oliveira et al., 2018; Doubrovine et al., 2019; Franco et al., 2019), and conclusions on the extent to which such a relationship exists are conflicting (Doubrovine et al., 2019; Franco et al., 2019). The direct relationships between average reversal frequency and Model G shape parameters appear unlikely (Doubrovine et al., 2019), which also brings into question the physical interpretations that were associated with them (McFadden et al., 1988). Defining PSV during and around the Triassic would result in a near-complete PSV record from discrete time intervals across the last 320 Myr. Each time interval, as defined by changes in apparent average polarity reversal frequency, will have been subject to PSV analysis, although PSV between 84 Ma and 23 Ma has not been re-evaluated since the original work of McFadden et al. (1991). Evaluating a near-complete PSV record across the last 320 Ma, with the reversal frequency record, and a palaeointensity record in which the Triassic was more well-defined, could provide greater insight into what has been revealed as more complex a relationship than originally proposed.

Despite having previously been subjected to numerous palaeointensity investigations (Bol'shakov et al., 1989; Cottrell et al., 2008; Garcia et al., 2006; Krs, 1967; Solodovnikov, 1992a; 1992b; 1992c; Thomas et al., 1995; 1997; 1998; Usui & Tian, 2017) and a study into its PSV (de Oliveira et al., 2018), uncertainties remain regarding palaeomagnetic behaviour during the PCRS. As well as a lack of palaeointensity data representing the last 13 Myr of the PCRS, the reliability of the data that is available for the PCRS has been questioned (e.g. Cottrell et al., 2008; Hawkins et al., 2021). The PCRS appears to be represented by two populations of palaeointensity data that present a strong and weak palaeomagnetic field, respectively. When all of this data is averaged, the PCRS appears to have been a time of relatively high intensity. It has been suggested that the actual strength of the PCRS field was in fact higher than this average, based on estimates from single crystal analysis (Cottrell et al., 2008). The reasoning being that whole rock specimens were

likely to produce underestimates due to alteration effects. Conversely, filtering of palaeointensity data for the PCRS, via the Q_{PI} framework, results in a much-reduced field intensity that is more in keeping with long-term behaviour (Hawkins et al., 2021). This has been used previously, to suggest that high palaeointensity estimates associated with the PCRS may be biased due to MD effects (Hawkins et al., 2021). There are additional complications surrounding our understanding of the palaeomagnetic field during the PCRS, due to the inclusion of sedimentary derived data in the previous PSV study on this time interval. Sedimentary formation can lead to smoothing of secular variation during remanence acquisition (Johnson & McFadden, 2015), that often makes them unsuitable for statistical analysis as they are not spot-readings. Removal of sedimentary data from this study reduces the number of VGP dispersion estimates to a number too low to provide meaningful insight (Franco et al., 2019).

Overall Study Aims & Approach

This study aims to accomplish a more complete understanding of the relationships between reversal frequency, palaeointensity, and PSV, and their evolution through geological time, through a multi-method approach, with an initial focus on better defining palaeomagnetic field behaviour throughout the Triassic. In doing so, this thesis aims to answer the following questions; **how was the geomagnetic field behaving during the Triassic** and **how has long-term behaviour of the geomagnetic field evolved across the last 320 Myr?** The process for this is two-fold. Firstly, to conduct a PSV study on the end Permian and Triassic that utilises pre-existing, published directional data. In addition to this, new PSV analysis of the PCRS is conducted that utilises the same method as previous PSV studies, allowing for a more direct comparison of PSV behaviour over the last 320 Myr. Such an approach is intended to answer the sub question: **what was the global variability of the geomagnetic field between 265 and 200 Ma?** Secondly, to conduct palaeointensity experiments, utilising a range of palaeointensity methods, on Triassic aged rocks that are not associated with its boundaries, with the primary aim of answering the sub question: **how strong was the geomagnetic field during the Triassic at localities situated in the northern and southern hemispheres?** Due to a lack of known sub-aerial basalt lavas of such an age, these experiments are conducted on less traditionally used lithologies. This simultaneously makes these studies investigations into the viability of non-traditionally used lithologies in obtaining accurate palaeointensity estimates.

Finally, by utilising improved records of palaeomagnetic observations across the last 320 Ma, statistical models are generated for discrete time intervals that represent distinct reversal frequency regimes. Within this section of the study, the focus is on the sub question: **what insight can statistical models provide into long-term evolution of the geomagnetic field?** These statistical models describe the geomagnetic field as a suite of spherical harmonic Gauss coefficients. Their construction is more fundamental than the previously discussed Model G as they represent the spherical harmonic expansion of the geomagnetic potential. They also have the additional advantage of being able to predict other characteristics of the palaeomagnetic field than those on which the models are based. This study generates optimised statistical models for a given time interval by minimising the misfit to palaeointensity and PSV observations from across that time. In doing so for times of different apparent reversal frequency, comparing trends in the three main descriptive characteristics of the palaeomagnetic field becomes easier, and it

provides greater insight into the relationships that may exist between them. Establishing better relationships between these characteristics would provide greater insight into the processes that generate the geomagnetic field. It also has the potential to provide clarity on uncertain or unknown palaeomagnetic behaviour such as the MDL, palaeointensity during the PCRS, and relative polarity reversal rates further back in geological time where the GPTS is currently lacking.

Chapter 2. Analysing Triassic and Permian geomagnetic palaeosecular variation and the implications for ancient field morphology

This chapter has been published in Geochemistry, Geophysics, Geosystems in November 2021 (Handford et al., 2021).

Abstract

Studying palaeosecular variation (PSV) can provide unique insights into the average morphology of the geomagnetic field and the operation of the geodynamo. Although recent studies have expanded our knowledge of palaeomagnetic field behaviour through the late Mesozoic, relatively little is known regarding the Triassic period (ca. 251.9-201.3 Ma). This study compiles the first Triassic virtual geomagnetic pole (VGP) database for the analysis of PSV, as part of a longer Post-Permo-Carboniferous Reversed Superchron (PCRS) time interval (265-198 Ma). VGP angular dispersion and its dependence on apparent palaeolatitude, are compared against a new PCRS compilation and published PSV compilations for intervals across the last ~320 Ma. We find that the Post-PCRS displays near latitudinal invariance of VGP dispersion while the PCRS displays very strong latitudinal dependence. PSV behaviour during the Post-PCRS appears indistinguishable to that previously reported for the interval preceding the Cretaceous Normal Superchron (Pre-CNS; 198-126 Ma). The near-constant behaviour between time intervals with significantly different apparent average polarity reversal frequencies does not support a suggested relationship between VGP dispersion and reversal frequency. The dispersion observed for the PCRS is consistent with the results of previous studies and represents behaviour that is potentially unique over the last ~320 Ma. A recently published approach to obtain a description of field morphology from equatorial VGP dispersion shows the PCRS geomagnetic field to have been more strongly axial dipole dominated than any interval since. This observation may be causally linked to the PCRS being the longest known superchron in the Phanerozoic geomagnetic polarity timescale.

Introduction

The geomagnetic field exists as a consequence of a dynamic system and shows variations across a range of timescales (Johnson & McFadden, 2015). Long-term behaviour is often described in terms of the intensity, reversal rate, morphology, and stability of the field. As all of these features are a result of the geodynamo, it follows that their variations should be intrinsically linked and that relationships may exist between them (Biggin et al., 2008; Gubbins, 1987; McFadden et al., 1991; Pal, 1991; Sprain et al., 2015; Tarduno et al., 2001). Identifying such relationships could allow for inferences regarding one aspect of the Earth's field behaviour, for which there is a sparse data population, based on knowledge of another over the same time. This could be of particular use in characterising reversal frequency and in providing a constraint on core-mantle interactions (Biggin et al., 2012). Obtaining a direct understanding of reversal frequency requires complete, and ideally well-dated, magnetostratigraphic sections which, are not available for most of Earth's history (Ogg, 2012). This is particularly the case for the Precambrian as biostratigraphy cannot be used and radiometric dating comes with large uncertainties (Bleeker. 2004). There is also the potential to obtain a greater understanding of geodynamo evolution. Periodic variations in the reversal record have been observed on similar time-scales to those of mantle processes; this constitutes support for the hypothesis that core-mantle boundary (CMB) heat flux variations influence geomagnetic field behaviour (Biggin et al., 2012; Tarduno et al., 2005).

Earth's polarity reversal record is largely well-defined since the latest Carboniferous (~320 Ma; Hounslow et al., 2018) and demonstrates extreme long-term variations. During superchrons, reversals are essentially absent and the Earth's magnetic field exhibits a stable polarity for tens of millions of years. Two such events have been identified in the last 350 Ma, the Permo-Carboniferous Reversed Superchron (PCRS; ~318-265 Ma; Haldan et al., 2009; Opdyke & Channell., 1996), and the Cretaceous Normal Superchron (CNS; 126-84 Ma; Ogg, 2012). In contrast, an apparent average reversal rate of ~11 per Myr (Myr^{-1}; Ogg, 2012) is assigned to a time interval referred to as the Jurassic hyperactivity period (~171-155 Ma; Ogg, 2012). The Triassic (ca. 251.9-201.3 Ma; Ogg, 2012) has a relatively incomplete reversal record (Hounslow et al., 2018). Although it is sufficiently well understood to provide accurate estimates of reversal frequency across the entire period, its incomplete nature has resulted in various proposed magnetostratigraphic sequences (Hounslow et al., 2018; Hounslow & Muttoni., 2010; Maron et al., 2019). The lack of an agreed upon geomagnetic polarity timescale (GPTS) for the Triassic has hindered its use for timescale definition, spawning the suggestion to describe Triassic magnetostratigraphy as a set of multichrons (Lucas, 2010; Lucas & Tanner., 2014). Such a description would contain less information than would be available from traditional chron to chron correlation, highlighting that although the number of reversals occurring during the Triassic is reasonably well constrained, the exact ages of the reversals are not.

The Earth's magnetic field is often described as a geocentric axial dipole (GAD). This description is believed to be accurate when a sufficient amount of time can be averaged (Schneider & Kent., 1990) but non-dipole contributions are ever present in the instantaneous field configuration. Studying the dispersion of virtual geomagnetic poles (VGPs) can provide an estimate of the extent of this contribution (Biggin et al., 2020; Veikkolainen & Pesonen, 2014). Analysing PSV in this way provides a measure of field stability and many recent studies have investigated a possible association between PSV and reversal frequency (Biggin et al., 2008; de Oliveira et al., 2018; Doubrovine et al., 2019; Franco et al., 2019; Veikkolainen & Pesonen, 2014).

Investigations into the relationship between PSV and reversal frequency have tended to focus on the CNS, PCRS, and Jurassic due to their nature as extreme high and low reversal frequency regimes (Biggin et al., 2008; de Oliveira et al., 2018; Doubrovine et al., 2019). Similarly, Franco et al. (2019) investigated PSV in the Illawarra Hyperzone of Mixed Polarity (IHMP; ~266.7-228.7 Ma), beginning after the PCRS, stating an average reversal rate of ~5.9 Myr^{-1}. Many of these studies have focused on sequential time periods resulting in a near continuous record of VGP dispersion from the CNS going back to the PCRS, with the exception of almost the entirety of the Triassic. Despite this, it is still unclear whether a relationship does exist between PSV and reversal frequency. McFadden et al. (1991) concluded that low reversal regimes would exhibit lower VGP dispersion at low latitudes, and a high latitudinal dependence. Both Biggin et al. (2008) and Doubrovine et al. (2019) described the occurrence of this behaviour during the CNS, while de Oliveira et al. (2018) obtained a similar, more extreme result for the PCRS. Other results suggest near latitudinal invariance during the Jurassic (Doubrovine et al., 2019) and IHMP (Franco et al., 2019) and therefore, it might be claimed that studies of extreme reversal regimes support the original claim of McFadden et al. (1991). Discrepancies appear when comparing these results with those from more recent time intervals, however. Doubrovine et al. (2019) found that the relationship between PSV and latitude for the last 5 or 10 Ma was similar to that observed for the superchrons, despite average reversal frequencies of ~4.4-4.8 Myr^{-1}. In contrast, Franco et al. (2019) concluded that the last 5 Ma exhibited comparable behaviour, and a similar reversal rate, to that which they described for the IHMP.

In addition to our lack of knowledge regarding PSV behaviour during the Triassic, and historically uncertain magnetostratigraphy, there is a significant shortage of palaeointensity data for this period. The Triassic is a period bounded by mass extinction events that coincided with eruptions of huge volumes of flood basalts (Ogg et al., 2016). It also comprises an interval of time in which all continents were arranged as the supercontinent Pangaea, with peak assembly during the middle Triassic (Lucas, 2005). This tectonic setting resulted in little large-scale volcanism after the Siberian Traps (ca. 252-251 Ma; Burgess et al., 2017; Wignall et al., 2015) until the eruption of the Central Atlantic Magmatic Province (CAMP; ca. 201.5 Ma; Ogg et al., 2016), associated with the break-up of Pangaea (Benton, 2016). This provides an explanation as to why a relatively minor proportion of known Triassic rocks are volcanic (Lucas, 2005). As a result, there is a ~50 Ma gap in the palaeointensity record (Anwar et al., 2016) due to the nature of absolute palaeointensity experiments which are heavily reliant on volcanic recorders and their associated intrusions (Donadini et al., 2007; Lerner et al., 2017). An incomplete reversal record, very few palaeointensity estimates, and a lack of PSV analysis have all resulted in a limited understanding of geomagnetic field behaviour during the Triassic when compared to other periods since the latest Carboniferous. As we will demonstrate here, however, there are a sufficient number of Triassic-aged rapidly cooled igneous units distributed globally to provide a first order description of the geomagnetic field through this period.

The last decade has provided many investigations into Triassic magnetostratigraphy with sufficient progress to justify a revised Triassic geomagnetic polarity timescale (GPTS; Haque et al., 2021; Kent et al., 2017, 2018, 2019; Li et al., 2016; Maron et al., 2019; Zhang et al., 2020). These advancements present the opportunity to analyse Triassic PSV behaviour within the context of the average reversal frequency for the period. Such an investigation would result in a continuous record describing PSV behaviour from the PCRS through to the CNS, whilst also facilitating an investigation into PSV behaviour between two prominent features of the reversal record: the PCRS and the high reversal

rate values associated with the Jurassic. At the same time, this offers the potential to categorise geomagnetic field behaviour during a time period still characterised by much uncertainty. In this study, an updated Triassic palaeomagnetic directional and VGP database is presented, using results taken from existing publications, and combined with data previously compiled for the late Permian. An analysis of VGP dispersion at different palaeolatitudes for this newly studied time interval, (265-198 Ma) referred to as the "Post-PCRS", is compared to data from a revised PCRS database using the same analytical process. Furthermore, comparisons are then carried out against previously published databases for the Pre-CNS (198-126 Ma), CNS (Doubrovine et al., 2019), and the last 10 Ma (Cromwell et al., 2018) before a discussion on the pattern of VGP dispersion with latitude during times of differing reversal frequencies and how this may relate to field morphology.

Method

Sourcing Data

Information from PSV analysis comes in two distinct forms: time series of magnetic field variations, such as information from long sediment cores, and statistical descriptions which rely on geologically instantaneous spot readings, such as those associated with lava flows (Johnson & McFadden, 2015). Data derived from sedimentary rocks are susceptible to smoothing of the recorded field during remanence acquisition, resulting in at least partial averaging of PSV (Lund & Keigwin, 1994) and inclination shallowing, affecting the final estimate of palaeolatitude (Tauxe & Kent, 2004). The general consensus is that igneous rocks, and in particular volcanic rocks, are a more reliable source of PSV information in older geologic periods (Biggin et al., 2008; Cromwell et al., 2018; McFadden et al., 1988), provided that they cooled quickly and that the group of rocks spans sufficient time to provide representative variability. As such this study exclusively uses data from igneous rocks, avoiding large, slow cooling intrusions that would not provide a spot-reading of the field. All datasets have been taken from lava flows, sills, dykes, or pyroclastic flow deposits with supporting evidence for fast cooling rates where appropriate and for the occurrence of welding when pyroclastic flow deposits have been used.

Triassic datasets were compiled from papers published up to and including those from March 2020. Most data arose from a literary search but a small number of datasets were sourced using the Global Palaeomagnetic Database (iggl.no/resources.html, Ivar Giæver Geomagnetic Laboratory). Datasets from the late Permian, after the PCRS, were sourced from the database compiled by Franco et al. (2019). The revised PCRS database was built around the work of de Oliveira et al. (2018) with the addition of a few new datasets. Following the approach of Biggin et al. (2008) site-mean directions of a similar age and geographic location were grouped into the same dataset.

After these initial constraints, both the PCRS and Post-PCRS databases were filtered using selection criteria in order to remove low quality data and potentially unsuitable studies. This study applied the selection criteria below. These are the same as those used by Doubrovine et al. (2019) but with a few additional requirements.

1. The age of the rock formation must be reasonably well constrained, preferably by the application of radiometric dating techniques. There must be no doubts that the dataset might not represent the geomagnetic field during the time interval to which it has been assigned i.e. the PCRS or Post-PCRS.

2. There must be no evidence that the characteristic remanent magnetisation (ChRM) directions are of secondary origin.

3. Data from igneous formations that were tectonically tilted or folded post-emplacement must have an associated structural correction. Where there was evidence of local block rotation between sampling sites, data were not used. A commentary outlining the reasoning behind the inclusion of each dataset, with respect to its tectonic setting, can be found in the supporting information (Table A.2).

4. Each dataset is composed of at least nine palaeomagnetic sites ($N \geq 9$), and each site-mean direction is calculated from the ChRM of a minimum of 3 independently oriented samples ($n \geq 3$).

5. ChRM components must have been isolated using stepwise demagnetisation techniques. Principal component analysis should have been utilised for at least one specimen per site and agree with any ChRM components inferred by other methods. This corresponds to a "demagnetisation code" greater than or equal to 3 (McElhinny & McFadden. 2000).

6. The uncertainties of the site-mean directions must be presented in the original study as either the Fisher concentration parameter (k) or the angle of 95% confidence about the mean direction (α_{95}).

7. The total Q score based on the first 6 Van der Voo criteria must be equal to or greater than 3.

8. All site-mean ChRM directions within a dataset have a k-value greater than or equal to 10.

In the supporting information, the effects of accounting for serial correlation and the removal of data derived from great circle analysis were considered, separately, for datasets which satisfied selection criteria 1-8. Serial correlation identifies cooling units that are likely representative of the same event in time, and as such may not be considered as individual palaeomagnetic data points (Cromwell et al., 2018; Watson & Berran, 1967). Meanwhile, obtaining directions from great circle analysis often results in the inability to obtain rigorous confidence limits for K (McFadden & McElhinny, 1988). The inclusion of great circle derived data has the potential to allow datasets to fulfil selection criteria 1-8 which may not have a well-defined Fisher concentration parameter and thus could be of lower quality than desired. In both cases the overall effects on the calculated VGP dispersions were minor (Figures A.1 & A.2). As a result, neither the inclusion of serial correlation or the exclusion of great circle derived data was utilised in the final data selection process due to the benefits associated with a greater N, and total number of datasets (Biggin et al. 2008).

Investigating Robustness with Additional Criteria

McElhinny & McFadden (1997) explored the possibility that PSV studies may be strongly biased by the quality of the data used, concluding that the resulting dispersion was at least partly due to the incorporation of lower-quality data. Additionally, the use of sampling site palaeolatitude during the conversion process of magnetic directions into VGPs causes

any latitudinal independent within-site dispersion of directions to result in latitudinal dependent VGPs (Biggin et al., 2008). This is mitigated by an inbuilt correction to the conversion process but, in order for it to be effective, n must be sufficiently large so that k is a good estimate of its true value (Biggin et al., 2008). In order to assess the robustness of the resulting VGP distribution, and the influence of data quality, further selection criteria have been applied to produce a second, higher quality database. These selection criteria have been chosen as they mitigate bias associated with low n and/or k values (Biggin et al., 2008).

9. ChRM site-mean directions used must have an associated estimated Fisher concentration parameter of at least 50 ($k \geq 50$).

10. Each site-mean direction is calculated from the ChRM of a minimum of 5 independent samples ($n \geq 5$).

The resulting datasets from the application of selection criteria 1-8 are termed Group 1 and where selection criteria 1-10 have been applied the datasets are termed Group 2. Group 2 datasets have been analysed in an identical process to those from Group 1 to ensure that a direct comparison of results is possible.

Measuring PSV

PSV is a measure of the variability of all of the geomagnetic field's observables; the most common way in which it is measured and assessed is by analysing VGP dispersion (Hulot & Gallet, 1996). This VGP dispersion, otherwise known as angular dispersion, is calculated using the following equation (Cox, 1970)

$$S^2 = \frac{1}{N-1}\sum_{i=1}^{N} \Delta_i{}^2 \tag{2.1}$$

where S is the angular dispersion, N is the total number of VGPs in a given dataset, and $\angle_i$ is the angular deviation of the i^{th} pole from the mean palaeomagnetic pole, in this case the mean VGP of the dataset.

The calculated VGP dispersion is the result of dispersion from two sources: a minor contribution from within-site dispersion, S_W, and a major contribution from between-site dispersion, S_B. S_W is the result of measurement errors and variations in the initial recording of the field. S_B is the dispersion between VGPs calculated from measurements at different sites due to the recording of a different field. S_B, therefore, is a measure of PSV and can be extracted by removing the contribution of S_W using the following equation

$$S_B{}^2 = S^2 - \frac{S_w{}^2}{n}. \tag{2.2}$$

In order to calculate S_W, an estimate of the precision parameter in pole space, K, is required. This is achieved by translating k, from directional space, under the reasonable assumption that the VGP distribution is Fisherian in nature.

$$K = k\left[\frac{1}{8}(5 + 18sin^2\lambda + 9sin^4\lambda)\right]^{-1} \tag{2.3}$$

Finally, S_W is approximated by the following equation

$$S_W \cong \frac{81}{\sqrt{K}} \tag{2.4}$$

and the contribution of within-site dispersion can be removed using Equation 2.2, isolating the VGP dispersion due to PSV. This process is carried out individually for each dataset in order to obtain an estimate of the dispersion associated with the PSV. This study used a non-parametric bootstrap in order to obtain 95% uncertainty estimates for S_B.

When conducting a study into VGP dispersion, it is desirable to remove VGPs that are likely to have resulted from excursional or transitional behaviour. The identification and removal of outlying VGPs is done in accordance with a cut-off angle. VGPs calculated using data from a time where the field was undergoing normal secular variation tend to cluster around a mean VGP, fit by a Fisherian distribution. Any VGPs lying farther from this mean VGP than the cut-off angle are deemed to be outliers and excluded. This separation between normal secular variation and that attributed to reversals is not grounded in a fundamental understanding of the physical system; reversals and excursions are probably natural outgrowths of normal secular variation. As measurements of S_B are strongly influenced by these outlying VGPs, however, and because the time that the field spends in such states is relatively short, they are removed. Moreover, it has been shown to be an effective approach to assessing characteristics of PSV produced by numerical dynamo simulations (Biggin et al., 2020). This study applies a variable cut-off (Vandamme, 1994), calculating the optimum $\measuredangle_{max}$ for the VGPs of a given dataset using the following equation

$$\Delta_{max} = 1.8S + 5. \tag{2.5}$$

Following the approach of Biggin et al. (2008) this study opts to use average magnetic latitude calculated from the angular distance between the mean VGP and the sampling site, rather than geographic palaeolatitude. The latter would require the use of plate reconstructions which would require some circular reasoning as they are often largely based on palaeomagnetic studies (Biggin et al., 2008).

Modelling VGP Dispersion

For ease of comparison with the results of previous studies (de Oliveira et al., 2018; Doubrovine et al., 2019), Model G (McFadden et al., 1988) has been used to parameterise the latitudinal dependence of PSV. It is widely accepted as a useful but imperfect descriptive tool (Doubrovine et al., 2019) and also has predictive power in determining the average axial dipole dominance of the ancient field (Biggin et al., 2020). Model G is described by the following equation

$$S_B = \sqrt{a^2 + (b\lambda)^2} \tag{2.6}$$

where a and b are known as the Model G shape parameters. These shape parameters have been determined by carrying out a least-squares fit between the estimated dispersion values and the model, and uncertainties in these coefficients were estimated using a jack-knife technique as carried out by McFadden et al. (1988).

Results

Datasets

The datasets that satisfied the Group 1 selection criteria for the Post-PCRS and PCRS time intervals are listed in Table 2.1. The corresponding site-level information is available in the supporting information (Datasets A.1 & A.2). Table 2.1 provides background

information regarding the lithology and rock units sampled, the source study, and country of origin. Most of the estimated ages presented for the Post-PCRS are the result of radiometric investigations; this is often not the case for the final PCRS datasets. Where there is no assigned numerical age, the age estimate was considered sufficient for the purpose of this study so long as the formation could be confidently attributed to the time interval in question. Within each dataset, the site co-ordinates associated with the site-mean directional information have been used; however, when this was not possible, the mean site location was attributed. In either case, average site co-ordinates are contained within Table 2.1 and displayed in Figure 2.1 along with the corresponding site identification code.

Also presented in Table 2.1 are the Van der Voo (1990) quality ratings assigned to each dataset, breakdowns of which can be found in the supporting information (Dataset A.3), the number of site-mean directions/VGPs, and the total number of samples per dataset.

Data that passed the two additional selection criteria (9 & 10) are presented in Table 2.2 for both the Post-PCRS and PCRS. This table provides the same information regarding the datasets as in Table 2.1 and is presented in the same format. For both time intervals there is a reduction in the number of datasets compared with the Group 1 results, as removal of site-mean data resulted in some datasets failing criteria 4. ($N \geq 9$). The reduction of site-mean data is displayed visually in Figure 2.2 with sites grouped according to their associated geological epoch. Overall the amount of site-level data decreased by about one-third after Group 2 selection criteria are applied (Figure 2.2)

Figure 2.2 also displays the ages of the studied and discussed reversal regimes, defined by their average polarity reversal rate which is represented by an accompanying reversal frequency model. The reversal frequency model was constructed using a 5 Ma sliding window and magnetostratigraphic data from Ogg (2012), with the exception of 250-200 Ma where the updated GPTS of Maron et al. (2019) has been used.

Both the Post-PCRS and PCRS databases display too great a hemispherical bias to make a formal assessment of equatorial symmetry. Since the available data did not support any significant asymmetry however, we decided to display VGP dispersions on one-hemisphere projections (Figures 2.3 & 2.4).

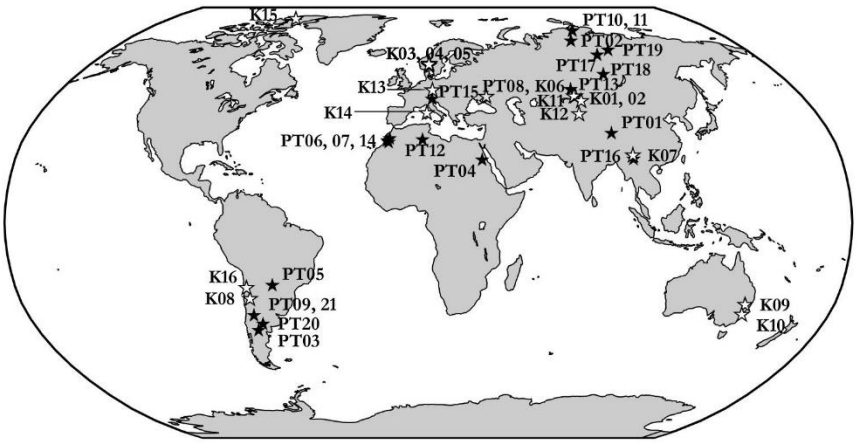

Figure 2.1: Sampling regions for the datasets contained in the Group 1 databases of the Post-PCRS and the PCRS. Black stars represent Post-PCRS datasets, white stars represent PCRS datasets. Accompanying site identification codes are referred to in Table 2.1.

Table 2.1: Post-PCRS and PCRS Group 1 datasets.

Site ID	Rock formation	Country	Lithology	Rock type	Lat (°N)	Long (°E)	Age (Ma)	N	n_{tot}	Q	Plat (°N)	S_B (°)	References
PT01	Qiangtang Block middle Triassic lavas	China	Basalt	Lava flow & volcanic breccia	33.5	92.0	241	28	219	5	23.6	12.6 +2.1/ -1.9	Song et al. (2020)
PT02	Norilsk Region Volcanics	Russia	Basalt	Lava flow	70.1	94.3	251	241	2039	5	61.0	25.2 +1.6/ -1.8	Pavlov et al. (2019), Pavlov et al. (2007), Gurevitch et al. (2004)
PT03	Los Menucos acidic dykes	Argentina	Rhyolite	Dyke	-40.4	291.6	244	12	90	5	-38.8	14.3 +5.1/ -6.2	Luppo et al. (2019)
PT04	Gezira & Bir Umhebal dyke complex	Egypt	Syenite	Dyke	23.5	33.4	226	20	88	5	19.9	16.1 +3.6/ -4.2	Lotfy & Elaal. (2018)
PT05	Alto Paraguay Province	Paraguay	Syenite	Dyke	-23.5	302.1	241	10	35	5	-34.1	24.9 +7.1/ -8.2	Ernesto et al. (2015)
PT06	Tasguint & Alezmi formations	Morocco	Basalt	Lava flow	30.7	351.8	200	13	93	4	20.3	11.4 +2.6/ -3.2	Ruiz-Martinez et al. (2012)
PT07	Zguid & Ighrem dykes	Morocco	Dolerite	Dyke	30.1	352.4	200	22	181	4	23.9	10.6 +2.9/ -2.7	Palencia-Ortas et al. (2011)
PT08	Ukranian Shield andesites	Ukraine	Andesite	Dyke	47.5	37.7	204	12	80	6	46.6	11.4 +2.9/ -3.4	Yuan et al. (2011)
PT09	Puesto Viejo Group	Argentina	Basalt & rhyolite	Lava flow & ignimbrite	-34.8	291.5	245	40	332	3	-42.5	14.8 +2.5/ -2.7	Domeier et al. (2011b), Valencio et al. (1975)
PT10	South Taimyr Igneous Complex intrusives	Russia	Dolerite	Sill	74.8	100.6	228	11	82	5	61.0	8.1 +2.1/ -2.7	Walderhaug et al. (2005)

PT11	South Taimyr Igneous Complex extrusives	Russia	Basalt	Lava flow	74.9	100.5	248	10	63	6	68.3	22.3 +7.0/ -10.0	Walderhaug et al. (2005)
PT12	CAMP volcanics	Morocco	Basalt	Lava flow	31.1	7.4	200	63	458	4	24.9	20.3 +2.2/ -2.4	Knight et al. (2004)
PT13	Semeitau igneous series extrusives	Kazakhstan	Basalt, rhyolite & trachyte	Lava flow & ignimbrite	50.1	79.6	248	12	150	5	45.4	12.0 +1.8/ -2.5	Lyons et al. (2002)
PT14	Issaldain & Ait-Aadel dolerites	Morocco	Basalt	Lava flow	31.5	352.8	middle Triassic	15	72	3	23.6	14.3 +3.0/ -3.5	Hailwood. (1975)
PT15	Dolomites Volcanics	Italy	Basalt	Pillow lava	46.4	11.7	238	10	51	3	16.3	15.2 +3.0/ -3.6	Manzoni. (1970)
PT16	Niuhetang Formation	China	Basalt	Lava flow	23.8	99.3	late Triassic	16	139	4	14.6	12.7 +3.8/ -3.5	Zhao et al. (2015)
PT17	Tunguska Basin intrusives	Russia	Dolerite	Dyke & sill	64.0	103.4	251	76	663	5	72.1	14.1 +2.0/ -2.0	Latyshev et al. (2018), Konstantinov et al. (2014)
PT18	Angara-Tasevva intrusives	Russia	Dolerite	Dyke & sill	56.1	99.8	251	42	431	4	57.1	15.6 +1.9/ -2.0	Latyshev et al. (2018)
PT19	East Siberian Traps	Russia	Basalt	Lava flow	66.1	111.6	250	24	118	5	62.7	17.0 +2.1/ -2.4	Kravchinsky et al. (2002)
PT20	Sierra Chica Complex	Argentina	Trachyandes-ite & rhyolite	Pyroclastic flow & lava flow	-38.0	294.5	263	40	246	5	-40.7	11.9 +2.4/ -2.5	Domeier et al. (2011a), Tomezzoli et al. (2009)
PT21	Upper Choiyoi Group	Argentina	Rhyolite	Ignimbrite, breccia, & tuff	-34.8	291.5	264	41	272	6	-47.5	12.2 +2.1/ -2.3	Domeier et al. (2011b)

K01	Bakaly formation	Kazakhstan	Basalt & basaltic andesite	Lava flow	47.5	80.7	286.3	88	502	4	37.1	9.6 +1.5/ -2.5	Bazhenov et al. (2016)
K02	Koldar formation	Kazakhstan	Dacite & rhyolite	Welded tuff & ignimbrite	47.5	80.0	306-273	15	67	4	32.2	12.7 +2.6/ -3.4	Abrajevitch et al. (2008)
K03	Lunner dykes	Norway	Larvikite & syenite	Dyke	60.3	10.5	271	37	267	3	23.0	5.6 +1.2/ -1.2	Dominguez et al. (2011)
K04	Vestfold Volcanic Plateau	Norway	Basalt	Lava flow	59.5	10.3	292	48	302	4	20.2	9.3 +1.5/ -1.5	Haldan et al. (2014)
K05	Krokskogen Volcanic Plateau	Norway	Basalt	Lava flow	60.0	10.3	284	55	384	4	23.0	9.7 +1.5/ -1.6	Haldan et al. (2014)
K06	Ukranian Shield trachytes	Ukraine	Trachyte	Dyke	47.3	37.8	282.6	19	108	4	12.8	12.4 +2.2/ -2.1	Yuan et al. (2011)
K07	Woniusi formation	China	Basalt	Lava flow	25.2	99.3	late Carbonif erous	13	65	5	42.6	17.4 +2.4/ -2.3	Huang & Opdyke. (1991)
K08	Punta del Agua formation	Argentina	Andesite & lapillite	Lava flow & volcaniclastic	-28.6	291.4	late Carbonif erous	15	79	3	-48.1	16.6 +6.1/ -7.7	Geuna & Escosteguy. (2004)
K09	New England orogen	Australia	Andesite, rhyolite, & dacite	Lava flow & ignimbrite	-30.8	150.5	321-306	49	248	5	-62.8	26.2 +3.3/ -3.3	Opdyke et al. (2000)
K10	Gerringong Volcanics	Australia	Basalt - andesite	Lava flow	-34.5	150.9	265	16	120	6	-66.7	19.4 +3.6/ -3.7	Belica et al. (2017)
K11	Junggar Block dykes	China	Diabase	Dyke	45.7	82.7	late Carbonif erous	11	64	3	22.4	8.1 +3.6/ -5.5	Li et al. (1989)
K12	Biyoulitie super formation	China	Basalt	Lava flow	40.7	79.7	early Permian	20	141	5	30.7	9.6 +2.0/ -2.0	Sharps et al. (1989)

K13	Bohemian Massif	Germany	Granite-porphyry & quartzporphyry	Dyke	49.8	12.0	280	10	144	3	7.7	8.3 +3.4/ -3.6	Soffel & Harzer. (1991)
K14	Sardo-Corso Massif intrusives	Italy/France	Basic	Dyke	41.1	9.3	early Permian	23	298	3	-3.0	8.9 +2.2/ -2.5	Vigliotti et al. (1990)
K15	Esayoo formation	Canada	Basalt	Lava flow	81.0	278.0	early Permian	12	81	4	43.5	10.8 +3.2/ -3.7	Wynne et al. (1983)
K16	Tabla formation	Chile	Rhyolite, andesite, & dacite	Lava flow & ignimbrite	-24.5	290.7	late Carbonif erous	10	30	4	-38.7	9.2 +2.6/ -3.2	Jesinkey et al. (1987)

Note 2.1: Site ID refers to an identification system used within this study, sites with codes beginning PT (Permo-Triassic) belong to the Post-PCRS database, sites with codes beginning K (Kiaman) belong to the PCRS database. Lat and Long are the mean site co-ordinates for the dataset, and Age is the nominal assigned age for the dataset. N is the number of site-mean directions within a dataset, and n_{tot} is the total number of directions. S_B is an estimate of virtual geomagnetic pole dispersion calculated using the process set out in the method, likewise Plat is the estimated magnetic palaeolatitude. "References" refer to the original studies from which the data was sourced. All of the provided information relates to site-mean directions from the referenced studies that pass Group 1 selection criteria.

Table 2.2: Post-PCRS and PCRS Group 2 datasets.

Site ID	Rock formation	Country	Lithology	Rock type	Lat (°N)	Long (°E)	Age (Ma)	N	n_{tot}	Q	Plat (°N)	S_B (°)	References
PT01	Qiangtang Block middle Triassic lavas	China	Basalt	Lava flow & volcanic breccia	33.5	92.0	241	28	219	5	23.6	12.6 +2.0/ -2.0	Song et al. (2020)
PT02	Norilsk Region Volcanics	Russia	Basalt	Lava flow	70.1	94.3	251	172	1475	5	61.2	26.2 +2.0/ -2.2	Pavlov et al. (2019), Pavlov et al. (2007), Gurevitch et al. (2004)
PT06	Tasguint & Alezmi formations	Morocco	Basalt	Lava flow	30.7	351.8	200	13	93	4	20.3	11.4 +2.6/ -3.2	Ruiz-Martinez et al. (2012)
PT07	Zguid & Ighrem dykes	Morocco	Dolerite	Dyke	30.1	352.4	200	17	150	4	23.6	9.4 +2.5/ -2.7	Palencia-Ortas et al. (2011)
PT08	Ukranian Shield andesites	Ukraine	Andesite	Dyke	47.5	37.7	204	12	80	6	46.6	11.4 +2.9/ -3.4	Yuan et al. (2011)
PT09	Puesto Viejo Group	Argentina	Basalt & rhyolite	Lava flow & ignimbrite	-34.8	291.5	245	37	313	3	-42.9	15.3 +2.6/ -2.9	Domeier et al. (2011b), Valencio et al. (1975)
PT10	South Taimyr Igneous Complex intrusives	Russia	Dolerite	Sill	74.8	100.6	228	11	82	5	61.0	8.1 +2.1/ -2.7	Walderhaug et al. (2005)
PT12	CAMP volcanics	Morocco	Basalt	Lava flow	31.1	7.4	200	39	350	4	25.4	21.5 +2.8/ -3.0	Knight et al. (2004)
PT13	Semeitau igneous series extrusives	Kazakhstan	Basalt, rhyolite & trachyte	Lava flow & ignimbrite	50.1	79.6	248	10	77	5	45.5	12.0 +2.3/ -3.1	Lyons et al. (2002)
PT16	Niuhetang Formation	China	Basalt	Lava flow	23.8	99.3	late Triassic	14	128	4	15.0	13.0 +3.8/ -3.4	Zhao et al. (2015)

PT17	Tunguska Basin intrusives	Russia	Dolerite	Dyke & sill	64.0	103.4	251	51	488	5	73.2	13.1 +2.0/ -2.1	Latyshev et al. (2018), Konstantinov et al. (2014)
PT18	Angara-Tasevva intrusives	Russia	Dolerite	Dyke & sill	56.1	99.8	251	34	343	4	59.4	14.7 +1.6/ -1.8	Latyshev et al. (2018)
PT19	East Siberian Traps	Russia	Basalt	Lava flow	66.1	111.6	250	10	57	5	68.0	15.0 +4.3/ -5.1	Kravchinsky et al. (2002)
PT20	Sierra Chica Complex	Argentina	Trachyandesite & rhyolite	Pyroclastic flow & lava flow	-38.0	294.5	263	28	187	5	-39.1	11.6 +2.4/ -2.5	Domeier et al. (2011a), Tomezzoli et al. (2009)
PT21	Upper Choiyoi Group	Argentina	Rhyolite	Ignimbrite, breccia, & tuff	-34.8	291.5	264	36	245	6	-47.4	12.7 +2.2/ -2.5	Domeier et al. (2011b)
K01	Bakaly formation	Kazakhstan	Basalt & basaltic andesite	Lava flow	47.5	80.7	286.3	62	373	4	37.3	9.0 +1.3/ -2.5	Bazhenov et al. (2016)
K03	Lunner dykes	Norway	Larvikite & syenite	Dyke	60.3	10.5	271	26	203	3	23.6	5.5 +1.5/ -1.2	Dominguez et al. (2011)
K04	Vestfold Volcanic Plateau	Norway	Basalt	Lava flow	59.5	10.3	292	38	251	4	21.4	9.5 +1.9/ -2.0	Haldan et al. (2014)
K05	Krokskogen Volcanic Plateau	Norway	Basalt	Lava flow	60.0	10.3	284	46	334	4	22.7	10.5 +1.7/ -1.8	Haldan et al. (2014)
K06	Ukranian Shield trachytes	Ukraine	Trachyte	Dyke	47.3	37.8	282.6	10	60	4	15.6	11.6 +2.1/ -2.2	Yuan et al. (2011)
K07	Woniusi formation	China	Basalt	Lava flow	25.2	99.3	late Carbonife rous	12	61	5	42.4	18.2 +2.0/ -1.7	Huang & Opdyke. (1991)
K09	New England orogen	Australia	Andesite, rhyolite, & dacite	Lava flow & ignimbrite	-30.8	150.5	321-306	28	159	5	-63.4	26.6 +3.8/ -4.0	Opdyke et al. (2000)

K10	Gerringong Volcanics	Australia	Basalt - andesite	Lava flow	-34.5	150.9	265	11	81	6	-71.8	17.5 +3.1/ -3.5	Belica et al. (2017)
K11	Junggar Block dykes	China	Diabase	Dyke	45.7	82.7	late Carbonifer ous	10	60	3	22.4	8.9 +3.5/ -5.4	Li et al. (1989)
K12	Biyoulitie super formation	China	Basalt	Lava flow	40.7	79.7	early Permian	18	131	5	30.1	9.4 +2.4/ -2.4	Sharps et al. (1989)
K14	Sardo-Corso Massif intrusives	Italy/France	Basic	Dyke	41.1	9.3	early Permian	14	138	3	-2.9	10.5 +2.9/ -3.4	Vigliotti et al. (1990)
K15	Esayoo formation	Canada	Basalt	Lava flow	81.0	278.0	early Permian	11	75	4	43.3	10.3 +3.6/ -4.3	Wynne et al. (1983)

Note 2.2: For full description see note of Table 2.1.

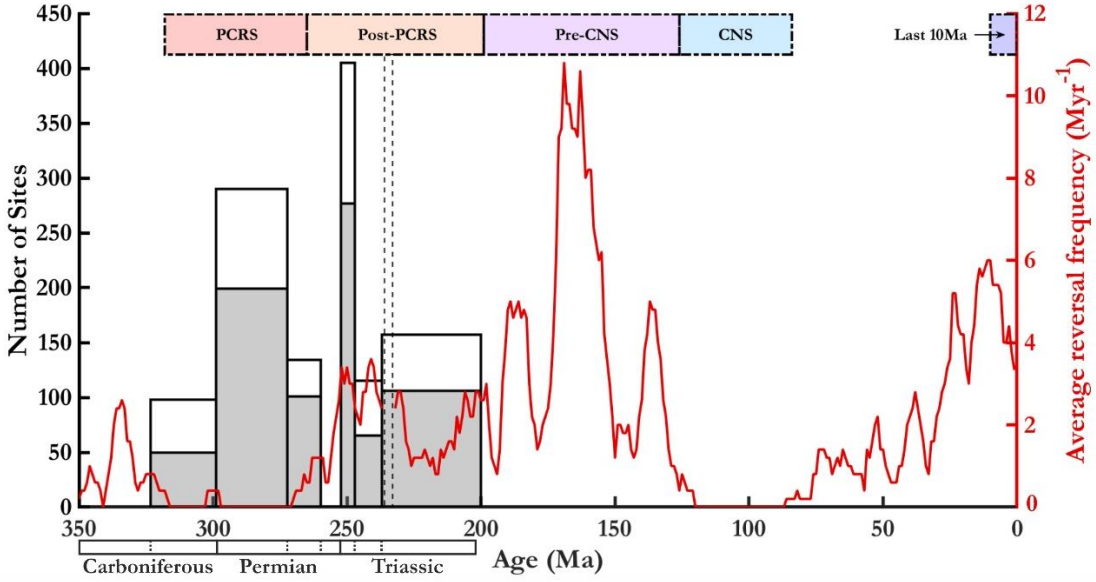

Figure 2.2: Graphical representation of the amount of site-level data in both the Group 1 database and the Group 2 database sub-divided by geological epoch. The full length of the bar chart represents the amount of Group 1 data and the length of the dark grey bars represents the amount of Group 2 data. Red line displays reversal frequency model constructed using a 5 Ma sliding window and magnetostratigraphic data from Ogg (2012) & Maron et al. (2019) with the different reversal regimes studied and discussed in this study highlighted.

Post-PCRS

There is a relatively even spread of formation dates from ~200 Ma back to ~264 Ma within the Post-PCRS compilation. This is despite a moderately large number of datasets associated with the Siberian Traps and with CAMP (Table 2.1). Reviewing the data at the site-mean level, it is noticeable that over half of the sites representing the Post-PCRS are early Triassic in age (Figure 2.2). This is testament to the volume of work conducted on the Siberian Traps and the importance of this event in geological history. The mean time interval between the ages of subsequent datasets is just over 5 Ma, and the greatest time gap exists during the late Triassic where magnetic field behaviour is unaccounted for about 22 Ma (Table 2.1). This is also the case for the late Permian for which there is no contributing data (Figure 2.2).

Latitudinal coverage is good with the number of low (< 30°), mid- (30°-60°), and high latitudinal sites (> 60°) almost evenly split, although each of these latitude bands is dominated by data from one hemisphere. Unsurprisingly, all of the high latitude datasets are related to the Siberian Traps. For low-latitude sites, the temporal range is greater, being derived from unrelated volcanic events. The mid-latitude data are primarily from South America and associated with the regional Permo-Triassic volcanism. There is also agreement in estimated dispersion values from Eurasia, however, one being late Triassic in age.

The PSV behaviour appears consistent at low-mid latitudes. Figure 2.3a shows closely grouped VGP dispersion values for latitudes < 50° lying within error of one another. Datasets from high palaeolatitudes display a far less consistent dispersion pattern despite all originating from the same volcanic event. Overall, only a weak latitudinal dependence of VGP dispersion is observed; estimated dispersion values commonly lie between 10° and 15° regardless of palaeolatitude.

The more robust Group 2 selection criteria removed 6 Group 1 datasets including those 2 with the greatest associated uncertainty of VGP dispersion (PT05 and PT11, Tables 2.1 & 2.2). From the 15 remaining datasets, just 4 were unaffected by the additional Group 2 selection criteria. The difference in the site-mean directional data comprising each dataset does not only change the estimated values of VGP dispersion but also the estimates of palaeolatitude (Tables 2.1 & 2.2).

While Group 2 data agreed better at high-latitudes, the overall observed PSV behaviour of the Post-PCRS remained largely unchanged regardless of whether Group 1 or Group 2 data were used (Figure 2.3). The Model G *a* parameter decreased slightly from 14.2° (11.3°-18.1°; Group 1) to 13.3° (9.8°-18.7°; Group 2). Modelling VGP dispersion using

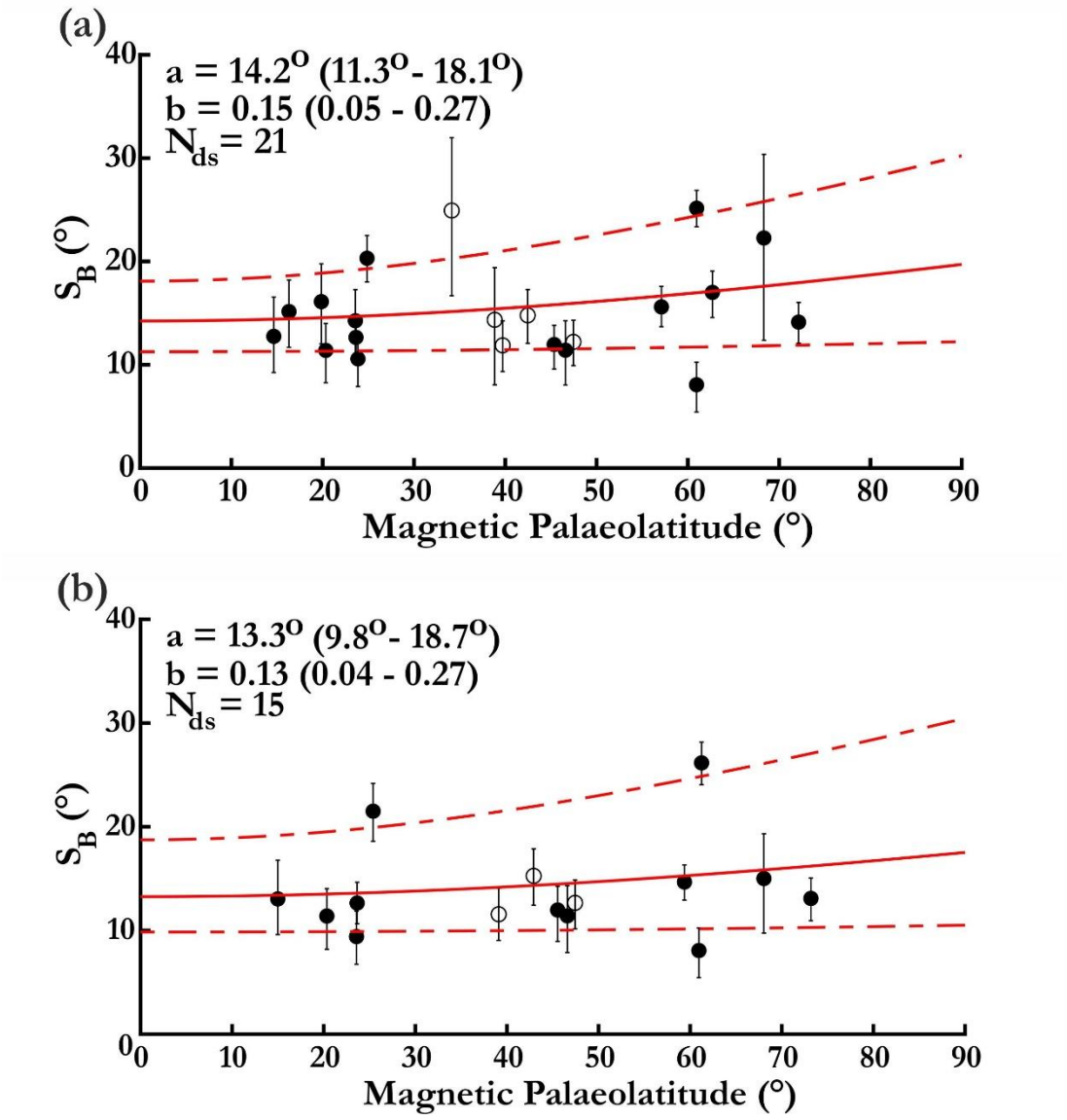

Figure 2.3: One hemisphere projection showing latitude dependence of virtual geomagnetic pole dispersion in the Post-PCRS (264-200 Ma). S_B values for northern and southern palaeolatitudes given by filled and empty circles respectively; error bars show their 95% confidence intervals. The solid red curve displays the best fit of Model G to the S_B values, dashed line represents the 95% confidence intervals given by the jack-knife method for 5000 replications. Estimates of Model G a and *b shape parameters are displayed alongside their associated uncertainties and the number of datasets analysed (N_{ds}). a) displays datasets after application of Group 1 selection criteria, b) likewise for Group 2 criteria.*

Group 2 datasets produced an even weaker latitudinal dependence than Group 1 datasets demonstrated by a slight decrease in estimated *b* value from 0.15 (0.05-0.27; Group 1) to 0.13 (0.04-0.27; Group 2).

PCRS

According to the numerical age estimates that are available, the database spans nearly all of the PCRS, starting from 265 Ma going back to at least 306 Ma. Within that time interval, coverage is consistently good through the middle and final stages of the PCRS but lacking slightly for the first few million years following its onset at ~318 Ma.

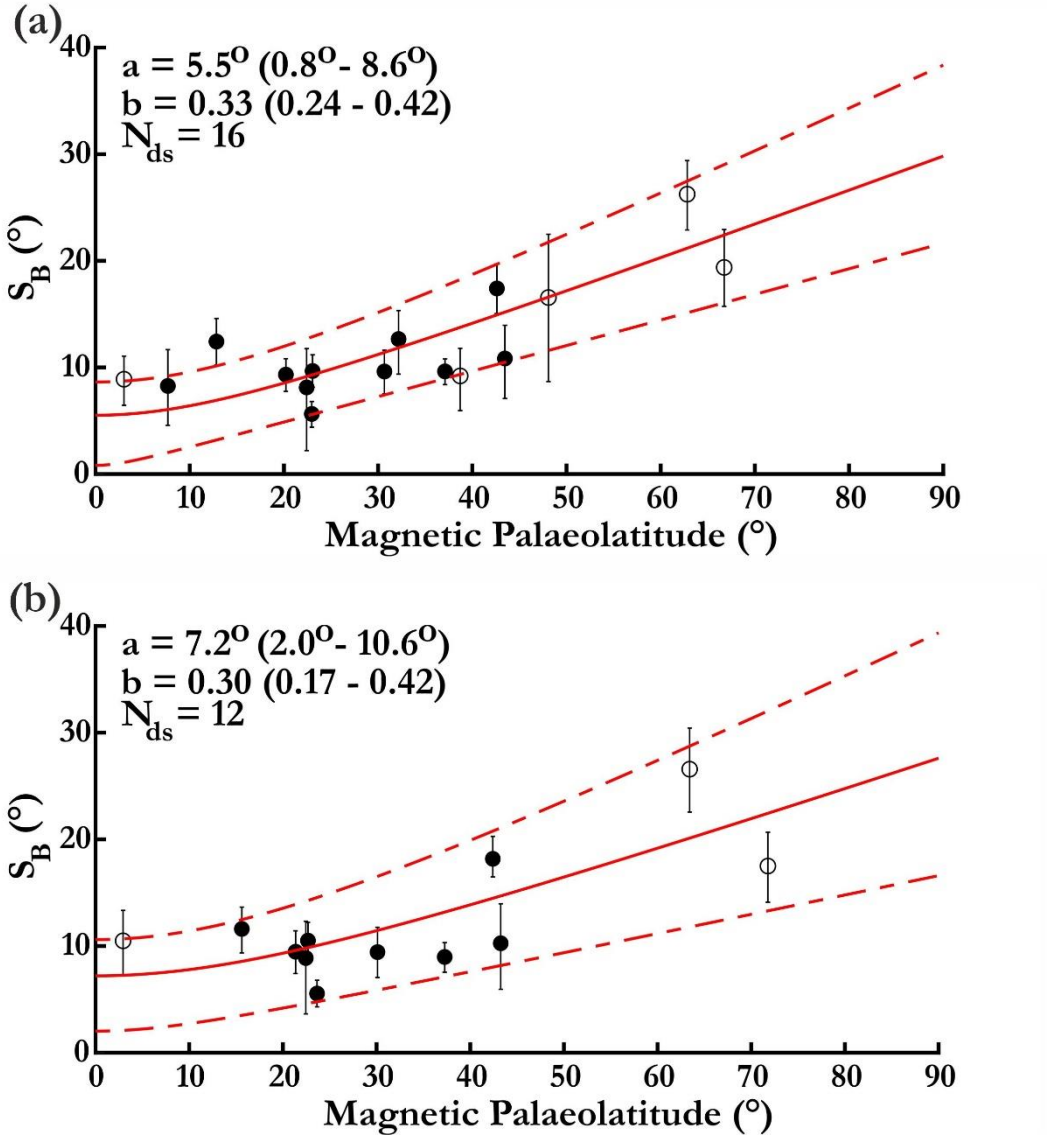

Figure 2.4: Latitude dependence of virtual geomagnetic pole dispersion and Model G curves for the PCRS (318-265 Ma). a) using Group 1 datasets, b) using Group 2 datasets See the caption of Figure 2.3 for description.

The "late Carboniferous" (323.2-298.9 Ma; Davydov et al., 2012) and "early Permian" (298.9-272.3 Ma; Henderson et al., 2012) aged datasets (Table 2.1) are likely to have formed in and around this time interval, however, and likely ensure that the temporal representation is reasonable.

The range of latitudinal coverage is very good at low and mid-latitudes. Unlike the Post-PCRS, there is representation from very low-latitude sites (< 10°). The PCRS database is lacking information at higher latitudes, however, with just 2 datasets above 60°. Both of these originate from Australia (Table 2.2) but are otherwise unrelated and separated by at least 40 Ma. Again, there is a hemispheric bias amongst the datasets with only 5 from 16 originating from the southern hemisphere.

Figure 2.4a displays a very strong relationship between VGP dispersion and latitude showing a very clear upwards trend. PSV behaviour is very consistent, particularly at low-mid latitudes, but even the high latitude estimates of VGP dispersion are within error of one another. The behaviour at mid-latitudes is also particularly consistent considering the seven datasets represent formations from five different countries: three from the northern hemisphere and two from the southern hemisphere.

All of the PCRS datasets were affected by the use of the Group 2 selection criteria and the subsequent removal of site-mean data; furthermore, four of the datasets were removed entirely (K02, K08, K13, K16, Tables 2.1 & 2.2). The difference between the observed dispersion patterns, when the two different sets of selection criteria were used, appeared to be greater for the PCRS than for the Post-PCRS for which some datasets were unaffected. In the PCRS, estimated dispersion values were, themselves, more dispersed when Group 2 datasets were used (Figure 2.4a, b). Despite neither of the high-latitude datasets being completely removed (K09 & K10, Tables 2.1 & 2.2), the removal of site-mean data within them altered their estimated scatter values so they were less consistent with one another (Figure 2.4b). Only datasets from low-latitudes displayed consistent estimates, although these had shifted, leading to an increased estimate of the Model G *a* parameter from 5.5° (0.8°-8.6°; Group 1) to 7.2° (2.0°-10.6°; Group 2). A clear trend still exists for the PCRS showing an increase in VGP dispersion with latitude, though this is slightly less well-established than in the Group 1 data as demonstrated by the increased uncertainty in estimated Model G parameters.

Discussion

Assessing the Robustness of VGP Dispersion

PSV analysis of the Post-PCRS palaeomagnetic directional and VGP database, containing the first compilation of Triassic data, documents a S_B-λ relationship similar to those from times of claimed high reversal frequency (Biggin et al., 2008; Doubrovine et al., 2019; Franco et al., 2019). By contrast, the PCRS demonstrates a much stronger latitudinal dependence of PSV demonstrated by the estimates of Model G *b* parameter which are approximately twice those estimated for the Post-PCRS (Figures 2.3 & 2.4). The Model G *a* parameter is also substantially lower. Both of these relationships can be thought of as robust features of their respective time intervals due to the general agreement when utilising databases of differing quality.

In the Post-PCRS, the use of higher quality Group 2 datasets reduced the estimates of both *a* and *b* relative to the Group 1 datasets.

The strong dependence of VGP dispersion with palaeolatitude observed for the Group 1 PCRS datasets is in general agreement with the results of a recent study of this superchron (de Oliveira et al., 2018). The use of Group 2 datasets somewhat reduces this agreement, though not significantly. The greatest difference observed when analysing Group 2 datasets is a rise in the Model G *a* parameter, suggesting higher dispersion at the

lowest latitudes. This could be a more accurate representation of the field than that presented by Group 1 datasets but here the issue of analysing a smaller amount of data is highlighted. The database has been reduced to 12 datasets and the removal of 1 dataset at very low latitude produces an estimate of the Model G *a* parameter which is much less well constrained by the palaeomagnetic data.

Although slight differences exist between the VGP dispersions observed using either Group 1 or Group 2 datasets, which can both strengthen and weaken proposed relationships, they are not significant and there is a general agreement for both the Post-PCRS and the PCRS. The higher quality datasets were compiled in order to significantly reduce the effects of bias, and their agreement with the lower quality, more numerous databases suggest that both observed VGP dispersions are unlikely to be an artefact of small *N* or *n* (Biggin et al., 2008). This establishes the respective features of both the Post-PCRS and PCRS as robust and justifies the use of Group 1 datasets for further analysis.

Comparison with Other Time Intervals

The associated Model G shape parameters (*a*, *b*, and the *b*/*a* ratio) for the Post-PCRS and PCRS intervals have been compared with those from previously compiled databases representing different time intervals. Here, we applied the Group 1 selection criteria, and the same initial constraints and method for the modelling of VGP dispersion, to the datasets from later time periods. This produced recalculated parameters which allow for a direct comparison of results. The recalculated shape parameters are given in Table 2.3 alongside the associated study, the time interval that they represent, and the estimated uncertainties on each parameter.

The time interval studied for the Post-PCRS has some crossover with the IHMP studied by Franco et al. (2019) and, as such, some of the datasets are shared. Franco et al. (2019) reported a low palaeolatitudinal dependence of VGP dispersion when analysing datasets from 265 Ma to 240 Ma, very similar to the results presented in this study for the Post-PCRS. This is further demonstrated by the similar estimates calculated for the Model G shape parameters (Table 2.3), suggesting consistent PSV behaviour throughout the Post-PCRS.

The study of de Oliveira et al. (2018) includes sedimentary-derived data and uses less-stringent selection criteria when analysing the PCRS. This is advantageous as more datasets are presented with increased representation at higher latitudes. The observed VGP dispersions may be compared in a similar manner to Group 1 and Group 2 datasets. There is a strong relationship between VGP dispersion and latitude with similarly low values at low latitudes presented by de Oliveira et al. (2018). This further suggests that the observed PSV behaviour is a robust feature of the geomagnetic field during the PCRS.

Previous studies have used the *b*/*a* ratio as a way of quantifying the type of PSV behaviour across a given time interval and have explored the possibility of a correlation with mean reversal frequency (de Oliveira et al., 2018; Doubrovine et al., 2019; Franco et al., 2019; McFadden et al., 1991). Figure 2.5a plots the *b*/*a* ratio values for the recalculated CNS and Pre-CNS intervals (Doubrovine et al., 2019), the PCRS and Post-PCRS intervals (this study), and a combined database for the Post-PCRS and Pre-CNS. Model G shape parameters have also been recalculated and plotted for the PSV10 database of Cromwell et al. (2018). All databases are of equal quality and represent the highest quality studies from 318 Ma to the present. Plotted alongside this is the same reversal frequency model previously presented in Figure 2.2.

Table 2.3: Comparison of Model G shape parameters and axial dipole dominance recalculated using our selection criteria applied to the datasets originally selected in the studies given.

Time interval	**Age range** (Ma)	**Average reversal frequency** (Myr^{-1})	**a** (°)	**b**	**b/a**	**AD/NAD$_{median}$**	**Study**
Last 10 Ma	10-0	4.9	12.0 +3.3/-1.9	0.27 + 0.04/-0.07	0.022 ± 0.0066	10.0 +18.9/-7.2	1
CNS	126-84	0.095	10.0 + 2.1/-2.8	0.22 + 0.05/-0.10	0.022 ± 0.012	15.1 +29.9/-10.2	2
Pre-CNS	198-126	4.2	12.7 + 2.6/-2.4	0.13 + 0.13/-0.09	0.010 ± 0.0075	8.8 +18.9/-6.0	2
Post-PCRS	264-200	2.0	14.2 + 3.9/-0.9	0.15 + 0.12/-0.10	0.011 ± 0.0073	6.9 +9.2/-5.0	3
Pre-CNS & Post-PCRS	264-126	3.1	13.3 + 2.3/-2.1	0.15 + 0.10/-0.10	0.012 ± 0.0083	7.9 +15.2/-5.3	3
PCRS	318-265	0.076	5.5 + 3.1/-4.7	0.33 + 0.09/-0.09	0.059 ± 0.052	58.4 +6345.1/-47.3	3
IHMP	*265-240*	*2.2*	*12.3 +20.7/-7.2*	*0.10 + 0.08/-0.05*	*0.0083 ± 0.0066*	*9.5 +114.3/-9.1*	*4*
PCRS	*318-265*	*0.076*	*4.1 + 3.2/-4.0*	*0.32 + 0.14/-0.12*	*0.078 ± 0.080*	*113.5 ± -*	*5*

Note 2.3: AD/NAD$_{median}$ is the estimation of the ratio of non-axial dipole field to axial dipole field (Biggin et al. 2020) with the associated uncertainty limits where reasonable. References: [1] Cromwell et al. 2018, [2] Doubrovine et al. 2019, [3] This study, [4] Franco et al. 2019, [5] de Oliveira et al. 2018.

Immediately obvious is the consistent *b/a* value throughout the Post-PCRS and the Pre-CNS and the higher values associated with the superchrons on either side (Figure 2.5a).

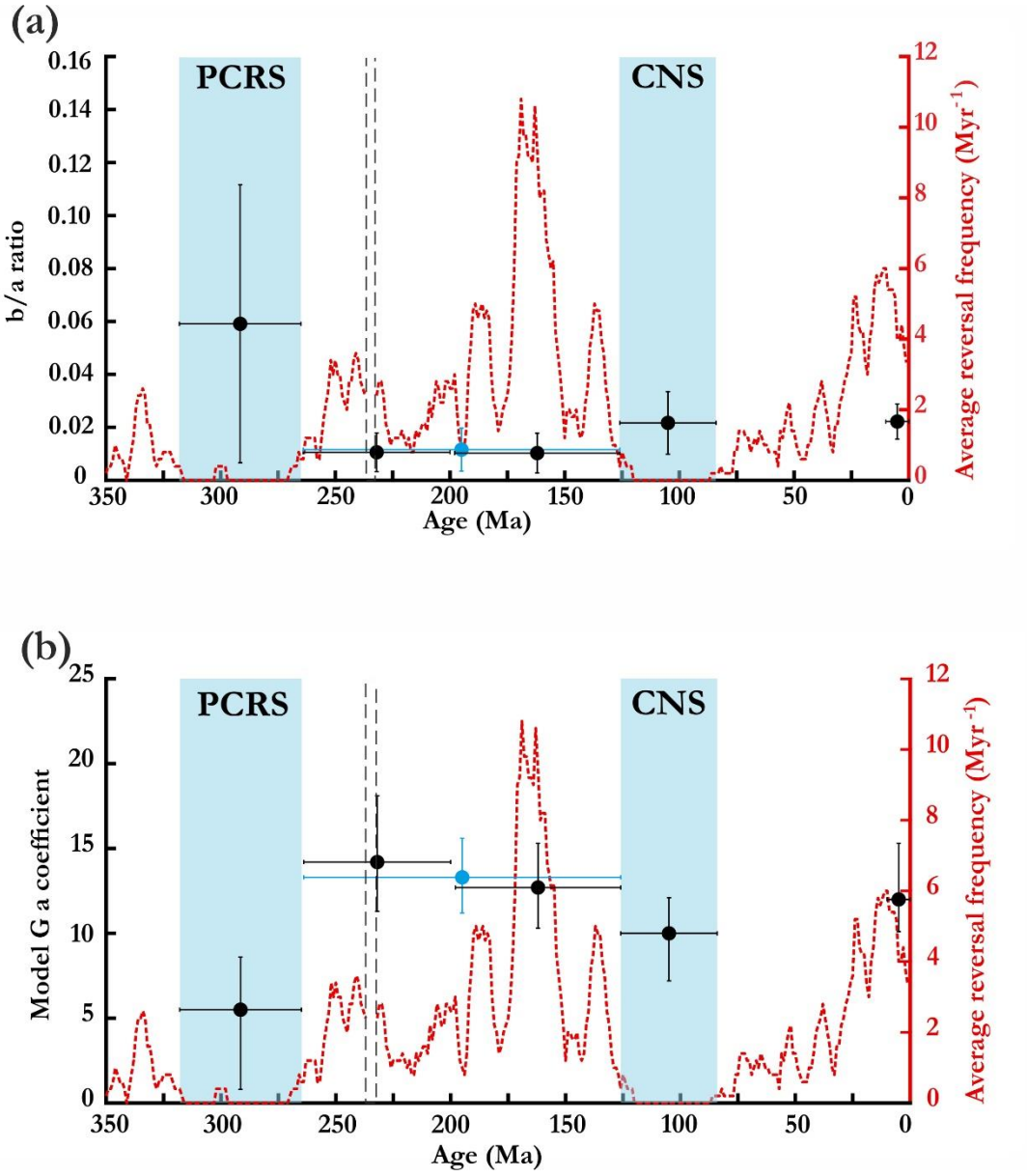

Figure 2.5: Variations in a) Model G b/a ratio b) Model G a parameter estimated for a range of time intervals. Last 10 Ma (10-0 Ma), (CNS (126-84 Ma), Pre-CNS (198-126 Ma), Post-PCRS (246-200 Ma), Pre-CNS & Post-PCRS (264-126 Ma), PCRS (318-265 Ma)). CNS & Pre-CNS data taken from Doubrovine et al. (2019), last 10 Ma data taken from Cromwell et al. (2018). Estimates of a) b/a ratio and b) Model g a parameter given by solid circles, vertical error bars represent the 95% confidence interval, horizontal error bars represent age range. The results displayed in blue are those from the combined database for the Post-PCRS and Pre-CNS. Dashed red line displays reversal frequency model constructed using a 5 Ma sliding window and magnetostratigraphic data from Ogg (2012) & Maron et al. (2019).

During the newly combined interval, reversal frequency shows a wide range of values (Figure 2.5a), which would appear to contradict the idea that an inverse relationship exists between the *b/a* ratio and reversal frequency (Franco et al., 2019). Rather, it supports the hypothesis that any potential relationship must be less straightforward (Doubrovine et al., 2019). The stronger latitudinal dependence of dispersion (i.e. the Model G *b* parameter) during both the PCRS (Figure 2.5a) and CNS (Doubrovine et al., 2019) are responsible for the higher *b/a* ratio compared to the times of geomagnetic reversals. This

could suggest that the different behaviours are indicative of a low/absent reversal regime and one in which reversals are present. However, the indistinguishable *b/a* ratio for the last 10 Ma, when compared to that of the CNS, is not consistent with this hypothesis (Doubrovine et al., 2019).

If the *b/a* ratio does not have a straightforward relationship with the average reversal frequency, then the consistently low value between the two superchrons must have an alternative explanation. Interestingly, there is an ongoing discussion around a proposed feature of the palaeointensity record across a similar time interval, the Mesozoic Dipole Low (MDL). This feature was first proposed by Prévot et al. (1990) and was defined as a period in which the virtual dipole moment (VDM) was one third of its present-day value between ~180-135 Ma (Perrin & Shcherbakov, 1997; Prévot et al., 1990). This hypothesis was supported by the work of Tanaka et al. (1995) in their construction and analysis of a global palaeointensity database, and low palaeointensity estimates obtained from the Siberian Traps (Heunemann et al., 2004; Shcherbakova et al., 2015).

Subsequent studies have suggested an MDL ~180-120 Ma (McElhinny & Larson., 2011), and recent low VDM estimates obtained from Permo-Triassic boundary rocks (~250 Ma) have led to proposals of an MDL extending back to this time (Anwar et al., 2016). The time interval corresponding to this longer MDL is largely encompassed by the time interval of low *b/a* ratios compiled for this study. Exploring this relationship further is very challenging due to the current global palaeointensity record. As it stands there are almost no VDM estimates for the entirety of the Triassic (Anwar et al., 2016). Furthermore, there is the possibility that the MDL is not a time interval of low intensity but rather represents the long-term average (Selkin & Tauxe, 2000). Another possibility is that the real MDL is a time of low field strength associated solely with the Jurassic hyperactivity period (Kulakov et al., 2019).

Obtaining new estimates of absolute palaeointensity values during the Triassic will be crucial in making possible the assessment of any relationships between geomagnetic observables and the palaeointensity record. The compilation of data from Triassic aged volcanic rocks and small-scale intrusions in Table 2.1 demonstrates that this is possible, as such rock formations have the potential to be viable palaeointensity recorders. The number of Group 1 datasets available per million year for Triassic PSV analysis (0.23 Myr^{-1}) is not substantially lower than other time intervals (e.g. CNS; 0.45 Myr^{-1}, Pre-CNS; 0.26 Myr^{-1}; Doubrovine et al. 2019, PCRS 0.30 Myr^{-1}; this study) even after removing datasets associated with the two major volcanic events that bookend the period. Due to the nature of palaeointensity experiments (Shaar & Tauxe, 2015; Thellier & Thellier, 1959) some formations that are suitable for palaeomagnetic studies are not suitable for palaeointensity studies, however. Nevertheless, we highlight the potential for future work to characterise the Triassic dipole moment using palaeointensity studies performed on such targets as identified in Table 2.1.

Implications for Field Morphology

A recent study by Biggin et al. (2020) investigated, across a wide range of models, the possibility of using Model G shape parameters to provide information about field morphology and, specifically, the dominance of the axial dipole contribution. Their finding was a strong, positive relationship between axial dipole dominance and the Model G *a* parameter. In order to assess what this would mean for the time intervals considered in this study, the different estimated *a* values must be analysed in a similar manner to that done for the *b/a* ratios (Figure 2.5b). The relationship between estimated *a* values and apparent average reversal frequency does not appear to be strongly inverse to that

observed when analysing the *b*/*a* ratio (Figure 2.5), as would be expected if the parameters co-varied inversely. The superchrons do display the lowest *a* values alongside higher estimated *b* values. Nevertheless, the estimated *a* value for the last 10 Ma is more comparable to that observed during the Pre-CNS, despite the associated estimated *b* value more closely resembling those of the two superchrons (Table 2.3). This would appear to support the conclusion of Biggin et al. (2020) that only a weak relationship exists between Model G shape parameters. The consequence of a relationship of this nature is that the original interpretation of the Model G shape parameters, as representing independent families of equatorially symmetric and equatorially anti-symmetric terms (McFadden et al. 1988; McFadden et al. 1991), is not well- supported (Biggin et al. 2020). A similar conclusion regarding the physical meaning of Model G shape parameters was reached by Doubrovine et al. (2019) who suggested that in strong-field, Earth-like dynamos the separation between the symmetric and anti-symmetric dynamo families becomes improbable despite being theoretically plausible.

Estimates of the Model G *a* parameter were used to establish the relative contribution of the axial dipole using the power law established by Biggin et al. (2020). The output is the median ratio of axial dipole to non-axial dipole contribution across the time interval (AD/NAD_{median}), with the median being used to avoid biasing due to brief, extreme events. The estimated ratios are displayed in Table 2.3. For the PCRS and Post PCRS, it is the first time that the field behaviour has been analysed in this way. The relative contribution of the axial dipole component of the field is somewhat similar for the Post-PCRS and Pre-CNS (Table 2.3), although a small increase is observed. Axial dipole dominance has since decreased, with the field over the last 10 Ma demonstrating a relative dipole contribution level similar to that during the Pre-CNS (Table 2.3). The most remarkable finding is the very strong axial dipole dominance of the PCRS field (Table 2.3), which is far greater than for any of the other ancient time intervals studied here or by Biggin et al. (2020). The closest values to this have come from much more recent, shorter time intervals on the order of 10 kyr (Biggin et al., 2020). The enhanced axial dipole dominance of the PCRS suggests that the Earth's magnetic field, during time instances within this interval, more closely resembled that of a GAD field than during any other time interval comparably studied. Put another way, dipole tilt (produced by the equatorial dipole terms) and all components of the nondipole field appear to have been heavily diminished relative to the axial dipole term during much of the PCRS. This offers a possible explanation for the enhanced duration of the PCRS, when compared to that of the CNS. Since collapse of the axial dipole is required to trigger a reversal (e.g. Olson et al., 2009), it being stronger and more dominant through most of the time interval would reduce the number of opportunities for a transitional field to dominate. The estimate of AD/NAD_{median} for the PCRS is a factor of 5 larger than the estimates for the other intervals since 265 Ma, with the upper range essentially describing a pure GAD field (Table 2.3). Associated uncertainty estimates for AD/NAD_{median} are inflated through incorporation of uncertainties associated with both the Model G *a* parameter and the power law fit of Biggin et al. (2020) that relates this to AD/NAD_{median}. Nevertheless, these uncertainty bounds still only narrowly incorporate the AD/NAD_{median} for the CNS and exclude the estimates for all intervals during which magnetic polarity reversals takes place. Therefore, although the formal establishment of the axial dipole dominance of the PCRS as statistically distinct from that of all other intervals must await the addition of further PSV data, we nevertheless consider it likely that, during the PCRS, the field was on average more axially dipolar than at any subsequent time.

The possible relationships between axial dipole dominance and VDM can be illustrated as two end-member scenarios with a spectrum between. In the first, the non-axial dipole field remains approximately constant through time with changes in the VDM being entirely accounted for by shifts in the median axial dipole component. In the second, all components of the field vary in unison. Our new findings regarding the PCRS appear to rule out the second scenario (since the axial dipole does appear to have been enhanced at the expense of the rest of the field during this time). The observation that average VDM also appears to have been elevated during the PCRS (Hawkins et al., 2021) rather supports the first scenario, or somewhere on the spectrum near to it. Likewise, if the duration of the MDL was shown to coincide with the time interval represented by the combined Pre-CNS and Post-PCRS then this could suggest that an increased contribution from the non-axial dipole field was a factor in the lower average VDM.

Conclusions

PSV behaviour during the Post-PCRS is very similar to that observed for the Pre-CNS despite these two intervals being characterised by different mean reversal rates. In terms of their PSV behaviour, we suggest that they can be adequately represented as a single interval. The variable reversal frequency and consistent b/a ratio is not consistent with the hypothesis that an inverse relationship exists between the two (Franco et al., 2019). This observation is further demonstrated by the indistinguishable estimates of b/a ratio for the CNS and the last 10 Ma (Doubrovine et al. 2019). Detailed analysis of PSV behaviour during the Jurassic hyperactivity period could help reveal whether PSV behaviour was, indeed, consistent throughout the Post-PCRS and Pre-CNS, and contribute to the ongoing discussion surrounding the nature of the relationship between VGP dispersion and reversal frequency. In order to conduct such a study, more high quality VGP datasets representing Jurassic hyperactivity behaviour are required than are currently available.

It would appear that the original interpretation of Model G shape parameters in terms of competing and co-varying contributions from quadrupole and dipole family harmonic terms (McFadden et al., 1988; 1991) is not appropriate. Over at least the last 318 Ma, superchrons seem to be characterised by a lower a parameter, which can likely be attributed to a more axial dipole dominated field (Biggin et al., 2020). This enhanced dipole dominance suppresses dipole tilt and the nondipole field, in turn suppressing VGP dispersion and the frequency of reversals. It appears that this behaviour was much more enhanced during the PCRS, in contrast to previous comparisons that have argued for similar PSV behaviour in the CNS and PCRS (de Oliveira et al. 2018, Haldan et al. 2014). The enhanced dipole dominance could go towards explaining the apparent longer duration of the superchron. It is also possible that the MDL is characterised by near latitudinal invariance of VGP dispersion and partially reduced axial dipole dominance, as attested to by the marginally higher Model G a parameter. Testing this hypothesis will require a much greater insight into global dipole moment variability, in particular for the Triassic, in order to better constraint the extent of the MDL. Considering the viability of the formations in Table 2.1 as potential targets for future palaeointensity studies would be a good first step towards addressing some of the gaps in the VDM record.

The low VGP dispersion at low-latitudes and the strong latitudinal dependence of VGP dispersion previously observed for the PCRS (de Oliveira et al., 2018) is a robust feature, demonstrated by the similarity in the pattern observed in this study using a higher-quality database. This behaviour is distinguishable from that observed during the Pre-CNS and

Post-PCRS and is the most extreme example of latitudinal-dependent VGP dispersion. This would suggest that the PCRS occurred during a time interval in which the Earth's magnetic field was greatly dipole dominated, and potentially of high intensity, making it a time interval worthy of intensive future study.

Acknowledgements

This research was the result of funding from The Leverhulme Trust (Research Leadership Award, RLA-2016-080), the Natural Environment Research Council (NE/T012463/1), and the Netherlands Organisation for Scientific Research (NWO). The additional PCRS data used in this study were compiled by Marcela Haldan at Utrecht University with funding from the NWO.

Data Availability Statement

The original datasets compiled for this research are available through EarthRef Digital Archive (https://earthref.org/ERDA/2481, ERDA), and are also provided in the supporting information. A complete breakdown of the supporting information is available in Appendix A. Previously compiled data are available through their respective publications, Cromwell et al. 2018 (PSV10), and Doubrovine et al. 2019 (CNS & Pre-CNS).

Chapter 3. Palaeointensity estimates from Triassic pillow basalts of the western Dolomites: implications for geomagnetic field evolution

Abstract

The palaeomagnetic field is commonly characterised by its polarity reversal frequency, field strength, and secular variation. Establishing if long-term variations of these characteristics occur independently, or via some defining relationships, is crucial to better understanding the geodynamo mechanism. Very poorly defined palaeointensity behaviour during the Triassic (~252-201 Ma) currently hinders such a determination. This study reports new palaeointensity results from pillow lavas of the Dolomites, Italy, whose age is well constrained to the middle Triassic. Despite their submarine nature, rock magnetic and microscopy investigations suggest that the lavas are reliable palaeomagnetic recorders, likely preserving a primary thermoremanent magnetisation. This is further supported by a positive conglomerate test. Palaeointensity estimates were obtained using the IZZI+ thermal Thellier protocol, and the Shaw double heating approach with additional steps to incorporate pseudo-Thellier experiments. Estimates of virtual dipole moments range between 3.0×10^{22} and 4.8×10^{22} Am^2. Analysis of these results, alongside the palaeointensity record for the last 320 Ma, suggests that they are in keeping with a long-term average persisting across much of the time interval from the Triassic until present-day. In contrast, the Permo-Carboniferous Reversed Superchron (~318-265 Ma) appears to represent a time interval of high geomagnetic field strength. The observed changes in geomagnetic field strength are reflected in variations in the degree of axial dipole dominance of the palaeomagnetic field. This is suggestive of a relationship between geomagnetic field strength and secular variation, highlighting the value of palaeosecular variation analysis, and the need for studies that aim to better define this relationship.

Introduction

A comprehensive palaeointensity record has the potential to greatly improve our understanding of the Earth's internal dynamics and its thermal evolution. Previously, a sudden increase in the strength of the geomagnetic field has been interpreted as representing the onset of inner core nucleation (Bono et al., 2019; Biggin et al., 2015) and a transition from solely thermal convection to a combination of this together with more efficient compositional convection (Davies et al., 2022). It is also proposed that relationships exist between observable characteristics of the geomagnetic field: reversal frequency, field strength, and palaeosecular variation (PSV) (Biggin et al., 2008; 2012; Gubbins, 1987; McFadden et al., 1991; Pal, 1991; Sprain et al., 2015; Tarduno et al., 2001) as a result of core-mantle boundary (CMB) heat flux variations due to whole mantle convection. Validating these relationships could allow independent determination of CMB heat flux using palaeomagnetism, making it a very powerful tool. Additionally, a more complete palaeointensity record would provide greater constraints on geodynamo simulations. Currently, a shortage of reliable data continues to inhibit the identification of long-term patterns in palaeointensity behaviour and agreement over proposed features. This problem is exacerbated by the high failure rates of palaeointensity experiments (Carvallo et al., 2006; Paterson et al., 2010), and a scarcity of suitable material across certain time intervals (Handford et al., 2021).

The behaviour of the Earth's magnetic field, across a given time interval, is most commonly characterised by its average polarity reversal frequency, its average field strength, and its secular variation. In order to gain a full understanding of the geodynamo mechanism, it must first be established whether long-term variations in reversal frequency, field strength, and secular variation occur independently of one another or if they share some defining relationships (Hulot & Gallet, 2003; Kulakov et al., 2019). The most recent, detailed analysis of the palaeointensity database (Kulakov et al., 2019) analysed its evolution between 200 Ma and 65 Ma, alongside Earth's polarity reversal record for the same interval. The resulting analysis produced first-order support for an inverse correlation between geomagnetic field strength and polarity reversal frequency. The palaeointensity data compiled for the study of Kulakov et al. (2019) contributed significantly to the improved coverage of the Mesozoic (ca. 252-66 Ma; Ogg et al., 2012) in a recent update to the PINT database (PINT v8.0.0, Bono et al., 2021). Substantial improvements were also made to data coverage during the Palaeozoic (Bono et al., 2021; Hawkins et al., 2021). In order to best utilise the improvements made to the palaeointensity database, and analyse the evolution of the strength of the Earth's magnetic field further back in geological time, it is important to first populate the palaeointensity record across the Triassic (ca. 252-201 Ma; Ogg et al., 2012). As it stands, just three palaeointensity estimates define the strength of the geomagnetic field between 249 Ma and 202 Ma (Eitel et al., 2014; 2016; Schwarz & Symons, 1969). A wealth of recent PSV studies, characterising geomagnetic field behaviour during intervals across the last ~320 Ma (Cromwell et al., 2018; de Oliveira et al., 2018; Doubrovine et al., 2019; Engbers et al., 2022; Handford et al., 2021), gives further importance to defining the strength of the Earth's magnetic field during the Triassic, as it would facilitate a comprehensive review into possible relationships between geomagnetic field strength and PSV.

A recent investigation into PSV, during the Triassic period, resulted in a compilation of palaeomagnetic data obtained from Triassic aged volcanic rocks and small-scale intrusions (Handford et al., 2021), simultaneously highlighting potential targets for future palaeointensity studies. This compilation included the volcanics of the Dolomites in the southern Alps. This study presents new palaeointensity estimates from pillow basalts of the Fernazza Formation (Fm), whose formation is well constrained to the middle Triassic (Storck et al., 2019; Mietto et al., 2012). A multi-technique approach is used in order to facilitate a comparison between estimated palaeointensity values obtained by methods based on different physical principles, allowing a more complete understanding of specimen behaviour and the potential reliability of results. The results of a conglomerate test on the Marmolada Conglomerate, following the Bayesian approach of Heslop & Roberts. (2018a), are also presented. The reliability of the palaeointensity estimates obtained from the Fernazza Fm is discussed at length, with the results then discussed in the context of the wider palaeointensity record and the results of recent PSV studies (Cromwell et al., 2018; Doubrovine et al., 2019; Engbers et al., 2022; Handford et al., 2021), in order to assess any possible relationships between secular variation and the evolving strength of the Earth's magnetic field.

Geological Setting & Sampling

The southern Alps experienced a phase of volcanic activity during the middle Triassic (247 Ma – 237 Ma; Ogg, 2012), inbetween subduction related to the Variscan orogeny (430-340/300 Ma, Casetta et al., 2021; Kroner & Romer, 2014; Stampfli, 2013) and the initial rifting of the Alpine Tethys (late Triassic/early Jurassic, Casetta et al., 2021; Stampfli, 2013). The main magmatic episode is estimated to have occurred between 242.653 ± 0.036 Ma and 237.579 ± 0.042 Ma, determined via U-Pb geochronology (Storck et al., 2019). For the first 4 Ma, activity was silicic and explosive, before a compositional change towards mafic products in the form of voluminous, primarily basaltic, lava flows and associated intrusive bodies (Storck et al., 2020; 2019). This interval of mafic production was relatively short-lived, likely lasting < 900 kyr (Storck et al., 2019). Effusive products are characterised by submarine pillow lavas, pillow breccias, lava breccias, hyaloclastites, and sub-aerial lava flows (Casetta et al., 2021), with all mafic products being shoshonitic (Casetta et al., 2021; Casetta et al., 2018a; 2018b; Bonadiman et al., 1994; Lustrino et al., 2019; Sloman, 1989). A potassium enriched composition of this nature is typically associated with destructive margins and a metasomatised mantle source (Joplin, 1968; Morrison, 1980; Sen & Stern, 2021; Sloman, 1989). This is at odds with the regional geological and geophysical observations, which indicate that deposition occurred in a strike-slip/extensional tectonic setting, due to the presence of horst and graben structures, and the formation of carbonate platforms (Bonadiman et al., 1994; Sloman, 1989). The misfit between geochemical data, and the geological/geophysical data has resulted in many proposed geodynamic and tectonic models to explain the peculiar magmatic suites of the southern Alps (Bernoulli & Lemoine, 1980; Bianchini et al., 2018; Bonadiman et al., 1994; Casetta et al., 2021; De Min et al., 2020; Doglioni, 2007; Lustrino et al., 2019; Storck et al., 2019; Zanetti et al., 2013). Examples from the most recent studies attribute the chemical composition to crustal contamination (Storck et al., 2020), or a Variscan associated, subduction-modified mantle source (Casetta et al., 2021;

Lustrino et al., 2019). Both have their limitations and the associated tectonic setting remains controversial.

The effusive phase of magma production is best preserved in the Dolomites (Casetta et al., 2021; Sloman, 1989), which was a main magmatic centre during the middle Triassic (Storck et al., 2019). Here, the middle Triassic stratigraphy is characterised by carbonate platforms, pelagic sedimentary deposits, and emersion horizons, all indicating a shallow marine environment, and the aforementioned volcanic successions and shallow intrusions (Brandner et al., 2016; Stork et al., 2019). In the western Dolomites, the basin associated deposits are separated by the shoshonitic lavas of the Fernazza Fm, represented by the deposition of the pre-volcanic Buchenstein Fm and the post-volcanic Wengen Fm (Figure 3.1b; Brandner et al., 2016). The timing of the emplacement of the Fernazza Fm is constrained by dates obtained from ashes within each of these basinal deposits. Storck et al. (2019) dated the upper Pietra Verde of the Buchenstein Fm at 238.646 ± 0.037 Ma and two ash beds of the Wengen Fm at 237.579 ± 0.042 Ma and 237.680 ± 0.047 Ma, respectively. These results agree with previous findings, such as the minimum date (Mundil et al., 2010) for the upper Pietra Verde obtained by Mundil et al. (1996), of 238.0 +0.4/-0.7 Ma, and that of an ash deposit 24 m above the Fernazza volcanics, within the locally distributed Frommer Member of the Fernazza Fm (237.773 ± 0.052 Ma, Mietto et al., 2012). This results in a maximum possible eruption duration of 0.87 ± 0.06 Ma, across a time interval that agrees with dates obtained from the coeval mafic intrusions of the Monzoni-Predazzo complex (238.190 ± 0.055 to 238.075 ± 0.087 Ma, Storck et al., 2019). In some sections, the Marmoldada Conglomerate sits directly atop the pillow basalts of the Fernazza Fm, indicating the start of the Wengen Fm (Brandner et al., 2016). Otherwise they are separated by basinal deposits with a carbonate source. The sudden change to the volcaniclastic and epiclastic sediments of the Marmolada Conglomerate represents a change in source material, likely from the erosion of a volcanic island forced by a lowering sea-level (Brandner et al., 2016).

The specimens used in this study were collected as cores, drilled from massive pillow lavas of the Fernazza Fm, that had typical diameters between 3 m and 5 m (e.g. Figure 3.1c). Sampling areas are shown in Figure 3.1a on a geological map of the region. These pillows were considered the most reliable palaeomagnetic recorders in a previous study (Manzoni, 1970), when compared with results obtained from mafic dykes in the area. The resulting combined palaeopole of Manzoni. (1970), for the Dolomites, was 240°E, 48°N, with the tectonic implication that the Dolomites experienced 50° anticlockwise rotation relative to northern Europe (Manzoni, 1970). Palaeomagnetic procedure was limited to alternating field (AF) demagnetisation, which suggested low-coercivity remanence carriers as specimens demagnetised to < 10% of their NRM value after demagnetisation in a maximum AF of 40 mT (Manzoni, 1970). This would appear to agree with a recent petrological study of basalt lava flows of the Dolomites, in which it was determined that they contained a compositional range of Ti-poor titanomagnetites (Casetta et al., 2021). Drill cores were also collected for this study from clasts of the Marmolada Conglomerate (Figure 3.1), in order to perform a conglomerate test to assess the possibility of the Fernazza Fm having experienced remagnetisation (Graham, 1949; Watson, 1956; Heslop & Roberts, 2018a). The close proximity of the source area of the Marmolada Conglomerate to the Fernazza Fm (Bosellini, 1996), suggests that the conglomerate may

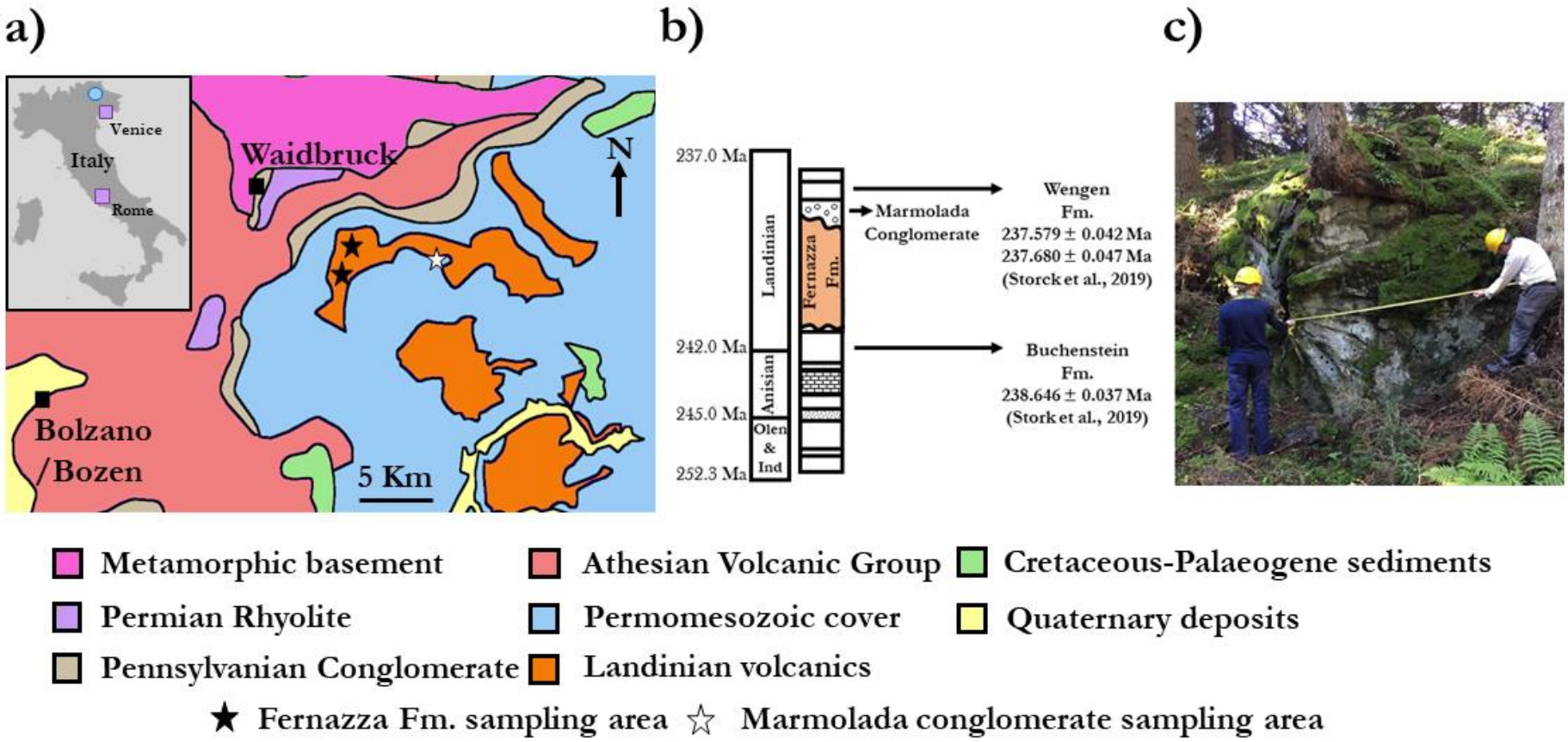

Figure 3.1: a) Simplified geological map of the central area of the province of South Tyrol, Italy. Stars indicate the sampling areas of this study. General sampling locality indicated by blue circle on map of Italy (insert). b) Generalised vertical section of the sampling area (modified from Brandner et al., 2016), highlighting the sampled Fernazza formation and Marmolada Conglomerate, and the dated lithologies that constrain their eruption dates. c) Field photo of a sampling site of the pillow lavas of the Fernazza formation which demonstrates the large size of the individual pillows, often multiple metres in diameter. Photo credit: Annique van der Boon.

well be comprised of clasts of the Fernazza Fm. Confidently identifying clasts as being representative of the Fernazza Fm, over previous phases of Alpine volcanic activity, is challenging, however. Therefore, the conglomerate test is not interpreted as being intraformational (Shipunov et al., 1998).

Some of the magmatic products of the western Dolomites have experienced hydrothermal alteration but this is varying in its extent (Casetta et al., 2021). Magnetic products of low-temperature alteration will carry a thermochemical remanent magnetisation (TCRM) that is expected to bias palaeointensity estimates (Fabian, 2009; Yamamoto et al., 2003). Prior to sampling, the physical condition of the outcrop was assessed, avoiding areas with extensive cracking that may have facilitated or exacerbated fluid penetration and rock alteration (Marescotti et al., 2000) and also avoiding outcrops that contained a high density of amygdales or mineral veins, formed through precipitation of hydrothermal fluids (Marescotti, 2000). Pilot holes were also drilled at each potential site and those that produced brown drilling mud, indicative of the alteration product clay, were abandoned. In addition to this, sampling was carried out in a manner that could facilitate an assessment of the effect that any TCRM component may have on the final palaeointensity estimates. The radial cross-sectional profile of pillow lavas, have the potential to present a systematic change in the degree of low-temperature oxidation experienced, decreasing towards the centre (Humphris, 1972; Humphris & Thompson, 1978). Therefore, for certain sites, the collection of samples across radial profiles was documented, in order to investigate the possibility of a relationship with obtained palaeointensity estimates and the degree of low-temperature oxidation experienced.

Method

Rock Magnetic Experiments & Microscopy

These methods were used to determine the magnetic mineralogy of the studied specimens in order to assess their suitability for palaeointensity experiments, and the likelihood of the held remanence being thermal in nature and of primary origin.

A Magnetic Measurements Ltd Variable Field Translation Balance (VFTB) was used to measure hysteresis parameters, thermomagnetic curves, and isothermal remanence acquisition curves. Multiple 150 mg powdered samples were used from each site to provide an understanding of the degree of homogeneity of a given site. Thermal experiments typically ran up to 600°C or 700°C. Repeated heating steps were applied when they had the potential to provide further information on the temperature during laboratory heating at which alteration may have occurred. Results were analysed through a combination of RockMag Analyzer 1.0 (Leonhardt., 2006) and HystLab v1.1.0 (Paterson et al., 2018). Thermomagnetic curves were used to obtain Curie temperature (T_C) estimates by utilising the differential method of Tauxe. (1998).

The dependence of sample magnetic susceptibility on temperature was analysed using an MFK1-FA Kappabridge susceptometer with CS-3 furnace (AGICO). Again, multiple crushed samples were used per site but in slightly larger quantities than for the VFTB. These experiments also typically ran up to 600°C or 700°C and selected samples were subject to cyclic heating steps where appropriate. Carbon coated, polished thin sections

were subject to Scanning Electron Microscope (SEM) analysis using a JEOL JSM 6610 SEM and a Zeiss Gemini 450 SEM at the Albert Crewe Centre for Electron Microscopy, University of Liverpool. This included Backscattered electron (BSE) imaging and energy dispersive X-ray (EDX) spectroscopy, analysed with Oxford Instruments; Aztec software. The thin sections were also subject to a range of optical microscopy techniques using a Meiji Techno Mt4000 series microscope.

Absolute Palaeointensity Techniques

Palaeointensity estimates were obtained by three different experimental methods: thermal Thellier (performed using the IZZI+ protocol, Tauxe & Staudigel, 2004), Shaw double heating technique (Shaw-DHT; Shaw, 1974; Tsunakawa & Shaw., 1994; Kono, 1978), and pseudo-Thellier (Paterson et al., 2016; Tauxe et al., 1995). Estimates obtained using the pseudo-Thellier approach were not considered for final site-level virtual dipole moment estimates (VDM) as they are associated with uncertainties of at least 25%, but have been shown to be useful as a complementary technique, justifying their use (Paterson et al., 2016; Thallner et al., 2021). Site-mean palaeointensity estimates were calculated by unweighted averaging of specimen-level thermal Thellier and Shaw-DHT results, where possible, and the minimum required number of site-level estimates was three ($n \geq 3$). Experiments were conducted on half-inch core specimens with Shaw-DHT and pseudo-Thellier measurements performed using a RAPID 2G superconducting rock magnetometer. Thermal Thellier measurements were similarly made or, on occasions, a JR6-6A Spinner Magnetometer (AGICO) was used.

Palaeointensity experiments were only conducted on specimens from site locations where sister specimens had produced consistent site-level characteristic remanent magnetisation (ChRM) directions from stepwise demagnetisation experiments, or where internally inconsistent directions could be explained by field relationships and observations. A combination of AF and thermal treatments were utilised in the ChRM isolation at each site. AF demagnetisation was completed with an LDA5 AF Demagnetizer (Agico) and thermal treatment was done using either a MMTD24 or MMTDSC Thermal Demagnetizer (Magnetic Measurements).

Thermal Thellier

The IZZI+ protocol alternates zero-field and infield steps, with partial thermal remanent magnetisation (pTRM) checks after every two step pairs (Tauxe & Staudigel, 2004; Lloyd et al. 2021b) as a check for thermal alteration. In this study, specimens were treated in batches where temperature steps were tailored according to the thermal demagnetisation behaviour observed in prior experiments. As the remagnetisation process is trying to replicate that which gave the samples their original thermal remanent magnetisation (TRM), thermal experiments are most effective when the laboratory applied field is close in magnitude to that of the original applied field (Biggin. 2006). As this is a relative unknown for the Triassic, an initial applied field of 30 μT was used. Where appropriate, additional specimens from the same site were subject to the same experiment with an applied laboratory field more closely resembling that of the ancient field as suggested by the initial results. Specimens were also subject to a 5 mT AF demagnetisation step before each measurement in order to remove soft remanences acquired during the experimental process, and improve Arai plot linearity (Dunlop et al., 2005).

The standardised palaeointensity definitions of Paterson et al. (2014) were used and the selection criteria are taken from that study albeit with slightly stricter k'. They are: $n \geq 5$, $\beta \leq 0.100$, $f \geq 0.35$, $q \geq 1$, $MAD_{anc} \leq 15$, $\alpha \leq 15$, DRAT ≤ 10, CDRAT ≤ 15, $k' \leq 0.35$. Slight relaxation in the selection criteria was permitted ($\beta \leq 0.110$, $k' \leq 0.48$, DRAT ≤ 10, CDRAT ≤ 15) when the number of parameters failing the original criteria were no more than two, and other specimens from the same site provided similar palaeointensity estimates whilst satisfying all criteria. Arai plots were analysed through paleointensity.org (Béguin et al., 2020).

Shaw

A standard Shaw experiment utilises AF demagnetisation of both the NRM and an imparted TRM, estimating the intensity of the original applied field from the ratio between the two (Shaw, 1974; Tsunakawa & Shaw., 1994). The ratio of anhysteretic remanent magnetisations (ARM) given before the laboratory heating and after are used to determine if any alteration occurred during the heating process and correct for it if required (Kono, 1978). A second heating step is then completed with another ARM correction applied in an attempt to recover the initial applied TRM field. This is done as a check on the reliability of the ARM correction. Specimens in this study were held at temperatures of 600°C for 40 minutes during the first TRM acquisition and 50 minutes during the second TRM acquisition. All initial experiments were conducted with a known laboratory field of 30 μT which was adjusted for subsequent experiments following the same approach utilised in the IZZI+ method.

Requirements regarding the classification of the ChRM direction and amount of data required for a reliable palaeointensity estimate are the same as those used when analysing IZZI+ data. The additional selection criteria related to the Shaw method follow those proposed by Yamamoto et al. (2003).

1. Linear portion of the NRM-TRM1* diagram used in the palaeointensity estimate represents at least 15% of the original NRM ($f_N \geq 0.15$).

2. The R^2 correlation of the portion of the NRM-TRM1*(R_N^2) and TRM1-TRM2* (R_T^2) diagrams used should be at least 0.99.

3. The slope of the portion of the TRM1-TRM2* is near unity (slope-T = 1 ± 0.05). Greater error was permitted for sites containing specimens which passed the original criteria where the palaeointensity estimate from the failing specimens agreed (slope-T = 1 ± 0.1). This is a similar approach to previous studies (e.g. Lloyd et al. 2021b).

The curvature parameter (k') is also included as an additional criterion following on from the investigation conducted by Lloyd et al. (2021a), who observed notable improvement in both the accuracy and precision of successful palaeointensity estimates when *k'* was used over the traditional R^2, as a measure of linearity.

4. Curvature parameter, *k'*, of the portion of the NRM-TRM1* (k'_N) and TRM1-TRM2* (k'_T) diagrams used, should not exceed 0.20. Marginally reduced criteria are permitted for one of either R^2 or *k'* ($R^2 \geq 0.985$, $k' \leq 0.210$). This appears

reasonable as the use of *k'* was proposed as an alternative criterion to R^2 (Lloyd et al., 2021a), yet is ordinarily applied conjunctively in this study.

Pseudo-Thellier

The pseudo-Thellier approach is a non-heating method in which the NRM of a specimen is progressively demagnetised using an alternating field, after which an ARM is imparted using the same steps (Paterson et al., 2016; Tauxe et al., 1995). NRM is plotted against ARM and an estimate of ancient field strength is determined by multiplying the slope of this pseudo-Arai plot by the strength of the applied laboratory field and a calibration factor. The calibration factor of Paterson et al. (2016) was chosen for this study.

When analysing the pseudo-Arai plots, the selection criteria of Paterson et al. (2016) were applied and paleointensity.org (Béguin et al., 2020) was used for the analysis.

Results

Rock Magnetism & Microscopy

Combined analysis of rock magnetic experiments, SEM and optical microscope images, and EDX data, suggest that the magnetic mineralogy is moderately homogeneous across the different sampling sites. The limited range of rock magnetic behaviour observed, likely represents varying degrees of alteration experienced by studied specimens. This is demonstrated in Figure 3.2 where the most extreme examples of thermomagnetic, and susceptibility versus temperature behaviour are presented (Figure 3.2b & 3.2c), alongside behaviour most representative of the average specimen (Figure 3.2a). In thermomagnetic experiments, magnetisation decays up to a temperature of ~500°C (Figure 3.2), resulting in consistent Tc estimates between 490°C and 500°C. Another consistent feature is the lower magnetisation values of the cooling curve when compared to those of the heating curve (Figure 3.2). This is an indicator of thermal alteration, and cyclic heating steps reveal that this occurs between 350°C and 500°C (Figure B.1). Given the inflection sometimes observed in the heating curve at ~350°C (Figure 3.2b), and the geological context of the specimens, it is most likely that thermal alteration is due to the inversion of maghaemite to haematite (Dunlop & Özdemir, 1997). The extent to which maghaemite influences thermomagnetic curves is variable, with some curves displaying close to reversible behaviour (Figure 3.2c). Susceptibility versus temperature curves display a mild Hopkinson peak ~500°C (Figure 3.2). The preceding decrease in susceptibility is relatively sharp but shallows close to 550°C. This behaviour is likely the result of specimens containing populations of Ti-poor titanomagnetites with a range of compositions. The estimates of T_C therefore, are likely to roughly represent that of the mean titanomagnetite composition (Lattard et al., 2006). The effects of maghaemite inversion are sometimes visible in the susceptibility versus temperature curves as minor inflections of the heating curve ~300°C (Figure 3.2). This also likely explains the decrease in room temperature susceptibility values, as haematite is of significantly lower susceptibility than maghaemite (Dunlop & Özdemir, 1997). Heating up to 700°C (Figure 3.2a, b) potentially results in greater thermal alteration than often exhibited in the thermomagnetic curves, although evidence of greater thermal alteration is also evident in susceptibility versus temperature curves when specimens were heated to a maximum temperature of 600°C (Figure 3.2c).

In both the thermomagnetic, and susceptibility versus temperature curves of the most reversible specimens, (Figure 3.2c) there is a slight increase in T_C of the cooling curve. This most likely represents partial oxyexsolution of titanomagnetite phase(s) towards pure magnetite.

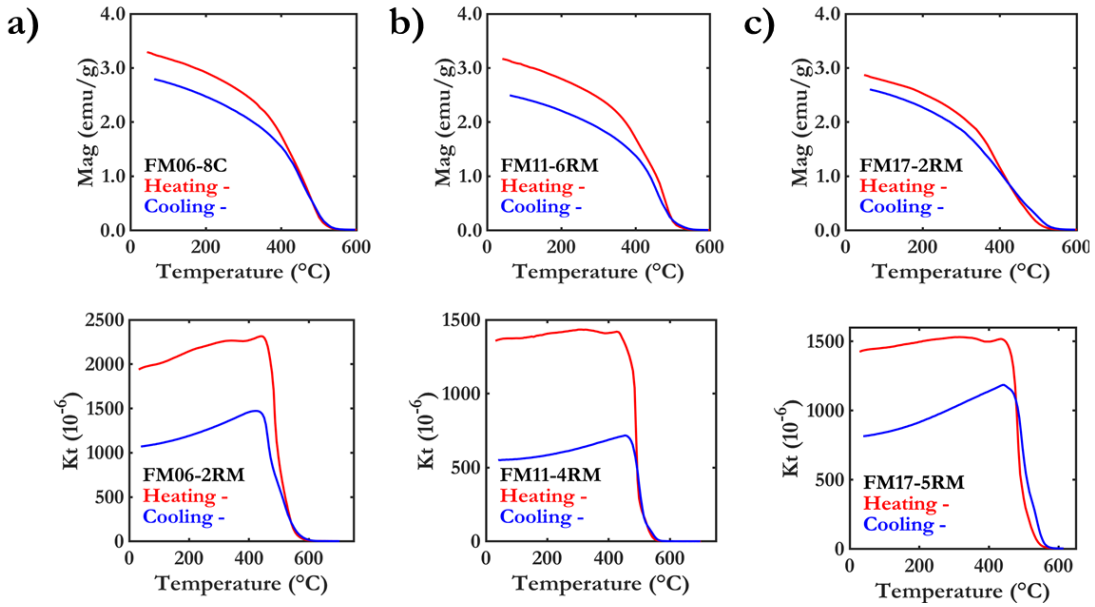

Figure 3.2: Rock magnetic results from specimens that are representative of the full range of rock magnetic behaviours. Thermomagnetic curves and susceptibility versus temperature curves are presented for each classification. a) behaviour most representative of average specimen, b) least reversible behaviour, c) most reversible behaviour.

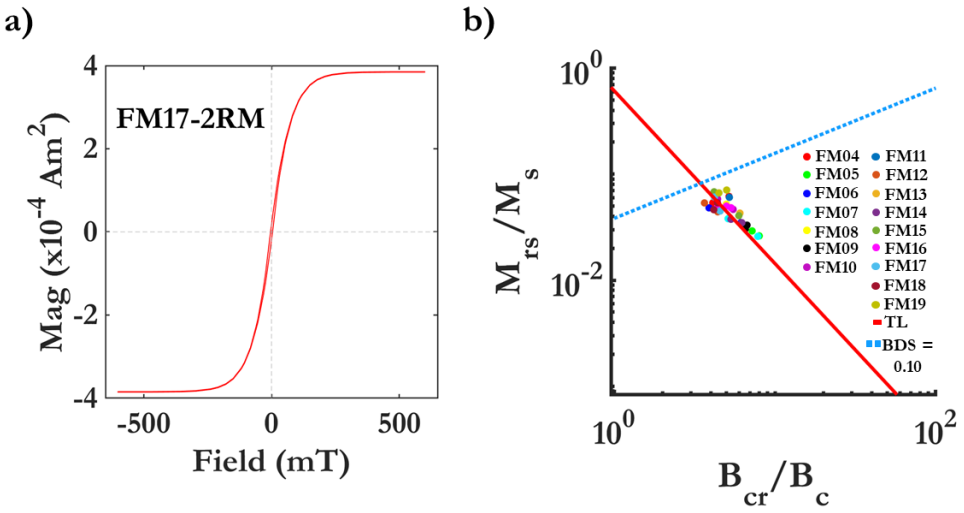

Figure 3.3: Hysteresis properties. a) Representative example of hysteresis loop processed with HystLab (Paterson et al., 2018). b) Graph showing the ratio of saturation remanence and saturation magnetisation versus ratio of coercivity of remanence and coercivity with bulk domain stability (BDS) trendline (TL, red line) (Paterson et al., 2017) and BDS = 0.10 (blue dotted line).

Hysteresis behaviour was relatively consistent across all specimens analysed. Saturation magnetisation was achieved by 250 mT, with specimens retaining little remanent magnetisation after the applied field was removed (Figure 3.3a). Representative hysteresis parameters have been plotted for each site alongside the bulk domain stability (BDS)

trendline (Paterson et al., 2017) and the line representing BDS = 0.10 (Figure 3.3b). The trendline was derived from the hysteresis parameters of (titano)magnetites (Paterson et al., 2017) and agreement between the plotted parameters and this trendline (Figure 3.3b) are further evidence to suggest the presence of titanomagnetite in the specimens of the Fernazza pillow lavas. Specimens with a BDS value below 0.10 are less stable due to enhanced multidomain (MD) contributions (Paterson et al., 2017; Yoshimura et al., 2020). All plotted parameters lie below BDS = 0.10 but often lie close to this theoretical cut-off (Figure 3.3b), and there does not appear to be a tendency for given sites to lie towards the top or bottom of the plotted distribution.

Microscopy images of the Fernazza Fm lavas agree with the recent descriptions of equivalent units by Casetta et al. (2021) and Nardini et al. (2022). Specimens demonstrate porphyritic to glomeroporphyritic textures with phenocrysts of clinopyroxene, plagioclase feldspar, and spinel (Figure 3.4). There is also evidence of secondary mineral infill, in the form of amygdales (Figure 3.4a). Individual glomeroporphyrys are best observed under transmitted cross-polarised light (Figure 3.4a & b), which shows them to consist of clinopyroxene and spinel grains. EDX analysis of the spinel grains shows them

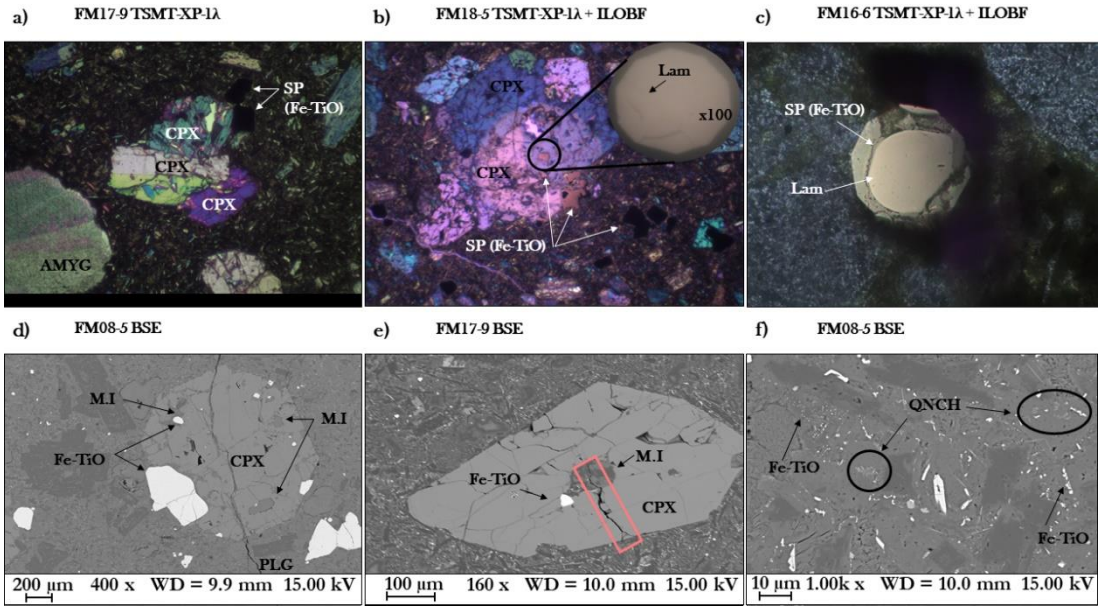

Figure 3.4: Microscopy images obtained with transmitted cross-polarised light (TSMT-XP, a-c) and brightfield images utilising incident light (ILOBF, b insert & c). Scanning electron microscope (SEM) images obtained from backscattered electrons (BSE, d-f). CPX – clinopyroxene, SP – spinel, PLG – plagioclase feldspar, Lam – lamellae, M.I – melt inclusion, QNCH – quench textures. Pervasive crack demonstrating the cross-cutting relationship between clinopyroxene and melt inclusion highlighted in e) (red box). SEM images are presented in an order of decreasing scale, with the features displayed in f) being representative of the groundmass.

to be Fe-Ti oxides (Figures B.2 & B.3). In some cases, the clinopyroxene grains host the (titano)magnetite grains (Figure 3.4b, d, e). Hosted and isolated (titano)magnetite grains are considered a primary phase since lamellae, suggestive of high-temperature oxidation, are observed (Figure 3.4b, c). SEM BSE images show that the (titano)magnetite inclusions often occur within melt inclusions (Figure 3.4d, e). Where the clinopyroxene host has experienced cracking, it has occurred after the crystallisation of these melt inclusions, demonstrated by cross-cutting relationships (Figure 3.4e). This evidence suggests that the (titano)magnetite inclusions are a primary phase, crystallising out of melt entrapped by

the growing clinopyroxene grain. Elemental composition maps obtained by EDX spectroscopy, display evidence of Fe-Ti oxides within the calcite amygdales (Figure B.4). The groundmass is composed of the same mineral assemblage as the phenocrysts, and is microcrystalline to hypohyaline (Figure 3.4a, b, e, f), sometimes displaying dendritic quench textures (Figure 3.4f). (Titano)magnetite grains generally show well-defined edges but sometimes show evidence of cracking (Figure 3.4d). Usually this is constrained to grain edges (Figure B.5) and likely formed due to a small degree of maghaematisation (Figure B.5). In the examples observed, the majority of the iron-oxide grains appear unaffected by cracking.

Palaeomagnetic Directions & Conglomerate Test

From the 19 sampling sites subject to palaeomagnetic directional analysis, 12 returned internally consistent ChRM directions with an $n \geq 5$ and with a general agreement between components analysed from both AF and thermal demagnetisation procedure. Typically, the NRM of specimens was demagnetised by 30 mT (Figure 3.5) and 560-590°C. The site-mean direction from site FM05 (Table 3.1) was significantly different to the rest but failed a reversal test following the approach of Heslop & Roberts (2018b). Site-level VGPs from the 11 remaining successful sites were used to calculate a palaeopole (54.8°N, 216.2°E, K: 57.4, A_{95}: 6.1°). This palaeopole plots close to the palaeopole calculated by Manzoni. (1970) (48°N, 240°E, A_{95}: 10°), with some site-mean VGPs from this study lying within their A_{95} confidence interval (Figure 3.6a). The two palaeopoles

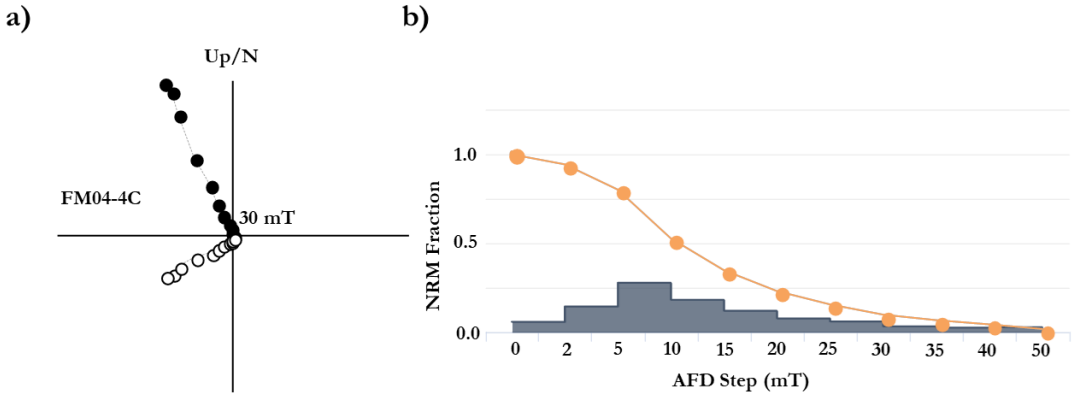

Figure 3.5: An example of typical AF demagnetisation behaviour experienced by pillow lava specimens of the Fernazza Fm. In this example, the data displayed was from specimen FM04-4C. a) Zijderveld plot, b) Intensity of specimen magnetisation with increasing AF demagnetisation steps. Remaining proportion of the NRM (orange circle), fraction of NRM lost between AF steps (grey profile).

do however, display statistically significant differences as demonstrated by the non-overlapping A_{95} confidence intervals (Figure 3.6a). Some sites that did not produce internally consistent ChRM directions were still selected for palaeointensity analysis (FM15, FM17, FM19) as they contained samples from different pillows and the ChRM directions grouped accordingly. These sites were located along roadside cuttings and it is thought that the pillows were made ex-situ during the excavation. In the cases of FM15 and FM19, directions from one pillow at each site showed good agreement with results from other sites. As such, these pillows have been interpreted as in-situ and the mean ChRM values from them utilised (Table 3.1).

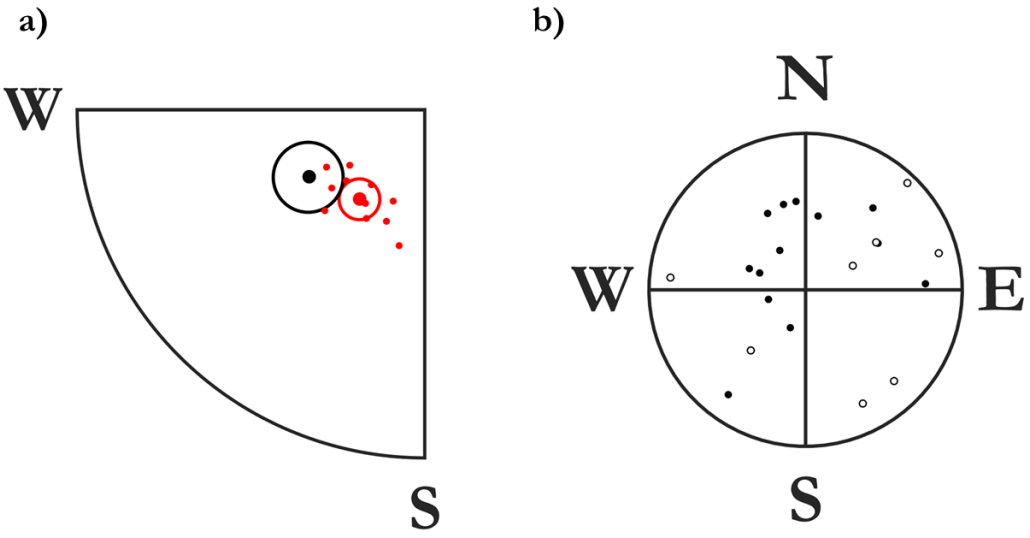

Figure 3.6: a) Comparison of mean VGPs from this study and Manzoni. (1970). Large red point represents mean VGP from this study, smaller circles represent VGPs from individual sites that make up the mean value. Black point represents mean VGP value from Manzoni (1970). In both cases the outer-ring represents A_{95} confidence interval. b) Stereoplot of ChRM directions isolated from specimens taken from clasts of the Marmolada conglomerate in order to carry out a conglomerate test. The resultant vector length (R) was 6.39 which resulted in a Bayes Factor of 2.07 (Heslop & Roberts, 2018a). The probability that the directions are of a uniformly random distribution was 0.67 (Heslop & Roberts, 2018a).

The conglomerate test on clasts from the Marmolada Conglomerate was performed following the Bayesian framework developed by Heslop & Roberts (2018a). Interpretable ChRM directions were isolated from specimens of 21 conglomerate clasts (Figure 3.6b; Table B.1), across two sampling sites. Directions from multiple specimens were interpreted and averaged for 5 of these clasts (Table B.1). The resultant vector length (R) from the 21 clasts was 6.39 which resulted in a Bayes Factor of 2.07. This produced a probability that the directions are of a uniformly random distribution of 0.67 which corresponds to weak support for the null hypothesis of uniformly random directional distribution (Heslop & Roberts, 2018a; Raftery, 1995).

Palaeointensity Estimates

Prior to conducting any palaeointensity experiments, the potential of secondary Fe-Ti oxides identified within amygdales (Figure B.4) to make a significant contribution to the remanence of bulk specimens was investigated. Individual amygdales were extracted from bulk specimens (Figure B.6), alongside micro-specimens composed of a mixture of calcite and bulk matrix material. In total, 10 specimens were studied, half of which were extracted amygdales and half were mixed specimens (Table B.2). The NRM of each specimen was measured before being subject to AF demagnetisation. Saturation magnetisation was also measured for each specimen and estimates of Curie temperature were obtained from thermomagnetic curves.

The NRMs measured for amygdale specimens were typically two orders of magnitude weaker than those of mixed specimens (Figure B.7a; Table B.2). The ability of amygdale specimens to acquire a remanent magnetisation was also significantly reduced, as evidenced by saturation magnetisation values that were lower by at least an order of

magnitude (Figure B.7b; Table B.2). Mixed specimens displayed coherent AF demagnetisation trends, from which ChRM directions could be isolated, this was not the case for amygdale specimens. Finally, estimated Curie temperatures were higher for amygdale specimens. These are suggestive of phases close to pure magnetite and perhaps haematite (Table B.2), mixed specimens displayed Curie temperatures closer to those that were estimated for bulk specimens (Table B.2). Overall, even when calcite amygdales constitute a relatively significant proportion of mixed specimens, the magnetic behaviour of the specimens appeared dominated by Fe-Ti oxides hosted within the bulk matrix. For this reason, it is believed that palaeointensity experiments conducted on specimens in which amygdales constitute a much less significant fraction, would be unaffected by the secondary Fe-Ti oxides that were identified within them. A more complete breakdown of these results is presented within the supporting information.

A summary of the palaeointensity results from the pillow basalts of the Fernazza Fm are presented in Table 3.1. A complete breakdown of all palaeointensity experiments can be found in the supporting information (Tables B.3, B.4, & B.5), separated by palaeointensity method and including critical values relative to the respective selection criteria. The success rates of palaeointensity experiments varied according to the experimental method but were relatively high across all three methods (thermal Thellier (30%), Shaw-DHT (57%), pseudo-Thellier (77%)) considering that palaeointensity experiments are often affected by high failure rates (Calvo et al., 2002; Calvo-Rathert et al., 2021; Carvallo et al., 2006; Perrin, 1998). These figures do not include specimens that passed the corresponding selection criteria but were excluded from the final site-mean calculations due to visual evidence of MD effects in Arai plots or the suggestion that an estimate was affected by experimental error.

Acceptable results from the IZZI+ thermal Thellier method were generally obtained from Arai plots that demonstrated an initial increase in magnetisation before a near-linear decrease, reaching magnetisation values < 10% of the NRM by 570°C (Figure 3.7a). For all cases, the temperature steps associated with the initial increase correspond to those of an overprint that demagnetised in a direction opposing the ChRM (Figure 3.7a). This overprint was commonly removed between 300°C and 400°C. Arai plots displaying the behaviour observed in Figure 3.7a, commonly failed β and/or k' (Table B.3) due to the zigzagging nature of the Arai plots. On occasion, highly zigzagging Arai plots still passed the selection criteria (Figure 3.7d) but were ultimately rejected due to the association with MD effects (Tauxe & Staudigel, 2004). The other commonly observed Arai plot behaviour is demonstrated in Figure 3.7b. Arai plot behaviour associated with an overprint is again observed but is followed by a sharp decrease, usually at 450°C (Figure 3.7b). A second slope is then observed that is usually mostly linear. In some cases, sections of this second slope pass the chosen IZZI+ selection criteria (Figure 3.7b) but consistently produce lower estimates than estimates obtained from specimens displaying linear behaviour (Table B.3). Palaeointensity estimates from Arai plots displaying this type of behaviour were not included in final site-mean estimates, even when the selection criteria were fulfilled. It was considered likely that this change in slope, across temperature steps of a single directional component, was due to MD effects (Dunlop & Özdemir, 2001; Levi, 1977) as passing pTRM checks make alteration of magnetic mineralogy (Kissel & Laj, 2004) an unlikely cause. The Arai plots from one batch of specimens were adversely affected by an oven calibration issue (Figure 3.7c). Where the affected results

passed the selection criteria and there was an agreement with multiple estimates from non-affected specimens, the palaeointensity estimates were included in the site-mean. Where this was not the case, estimates were rejected to ensure results were not biased by artefacts arising from the experimental issue.

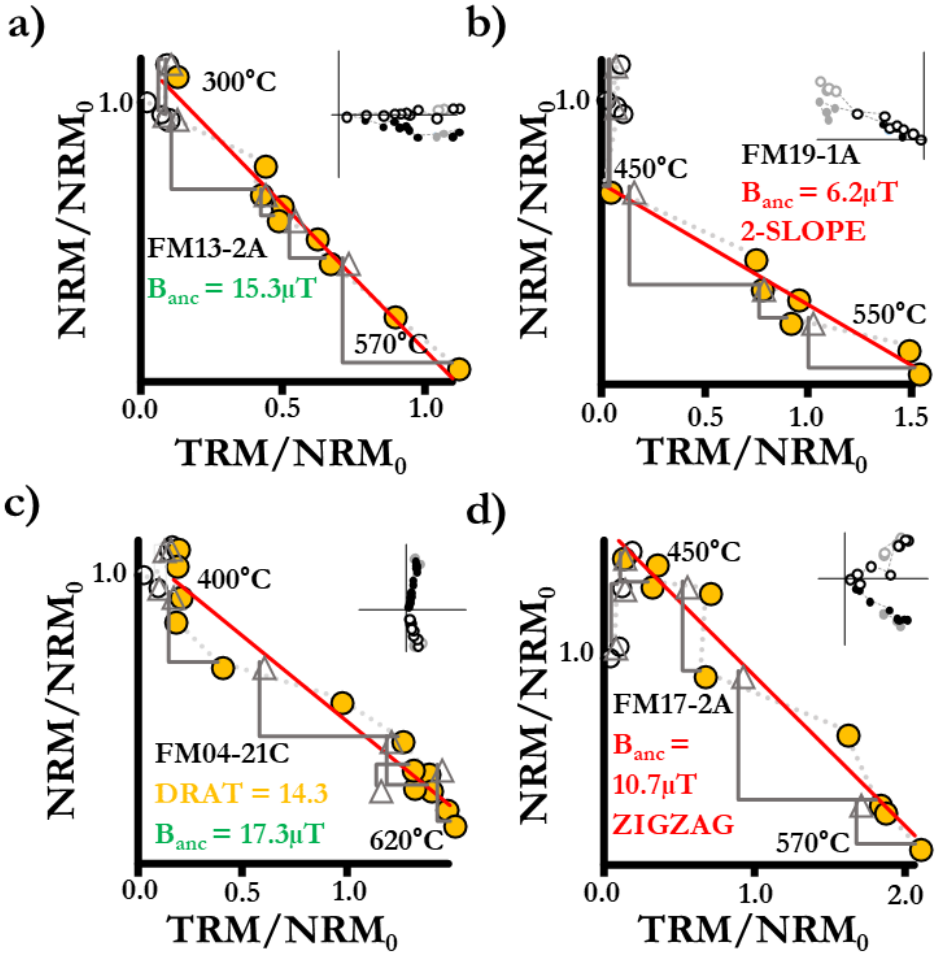

Figure 3.7: Representative Arai plots and Zijderveld plots (Zijderveld, 1967) of the thermal Thellier experiments. Filled circles (orange) represent the temperature steps selected for the palaeointensity estimates, with a best-fit line to these points (red). The start and end temperature steps are provided. Open triangles represent the pTRM checks. Black circles of the Zijderveld plot correspond to the same temperature steps as those chosen for palaeointensity analysis. Palaeointensity estimates are highlighted as accepted (green) or rejected (red). Zijderveld plots presented in specimen coordinates, with temperature steps selected for Arai plot interpretations in black.

The majority of palaeointensity estimates obtained via the Shaw-DHT method appear to have been obtained from specimens where ARM is a reasonable analogue to TRM, especially across the chosen coercivity range. This has been inferred by the similarity between the behaviour of the TRM plots and the ARM plots (Figure 3.8a, b, c). The applied alteration correction (ARM0/ARM1) varies across specimens, indicating varying degrees of specimen alteration during TRM acquisition. This is well demonstrated by results from site FM04 (Figure 3.8a, b, c), where the largest number of specimens were collected across a well-documented radial profile of an individual pillow. Despite the range of thermal alteration experienced, 13 specimens from FM04 produced estimates from the Shaw-DHT method between 9.8 and 14.9 μT. The corresponding σ_B/B ratio

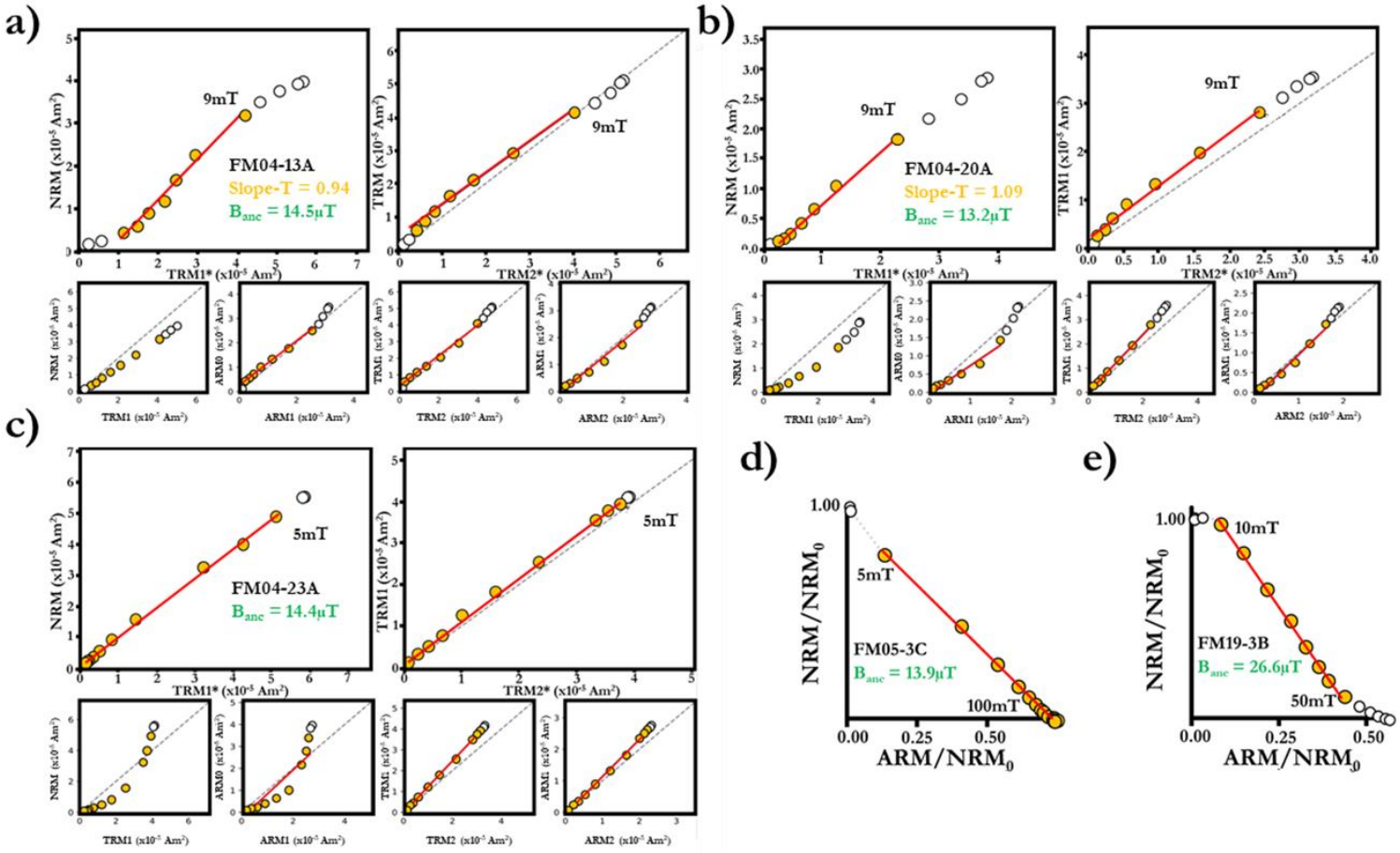

Figure 3.8: (a-c) Shaw results from site FM04. Top left – NRM remaining versus remaining TRM of first heating after ARM correction (TRM1); top right – TRM remaining versus remaining TRM of second heating after ARM correction (TRM2*); bottom left – remaining magnetisations of NRM, uncorrected TRMs and ARMs after first heating; bottom right – likewise after second heating, similar demagnetisation trends between TRMs and ARMs in bottom plots suggestive of analogous behaviour. ARM0 versus ARM1 provides visual representation of ARM correction. d-e) Representative pseudo-Arai plots displaying two commonly observed behaviours. a-e) Filled circles (orange) represent the temperature steps selected for the palaeointensity estimates, with a best-fit line to these points (red).*

Table 3.1: Palaeomagnetic results and palaeointensity estimates.

Site	**Lat** (°N)	**Long** (°E)	**Dec** (°)	**Inc** (°)	**n/ n_{dir}**	**k**	**α_{95}**	**B_{th}** (μT)	**σB_{th}** (μT)	**n/ n_{th}**	**B_{sh}** (μT)	**σB_{sh}** (μT)	**n/ n_{sh}**	**B_{pt}** (μT)	**σB_{pt}** (μT)	**n/ n_{pt}**	**B** (μT)	**σB** (μT)	**V(A)DM** (x10^{22} Am^2)	**Q_{PI}**
FM03	46.5	11.6	355.5	18.1	5/7	34	13.3	-	-	-	-	-	-	-	-	-	-	-	-	-
FM04	46.5	11.6	337.3	13.0	7/7	37	10.0	15.1	3.7	3/8	13.1	1.5	13/17	14.1	2.2	17/17	13.5	2.1	3.4	7
FM05	46.5	11.6	***123.8***	***-28.5***	6/7	18	16.5	-	-	0/7	18.1	0.5	2/8	15.3	2.2	5/8	18.1	0.5	-	-
FM06	46.5	11.6	339.9	31.6	7/7	9	21.4	18.0	-	1/6	21.9	2.7	2/5	14.8	3.3	2/3	20.6	3.0	4.7	6
FM08	46.5	11.6	356.0	29.3	6/6	57	9.0	16.8	-	1/7	13.8	2.4	5/10	18.3	5.3	9/10	14.3	2.4	3.3	6
FM09	46.5	11.6	347.8	34.0	7/7	48	8.8	-	-	-	16.1	2.1	4/4	16.1	3.7	3/4	16.1	2.1	3.6	5
FM10	46.5	11.6	347.9	24.3	7/7	41	9.6	8.0	0.3	3/8	15.6	3.9	4/7	19.7	2.3	6/7	12.4	4.9	3.0	6
FM11	46.5	11.6	349.5	16.8	5/7	23	16.4	21.9	-	1/3	18.5	6.3	6/9	24.8	6.7	8/10	19.0	5.9	4.8	5
FM13	46.5	11.6	0.6	6.4	6/6	14	37.2	15.3	0.1	2/8	18.0	-	1/4	18.1	6.2	2/3	16.0	1.8	4.1	6
FM14	46.5	11.6	336.6	25.5	6/7	127	6.0	-	-	0/4	15.2	2.3	3/5	13.3	3.0	6/6	15.2	2.3	3.6	4
FM15	46.5	11.6	12.9	4.1	3/7	19	39.7	-	-	0/3	22.7	1.8	2/7	18.5	2.6	2/7	22.7	1.8	-	-
FM16	46.5	11.6	338.9	38.7	5/7	36	13.1	10.9	2.2	4/6	16.7	2.9	3/5	19.0	2.2	4/5	13.4	3.8	2.9	4
FM17	46.5	11.6	-	-	-	-	-	19.0	4.2	2/8	12.4	-	1/5	22.9	4.0	3/5	16.8	4.9	3.9	5
FM18	46.5	11.6	332.4	33.5	6/8	17	17.0	15.0	0.5	3/8	14.6	3.1	5/6	17.1	5.6	3/5	14.7	2.4	3.3	6
FM19	46.5	11.6	352.0	15.8	2/7	16	25.0	11.7	3.1	3/7	16.9	4.5	4/5	20.9	8.2	2/3	14.7	4.6	3.7	4

Note 3.1: Site identifiers and site location (Lat, Long). Declination (Dec) and inclination (Inc) of the characteristic remanence directions provided alongside corresponding Fisher statistics (k, α_{95}). Directions and statistics presented for tilt-corrected site-mean ChRM directions. n/n_{dir} denotes the number of specimens utilised in final determination of Chrm/total number of specimens subjected to palaeomagnetic experiments. Bold/italicised interpreted as ex-situ. Site-level palaeointensity estimates (B_{method}) and corresponding standard deviations (σB_{method}) presented for each palaeointensity method (Thellier: th, Shaw: sh, pseudo-Thellier: pt). n/n_{method} denotes the number of specimens utilised in final site-mean palaeointensity estimates/total number of specimens subjected to corresponding palaeointensity method. Combined site-level palaeointensity estimates (B) and standard deviation (σB) for successful Thellier and Shaw experiments presented with corresponding virtual (axial) dipole moment (VADM) and assigned Q_{PI} score (Biggin & Paterson, 2014; Kulakov et al., 2019).

can be attributed, with some confidence, as being less than 0.15, following the *n*-dependent cut-off approach proposed by Paterson et al. (2010) that compensates for the number of palaeointensity estimates being below that required for a reliable estimate (n = 24; Paterson et al., 2010).

Pseudo-Arai plots were generally linear which has resulted in a very high success rate for the method (Table 3.1). Specimens tend to display one of two types of behaviour (Figure 3.8d, e). The first sees a slight change in pseudo-Arai slope across a low coercivity range associated with an overprinted direction (Figure 3.8d). The second type of behaviour also sees this initial slope change but also a gradual tailing off effect at high coercivities, by which point the NRM of the specimen has demagnetised by ~90% (Figure 3.8e). For almost all sites there is a good agreement between estimates derived from the pseudo-Thellier method and those from the Shaw-DHT method, especially when the 25% error associated with the pseudo-Thellier method is considered. The exception to this is site FM17 (Table 3.1) but here there was only one accepted estimate from the Shaw-DHT results and the pseudo-Thellier estimate shows good agreement with the more numerous thermal data (Table 3.1).

A wider comparison of estimates across all methods shows that there is generally good agreement (Table 3.1). Where estimates from the thermal Thellier and Shaw-DHT methods, show a greater deviation from one another (≥ 25%), it is the estimates from the thermal Thellier method that are the lower of the two (FM10, FM16, FM19, Table 3.1).

Discussion

Reliability of Palaeointensity Estimates

The composition of the titanomagnetite grains within the pillow lavas of the Fernazza Fm are lower in Ti-content than the TM60 grains typically observed in submarine basalts (Dunlop & Özdemir, 1997). Casetta et al. (2021) concluded that lava flows of the Fernazza Group contained spinel grains ranging in composition between TiO_2 = 0.1-17.4 wt%. This corresponds to a compositional range from magnetite to a titanomagnetite with approximate ulvöspinel end-member mole fraction (X_{Usp}) of ~0.52 (Evans et al., 2006). Titanomagnetite grains with an X_{Usp} value of ~0.52 would be expected to have 250°C < T_C < 300°C (Lattard et al., 2006). This agrees with the demagnetisation behaviour of the ChRM observed in the thermal Thellier experiments. Well-behaved, successful specimens typically displayed linear portions on the Arai plots from 300°C to 570°C (Figure 3.7a), the latter a Curie temperature representative of a phase close to pure magnetite. It is known that magnetite grains can form at sea-floor conditions through the disproportionation of cation-deficient titanomaghaemite (Kent & Gee, 1994), which would result in a chemically altered, secondary magnetisation. The presence of fine-scale ilmenite lamellae in the titanomagnetite grains (Figure 3.4b, c) suggests that they are the result of high-temperature oxyexsolution above, or close to, the Curie temperature. The Ti-poor titanomagnetites are therefore interpreted as a primary phase. Together with evidence that low temperature oxidation was limited, as will be expounded below, these are likely to be associated with a primary thermoremanence (Haggerty, 1991: Wilson & Watkins, 1967). High-temperature oxidation may explain the discrepancy between the T_C estimates obtained from analysis of the thermomagnetic curves (~500°C) and the

maximum unblocking temperatures of ~570°C (Figure 3.2). Kent & Gee. (1994) proposed that a maximum unblocking temperature 50°C to 100°C above that of the dominant T_C was the result of fine-grained TM60, that had experienced a large amount of maghaematisation, carrying most of the NRM and less-oxidised, MD TM60 grains dominating high-field magnetic properties. The explanation being that SD grains oxidised faster and more thoroughly due to their larger specific surface area. Extending this thinking to the relatively Ti-poor titanomagnetites of the Fernazza Fm lavas, fine grained titanomagnetites are more likely to have experienced the latter stages of high-temperature oxidation, resulting in titanomagnetites closer to pure magnetite predominantly carrying the NRM. Larger grains are likely to be less oxidised resulting in titanomagnetites with a higher Ti-content dominating the rock magnetic experiments.

The Ti-poor titanomagnetites observed in the lavas of the Fernazza Fm are more typically associated with subaerial lavas (Dunlop & Özdemir, 1997). This is primarily because a combination of a slower cooling rate, within subaerial interiors, and higher oxygen fugacity facilitate high-temperature oxidation more readily (Dunlop & Özdemir, 1997). The absence of skeletal titanomagnetite grains, commonly associated with submarine lavas, is indicative of a relatively slow cooling rate. Some mineral species display feathery quench textures that could indicate a slower rate of cooling but not as slow as typically experienced by sub-aerial flows (Figure 3.4f). The pillow lavas sampled in this study ranged from ~2 m to ~5 m in diameter, with a typical diameter of ~3 m. This would facilitate a slower rate of cooling than experienced by most pillows, which typically range up to 1 m in diameter (Arndt, 2011). The growth of pillows comparable to the sizes of those from this study can take days compared to hours for smaller pillows (Walker, 1992), after which significantly slower cooling of the interior occurs. As pillow size is primarily controlled by the viscosity of the extruding melt (Walker, 1992) and the SiO_2 content is a primary control of melt viscosity, it would appear that the SiO_2 saturated nature of the Fernazza lavas (Casetta et al., 2018b; 2021) is the primary cause of the formation of large pillow structures. The presence of trachyandesitic pillows within the Fernazza Fm presents the possibility that the most massive pillows sampled were andesitic, a typical composition of such large pillows (Walker, 1992).

The shoshonitic nature of the Fernazza lavas would appear to offer a mechanism for a higher oxygen fugacity. Potential mantle sources for shoshonitic basalts have been predicted to have higher oxygen fugacity than comparable sources for low-K tholeiite, calc-alkaline, and enriched intraplate magmas (Rowe et al., 2009). However, the fugacity values calculated by Casetta et al. (2018b), relative to the Quartz-Fayalite-Magnetite buffer (Frost, 1991), are comparable to those expected of back-arc-basin/arc melts (Cottrell et al., 2021). Melts from back-arc/arc settings are of higher oxygen fugacity than those associated with mid-ocean ridge basalts (MORBs), the typical source when submarine basalts have previously been studied for their palaeointensity potential (Carlut & Kent, 2002; Kent & Gee, 1996; Xu et al., 1997; Zhou et al., 2001). Regardless of the specific tectonic setting associated with the Fernazza Group lavas, the higher oxygen fugacity when compared to MORB settings likely contributes to the facilitation of high-temperature oxidation, and the different magnetic mineralogy when compared to previously studied submarine pillow lavas (Carlut & Kent, 2002; Kent & Gee, 1996; Xu et al., 1997; Zhou et al., 2001). Although, in this case, the shoshonitic nature of the melt may not have actively encouraged high-temperature oxidation, the Ti-depleted nature of

the melt (Casetta et al., 2021; Morrison, 1980) likely influenced the production of titanomagnetite grains with a Ti-poor affinity.

As well as containing titanomagnetite grains with a range of Ti-content unusual for submarine lavas, the Fernazza Fm pillows also appear to have experienced less low-temperature oxidation than might be expected. Typically, fine titanomagnetite grains in quenched submarine pillows experience low-temperature oxidation, resulting in maghaemite formation, within the first 500 Kyr following their eruption (Irving, 1970; Johnson & Atwater, 1977; Johnson & Pariso, 1993). This effect appears reduced in the specimens of this study as demonstrated by thermomagnetic curves with a higher degree of reversibility (Figure 3.2) than those typically associated with submarine lavas (Dunlop & Özdemir, 1997). This interpretation is further supported by a reduced maghaemite associated signature in the susceptibility-temperature curves and a distinct Hopkinson peak (Figure 3.2), a soft NRM typically removed by maximum AF values of 30 mT (Figure 3.5), and the observed restriction of cracks to grain edges (Figure B.5). Hydrothermal fluids typically enter pillows through radial cracks that form due to the rapid cooling of the extruding lava (Humphris, 1972; Humphris & Thompson, 1978). In larger pillows, these radial cracks will permeate throughout less of the pillow resulting in a core that is relatively fresh and unaffected by circulating hydrothermal fluids. The possibility of falling sea-levels, associated with the formation of the Marmolada Conglomerate (Brandner et al., 2016), may have further reduced the interaction between hydrothermal fluids and the Fernazza Fm in localised areas.

Despite the seemingly limited occurrence and influence of maghaemite, the potential effects on obtained palaeointensity estimates are still considered. Maghaematisation of (titano)magnetite, after it has acquired a TRM, results in a grain that is carrying magnetisation via a TCRM, as defined by Fabian. (2009) as any chemically modified TRM. The result is a change in unblocking behaviour, compared to that of the original (titano)magnetite grain, that can result in underestimated or overestimated palaeointensity values. It has been demonstrated, both experimentally and theoretically, that such effects can produce linear Arai plots in Thellier-style experiments (Draeger et al., 2006; Fabian, 2009). It has also been shown that accurate palaeointensity estimates can be obtained from submarine pillow lavas that have experienced a limited degree of low-temperature oxidation (Grommé et al., 1979). The results from the radial profile across the pillow sampled at site FM04 suggest that the degree of experienced low-temperature oxidation had a negligible effect on the final palaeointensity estimates. 13 accepted results were obtained from the Shaw-DHT method, spanning across a ~1.7 m radial profile. As predicted by the circulation model for hydrothermal alteration of individual pillows (Humphris, 1972; Humphris & Thompson, 1978), specimens from the core of the pillow appear to have experienced very little low-temperature oxidation. Rock magnetic results demonstrate that any thermal alteration, as a consequence of laboratory heating, is likely attributable to the inversion of maghaemite (Figure B.1). As the ARM correction of the Shaw experiment compensates for thermal alteration during TRM acquisition, the magnitude of the correction can be viewed as a proxy for the degree of maghaemite inversion, and subsequently, low-temperature oxidation. The size of the ARM correction systematically increases as the sampling position of the studied specimen goes from the core to the outermost edge of the pillow (Figure 3.8). The ARM correction aims to correct the palaeointensity estimate to that which would be estimated by the original carrier, prior

to laboratory heating. For a specimen dominated by maghaemite as a magnetic carrier, this would result in a correction to the TCRM that is being carried, that would represent an underestimated/overestimated value. In the case of specimens from FM04, one would expect to observe this effect as a systematic trend across the pillow profile in the estimated palaeointensity values, according to the systematic variation in maghaemite/degree of low-temperature oxidation. The consistent palaeointensity estimates obtained (Table 3.2) would suggest that the degree of oxidation, in even the most affected specimens close to the pillow rim, is not sufficient to produce biased estimates. Strong agreement between estimated values obtained across the different palaeointensity methods suggests that those from the thermal Thellier and the pseudo-Thellier method are also reliable. Unfortunately results could not be obtained from specimens towards the centre of the pillow with the thermal Thellier method as they demonstrated two-slope behaviour. This was likely due to an increased influence of MD grains as slower cooling rate in the pillow interior encouraged the growth of larger grains. The domain state independent nature of the Shaw method (Lloyd et al., 2021b) made it more ideally suited and can explain the higher success rate of, not only site FM04, but the overall success rate close to double that observed for the thermal Thellier method across all sites (Table 3.1).

Table 3.2: Shaw palaeointensity estimates from site FM04.

Specimen	**Distance from centre** (m)	$\mathbf{B_{anc}}$ (μT)
FM04-10A	0.05	11.8
FM04-12A	0.35	13.3
FM04-13A	0.40	14.5
FM04-14A	0.45	13.9
FM04-15A	0.50	10.9
FM04-16A	0.60	13.4
FM04-17A	0.75	14.9
FM04-18A	0.90	11.7
FM04-19A	1.05	9.8
FM04-20A	1.05	13.2
FM04-21A	1.15	14.1
FM04-22A	1.40	13.9
FM04-23A	1.55	14.4

Note 3.2: Palaeointensity estimates obtained via the Shaw method across the radial pillow profile sampled at site FM04. Specimen level results presented in order of increasing distance from the pillow centre.

All of the 14 sites selected for palaeointensity analysis produced accepted specimen-level estimates (Table 3.1). Final VDM estimates were obtained from 12 sites with a combined $n \geq 3$ using the thermal Thellier and Shaw-DHT methods. In the case of site FM17 no VDM could be calculated as a result of the separate ex-situ blocks sampled. Site palaeolatitude was established from the plate reconstructions of Torsvik & Cocks. (2016) in order to calculate a virtual axial dipole moment (VADM). The quality of palaeointensity (Q_{PI}) scores (Biggin & Paterson, 2014; Kulakov et al., 2019) assigned to the final V(A)DM estimates range from 4 to 7 with a median value of 5.5 and a mean value of 5.3. Variation in the final scores is primarily attributable to poorly defined site-mean palaeomagnetic directions ($k < 50$, Kulakov et al., 2019), in agreement with the observations of Manzoni.

(1970), and a lack of successful thermal Thellier estimates from some sites. The first leads to failure of Q_{DIR} and the latter Q_{TECH}. As only one lithology was investigated in this study Q_{LITH} was always zeroed, and despite evidence suggesting the nominal effect of maghaemite on the final palaeointensity estimates, the conservative decision was taken to make Q_{TRM} zero for all sites. A full breakdown of the Q_{PI} assessment is presented in the supporting information (Table B.6).

Comparison with Palaeointensity Record

Final site-mean VDM estimates from the pillow lavas of the Fernazza Fm range from 3.0 x 10^{22} to 4.8 x 10^{22} Am^2 (Table 3.1). The V(A)DM estimates have been assigned an age of 238.2 ± 0.5 Ma (Storck et al., 2019), which lies in the middle of the maximum eruption duration based on dates obtained from beds of the Buchenstein Fm (Storck et al., 2019) and the Frommer member (Mietto et al., 2012). The magnitude of the V(A)DM estimates from this study lie in-between the two estimates within the most recent update to the PINT database (Bono et al., 2021) between 249 Ma and 202 Ma (Figure 3.9). The pre-existing VDM estimate in the middle of the Triassic (7.1 x 10^{22} Am^2, Figure 3.9) has an associated Q_{PI} value of 2 and fails many of the criteria primarily due to the age of the original study (Schwarz & Symons, 1968), as modern experimental and analytical techniques were not routinely applied. The associated age of 225 Ma also carries with it an error of 30 Ma (Wanless, 1966), so that the formation could in fact lie outside of the Triassic. The other Triassic VDM estimate (2.7 x 10^{22} Am^2) comes from the study of Eitel et al. (2014) who conducted a palaeomagnetic investigation on impact melt breccias associated with the Rochechouart meteorite impact. Unlike the palaeointensity estimates of this study, that were obtained from lava flow sequences covering a duration of up to 0.9 Ma, an estimate obtained from an impact melt provides information on a single time instance. It would appear then, that the V(A)DM estimates presented in this paper provide the most reliable insight into the strength of the geomagnetic field during the Triassic.

This improved definition of the geomagnetic field strength during a key interval, and the results of recent studies focused on PSV behaviour across intervals over the last ~320 Ma (Cromwell et al., 2018; de Oliveira et al., 2018; Doubrovine et al., 2019; Engbers et al., 2022; Handford et al., 2021), provide an opportunity to investigate a possible relationship between virtual geomagnetic pole (VGP) dispersion patterns and the intensity of the Earth's magnetic field. For this, the PINT record has been analysed in the same discrete time intervals as those in the PSV study of Handford et al. (2021), with the exception of the last 10 Ma (PCRS; 318-265 Ma, Post-PCRS; 265-198 Ma, Pre-CNS; 198 - 126 Ma, CNS; 126-84 Ma). Directional data from the second half of the last 10 Ma was recently incorporated into an updated Miocene era (23.0-5.3 Ma) PSV study (Engbers et al., 2022), and as such the intervals of the last 5 Ma and the Miocene have been adopted in this study.

For each interval, the median V(A)DM value and interquartile range were calculated (Table 3.3), after the application of a data quality filter of $Q_{PI} \geq 3$, following the approach of Bono et al. (2021). The median value for most intervals, lay within the interquartile range of the long-term median V(A)DM value calculated in this study (4.6 x 10^{22} Am^2, Table 3.3; IQR 2.9 x 10^{22} - 7.1 x 10^{22} Am^2, Figure 3.9). The exceptions are the Post-PCRS and the PCRS. V(A)DM data from in and around the Permo-Triassic boundary (PTB:

252-249 Ma; this study), accounts for almost 87% of the Post-PCRS data and has a median value of 2.3 x 10^{22} Am^2. Spatial coverage for the PTB is very poor, as all data in the PINT database is derived from Siberian Traps material. The apparent reduced geomagnetic field strength could be a local, time-limited feature and as such palaeointensity data from the PTB is required that is not associated with the Siberian Traps. Regardless, the new results of this study suggest that this behaviour is not representative of the Post-PCRS as a whole, and removal of the PTB data produces a median V(A)DM value of 3.6 x 10^{22} Am^2, although data distribution is now sparse. This would leave the PCRS as the only outlying time interval, with regards to its average geomagnetic field strength (Figure 3.9). It has previously been suggested that this may be attributable to it being a time interval in which the geomagnetic field was strongly axially dipole dominated (Handford et al., 2021). This was based on high estimates of the AD/NAD_{median} value, a measure of axial dipole dominance calculated using the power law relationship with the Model G *a* parameter (Biggin et al., 2020). The Model G *a* parameter is, itself, an estimate of equatorial VGP dispersion (McFadden et al., 1988).

Table 3.3: Comparison of median palaeointensity values and estimated degree of axial dipole dominance for the studied time intervals across the last ca. 320 Ma.

Time Interval	**Age Range** (Ma)	**Median V(A)DM (Q1, Q3) QPI ≥ 1** (x 10^{22} Am^2)	**Median V(A)DM (Q1, Q3) QPI ≥ 3** (x 10^{22} Am^2)	**AD/NAD_{median}** (1)
PCRS	318-265	9.2 (5.9, 10.8)	8.4 (4.5, 10.7)	58.4 +6345.1/−47.3
Post-PCRS	265-198	2.5 (1.8, 3.4)	2.5 (1.7, 3.4)	6.9 +9.2/-5.0
Pre-CNS	198-126	3.8 (2.4, 5.2)	4.6 (3.3, 6.9)	8.8 +18.9/-6.0
CNS	126-84	4.9 (3.6, 7.1)	5.4 (4.0, 7.6)	15.1 +29.9/-10.2
Miocene	23.0-5.3	3.8 (2.3, 6.1)	3.5 (2.1, 5.3)	3.5 +8.9/-2.4
Last 5 Ma	5.3-0.0	6.2 (4.0, 8.6)	5.4 (3.5, 7.7)	9.7 +19.2/-6.9
Long-term	320-0	5.2 (3.4, 8.4)	4.6 (2.9, 7.1)	-

Note 3.3: Median virtual (axial) dipole moment (V(A)DM) and associate lower quartile (Q1) and upper quartile (Q3) values as taken from PINT v8.0.0 (Bono et al., 2021) after the application of QPI1 and QPI3 filtering, respectively. (1) Estimates of the degree of axial dipole dominance (AD/NAD_{median}) calculated from Model G shape parameters (Handford et al., 2021).

Estimates of AD/NAD_{median} have also been calculated previously for the CNS, Pre-CNS, and the Post-PCRS (Handford et al., 2021), providing an opportunity for their comparison against the V(A)DM record. AD/NAD_{median} values were also calculated for the last 5 Ma and the Miocene. These were derived from Model G fits to VGP scatter patterns (McFadden et al., 1988) observed for each interval, completed following the approach of Handford et al. (2021). For the last 5 Ma, directional data was sourced from the larger PSV10 database (0-10 Ma) of Cromwell et al. (2018). For the Miocene, the CS1 subset of Engbers et al. (2022) was chosen as this most closely resembled the selection criteria applied to data in the time intervals studied by Handford et al. (2021). From the Post-PCRS through to the Pre-CNS and the CNS, estimated AD/NAD_{median} values show a gradually increasing trend, in keeping with the increasing median V(A)DM values of the intervals (Figure 3.10; Table 3.3). Both the estimates of AD/NAD_{median} and median V(A)DM then decrease during the Miocene before increasing again during the last 5 Ma (Figure 3.10; Table 3.3). Although this positive relationship between the degree of axial dipole dominance and the intensity of the palaeomagnetic field is somewhat intuitive, it is not an essential condition and its occurrence might suggest that the intensity of the

non-dipole field varies less than that of the dipole. This result demonstrates how PSV studies can act as powerful tools in helping to better define the palaeomagnetic field.

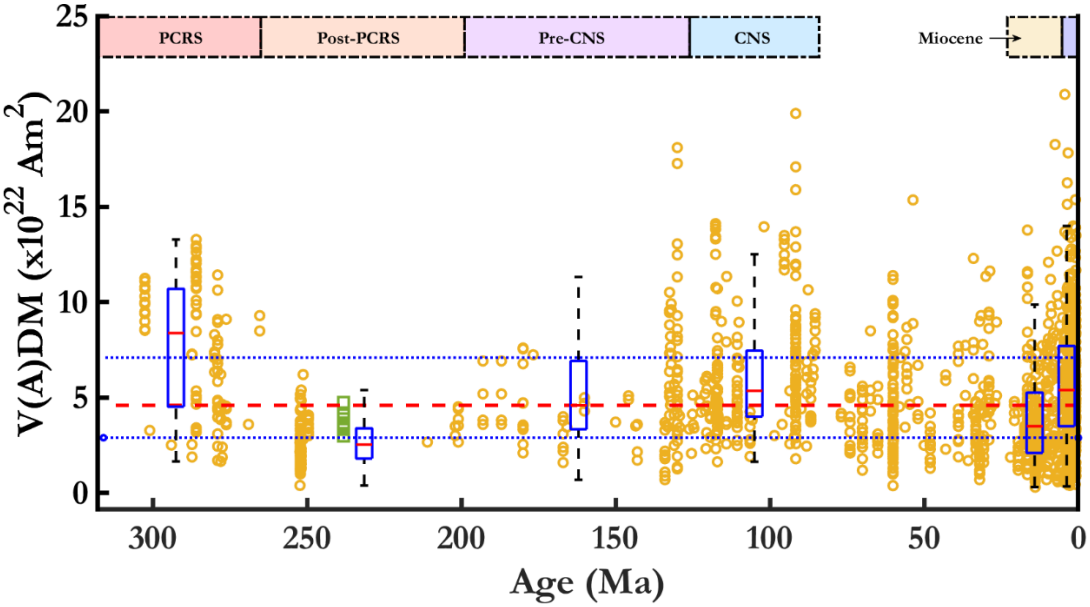

Figure 3.9: The virtual (axial) dipole moment (V(A)DM) record between 320 Ma and present-day. V(A)DM values, with $Q_{PI} \geq 3$, from v8.0.0 of the PINT database (Bono et al., 2021, yellow circle) plotted alongside site-level V(A)DM estimates from this study (green square). Boxplots for each time interval studied (PCRS, Post-PCRS, Pre-CNS, CNS, Miocene, Last 5 Ma) represent the median value for the interval (red), alongside the interquartile range (blue), and the maximum and minimum V(A)DM values after the removal of outliers (black). Boxplots are plotted against the mean age of the associated time interval. The long-term average V(A)DM value is given by the dashed line (red) alongside the interquartile range, dotted lines (blue).

Any relationship between the degree of axial dipole dominance and the average intensity of the palaeomagnetic field does appear somewhat complex, however. Although the general evolutionary trends of the two geomagnetic field characteristics display some agreement (Figure 3.10), a lesser degree of axial dipole dominance resulted in stronger dipole moments during the intervals that occurred after the CNS (Figure 3.10; Table 3.3). This could indicate a regime change in the geodynamo during or after the CNS. Alternatively, and perhaps more likely, the greater intensities relative to AD/NAD_{median} values associated with time intervals since the CNS, may be a consequence of analysing the geomagnetic field across shorter time-scales. In doing so, greater emphasis can be placed on relatively short-term features that would not be highlighted when incorporated into a longer time interval for analysis. This is similar to how, in this study, the strength of the geomagnetic field appears broadly consistent since the Triassic, but the interval associated with the increased polarity reversal rate during the Jurassic (171-155 Ma) has been demonstrated to have been a time in which the geomagnetic field was demonstrably weaker than during surrounding intervals (Kulakov et al., 2019). In either case, better characterising the relationship between AD/NAD_{median} is difficult due to the large errors associated with estimates of AD/NAD_{median}, that often result in statistically indistinct values (Table 3.3).

In order to further explore the relationship between axial dipole dominance and the V(A)DM record, better constraints are required on the strength of the geomagnetic field during the Post-PCRS. In particular, more palaeointensity data for the sparsely populated Triassic, and estimates derived from PTB material not associated with the Siberian Traps.

By contrast, the V(A)DM record is relatively well populated between the CNS and the Miocene (84-23 Ma) but a modern PSV investigation is lacking. McFadden et al. (1991) generated VGP scatter patterns across this interval, but these are unsuitable for comparison with the results from modern studies.

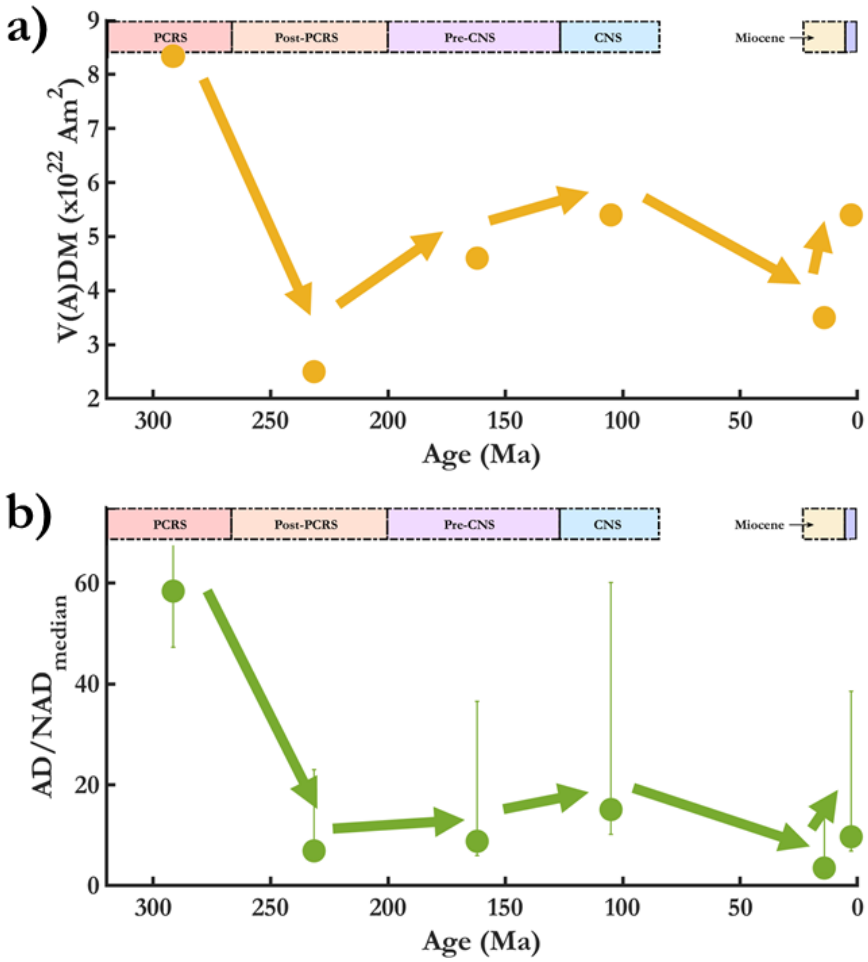

Figure 3.10: Evolution in a) median virtual (axial) dipole moment V(A)DM and b) axial dipole dominance (AD/NAD_{median}) across the last 320 Ma. Overall trends highlighted with arrows. Error bars provided for estimates of AD/NAD_{median}.

Conclusions

The palaeointensity results from the pillow basalts of the Fernazza Fm are likely representative of the middle Triassic geomagnetic field. A slow rate of cooling and higher oxygen fugacity, than that associated with a typical MORB setting, facilitated high-temperature oxidation and the formation of primary, Ti-poor titanomagnetite grains. The degree of low-temperature oxidation experienced by the studied pillow lavas appeared reduced when compared with more typical submarine lavas. In part, this could be due to the reduced surface area to volume ratio of pervasive cracks, and fluctuation in sea-levels post eruption. The low-temperature oxidation that did occur appears unlikely to have significantly biased the palaeointensity estimates. A positive conglomerate test on specimens from clasts of the Marmolada Conglomerate provides evidence that the

magnetisation carried by the Fernazza lavas is primary, and supports the palaeointensity estimates as being representative of the geomagnetic field during their formation.

The new V(A)DM estimates from this study (3.0×10^{22} to 4.8×10^{22} Am^2), represent the most reliable description, to date, of the strength of the geomagnetic field during the Triassic. When averaged across long time intervals, geomagnetic field strength appears to have remained approximately constant from at least the middle Triassic, in keeping with a long-term average. It would appear that any variations in geomagnetic field strength between different time intervals are also reflected the different degrees of contribution from the axial dipole component of the geomagnetic field, suggesting an interrelation. The PCRS could represent a unique time over the last ~320 Ma, during which the geomagnetic field was significantly stronger, potentially as a result of the enhanced dipole dominance previously suggested for the interval (Handford et al., 2021). Two main areas for future work have been highlighted, to further explore the relationship between secular variation and geomagnetic field strength. The first, continual improvement to the palaeointensity record during the Post-PCRS. Within this interval, Triassic-aged data is still sparse, and the strength of the PTB is defined exclusively by data derived from material associated with the Siberian Traps. The second area is an updated, detailed investigation into the PSV behaviour between 84 Ma and 23 Ma as this would result in a continuous account of PSV behaviour for the last ~320 Ma.

Acknowledgements

This research was undertaken with funding from The Leverhulme Trust (Research Leadership Award, RLA-2016-080). All data from Shaw-DHT experiments was analysed using a Jupyter notebook developed by Daniele Thallner at the University of Liverpool. The Author would like to thank Dr Matt Bilton, Dr Heath Bagshaw, and the SEM Shared Research Facility at the University of Liverpool for the support received for the acquisition of high-resolution BSE images and EDX analyses. In addition, the author wishes to acknowledge the experimental data collected by Banusha Kugabalan, and the insightful petrological discussions with Janine L. Kavanagh that contributed to this chapter. Palaeomagnetic sampling was undertaken alongside Annique van der Boon at the University of Liverpool.

Chapter 4. Triassic palaeointensity estimates from Argentina: investigating the viability of ignimbrites as palaeointensity recorders of the ancient geomagnetic field

Abstract

When analysing palaeointensity records since the Permo-Carboniferous Reversed Superchron (PCRS), a paucity of data is apparent during and around the Triassic (ca. 252-201 Ma). In part, this can be attributed to a lack of basaltic lava units having been attributed to the Triassic, the most utilised rock-type for palaeointensity experiments. This study investigates the plausibility of obtaining reliable palaeointensity estimates from ignimbrite units of this age, an approach with potentially far-reaching consequences in better populating the palaeointensity record. This study presents new palaeointensity results from rhyolitic ignimbrites and basalt sills of the Puesto Viejo Group, located in the San Rafael depocenter of Mendoza, Argentina. Estimates of virtual dipole moment ranged between 0.9 x 10^{22} and 2.1 x 10^{22} Am^2 with an average Q_{PI} value of 6. Estimates were assigned a likely age of 235.8 ± 2.0 Ma. The overlapping range of palaeointensity estimates obtained from the different lithologies, in conjunction with the bimodal tectonic setting that they represent, was interpreted as support for the reliability of the estimates obtained from ignimbrite specimens. In the absence of similar evidence, estimates obtained from dacitic ignimbrite units of the Los Menucos Complex of Patagonia, Argentina, could not be ascertained as being reliable. Furthermore, after detailed evaluation of the nature of the magnetic remanence carriers, via rock magnetic experiments and microscopy, estimates obtained from these units were interpreted as likely being unreliable. Analysing the reliable estimates of V(A)DM from Puesto Viejo, alongside recently obtained estimates of a similar assigned age, indicated a slight reduction in the intensity of the geomagnetic field persisting from the Permo-Triassic boundary (ca. 252 Ma) until a few tens of millions of years preceding the onset of the Cretaceous Normal Superchron (127-84 Ma).

Introduction

Our understanding around the strength of the palaeomagnetic field during, and immediately preceding the Triassic, has previously been highlighted as a gap in our knowledge of palaeointensity evolution since the Permo-Carboniferous Reversed Superchron (PCRS; ~318-265 Ma; Haldan et al., 2009; Opdyke & Channell., 1996) (Anwar et al., 2016; Biggin & Thomas, 2003, **Chapter 3**). It appears that this shortage of data has arisen due to a lack of geological material most traditionally utilised for palaeointensity analysis, being associated with dates from around this time (Handford et al., 2021). Recent improvement has been made to the palaeointensity record (**Chapter 3**) but further reliable data is required to provide greater insight into the variability of palaeointensity across this time interval. The palaeointensity results from the middle Triassic lavas of the Dolomites (**Chapter 3**), suggested that the strength of the geomagnetic field during the Post-PCRS (265-198 Ma; Handford et al., 2021) displayed little variation when compared with the long-term average over the last 318 Myr. This was proposed under the assumption that the low palaeointensity estimates in the PINT database (PINT V8.0.0, Bono et al., 2021) from around the Permo-Triassic boundary (PTB; ca. 251.9 Ma; Ogg, 2012), are not representative of the average palaeointensity across the Post-PCRS, and instead represent some local, time limited feature (**Chapter 3**). Treating the Post-PCRS palaeointensity data in this way led to the suggestion of a relationship between the strength of the palaeomagnetic field and its degree of axial dipole dominance, in turn suggesting some degree of covariance between palaeosecular variation (PSV) and palaeointensity (**Chapter 3**). Putting the PTB data aside in this manner, leaves very little data defining the Post-PCRS, however. In order to better define the strength of the Post-PCRS, more palaeointensity estimates are required, and the assumption surrounding the treatment of PTB data requires further validation.

Southern South America is known to contain numerous Mesozoic aged basins that characterise a largely extensional regime (Lovecchio et al., 2020), the earliest of which formed during the Post-PCRS. These basins are generally characterised by sedimentary deposits interlayered with volcanic tuffs, ignimbrites, and more scarcely, igneous lithologies (Barredo et al., 2012; Martínez Dopico et al., 2019; Monti & Franzese, 2019; Ottone et al., 2014; Spikings et al., 2016). The Los Menucos Complex and the Puesto Viejo Group feature in the compilation of Post-PCRS palaeomagnetic data of Handford et al. (2021), and, between them, their lithological units cover a range of dates across the early to late Triassic. Of particular interest, are the dacitic ignimbrites of the Los Menucos Group, whose associated date (248 ± 2 Ma; Luppo et al., 2018) places their formation close to the PTB, and the rhyolitic ignimbrites and coeval basaltic sills (Domeier et al., 2011b; Valencio et al., 1975), of the Puesto Viejo Group that have a formation date (235.8 ± 2.0 Ma, Ottone et al., 2014) close to that of Fernazza formation (Fm) lavas of the Dolomites (ca. 238.2 ± 0.5 Ma, **Chapter 3**). If successful, palaeointensity results from the Los Menucos Complex would provide insight into the global variability of the palaeomagnetic field around the PTB. Likewise, results from the Puesto Viejo Group would facilitate assessment of geomagnetic field strength around a time where, currently, palaeointensity estimates strongly influence the definition of the Post-PCRS palaeointensity.

Ignimbrites have previously been identified as potentially viable palaeointensity recorders (Sbarbori et al., 2009; Gee et al., 2010), due to the observed presence of single domain (SD) sized iron-oxides (Schlinger et al., 1991), and the possibility that their silica rich matrices may offer protection against the thermal alteration of the SD magnetic carriers during laboratory heating. Despite this, palaeointensity estimates direct from ignimbrites or welded tuffs, i.e. not from baked margins associated with later volcanic activity, account for just ~1% of data in the palaeointensity database (PINT v8.0.0; Bono et al., 2021). This is likely due to the difficulty in ascertaining the reliability of estimates obtained from ignimbrites, as they often form in environments where interaction with hydrothermal fluids is common, resulting in the formation of secondary magnetic phases. Palaeointensity investigations that utilise ignimbrites almost exclusively study recent formations (< 1 Ma; Avery et al., 2018; Bowles et al., 2015; Gee et al., 2010; Mochizuki et al., 2013; Sbarbori et al., 2009; Takai et al., 2002), reducing the likelihood of observing effects due to hydrothermal alteration. The Bishop Tuff, of eastern California, represents the most comprehensively studied ignimbrite sequence for palaeointensity analysis (Gee et al., 2010; Fu et al., 2017; Avery et al., 2018). The most recent of these studies (Avery et al., 2018) obtained accurate palaeointensity estimates from the most densely welded sections, but highlighted the need for a thorough understanding of the thermal history when attempting to use ignimbrite units to obtain palaeointensity estimates. Relatively low emplacement temperatures and/or vapour phase alteration (VPA) (Vaniman, 2006), post-emplacement, can result in the recording of a chemical remanent magnetisation (CRM) or thermochemical remanent magnetisation (TCRM), that have the potential to produce palaeointensity data that is of a high technical quality, but ultimately biased (Draeger, 2006; Fabian, 2009). Conducting palaeointensity studies on ignimbrites, in conjunction with similarly-aged lithological units that are more well-suited to palaeointensity experiments, such as lava flows and fast-cooled intrusions, would facilitate a test on the accuracy of the palaeointensity estimates obtained from the ignimbrites. In this respect, the previously identified units in Argentina are well suited, and would allow an investigation into the feasibility of ignimbrites as accurate palaeointensity recorders of the ancient palaeomagnetic field. If found to be reliable, palaeointensity data from ignimbrites has the potential to address gaps in the current palaeointensity record, where identified units composed of lithologies that are traditionally considered ideal for palaeointensity analysis are limited. This is of greater significance when it is considered that volcanic tuffs preserved in sedimentary basins have been shown to contain a more complete time-series record of volcanism, when compared with magmatic products (McKay et al., 2016; Perkins & Nash, 2002). More specifically, reliable estimates would highlight the ignimbrites of the numerous early Mesozoic aged basins of southern South America, as viable future palaeointensity targets to better define Post-PCRS palaeointensity.

This study, assesses the suitability for palaeointensity analysis of specimens of the early Triassic, dacitic ignimbrite of the Los Menucos Complex and rhyolitic ignimbrites, approximately coeval basaltic sills, and Landinian (241.5-237.0 Ma; Ogg, 2012) aged basalts from the Puesto Viejo Group (Ottone et al., 2014). Palaeointensity estimates were obtained across three experimental methods: thermal Thellier with use of the IZZI+ protocol, Shaw double heating protocol (Shaw-DHT), and pseudo-Thellier. The reliability of the estimated palaeointensity values is discussed at length with particular focus on the results from ignimbrite sampling sites. An assessment is made on the

likelihood of obtaining reliable palaeointensity estimates from ignimbrites further back in the geological record than those typically used, and an evaluation is made on potential implications for a previously published palaeointensity estimate from Permian ignimbrites (Krs, 1967). The results are then discussed within the context of the Post-PCRS and the implications for the strength of the geomagnetic field across this time interval.

Geological Setting & Sampling

Southern South America experienced multiple stages of relatively large-scale volcanic activity throughout the Triassic, whilst still a part of Gondwana (Kay et al., 1989), a consequence of plate interactions being primarily restricted to the outer boundaries of supercontinents.

Patagonia, encompassing the southernmost tip of South America, is home to a silicic large igneous province that was revealed by recently established temporal equivalence between La Esperanza Plutonic-Volcanic Complex and the Los Menucos Group (Martínez Dopico et al., 2019). This volcanic activity is believed to be the result of subduction initiated by a Carboniferous aged continental collision. (Martínez Dopico et al., 2019; Vaughan & Pankhurst, 2008; Kay et al., 1989). Initial Permian magmatism is consistent with extensional activity after the subduction of an area represented by the Deseado Massif beneath that associated with the Patagonian Massif (Pankhurst et al., 2006, Kay et al., 1989). A change in source material occurred ~260 Ma which has previously been attributed to slab break-off of the subducting slab (Pankhurst et al., 2006), though a more recent investigation advises caution when interpreting the associated tectonic setting (Martínez Dopico et al., 2019, Veevers. 1989). Here the diachroneity of supercontinent cycle stages is demonstrated (Pastor-Galán et al. 2019). Local major plate reorganisation was occurring after major assembly of the supercontinent but before the initial breakup. This was due, to some extent, to the suturing of arc and exotic terranes to Gondwana (Kay et al., 1989).

The western margin of southern South America contains numerous NW-SE trending rifts (Figure 4.1a; Ramos, 2004; Ramos, & Kay, 1991; Milana, & Alcober, 1994; Spikings et al., 2016; Uliana et al., 1989), considered an early manifestation of the break-up of Gondwana (Ottone et al. 2014). Another example of the diachronic nature of the supercontinent cycle. Triassic activity is presented as a series of grabens and half-grabens, oblique to the palaeo-Pacific margin of Gondwana (Monti & Franzese, 2019). These rifts are thought to represent intracontinental volcanism following on from arc volcanism, the result of accretionary activity along the western margin of Gondwana (Franzese & Spalletti. 2001).

The above are just two regions of volcanic activity formed as a consequence of the collisional accretion of pre-existing continental crust that has been proposed for southern South America (Ramos, 1988). The details of these terrains, and the timings of their collisions, are disputed (Vaughan & Pankhurst. 2008), as is the classification of Patagonia as an allochthonous region (Cingolani et al., 1991, Rapalini, 1998). Although the exact causes of the Triassic aged volcanism and the interactions between different complexes are not yet fully understood, it is clear is that there are significant volumes of volcanic, and volcanic related, material erupted throughout the Triassic, and more broadly the Post-PCRS, in southern South America. Better understanding the evolution of these volcanic

regions has been the focus of many recent studies, through extensive mapping and radiometric dating (Falco et al., 2022; González et al., 2021; Lema et al., 2008; Luppo et al., 2018; Martínez Dopico et al. 2019; Mišković et al., 2009; Reitsma, 2012; Spikings et al., 2016; Monti & Franzese. 2019), presenting an opportunity to carry out palaeointensity investigations on rock formations with the potential to provide information on a missing period in the global record. The Los Menucos Complex and the Puesto Viejo Group, have been selected as the subjects of this study as they are associated with recent radiometric dates (Luppo et al., 2018; Ottone et al., 2014) and have both previously been the subject of successful palaeomagnetic investigations (Luppo et al., 2019; Domeier et al., 2011b).

Los Menucos Complex

The Los Menucos complex (Figure 4.1a, d, e) is an example of the voluminous silicic volcanic activity that occurred in northern Patagonia. It was recently correlated with the nearby La Esperanza plutonic-volcanic Complex (Luppo et al., 2018; 2019), which, when combined, contain a volume of magmatism comparable to a moderately sized large igneous province (Martínez Dopico et al., 2019).

The Los Menucos complex contains widely distributed ignimbrite sequences varying from dacitic to rhyolitic in composition, with interlayered mesosilicic lava flows and volcano-sedimentary beds (Figure 4.1e; Falco, 2019; Luppo et al., 2018). Recent dating results, obtained using U-Pb SHRIMP geochronology, showed the volcanism to have taken place in about 10 Ma around the PTB (Luppo et al. 2018), with a change in magmatic composition from rhyolitic to dacitic ca. 252 ± 2 Ma (Luppo et al., 2018). The samples used in this study were collected as oriented drill cores from the dacitic ignimbrites of the Sierra Colorada Fm, as described by Falco 2019, near the top of the geological section (Figure 4.1d, e). Ignimbrites from the upper section of the formation have been independently dated via U-Pb methods, and the results displayed good agreement (248.8 ± 1.0 Ma; Falco, 2019; 248 ± 2 Ma; Luppo et al. 2018). The basal section has been dated at 251.5 ± 2.0 Ma (Falco, 2019), constraining the eruption duration. Samples were collected likewise from acidic dykes intruding the ignimbrites, which have been dated using U-Pb dating as 244 ± 2 Ma (Luppo et al. 2019), and a sole sampling site was established for the basic dykes that intrude the older granite units (255 ± 2 Ma; Martínez Dopico et al., 2017) and have a bracketed age of 253-245 Ma (Luppo et al., 2019).

A previously published palaeomagnetic pole was calculated using directional data obtained from the acidic dykes and this was considered consistent with most reference paths for Gondwana/South America (Luppo et al., 2019). Other palaeomagnetic measurements were carried out on the late Permian units of the Los Menucos Complex, namely the Rhyolite Dome, basic dykes, and Collinao Dacite for which there is a U-Pb age of 253 ± 2 Ma, slightly older than the dacitic ignimbrites (Luppo et al., 2019). The results of rock magnetic experiments on the acidic dykes suggested both magnetite and (titano)haematite contribute to the bulk susceptibility with a titanohaematite phase potentially carrying the characteristic remanence (Luppo et al., 2019).

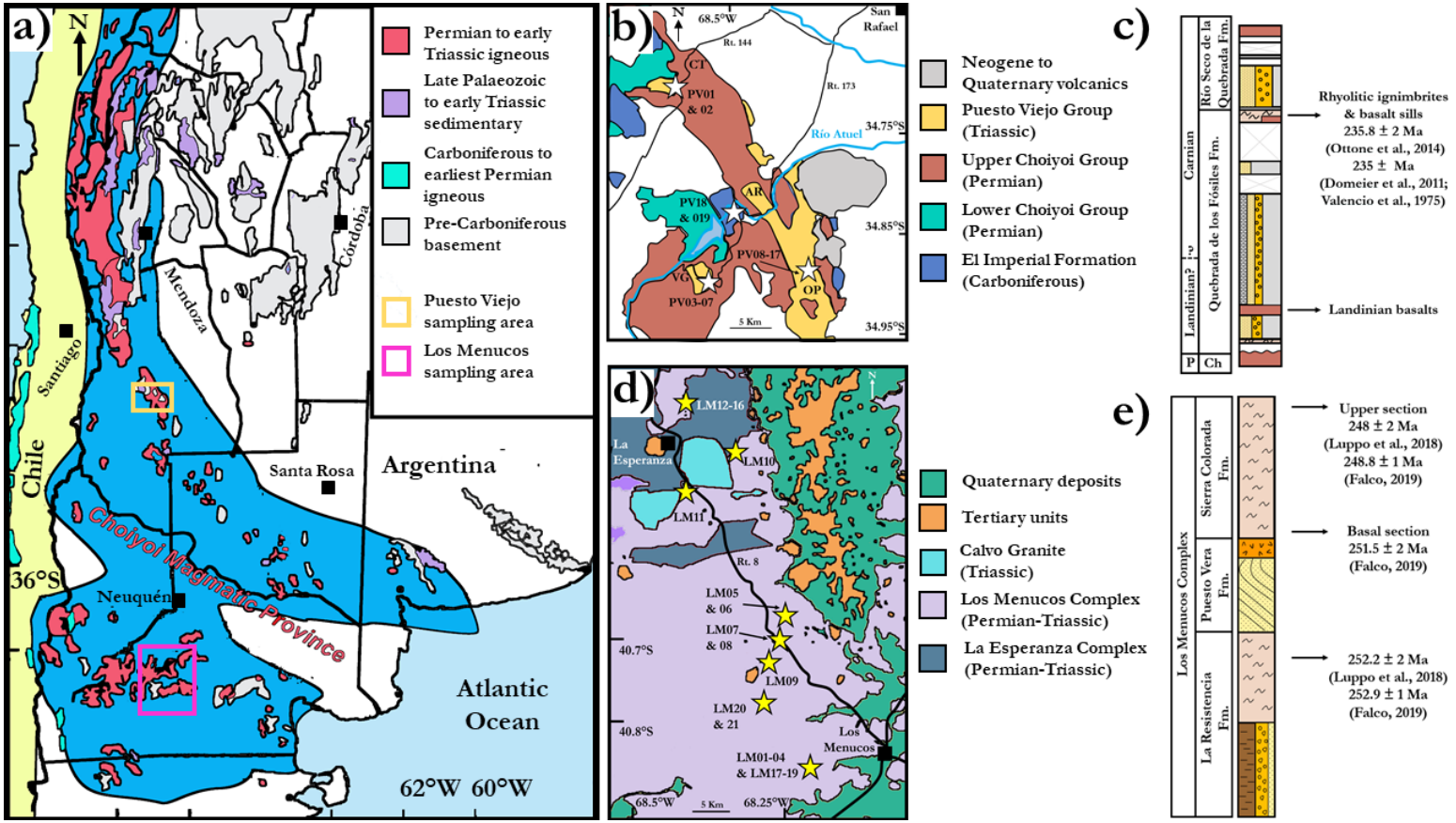

Figure 4.1: a) Simplified geological map of southern South America with sampling areas located (Los Menucos – yellow, Puesto Viejo – pink), modified from Luppo et al. (2019). b) Simplified geological map showing the distribution of the Puesto Viejo (PV) Group in the San Rafael depocenter, modified from Domeier et al. (2011). Stars indicate sampling sites. Local sampling areas as indicated by Domeier et al. (2011, Cuesta de los Terneros (CT), Atuel River (AR), Valle Grande (VG), Old Puesto (OP). c) Generalised vertical section (GVS) of PV modified from Ottone et al. (2014). d) Simplified geological map of the Los Menucos (LM) area, modified from Luppo et al. (2018), e) GVS of LM Group, modified from Falco (2019).

Puesto Viejo Group

The San Rafael depocenter is a small Triassic basin, related to the larger NW-SE trending rifts of the western margin (Figure 4.1a), that is located in southern Mendoza Province (Monti, & Franzese. 2019; Ottone et al. 2014). Deposition of Triassic material resulted in the formation of the Puesto Viejo Group which lies unconformably atop the Permian Choiyoi (Kleiman, & Salvarredi, 2001).

The Puesto Viejo Group captures a changing alluvial-fluvial environment with sedimentary successions. These are interlayered with acidic pyroclastic deposits and basalts (Figure 4.1c), representing the final stages of Gondwanan volcanism in the San Rafael Massif (Monti, & Franzese. 2019, Ottone et al. 2014). The group is categorised as containing two formations, the Quebrada de los Fósiles (QF) and the Río Seco de la Quebrada that overlies it. Samples used in this study were taken from pepperitic basalts towards the base of the QF, rhyolitic ignimbrites representing the top of the formation, and the basaltic sills that cut the rhyolitic ignimbrites (Figure 4.1b, c). U-Pb SHRIMP dating of the rhyolitic ignimbrites obtained an age estimate of 235.8 ± 2.0 Ma (Ottone et al. 2014), consistent with the average recalculated K-Ar estimate of Valencio et al. (1975) of 235 ± 4 Ma, by Domeier et al. (2011b). The basalt sills appear approximately coeval as Domeier et al. (2011b) obtained a range of estimates between 235.8 ± 2.0 Ma to 239.3 ± 2.0 Ma, using Ar-Ar dating. Furthermore, the samples collected by Valencio et al. (1975) were a combination of ignimbrites and basalts with overlapping ages. The age of the pepperitic basalt flows are less well constrained, relying on geological relationships and interpretation, and they are thought to have formed during the Landinian (Ottone et al., 2014).

A previous palaeomagnetic investigation, by Domeier et al. (2011b), suggested that the magnetisation of the volcanic rocks of the Puesto Viejo group was primary, with a positive reversal test supporting averaging of secular variation. Rock magnetic experiments were interpreted as revealing magnetite and haematite carriers in both rock types, with sample level agreement of the magnetite and haematite components for the basalt sills. Sampling areas of the Puesto Viejo Group in this study were based on those from the study of Domeier et al. (2011b), with localities from Cuesta de los Terneros, the Atuel River area, the Old Puesto area, and the Valle Grande area (Figure 4.1b).

Method

In total, 40 palaeomagnetic sampling sites were established for the purposes of this study, with specimens collected as standard 1-inch diameter drill cores. Sampling of the Los Menucos Complex included 13 dacitic ignimbrite sites, 7 acidic dyke sites, and a sole basic dyke site. In the San Rafael depocenter, 9 rhyolitic ignimbrite sampling sites were established, alongside 5 separate sites of basaltic sills and lava flows, respectively.

The methods utilised in the rock magnetic, microscopic, and palaeomagnetic and palaeointensity experiments follow those outlined in **Chapter 3**. Specimens from each sampling site were first subject to a combination of alternating field (AF) and thermal, stepwise demagnetisation methods. Specimens from sites associated with a consistent, isolated characteristic remanent magnetisation (ChRM) direction were then selected for

palaeointensity investigation, with steps for the palaeointensity experiments determined according to the previously observed demagnetisation behaviour. A combination of thermal Thellier performed using the IZZI+ protocol (IZZI+, Tauxe & Staudigel, 2004), the Shaw double heating technique (Shaw-DHT, Shaw, 1974; Tsunakawa & Shaw., 1994; Kono, 1978), and the calibrated pseudo-Thellier method (Paterson et al., 2016; Tauxe et al., 1995), was utilised in determining palaeointensity estimates. Site-mean palaeointensity estimates were calculated by unweighted averaging of specimen-level thermal Thellier and Shaw-DHT results where possible, and the minimum required number of site-level estimates was three ($n \geq 3$).

In addition to these procedures, the volume-normalised susceptibility of half-inch ignimbrite specimens was determined. Susceptibility values were measured with a Bartington MS2 Susceptibility System (Bartington Instruments). Variation in these values was compared with variations in specimen density which was determined through the principle of density = mass/volume. Volume was calculated using measurements made with a Vernier calliper with mm resolution, and mass was determined using a balance with a resolution of 0.01g.

Results

In order to aid readability, the results of all experimental procedures from the two distinct sampling localities, Los Menucos and Puesto Viejo, will be presented and discussed in isolation, alongside initial interpretations, before a synthesised discussion is presented.

Los Menucos Results

Palaeomagnetic Directions

Stepwise demagnetisation techniques revealed two magnetic remanence components of the dacitic ignimbrites of the Los Menucos complex. The first, an overprint removed by AF steps of 10-15 mT and, typically, temperatures of 300°C (Figures 4.2a, b). Most specimens studied, experienced complete demagnetisation somewhere between 60 mT and 80 mT, and temperatures greater than 600°C (Figures 4.2a, b). Some specimens were not completely demagnetised by 700°C, but there was no correlation between such specimens and any particular sampling site. This ChRM component was typically origin trending (Figure 4.2c). Isolating a ChRM in dyke specimens was more difficult, with some Zijderveld plots characterised by noise and no clear magnetic components (Figure 4.2d). Where components could be distinguished in dyke specimens, overprints were typically removed between 10-15 mT, and 200-250°C (Figure 4.2e). Complete demagnetisation commonly occurred between 25 mT and 50 mT, and 550°C and 600°C (Figure 4.2f).

Out of the 21 sites that were sampled from the Los Menucos Group, 10 produced internally consistent ChRM directions (Table 4.1). At all 10 of the successful sites, the dacitic ignimbrite was sampled. In the slightly older Collinao Dacite units studied by Luppo et al. (2019), only normal polarity ChRM directions were observed. In this study, 6 of the site-mean ChRM directions of the dacitic ignimbrite are of reverse polarity. When subject to a Bayesian test for common mean direction (Heslop & Roberts, 2018b), the results are a Bayes factor (BF) of 5.72 and an estimated probability of common mean direction of 0.85, indicating positive support for antipodal mean directions. The

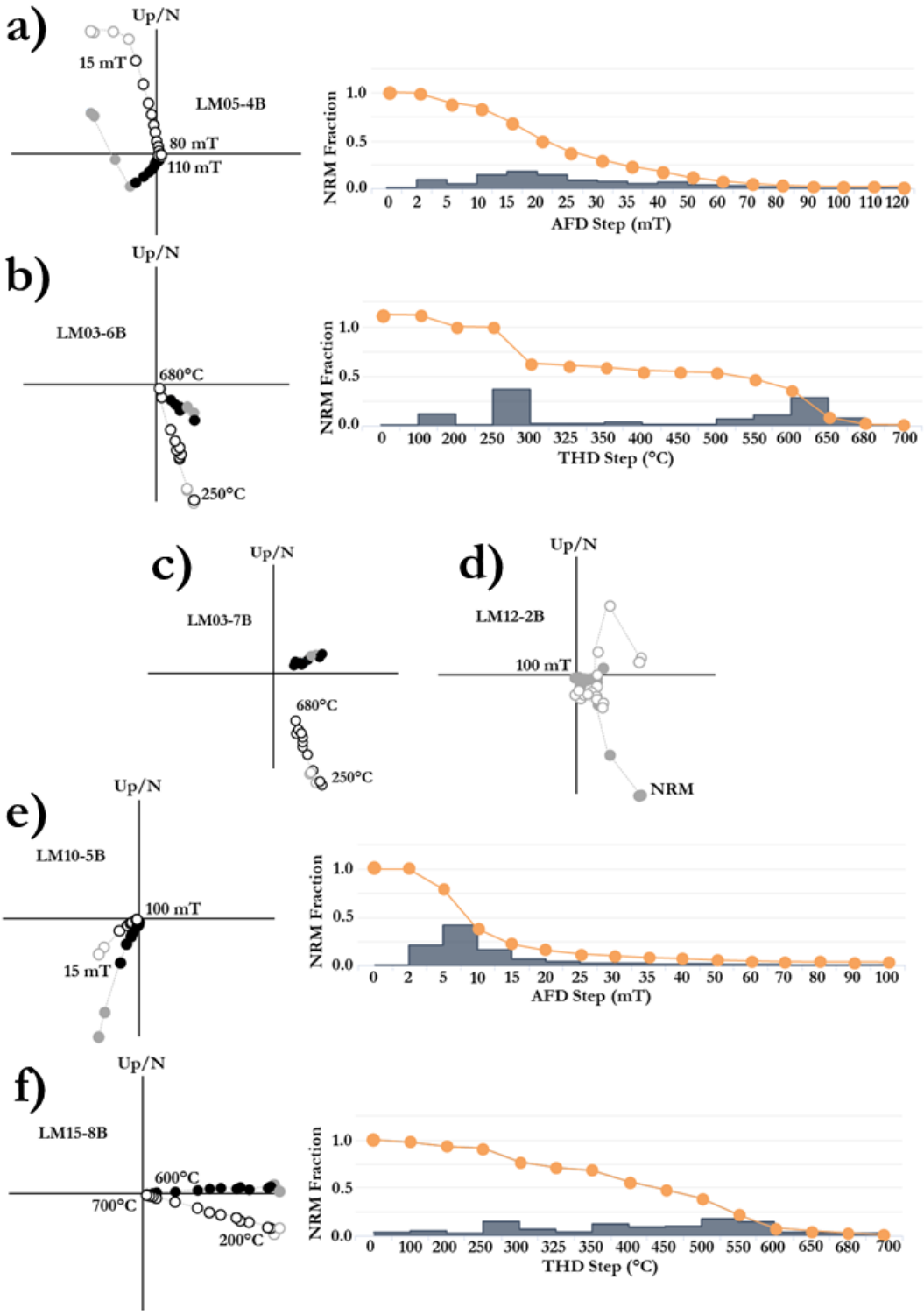

Figure 4.2: Example demagnetisation behaviour of specimens from the Los Menucos (LM) Complex. Typical Zijderveld plots displaying palaeomagnetic directions and demagnetisation behaviour of dacitic ignimbrites (a-c). Remaining NRM fraction after each demagnetisation step displayed where additional insight was provided (orange), fraction of NRM removed indicated by grey bars. d) Unsuccessful isolation of ChRM from a dyke specimen, e) AF and f) thermal demagnetisation behaviour when ChRM successfully isolated.

Table 4.1: Palaeomagnetic results from Los Menucos sampling sites.

Site	Unit	Lithology	Age (Ma)	Lat (°S)	Long (°W)	Dec (°)	Inc (°)	n/ n_{dir}	k	α_{95}
LM01	Ignimbrite	Dacite	248 ± 2	40.9	68.3	154.3	70.5	7/7	65	7.6
LM03	Ignimbrite	Dacite	248 ± 2	40.9	68.3	145.7	68.0	7/7	2170	1.3
LM04	Ignimbrite	Dacite	248 ± 2	40.9	68.3	142.8	64.9	7/8	189	4.4
LM05	Ignimbrite	Dacite	248 ± 2	40.7	68.3	296.7	-60.0	6/6	68	8.2
LM06	Ignimbrite	Dacite	248 ± 2	40.7	68.3	291.4	-77.4	7/7	68	7.4
LM07	Ignimbrite	Dacite	248 ± 2	40.7	68.3	329.9	-77.0	6/7	682	2.6
LM08	Ignimbrite	Dacite	248 ± 2	40.7	68.3	301.7	-70.4	6/7	5223	2.9
LM18	Ignimbrite	Dacite	248 ± 2	40.9	68.2	172.2	65.8	7/7	135	5.2
LM20	Ignimbrite	Dacite	248 ± 2	40.8	68.3	320.0	-66.0	9/9	157	4.1
LM21	Ignimbrite	Dacite	248 ± 2	40.8	68.3	338.8	-63.0	8/10	124	5.0

Note 4.1: Site identifiers and site location (Lat, Long). Declination (Dec) and inclination (Inc) of the characteristic remanence directions alongside corresponding Fisher statistics (k, α_{95}). Directions and statistics presented for tilt-corrected site-mean ChRM directions. n/n_{dir} denotes the number of specimens utilised in final determination of Chrm/total number of specimens subjected to palaeomagnetic experiments.

palaeopole computed from the 10 dacitic ignimbrite VGPs (61.8°S, 342.5°E, A95: 8.6°) shows a general agreement with the slightly older palaeopole calculated from the Collinao Dacite (48.3°S, 349.9°E, A95: 15.1°, Figure 4.3). The discrepancy between the two can be explained by the latest Permian to earliest Triassic counter clockwise rotation of the North Patagonian Massif proposed by Luppo et al. (2019), as the younger VGP from this study lies closer to the corresponding Gondwanan reference poles (Luppo et al., 2019 and references therein).

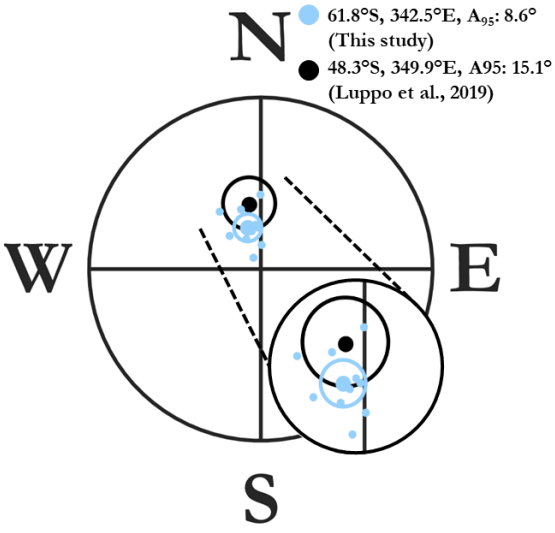

Figure 4.3: Comparison of mean VGPs of the Los Menucos Complex from this study (blue) and Luppo et al. (2019) (black). Large blue point represents mean VGP from this study, smaller circles represent VGPs from individual sites that make up the mean value. Black point represents mean VGP value from Luppo et al. (2019). In both cases the outer-ring represents A_{95} confidence interval. Insert) zoomed-in view of the indicated area to better display the spread of site-level VGPs.

In the acidic dykes and the basic dyke sampled, it was not possible to isolate consistent within-site ChRM directions (Figure C.1). This is in contrast with the previous

palaeomagnetic study into the acidic dykes (Luppo et al., 2019), where a high success rate was observed.

Rock Magnetism & Microscopy

Within a given sampling site of the dacitic ignimbrite, results of the rock magnetic experiments displayed homogeneous behaviour. The differences in behaviours were observed between different sampling sites, and can be attributed to varying degrees of influence by the magnetic phases within the lithology. The different behaviours could be broadly divided into two distinct categories which were termed 'LMIA' and 'LMIB'.

- LMIA (LM03, LM04, LM05, LM06, LM08, LM18)

Rock magnetic behaviour appeared to be strongly influenced by maghaemite due to the consistent inflection in susceptibility versus temperature heating curves at temperatures between 200°C and 300°C (Figure 4.4a). This inflection was not present in the corresponding cooling curves, which is consistent with the inversion of maghaemite to haematite (Dunlop & Özdemir, 1997). This interpretation is further supported by the reduced room temperature magnetisation values observed after laboratory heating, as haematite is of lower magnetic susceptibility than maghaemite (Dunlop & Özdemir, 1997). LMIA type rock magnetic behaviour is suggestive of magnetite, or Ti-poor titanomagnetite, as the ChRM carrier, due to a sudden decrease in both the susceptibility and the bulk magnetisation at temperatures close to 580°C (Figure 4.4a, b, c). This is supported by estimates of Curie temperature (T_C, Table C.1). Some heterogeneous behaviour was observed within the sampling sites as some specimens displayed behaviour suggestive of a second phase (Figure C.2a) with a higher T_C of approximately 650°C (Table C.1), likely (titano)haematite. In part, this phase could have been the result of maghaemite inversion during laboratory heating, however non-saturated IRM acquisition curves, resulting from a maximum applied field of 0.6 T (Figure C.2b), suggest that (titano)haematite was also present in specimens prior to heating.

- LMIB (LM01, LM07, LM20, LM21)

Within-site rock magnetic behaviour appeared more homogeneous than that of specimens displaying LMIA type behaviour. Estimated Curie temperatures indicated two prominent magnetic phases, one unblocking at 580°C and the other at 660°C (Table C.1). This was reflected in thermomagnetic heating curves that were more indicative of a magnetite-haematite mix than those categorised as representing LMIA type behaviour (Figure 4.4e). IRM acquisition curves did not reach saturation after the application of a 0.6 T external field (Figure C.2c). Thermomagnetic curves display more reversible behaviour, after heating to 400°C, than those displaying type LMIA behaviour (Figure 4.4c, f), which likely represents a reduced contribution to specimen alteration during laboratory heating from maghaemite inversion. This was particularly prominent with specimens from site LM01. The room temperature bulk magnetisation decreased much more significantly after heating to 700°C (Figure 4.4f), which could suggest that the majority of alteration could be attributed to the oxidation of magnetite to haematite at temperatures above its T_C. The characteristic hump in the susceptibility versus temperature heating curve, associated with the presence of maghaemite, was greatly reduced in these specimens and curves were generally more reversible than previously described (Figure 4.4d). The overall behaviour suggested that the maghaemite contribution in LMIB specimens was minor.

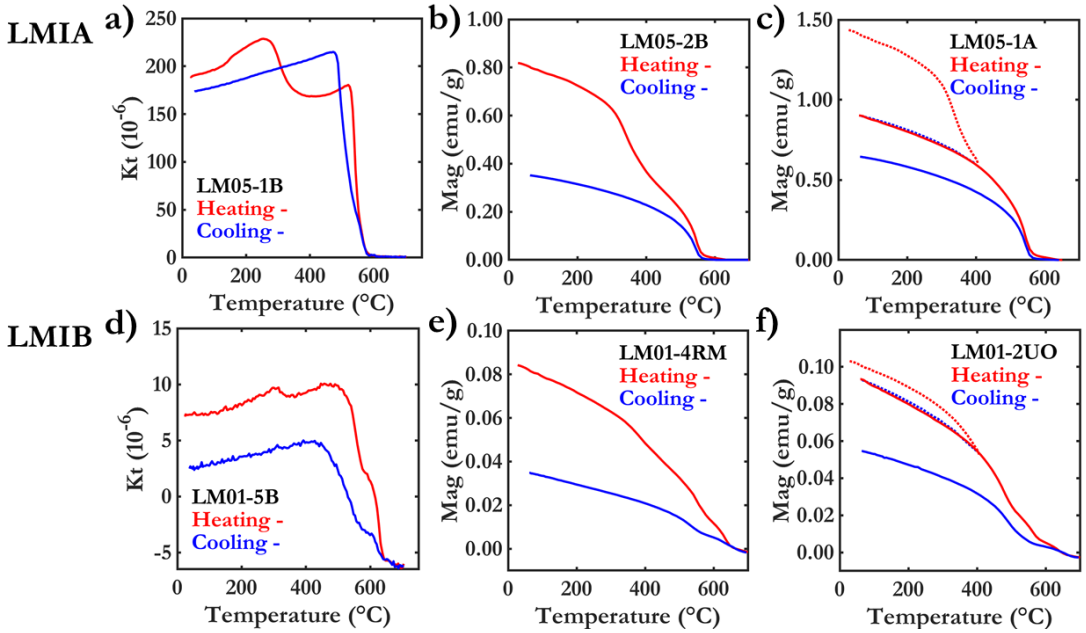

Figure 4.4: Rock magnetic results from specimens that are representative of the full range of rock magnetic behaviours displayed by specimens from the Los Menucos Complex. Susceptibility versus temperature curves (a & d) and thermomagnetic curves (b & e) are presented for LMIA and LMIB type behaviours. Cyclic thermomagnetic curves constrain the temperature at which laboratory induced thermal alteration was experienced (c & f).

Representative hysteresis parameters were plotted for each site alongside the bulk domain stability (BDS) trendline (Paterson et al., 2017) and the line representing BDS = 0.10 (Figure 4.5a). Specimens with a BDS value below 0.10 are less stable due to multidomain (MD) contributions, and so it has been suggested that they are less likely to yield meaningful results (Paterson et al., 2017; Yoshimura et al., 2020). The Los Menucos data

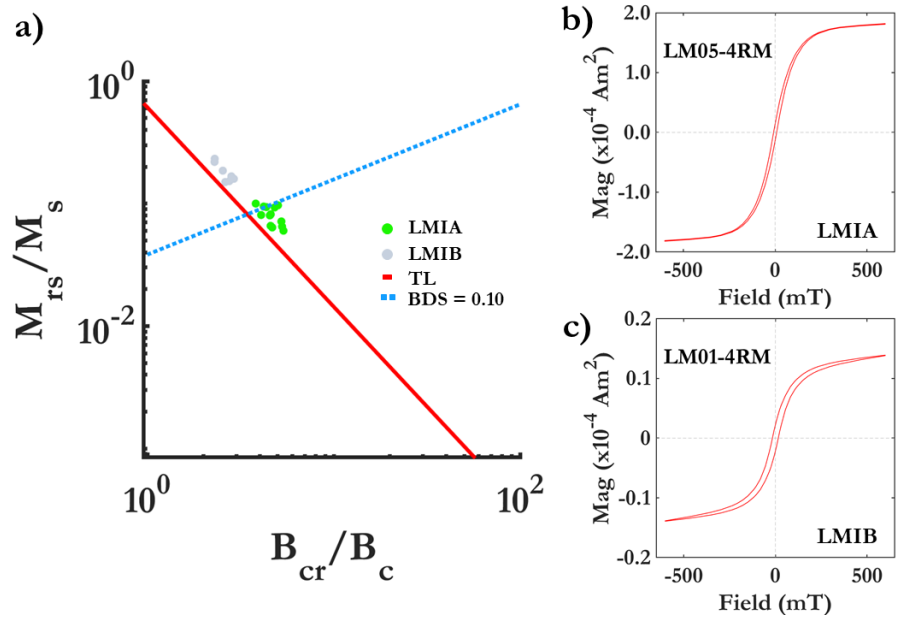

Figure 4.5: Hysteresis properties for Los Menucos specimens. a) Graph showing the ratio of saturation remanence and saturation magnetisation versus ratio of coercivity of remanence and coercivity with bulk domain stability (BDS) trendline (TL, red line) (Paterson et al., 2017) and BDS = 0.10 (blue dotted line). Representative examples of hysteresis loops associated with each categorised rock magnetic behaviour b) LMIA c) LMIB processed with HystLab (Paterson et al., 2018).

grouped into two clusters. Specimens that displayed LMIA type rock magnetic behaviour (Figure 4.5b) plotted near or below the BDS = 0.10 line, and those displaying LMIB type behaviour (Figure 4.5c) displayed a BDS value greater than 0.10 (Figure 4.5a). Although the plotted hysteresis parameters broadly follow the BDS trendline, there was a tendency for them to sit above the trend (Figure 4.5a). The trendline was derived from the hysteresis parameters of (titano)magnetites (Paterson et al., 2017) and specimens with BDS values above the trendline likely contain some haematite contribution, agreeing with the interpretation of the rock magnetic data.

Backscattered SEM images of ignimbrite specimens collected from Los Menucos showed an assemblage of lithic clasts, iron-oxide grains (Figure C.3), and other non-iron bearing minerals. These are hosted within a glassy matrix that has potentially undergone varying degrees of devitrification and contains iron-oxide microlites. There was evidence of localisation of iron-oxide grains (Figure 4.6a), potentially caused by preferential formation along cracks and pores as hydrothermal fluids circulated, although there was little evidence of pervasive cracking running through lithic clasts or large mineral grains in the specimens analysed. It is possible that localisation is cause by the heterogenic nature of

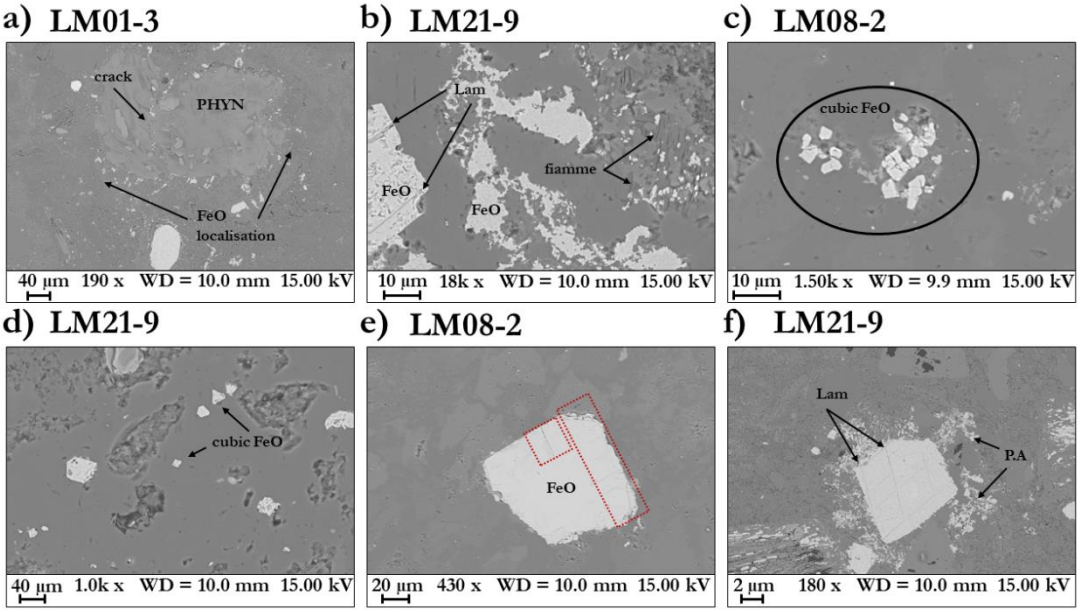

Figure 4.6: Scanning electron microscope (SEM) images of Los Menucos specimens, obtained from backscattered electrons. PHYN – phenocryst, Lam – lamellae, P.A – platy assemblages. Banded structure highlighted (dashed line). Pervasive cracking highlighted (red box).

ignimbrites, as pre-existing material is recycled and redistributed. Pore spaces were apparent in all specimens studied, identified by the darkened areas where there is a void of material (Figure 4.6), there was also evidence to suggest the presence of micro-scale fiamme (Figure 4.6b). Iron-oxide microlites within the matrix appear cubic, and were interpreted as magnetite. There was evidence of these grains measuring << 1 µm, potentially falling within the SD size range (Dunlop & Özdemir, 1997; Figure 4.6c, d). These grains are found in specimens that exhibit both LMIA and LMIB type rock magnetic behaviour. Larger iron-oxide grains show signs of cracking (Figure 4.6e). This observation is most prominent in specimens that display LMIA behaviour and likely represent shrinkage cracks associated with maghaemite formation (Dunlop & Özdemir, 1997). In specimens displaying LMIB type behaviour, assemblages of platy iron-oxides

are observed in isolation and surrounding larger iron-oxide grains, such as that imaged in specimen LM21, that also displays lamellae structures (Figure 4.6f). Energy dispersive X-ray spectroscopy (EDX) revealed consistent elemental composition of iron-oxides across specimens displaying both LMIA and LMIB type behaviour. Iron-titanium oxides were relatively Ti-poor regardless of the size or texture of quantified grains (Figure C.3).

Palaeointensity Estimates

Due to the strong influence of maghaemite in the rock magnetic behaviour, and the visible signs of widespread maghaematisation observed through microscopy analysis, specimens from sites displaying LMIA type behaviour were not selected for palaeointensity analysis. This decision was taken in the belief that it would be unreasonable to expect specimens that have experienced such high levels of maghaematisation to produce palaeointensity estimates that escape the biasing effects of TCRM acquisition outlined in **Chapter 3**. Where the possibility of acquiring reliable palaeointensity estimates from specimens that have experienced low-temperature oxidation was previously demonstrated, the extent to which alteration had occurred was limited (**Chapter 3**).

Palaeointensity experiments were conducted on specimens from sites displaying LMIB type behaviour since they exhibited a reduced occurrence of maghaematisation. Out of these four sites (LM01, LM07, LM20, LM21), two produced successful results from thermal Thellier experiments (LM01 & LM21, Table 4.2). Seven specimens were analysed from site LM01 and all seven produced palaeointensity estimates that satisfied the stricter selection criteria (Table C.2). Estimated values of palaeointensity (B_{anc}) were reasonably consistent giving $\sigma B_{anc}/B_{anc} = 0.18$, though this lies just outside the *n*-dependent cut-off proposed by Paterson et al. (2010). This approach compensates for the number of palaeointensity estimates being below that required for a reliable estimate (n = 24; Paterson et al., 2010), providing confidence that the ratio lies below the commonly used cut-off of 0.25 (Paterson et al., 2010). The mean palaeointensity estimate from site LM01 (31.1 μT; Table 4.2) shows good agreement with the mean value from the three successful specimens from site LM21 (27.8 μT; Table 4.2). The range across which Arai plots were used to estimate palaeointensity values was similar for specimens from both sites. Starting temperatures for specimens from LM01 were typically 400°C (Figure 4.7a) and those from LM21 started at 500°C (Figure 4.7b, d). At both sites, final temperatures were 660°C or 680°C (Figure 4.7a, b). Where the observed behaviours between the sites did differ was in measurements made at temperature steps prior to those used in determining palaeointensity estimates. For specimens from LM01, the proportion of NRM remaining at the first used temperature step is around 90% (Figure 4.7a), and the preceding low-temperature range is associated with a very distinct magnetic overprint (Figure 4.7a). The NRM of specimens from LM21 decreases to approximately 40% of the original value before the first used temperature step and Arai plots display two-slope behaviour (Figure 4.7b, d). Zijderveld plots again show an overprint associated with this temperature range but it is much less distinct from the ChRM (Figure 4.7b, d). The Arai plots during these lower temperature steps display zigzagging behaviour indicative of MD contributions (Figure 4.7b, d). The four failed specimens from LM21 did so due to a combination of the continuation of this zigzagging at higher temperatures, causing failure of linearity parameters β and/or k', and the failure of pTRM checks (Figure 4.7d). Highly zigzagging

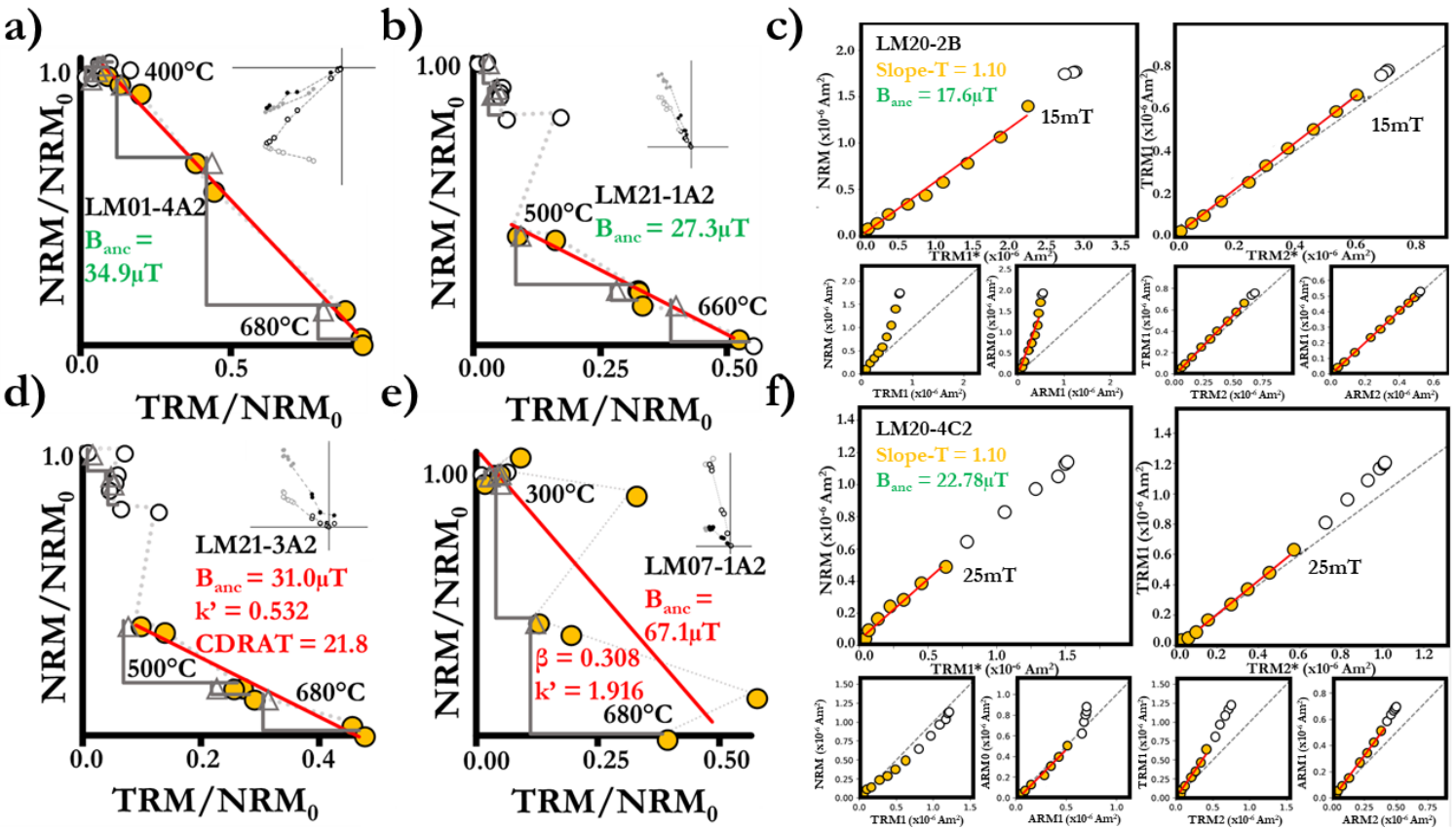

Figure 4.7: Representative results of palaeointensity experiments conducted on specimens from the Los Menucos Group. (a, b, d, e) Arai plots and Zijderveld plots (Zijderveld, 1967) of the thermal Thellier experiments. Filled circles (orange) represent the temperature steps selected for the palaeointensity estimates, with a best-fit line to these points (red). The start and end temperature steps are provided. Open triangles represent the pTRM checks. Black circles of the Zijderveld plot correspond to the same temperature steps as those chosen for palaeointensity analysis. Palaeointensity estimates are highlighted as accepted (green) or rejected (red). Zijderveld plots presented in specimen coordinates, with temperature steps selected for Arai plot interpretations in black. (c & f) Shaw results. Top left – NRM remaining versus remaining TRM of first heating after ARM correction (TRM1); top right – TRM remaining versus remaining TRM of second heating after ARM correction (TRM2*); bottom left – remaining magnetisations of NRM, uncorrected TRMs and ARMs after first heating; bottom right – likewise after second heating, similar demagnetisation trends between TRMs and ARMs in bottom plots suggestive of analogous behaviour. ARM0 versus ARM1 provides visual representation of ARM correction.*

Table 4.2: Palaeointensity results from Los Menucos sampling sites.

Site	RM Type	Density (Mgm^{-3})	VNS	n_{VNS}	B_{th} (μT)	σB_{th} (μT)	n/n_{th}	B_{sh} (μT)	σB_{sh} (μT)	n/n_{sh}	B_{pt} (μT)	σB_{pt} (μT)	n/n_{pt}	B (μT)	σB (μT)	VDM ($x10^{22}$ Am^2)
LM01	LMIB	2.3	97	3	31.1	5.6	7/7	13.1	-	1/7	*8.3*	*4.4*	*3/4*	31.1	5.6	4.6
LM03	LMIA	2.4	1948	7	-	-	-	-	-	-	-	-	-	-	-	-
LM04	LMIA	2.3	1707	4	-	-	-	-	-	-	-	-	-	-	-	-
LM05	LMIA	-	-	-	-	-	-	-	-	-	-	-	-	-	-	-
LM06	LMIA	-	-	-	-	-	-	-	-	-	-	-	-	-	-	-
LM07	LMIB	2.5	330	5	-	-	0/7	42.1	1.3	2/5	19.1	2.3	5/6	42.1	1.3	-
LM08	LMIA	2.6	2040	3	-	-	-	-	-	-	-	-	-	-	-	-
LM18	LMIA	-	-	-	-	-	-	-	-	-	-	-	-	-	-	-
LM20	LMIB	2.4	146	4	-	-	0/7	18.5	3.9	3/4	9.0	0.3	3/4	18.5	3.9	2.9
LM21	LMIB	2.4	81	4	27.8	0.9	3/7	-	-	0/9	15.9	-	1/9	27.8	0.9	4.6

Note 4.2: Site-level palaeointensity estimates (B_{method}) and corresponding standard deviations (σB_{method}) presented for each palaeointensity method (Thellier: th, Shaw: sh, pseudo-Thellier: pt). n/n_{method} denotes the number of specimens utilised in final site-mean palaeointensity estimates/total number of specimens subjected to corresponding palaeointensity method. Combined site-level palaeointensity estimates (B) and standard deviation (σB) for successful Thellier and Shaw experiments presented with corresponding virtual dipole moment (VDM) and Q_{PI} score (Biggin & Paterson, 2014; Kulakov et al., 2019). Additional information provided on typical rock magnetic behaviour revealed at each site (RM Type), mean specimen density and mean volume normalised susceptibility values (VNS) from n number of specimens (n_{VNS}).

Arai plots was also the primary cause of failure of specimens from LM07 and LM20 (Figure 4.7e), but at these sites pTRM checks frequently passed.

There was little crossover between sites producing palaeointensity results from both the Shaw-DHT method and thermal Thellier, leaving little room for direct comparison. The estimated pseudo-Thellier results were used in a comparative sense, with the results of the heating methods, as a potential indicator of undetected alteration during laboratory heating (Thallner et al., 2021). The speed of the method, when conducted using a RAPID measuring system, and the potential to combine the process with the Shaw method (Thallner et al., 2021), makes the pseudo-Thellier method an attractive, additional check for specimen alteration. Best-fit line segments that passed selection criteria were generally obtained from curved pseudo-Arai plots. Passing sections were always within the higher coercivity range, usually starting at 30 mT (Figure C.4a). The sole result from site LM21, and one of the estimates from LM01 were the exception to this. In these cases, pseudo-Arai plots were primarily linear, after the removal of a magnetic overprint that was cleaned after 15 mT (Figure C.4b). Agreement between estimates obtained from the three different palaeointensity procedures is generally poor at site-level. Estimates from pseudo-Thellier experiments are approximately half the strength of those obtained utilising Shaw-DHT protocol for sites LM07 and LM20 (Figures C.4c, d). In this respect, estimates from LM01 show better agreement (Table 4.2). The results from pseudo-Thellier and Shaw-DHT experiments do not agree with those obtained from the thermal Thellier method, however (Table 4.2). This is also the case for site LM21, although no Shaw-DHT data is available from this site for further comparison.

Reliability of Palaeointensity Estimates

Thermal Thellier results of high technical quality appear to agree with the rock magnetic interpretation that specimens displaying LMIB type behaviour are less strongly influenced by the effects of maghaemite (e.g. pTRM steps checking for alteration pass the selection criteria). The moderate to poor agreement between estimates obtained via the pseudo-Thellier methods with those obtained via the thermal Thellier and Shaw-DHT method at most sites, could suggest undetected thermal alteration by the pTRM checks, or failure of the ARM corrections. For site LM01, the consistently low magnitude of ARM corrections would suggest that minimal alteration has occurred, and that the passing pTRM checks are likely accurate, however. This is further supported by the general agreement between pseudo-Thellier estimates and Shaw-DHT estimates from this site (Table 4.2). Despite a large number of studies that have demonstrated the reliability of palaeointensity estimates obtained through Shaw methods (Ahn et al., 2016; Yamamoto et al., 2010; Yamamoto & Yamaoka, 2018), those obtained via application of Thellier based methods are still widely preferred, in part due to the deeper theoretical understanding of the method, and the possibility that full TRM palaeointensity methods could result in underestimated values (Cromwell et al., 2017). The large number of consistent thermal Thellier results, of high technical quality from site LM01 would appear to represent the most reliable palaeointensity estimates from Los Menucos. In order to present these results with more confidence, further consideration must be given to the ignimbrite nature of the specimens, in an attempt to develop a deeper understanding of their thermal history.

Estimated T_C values (Table C.1), combined with the cubic iron-oxide grains identified in SEM images (Figure 4.6c, d), suggest that magnetite and/or Ti-poor titanomagnetite

contribute to the ChRM. These phases are similar to those identified in the Collinao Dacite (Luppo et al., 2019), which is close in age and of a similar composition. Nucleation and growth of such grains occurs post-emplacement, and if formed above their T_C will carry a TRM (Gee et al., 2010). Specimens from all sites of the dacitic ignimbrites display consistent density values > 2.0 Mgm^{-3} (Table 4.2). From the thermal modelling results of Riehle et al. (1995), the density values of the dacitic ignimbrites are suggestive of emplacement temperatures well above the T_C of magnetite. Corroborated by the presence of fiamme, there is evidence to suggest that these (titano)magnetite grains carry a TRM. Unlike the Collinao Dacite investigated by Luppo et al. (2019), dacitic ignimbrites that demonstrate LMIB type behaviour also contain haematite (Figure C.2c), often carrying over half of the original NRM. Although the crystallisation of haematite is possible during higher oxidation state eruption processes, any primary haematite component would be more likely attributed to a detrital origin (Jeong et al., 2021). This would be carried by individual haematite grains, or those within lithic fragments, that have been incorporated into the pyroclastic flow from the underlying substrate (Jeong et al., 2005; 2021). Lithic clasts are visible in SEM images but rarely contain an abundance of iron-oxides (Figure 4.6a). Larger, moderately to well-rounded iron-oxides are also present that could be detrital in origin (Figure 4.6a) and with a critical diameter of ~15 μm for SD behaviour (Dunlop & Özdemir., 1997), it is possible that such grains could contribute to the NRM.

Analysis of magnetic susceptibility offers perhaps the most conclusive and likely origin of the bulk of the haematite signature. Bulk magnetic susceptibility values have been used in conjunction with density estimates in previous magnetic studies of ignimbrites, as a method of determining the likelihood of specimens having experienced significant VPA (Avery et al., 2018; Palmer et al., 1996). VPA is a common occurrence in tuffs and ignimbrites due to their high emplacement temperatures and ongoing exposure to fumarolic activity. On entering pore spaces, vapour condenses and encourages oxidation of pre-existing mineral phases (Vaniman, 2006; Wright et al., 2011). For different flow units within the same formation, where source material and the compositional constituents of the separate flows are comparable, the primary control of the bulk susceptibility is the degree of compaction experienced. A greater degree of compaction would result in an increased concentration of magnetic grains, and thus increased susceptibility. This would also result in greater density values. Although compaction has such a strong influence on bulk susceptibility, differences of an order of magnitude or greater cannot be explained by differences in the degree of compaction alone (Avery et al., 2018). Such differences must be attributed to differences in magnetic mineralogy. When studying distinct units of the same lithology and formation, a possible cause of the difference in bulk susceptibility values is some alteration of the original magnetic mineralogical composition.

Volume normalised susceptibility values are typically an order of magnitude lower for specimens that displayed LMIB type behaviour than those that displayed LMIA type behaviour (Table 4.2). In contrast to this, estimated density values are consistent. These density estimates do come with relatively large associated uncertainties, but regardless of this, compaction differences alone have previously been dismissed as the cause of similarly large differences in susceptibility values (Avery et al., 2018; Gee et al., 2010; Palmer et al., 1996). It is most likely then, that the reduced susceptibility is a result of VPA of the original (titano)magnetite grains, previously identified, resulting in secondary

haematite formation. Further evidence to support this can be seen through closer comparison of the SEM images acquired from specimens displaying type LMIA and LMIB behaviour respectively. The matrix of specimens displaying LMIB type behaviour appears to have experienced a greater degree of devitrification, as fewer areas appear free of the vuggy texture associated with devitrification (Figure 4.6a, f) Often, the vugs present in LMIB specimens are filled with platy textured iron oxide grains (Figure 4.6f). These grains are interpreted as being haematite in most cases, due to its absence in LMIA specimens. This texture can also be observed around the edges of larger (titano)magnetite phenocrysts (Figure 4.6f) which could represent some degree of replacement, but either way is suggestive of secondary alteration.

Despite producing thermal Thellier results, following the IZZI+ protocol, of high technical quality, and an initially promising interpretation of the magnetic carriers, palaeointensity estimates from LMIB specimens could be biased by the contribution of a TCRM, and possibly a CRM (Draeger et al., 2006; Fabian, 2009; Shcherbakov et al., 2021). This result highlights the importance of evaluating and understanding the hydrothermal processes that are likely to occur in the environmental conditions in which ignimbrites form.

In areas, the matrix of LMIA specimens appears more vitric and displays an absence of platy, secondary textures. This could suggest that the primary iron-oxides, hosted within such areas, have experienced a reduced degree of thermal alteration as the more vitric matrix offers protection against continued exposure to an active hydrothermal setting. Isolating the magnetic signal carried by these grains is near impossible in these specimens due to the simultaneous presence of maghaematised grains, but it does suggest that it is possible for these primary grains to remain unaltered within ancient ignimbrite units.

Puesto Viejo Results

Palaeomagnetic Directions

Specimens of the rhyolitic ignimbrite displayed some variation in their demagnetisation behaviour, according to the different sampling localities and their association with remagnetising intrusive bodies. Those obtained from sites PV01 and PV10 typically displayed a magnetic overprint that was removed after exposure to a 25 mT strength AF field (Figure 4.8a). Decay in magnetisation strength post this step was gradual, with complete demagnetisation by 80 mT (Figure 4.8a). AF demagnetisation of specimens from site PV11 often failed to isolate a ChRM (Figure 4.8c). Discrepancies were apparent in thermal unblocking behaviour between sites. Overprints were typically removed by temperatures of 350°C in specimens from site PV01, 250°C from site PV10, and 400°C from site PV11. Specimens from sites PV10 and PV11 were fully demagnetised by 580-600°C (Figure 4.8b), whereas demagnetisation of specimens from site PV01 required additional temperature steps above 600°C (Figure 4.8d). Basalt sill specimens saw an overprint removed by 10 mT through AF demagnetisation (Figure 4.8e), but less success was had with thermal demagnetisation. Typical Zijderveld plots resulting from thermal demagnetisation were noisy, with any magnetic components difficult to distinguish (Figure 4.8f). On the occasions where a ChRM component could be distinguished, the overprint was removed by 400°C. Basaltic lavas were characterised by an overprint that was removed by 10 mT (Figure 4.8g) and, most commonly, 300-350°C (Figure 4.8h).

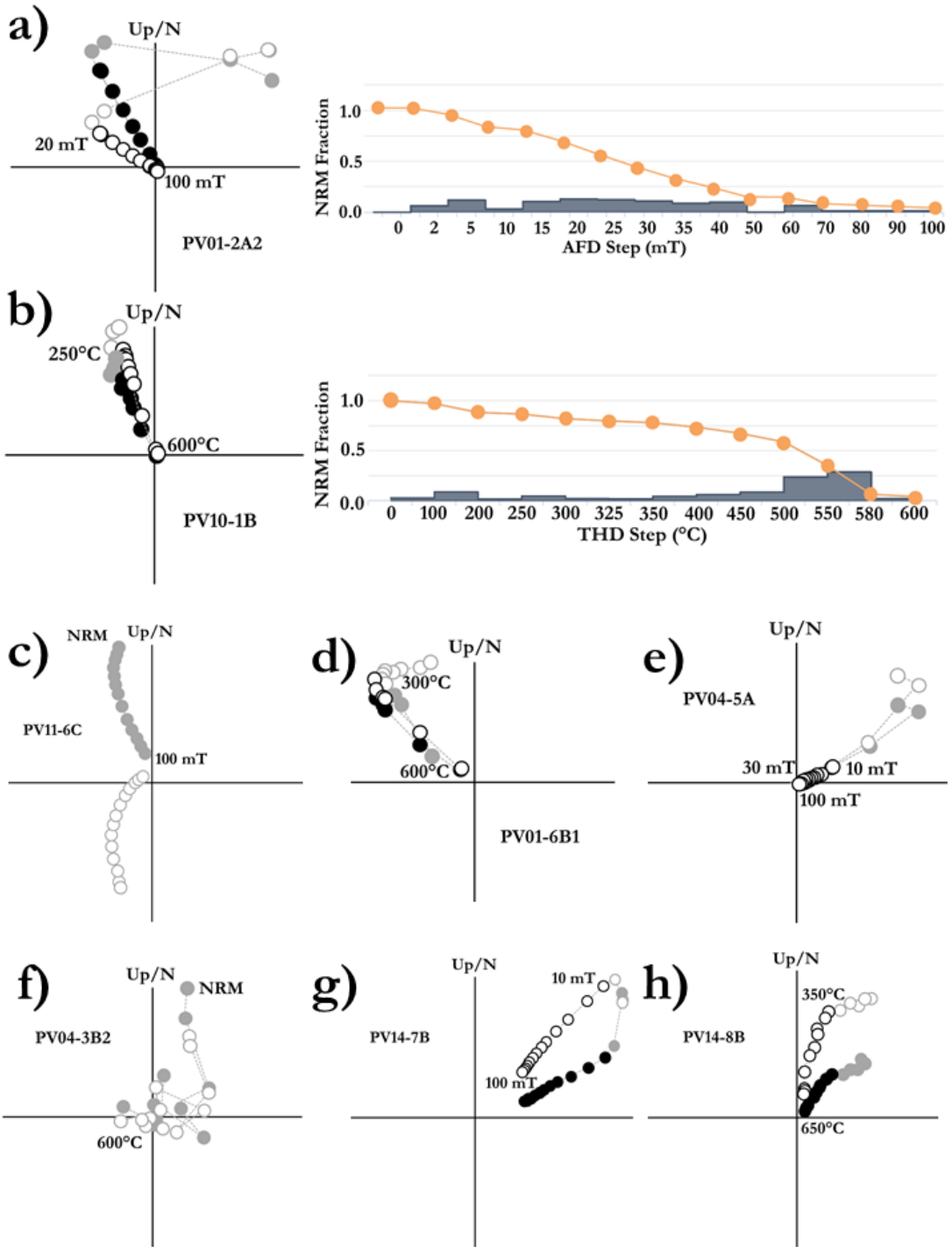

Figure 4.8: Example demagnetisation behaviour of specimens from the Puesto Viejo (PV) Group. Typical Zijderveld plots displaying palaeomagnetic directions and demagnetisation behaviour of rhyolitic ignimbrites (a-d), basalt sills (e, f), and basalt lavas (g, h). Remaining NRM fraction after each demagnetisation step displayed where additional insight was provided (orange), fraction of NRM removed indicated by grey bars.

Table 4.3: Palaeomagnetic results from Puesto Viejo sampling sites.

Site	Unit	Lithology	Age (Ma)	Lat (°S)	Long (°W)	Dec (°)	Inc (°)	n/ n_{dir}	k	∝95
PV01	Ignimbrite	Rhyolite	235.8 ± 2	34.7	68.6	310.8	-36.7	9/9	96	5.3
PV04	Sill	Basalt	-	34.9	68.5	354.5	-67.2	11/11	56	6.2
PV05	Sill	Basalt	-	34.9	68.5	346.2	-59.0	9/9	123	4.7
PV06	Sill	Basalt	-	34.9	68.6	55.1	-73.0	11/12	45	6.9
PV09	Sill	Basalt	-	34.9	68.4	5.5	-50.1	10/10	118	4.5
PV10	Ignimbrite	Rhyolite	235.8 ± 2	34.9	68.4	336.1	-48.5	8/8	15	14.6
PV11	Ignimbrite	Rhyolite	235.8 ± 2	34.9	68.4	***58.5***	***14.1***	7/10	7	25.3
PV13	Lava	Basalt	-	34.9	68.4	358.3	-65.7	11/11	72	5.4
PV14	Lava	Basalt	-	34.9	68.4	17.2	-55.6	9/10	24	10.8
PV15	Lava	Basalt	-	34.9	68.4	35.7	-66.9	11/11	249	2.9
PV16	Lava	Basalt	-	34.9	68.4	9.5	-67.5	11/11	110	4.4
PV17	Lava	Basalt	-	34.9	68.4	***196.7***	***4.5***	8/8	12	16.8

Note 4.3: See note of Table 4.1 for description. Bold/italicised directions interpreted as ex-situ.

Specimens rarely exhibited complete demagnetisation after steps of 100 mT and 650°C, respectively (Figure 4.8g, e). The secondary component was origin trending, however.

Sites composed of each of the three targeted lithologies in the Puesto Viejo sampling area produced consistent site-mean directions (Table 4.3). From the 11 sites sampling the rhyolitic ignimbrite and the coeval basaltic sills, 8 produced consistent within-site directions. At site PV11, an ex-situ outcrop was sampled that displayed evidence of

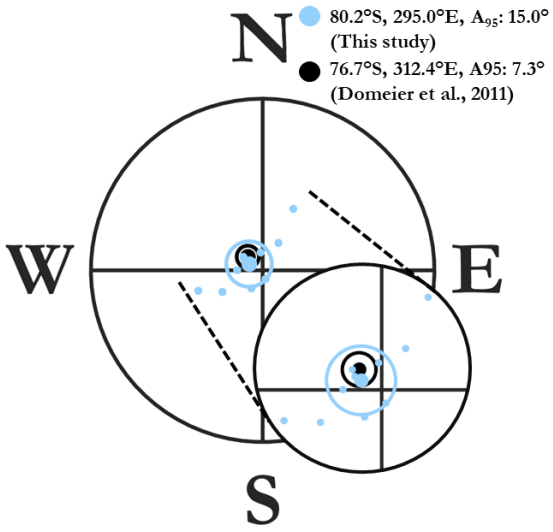

Figure 4.9: Comparison of mean VGPs of the Puesto Viejo Group from this study (blue) and Domeier et al. (2011) (black). See caption of Figure 4.3 for description.

faulting, and so the site-mean direction was not included in the calculation of the palaeomagnetic pole. Tectonic corrections were applied in accordance with the findings of Domeier et al. (2011b), who investigated the primary or secondary nature of the bedding orientation with regards to the unit formation. They concluded that the structural attitude of Puesto Viejo units around Cuesta de los Temeros (Figure 4.1b) was secondary and that tectonic corrections were required according to the local bedding information. This was relevant to site PV01 of this study (Figure 4.1b). Most sections in the Valle Grande (Figure 4.1b) were determined to display primary attitude but secondary attitude

was concluded for the site PV31 in the study of Domeier et al. (2011b). This correlates with site PV06 in this study (Figure 4.1b), and so a tectonic correction was also applied according to local bedding orientation.

The combined palaeomagnetic pole for the ignimbrite and sill ChRM directions is in general agreement with that previously calculated for equivalent units (Domeier et al., 2011b), but demonstrates greater variation (76.7°S, 312.4°E, A_{95}: 7.3°; Domeier et al., 2011, 80.2°S, 295.0°E, A_{95}: 15.0°; this study; Figure 4.9). ChRMs of the older basalt lava flows produce a palaeomagnetic pole at 73.6°S, 252.3°E, A_{95}: 24.0°, but are unlikely to have averaged secular variation as directions were only obtained from four sites and sampling sites were in close proximity. A loose block was sampled at site PV17 and so the site-mean direction was not included in this calculation.

Rock Magnetism & Microscopy

The rock magnetic results reveal a range of behaviours that broadly correlate with the three types of lithology sampled from the Puesto Viejo Group, the rhyolitic ignimbrites, basaltic sills, and basalt lava flows (Figure 4.10). The behaviour across the ignimbrite sites is relatively consistent but results from the sills and lava flows are suggestive of a much more complex and heterogeneous magnetic mineralogy between sampling sites and, in some cases, within a given sampling site.

- Puesto Viejo ignimbrites (PVI; PV01, PV10, & PV11)

Rhyolitic ignimbrite sites display two T_C values, one ~560-580°C and another ~620°C, broadly agreeing with the opinion of Domeier et al. (2011) that magnetite and haematite are the main carriers of the ChRM. In general, specimens displayed just one of these T_C values, though in some cases both were present (Table C.5). These differences occured at site-level, with PV01 often dominated by the higher T_C and PV10 and PV11, the lower T_C (Table C.5). Some thermomagnetic plots showed evidence of a phase with a T_C ~400°C, and in a few specimens from site PV11 this phase represented the dominant T_C. Samples heated up to 700°C produced irreversible thermomagnetic curves and susceptibility versus temperature curves (Figure 4.10a, b) but demonstrated much greater reversibility when heated up to 600°C (Figure 4.10c), suggestive of magnetite oxidation to haematite/maghaemite. Susceptibility versus temperature curves demonstrated shapes characteristic of a magnetite-haematite mix, often including evidence of the Verwey transition followed by a slope change and continuous susceptibility decay up to temperatures ~700°C (Figure 4.10a).

- Puesto Viejo sills (PVS; PV04, PV05, PV06, & PV09)

A wide range of rock magnetic behaviours were displayed that can be categorised by two sets of thermomagnetic/susceptibility versus temperature curves, that have been termed 'Type PVSA' and 'Type PVSB' (Figures 4.10d-m). Other behaviours were present but appear to represent a combination of the two behaviours (Figure C.5). Specimens displaying 'Type PVSA' behaviour were characterised by a susceptibility versus temperature curve that appeared to contain multiple phases in the heating leg (Figure 4.10d). There was a significant susceptibility decrease present at ~450°C, that was preceded by a distinct Hopkinson peak. The shape of the cooling curve was close to that of the heating curve, as were room temperature susceptibility values, but the two curves differed by the absence of an inflection at ~450°C in the cooling curve (Figure 4.10d).

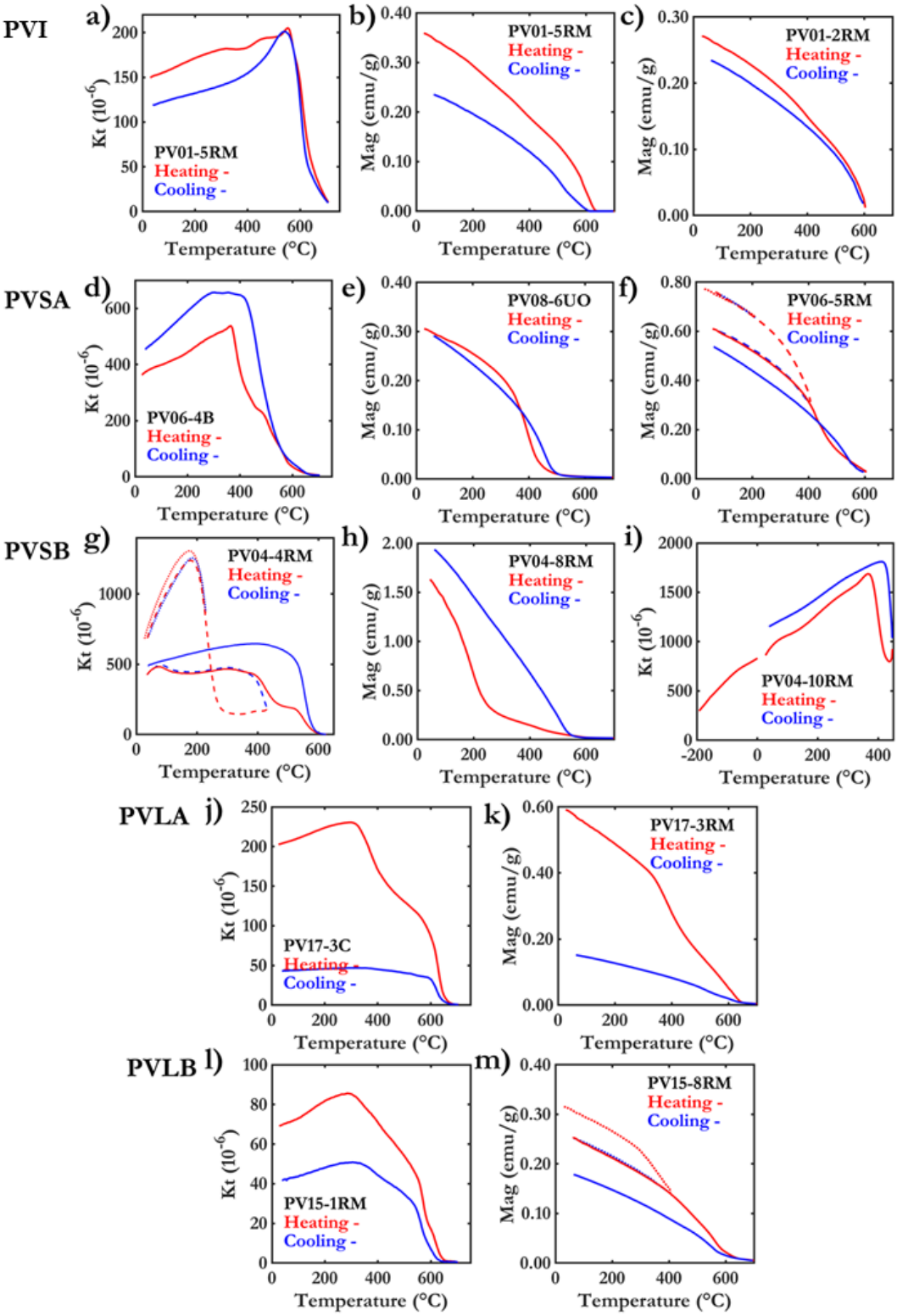

Figure 4.10: Rock magnetic results from specimens that are representative of the full range of rock magnetic behaviours displayed by specimens from the Puesto Viejo Group. Susceptibility versus temperature curves (a, d, g, i, j, l) and thermomagnetic curves (b, c, e, f, h, k, m) are presented for PVI, PVSA, PVSB, PVLA, and PVLB type behaviours. Cyclic heating steps constrain temperatures at which laboratory induced thermal alteration occurred (f, g, m), first heating and cooling cycle (dotted-line), second (dashed-line), final (solid-line). i) Low-temperature susceptibility experiment conducted in two-steps for the same crushed specimen (-200°C - 0°C, room temperature - 420°C).

On occasion, susceptibility continued to decrease above 600°C (Figure 4.10d). This behaviour was restricted to samples from site PV06 and is likely due to the presence of haematite. Cyclic heating steps, in air, demonstrated continual alteration during laboratory heating indicative of progressive oxyexsolution (Figure 4.10f). The samples likely contain a range of titanomagnetite compositions with a significant proportion of the observed behaviour attributable to a titanomagnetite with approximately $\chi_{usp} = 0.3$, as estimated by a T_C of ~450°C (Table C.5, Lattard et al., 2006).

The distinctive feature of PSVB type behaviour was an initial increase in susceptibility before a sharp drop to roughly 20% of the room temperature value at ~300°C (Figure 4.10g). The remaining susceptibility gradually decreased to zero at close to 600°C (Figure 4.10g). The corresponding cooling curve was irreversible and usually displayed a sharp increase in susceptibility from ~580°C. Room temperature susceptibility values typically reduced by around a half after the heating and cooling cycle. Cyclic temperature steps revealed reversible behaviour up to ~300°C, followed by behaviour that more closely resembled that of 'Type PVSA' when subsequently heated to greater temperatures (Figure 4.10g). The thermal stability of the low-temperature feature supports the suggestion that the decrease in susceptibility is representative of a T_C and not alteration. Estimated T_C values, derived from the thermomagnetic curves, of ~230°C (Table C.5) would suggest that this was a titanomagnetite $\sim\chi_{usp} = 0.55$ (Lattard et al., 2006). Low-temperature susceptibility behaviour also suggested that this phase was thermally stable in nature (Figure 4.10i). Curves displayed an approximately linear increase in susceptibility with increasing temperature prior to the sharp drop off observed in high-temperature experiments (Figure 4.10i). This strong temperature dependence of susceptibility agrees with previously observed behaviour of Ti-rich titanomagnetites during low-temperature experiments (Moskowitz et al., 1998).

Overall, the magnetic behaviour of the basaltic sills appears to be dominated by varying proportions of a wide range of titanomagnetites with a higher abundance of certain compositions. Laboratory heating encouraged progressive oxyexsolution of all specimens that resulted in magnetic behaviour that was predominantly controlled by near-pure magnetite.

- Puesto Viejo lavas (PVL; PV13, PV14, PV15, PV16, PV17)

All flows sampled, displayed broadly similar rock magnetic behaviour but again demonstrated two "end-member" possibilities that have been termed 'Type PVLA' and 'Type PVLB'. For Type PVLA behaviour, both the thermomagnetic curve and the susceptibility versus temperature curve displayed a sharp decrease occurring around 300-400°C and curves were highly irreversible, with cooling curves displaying much lower room temperature values (Figure 4.10j, k). This a strong indication of maghaemite to haematite inversion. T_C estimates from the thermomagnetic curves were typically 620-630°C (Table C.5), also consistent with haematite (Dunlop & Özdemir, 1997). In part, this will be representative of the haematite formed during heating but non-saturated IRM curves suggest that haematite was also present prior to heating (Figure C.6). Specimens with Type PVLB behaviour again display features indicative of maghaemite. The variation from Type PVLA behaviour is that these features are present, though reduced in size, on the susceptibility versus temperature cooling curves (Figure 4.10l). This suggests that the decrease in susceptibility around 300-400°C is not entirely attributable to the inversion of

maghaemite. The reduced difference between room temperature magnetisation (Figure 4.10m) would also suggest that less haematite has been produced during the laboratory heating process, though values from the cooling curves are still approximately half those from the heating curves.

For the majority of sites, the BDS value was greater than 0.10 (Figure 4.11a). Estimated BDS values below 0.10 were generally from measurements made using the basaltic sill sites, and of these all of them displayed PVSB type behaviour (Figure 4.11d). This is part of a more general trend with specimens that displayed PVSA type behaviour (Figure 4.11e) producing the highest BDS values from the basaltic sills. As the BDS value decreased between specimens, the rock magnetic behaviour more closely resembled that of type PVSB. Estimated BDS values follow the trendline but with a tendency to plot above it (Figure 4.11a) but in this case rock magnetic evidence would suggest that this is not due to a haematite contribution.

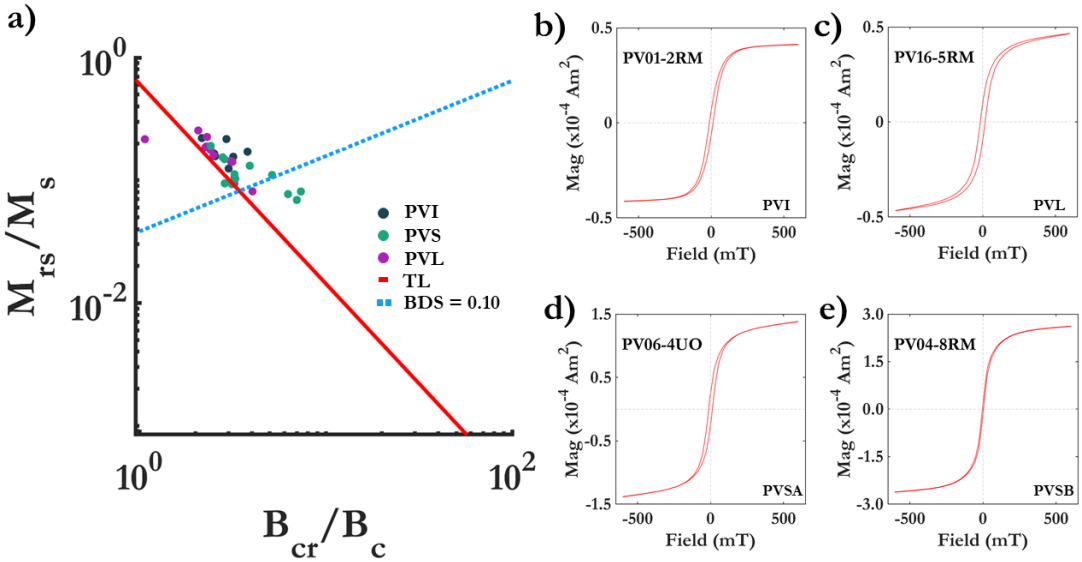

Figure 4.11: Hysteresis properties for Puesto Viejo specimens. a) See caption of Figure 4.5 for description. Representative examples of hysteresis loops associated with each categorised rock magnetic behaviour b) PVI, c) PVL, d) PVSA, e) PVSB processed with HystLab (Paterson et al., 2018). PVL presented as one behaviour type due to similarity in hysteresis parameters of specimens displaying PVLA and PVLB behaviour, respectively.

Backscattered electron SEM images of ignimbrite specimens from the Puesto Viejo group displayed iron-oxide grains located within a silicate rich matrix that shows lighter and darker regions (Figure 4.12a, b). At site PV01 (Figure 4.12a) the iron-oxide grains displayed a wider range of sizes, with a greater abundance of larger grains than observed at other sites. Site PV10 represents the baked region of an ignimbrite associated with the basalt sills sampled for this study. Images from this site show the two-shade matrix as a banded structure (e.g. Gimeno, 2003), likely depicting a chloritized matrix that the iron-oxides tend to form around (Jeong et al., 2021) (Figure 4.12b, c). Similar structures are also observed from SEM analysis of site PV11 but to a lesser extent (Figure 4.12e). Two specimens were selected for SEM analysis from PV10 with varying degrees of oxidation determined by the red or white appearance (Figure C.7). These banded structures were significantly more visible in the more oxidised, specimen (Figure 4.12c). This specimen also included examples of skeletal cruciform magnetite (Figure 4.12d). In the specimen analysed from site PV11, a much smaller proportion of lithic clasts were observed, with

the specimen mostly composed of silica-rich matrix (Figure 4.12e). Iron-oxides identified through EDX analysis of PV11 were rare (Figure C.8a, b).

EDX analysis of iron-oxides identified in specimens of the basaltic sills agree with the interpretation from rock magnetic analysis that they contain a compositional range of titanomagnetites (Figure C.8c). Data was obtained for grains ranging in diameter from ~2 μm to 10s of microns. The larger grains appeared to be higher in titanium content although this was variable, as was the ratio of iron to titanium in the smaller grains. Most grains displayed well-defined edges with limited signs of weathering (Figure 4.12f). The observed cracks and shading differences, indicative of two phases within a grain and thus compositional alteration, appeared confined to grains of a size typically associated with the MD range. This observation could be a limitation of the microscopy, however.

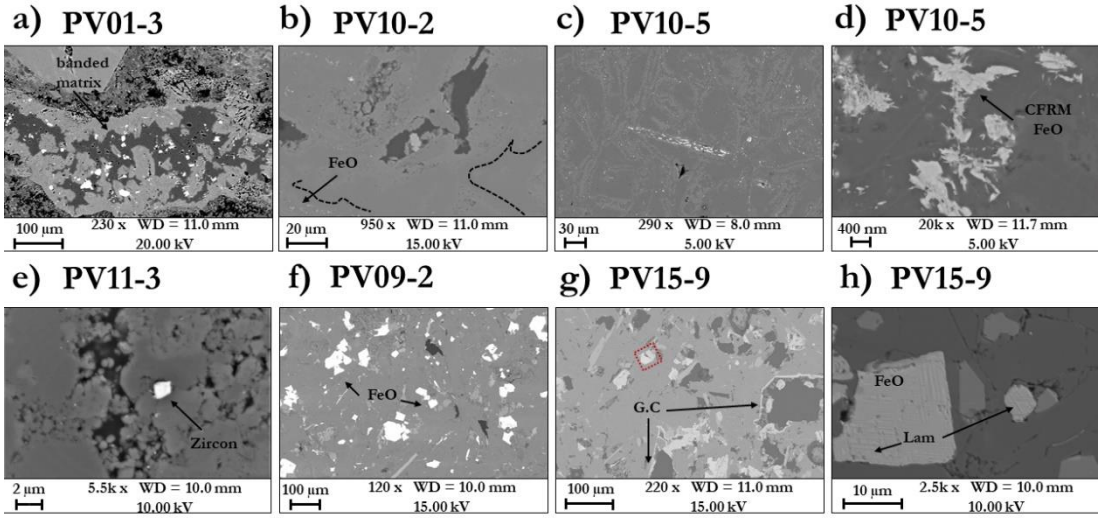

Figure 4.12: Scanning electron microscope (SEM) images of Puesto Viejo specimens, obtained from backscattered electrons. CFRM – cruciform structure, G.C – grain coating, Lam – lamella. Pervasive cracking highlighted (red box).

Iron-oxide grains within the basalt lava flows displayed varying degrees of alteration (Figure 4.12g), there was evidence of grain cracking which at worst almost cut grains into two (Figure 4.12g). In areas, the specimen analysed from site PV15 displayed significant levels of grain coating (Figure 4.12g). This was observed to a much lesser extent in the other lava flow specimens analysed but the presence of significant secondary mineralisation cannot be ruled out for any lava flow sample, especially when considering that the rock magnetic results were often suggestive of the presence of maghaemite. PV15 is the only basalt specimen analysed in which titanomagnetite grains with well-defined exsolution lamellae were observed (Figure 4.12h), alteration textures were also visible in these grains as there was evidence of pitting (Figure 4.12h).

Palaeointensity Estimates

The consistent presence of maghaemite in the sampled lava flows is immediate cause for concern. The suggestion of a somewhat reduced effect, presented by some of the more reversible rock magnetic behaviour is encouraging, but crucially the widespread alteration textures observed in the SEM images, and in particular the grain coatings of iron-oxides, would make any palaeointensity estimates from these specimens highly uncertain due to potential bias associated with TCRM acquisition via this mechanism (Fabian, 2009). As

such, specimens from the basalt lava flows were not subjected to palaeointensity experiments.

Of the three ignimbrite sites from which specimens were subject to thermal Thellier experiments, two resulted in at least one palaeointensity estimate. Four out of eleven specimens were successful from site PV10, and one out of ten from site PV11 (Table 4.4). Interpreted best fit line segments of the Arai plots consistently fell across an unblocking temperature range associated with magnetite, with typical end temperatures of 580°C. For specimens from site PV10, starting temperatures were usually 200°C (Figure 4.13a, b). For two of the four accepted results at site PV10, heating up to 580°C resulted in full demagnetisation with no suggestion of a second direction from the associated Zijderveld plots (Figure 4.13b). In the case of the remaining two specimens, demagnetisation over the magnetite temperature range removed around 80% of the NRM (Figure 4.13a). The remainder of the Arai plot is highly zigzagging and the temperature steps correlate with a directional change in the associated Zijderveld plot (Figure 4.13b). The only specimen that satisfied the selection criteria from site PV11, produced a curved Arai plot (Figure 4.13d). The starting temperature of the interpreted section was 400°C and the temperature steps prior to this were associated with a clear directional overprint (Figure 4.13d). The Zijderveld plot of the remaining temperature steps demonstrated origin trending decay (Figure 4.13d). This behaviour was consistent across other specimens from the site and in these examples the failure of the high-temperature component was primarily due to failure of pTRM checks.

Unlike for the thermal Thellier method, results were obtained across sites of the dacitic ignimbrite and the basalt sills when utilising the Shaw-DHT protocol. From the 29 ignimbrite specimens studied, 21 produced results that passed the selection criteria. Specimens appear to have experienced a range of thermal alteration, as demonstrated by their associated alteration corrections (Figure 4.13c, e, f). It would also appear that the use of ARM as an analogue for TRM is more appropriate for some specimens than others, as the similarity between the NRM-TRM1 plot and the ARM0-ARM1 plot varied across specimens (Figure 4.13c, e, f). For sites PV01 and PV10, low σB (Table 4.4) would suggest that this had little bearing on the palaeointensity estimates, but specimens from site PV11 produced estimates that grouped either side of the calculated mean, that resulted in a large σB (Table 4.4; Table C.7). Specimens of the basaltic sills experienced significant thermal alteration after the first heating but became very thermally stable after this. This behaviour was anticipated from the rock magnetic behaviour and is demonstrated by the curved NRM-TRM1 plots, and TRM1-TRM2 slopes consistently close to unity (Figure 4.13f). Estimated palaeointensity values were consistent across all sites sampling both lithologies, despite being subject to a variety of applied field strengths (10 μT, 15 μT, & 30 μT; Table C.7). Site PV11 was the exception, as it produced estimates of ancient field strength approximately twice those from other sites (Table 4.4). The overprint identified by thermal demagnetisation of specimens from PV11 was not easily identified by AFD. Zijderveld plots displayed curvature that was suggestive of overlapping unblocking coercivities of the multiple magnetisation components (Figure 4.8C). The difficulty in isolating the ChRM could explain the high variation in estimated palaeointensity values and the disagreement with the estimate obtained via the thermal Thellier technique. Specimens from site PV05 failed to produce any palaeointensity estimates due to non-linear portions of the NRM-TRM1 plot, causing failure of R_n^2 and/or k_n' (Table C.7).

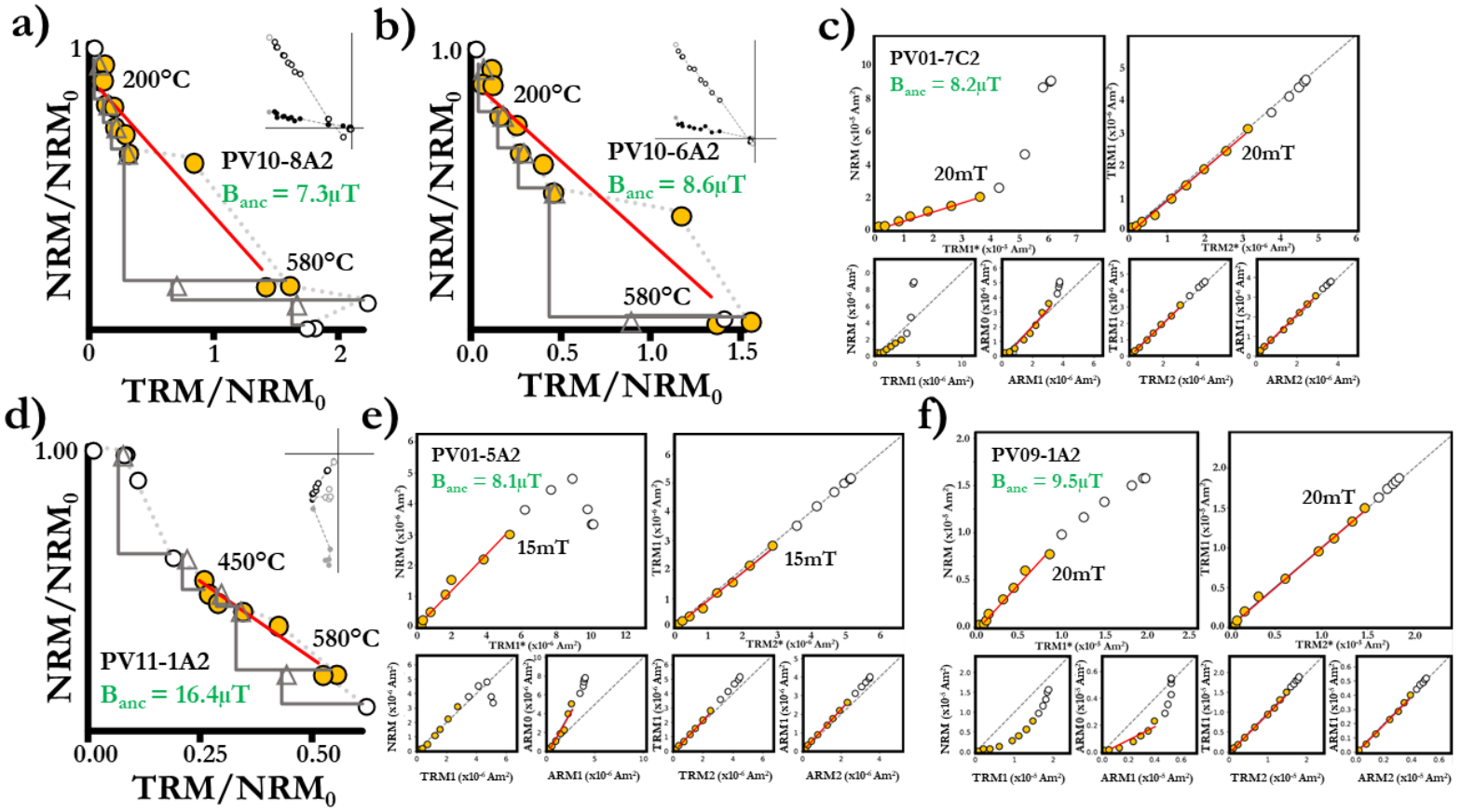

Figure 4.13: Representative results of palaeointensity experiments conducted on specimens from the Los Menucos Group. (a, b, d) Arai plots and Zijderveld plots (Zijderveld, 1967) of the thermal Thellier experiments, (c, e, f) Shaw results. See caption of Figure 4.7 for description.

Table 4.4: Palaeointensity results from Puesto Viejo sampling sites.

Site	**Density** (Mgm^{-3})	**VNS**	$\mathbf{n}_{VNS}$	$\mathbf{B}_{th}$ (μT)	$\sigma\mathbf{B}_{th}$ (μT)	$\mathbf{n}/\mathbf{n}_{th}$	$\mathbf{B}_{sh}$ (μT)	$\sigma\mathbf{B}_{sh}$ (μT)	$\mathbf{n}/\mathbf{n}_{sh}$	$\mathbf{B}_{pt}$ (μT)	$\sigma\mathbf{B}_{pt}$ (μT)	$\mathbf{n}/\mathbf{n}_{pt}$	**B** (μT)	$\sigma\mathbf{B}$ (μT)	**VDM** ($x10^{22}$ Am^2)	**QPI**
PV01	2.4	660	6	-	-	0/3	7.4	1.1	10/12	4.4	1.1	3/12	7.4	1.1	1.6	7
PV04	-	-	-	-	-	0/2	6.5	3.5	3/12	-	-	0/12	6.5	3.5	1.0	6
PV05	-	-	-	-	-	0/3	-	-	0/8	-	-	0/8	-	-	-	
PV06	-	-	-	-	-	0/3	7.5	2.1	7/10	8.7	2.4	5/10	7.5	2.1	1.1	6
PV09	-	-	-	-	-	0/3	7.2	2.0	7/10	9.2	3.1	3/10	7.2	2.0	1.4	6
PV10	-	-	-	10.0	2.7	4/11	11.0	3.6	4/8	5.9	1.8	2/9	10.5	3.0	2.1	5
PV11	2.1	8	6	16.4	-	1/10	***22.9***	***8.3***	7/9	***6.7***	***2.8***	5/9	22.1	8.0	-	0
PV13	-	-	-	-	-	-	-	-	-	-	-	-	-	-	-	-
PV14	-	-	-	-	-	-	-	-	-	-	-	-	-	-	-	-
PV15	-	-	-	-	-	-	-	-	-	-	-	-	-	-	-	-
PV16	-	-	-	-	-	-	-	-	-	-	-	-	-	-	-	-
PV17	-	-	-	-	-	-	-	-	-	-	-	-	-	-	-	-

Note 4.4: See note of Table 4.2 for description. Bold/italicised palaeointensity estimates interpreted as likely being unreliable.

In general, the palaeointensity estimates obtained using the pseudo-Thellier method, applied to Puesto Viejo specimens, showed good agreement with the results from other palaeointensity methods (Table 4.4), especially when considering the high degree of associated uncertainty. Again, the exception was for specimens from site PV11, where pseudo-Thellier estimates were significantly lower than the mean estimates from both the thermal Thellier and the Shaw method (Table 4.4). Thermal alteration during laboratory heating, associated with the thermal Thellier and Shaw-DHT experiments, could have potentially gone unnoticed or have been unaccounted for in full, explaining the discrepancy between palaeointensity estimates, but again difficulty in isolating the ChRM through AF demagnetisation cannot be overlooked as a possible cause. Estimates from the remaining ignimbrite sites displayed greater consistency with the results from other methods, but success rates were relatively low (Table 4.4). Passing pseudo-Arai plots were primarily straight and those that failed did so because of curved and/or two-slope behaviour. Some specimens from site PV10 produced pseudo-Arai plots too noisy for interpretation. Where estimates were obtained from basaltic sill sampling sites, there was good agreement with results obtained via the Shaw method (Table 4.4). Once again specimen failure was primarily down to pseudo-Arai plot curvature (Table C.8).

Reliability of Palaeointensity Estimates

- PVI (PV01, PV10, PV11)

Iron-oxide grains imaged from site PV01, are generally well defined and in many cases exhibit a cubic shape (Figure 4.12a). Possible matrix alteration is visible through the lighter and darker regions of some glass shards within the matrix (Figure 4.12a) but iron-oxide grains do not appear to follow a pattern according to these different areas. The difference between volume normalised susceptibility (VNS) values between specimens from PV01 and PV11, cannot be explained by variations in the experienced degrees of compaction alone (Avery et al., 2018). VPA likely contributed to the reduced susceptibility of PV11 specimens, and so values of the same order of magnitude might be expected if the haematite phase within PV01 specimens had formed via the same processes. This would imply that the haematite phase at site PV01 has a primary origin in relation to the ignimbrite deposition. Detrital haematite grains could account for the more rounded, larger grains observed in the SEM images (Figure 4.12a). Some smaller grains broadly follow the edges of glass shards, an indication of nucleation and growth after emplacement (Avery et al., 2018). A mean density > 2.0 Mgm^{-3} (2.4 Mgm^{-3}, Table 4.4) indicates a likely emplacement temperature above the observed T_C values of the two magnetic phases (Table C.5, Riehle et al., 1995), making it likely that both the microlites and phenocrysts carry a TRM.

Susceptibility values for PV11 are two orders of magnitude lower than those observed for PV01, agreeing with the lack of iron-oxide grains observed through SEM analysis. Coupled with lower mean density values (2.1 Mgm^{-3}, Table 4.4), this is suggestive of a reduced degree of initial compaction during deposition of the ignimbrite. As a result, the ignimbrite sampled at PV11 is of higher porosity and experienced increased exposure to hydrothermal processes such as chloritisation (Yuguchi et al., 2021a; 2021b; Morad et al., 2011). This concurs with the chloritised matrix pattern observed in the SEM images which is similar to that observed by Jeong et al. (2021), when studying the Southern Kusandong Tuff of South Korea. Formation of secondary magnetic phases likely

occurred at temperatures up to approximately 350°C to 400°C, as suggested by the magnetic overprint identified in the Zijderveld plots (Figure 4.13d). Palaeointensity estimates obtained from the Shaw-DHT and pseudo-Thellier method are affected by difficulties in ChRM isolation and so cannot be deemed to be reliable. The sole result obtained by the thermal-Thellier method utilises a temperature range associated with the ChRM, the mean density value lies just above 2.0 Mgm^{-3}. It is possible that this palaeointensity estimate could be an accurate description of the geomagnetic field during the initial emplacement of the sill but it is of limited use in isolation.

The more widespread occurrence of potential chloritsation at site PV10, a baked region of the same unit sampled at PV11, would suggest that as the sill was emplaced, larger volumes of hydrothermal fluids entered the pore spaces causing more extensive chloritisation. This also points to the convection of hydrothermal fluids as a primary form of heat transfer in the baking of the country rock over more direct conductive transfer from the igneous intrusion. Chloritisation results in the formation of voids, or vugs, in the matrix (Jeong et al., 2021; Morad et al., 2011). Concentrations of metal ions, including iron, in the hydrothermal fluid gradually decrease (Yuguchi et al., 2021a; 2021b), precipitating into the vugs (Jeong et al., 2021). This is the likely origin of the more platy iron-oxides observed in and around the chloritised matrix (Figure C.9). This would make them of secondary origin, and in the case of PV10, likely related to the intrusion of the sill. Susceptibility values from PV10 are two orders of magnitude higher than those from specimens of PV11 (Table 4.4) and would suggest that at least the bulk of these secondary iron-oxides are (titano)magnetite. The country rock sampled at site PV10 appears to have been heated to much higher temperatures than occurred at site PV11. Specimens containing a small titanohaematite component, as indicated by non-saturated IRM acquisition curves, display an overprint that is removed between 580°C and 600°C (Figure 4.13a). Some specimens do not display evidence of a haematite component (Figure 4.13b) and have likely experienced complete remagnetisation by the intrusion of the sill. Palaeointensity results from specimens that displayed a titanohaematite component only utilised a temperature range associated with titanomagnetite unblocking, and the results showed good agreement with those from specimens that did not contain a titanohaematite component (Figure 4.13a, b). This suggests that the small contribution to the specimen NRM from the titanohaematite component, likely carrying a TCRM after oxidation of TRM carrying iron-oxides, had minimal effect on the palaeointensity estimates. Attempting to determine the temperature at which the secondary magnetite grains, associated with the intrusion of the sill, formed, after the country rock experienced heating up to ~600°C, is crucial to the reliability of the estimated palaeointensity values. The process of chloritisation typically occurs at temperatures below 350°C (Galán & Ferrell, 2013; Lopes et al., 2019; Yuguchi et al., 2021b; 2021c), well below the T_C of magnetite. If this were the case, the platy magnetite grains observed would carry a CRM. The presence of cruciform (titano)magnetite surrounding the chloritised matrix suggests that the baked margin experienced rapid cooling, however. The ChRM utilised in palaeointensity experiments is likely carried by original grains formed from nucleation and growth in the glassy matrix that have experienced complete remagnetisation (Figure C.7) and secondary titanomagnetite grains formed after reheating associated with the intrusion of the adjacent sill. Evidence of rapid cooling would suggest that the latter carry a TRM but some fraction of a TCRM cannot be entirely dismissed.

- PVS (PV04, PV05, PV06, PV09)

Results are only present from Shaw and pseudo-Thellier methods, due to the progressive oxyexsolution that occurs during laboratory heating. These effects result in an ever-changing mineralogy for each successive temperature step above ~300°C in thermal Thellier experiments, explaining the changing slopes of the Arai plots and sharp decrease in magnetisation observed (Figure C.10). Agreement between the non-heating pseudo-Thellier method and the Shaw method would suggest that, although the same oxyexsolution has occurred during full TRM acquisition, resulting in much higher imparted remanence intensities than the NRM due to magnetite formation, the ARM correction has been able to successfully account for this. This is an example of when imparting a full TRM has been more beneficial than imparting multiple pTRMs. SEM images displayed well-defined titanomagnetite grains, often cubic in shape, and showing limited signs of cracking or coating suggestive of secondary remanence. The presence of compositionally intermediate titanomagnetite grains indicates a rapid cooling of the sills (Dunlop & Özdemir, 1997), and exsolution during laboratory heating would suggest that subsequent heating to such temperatures has not previously occurred post cooling. As such the titanomagnetite grains within the sills likely carry a TRM, with the ChRM isolated via AF demagnetisation.

Good agreement between the final estimates of virtual dipole moment (VDM) from the basaltic sill sites (PV04, PV06, & PV09; Table 4.4) and the rhyolitic ignimbrite most likely carrying a primary TRM (PV01; Table 4.4) is further evidence to suggest that the ChRM is primary in nature, when it is considered that their formations have previously been shown to be approximately coeval (Domeier et al., 2011; Valencio et al., 1975). Following this, results from these sites passed the Q_{TRM} criterion of the Q_{PI} criteria (Table C.9). These results suggest that the ARM correction of the Shaw protocol is capable of successfully accounting for large amounts of laboratory induced alteration associated with the oxyexsolution of titanomagnetite grains. Despite some uncertainty surrounding the nature of their magnetic remanence, good level of agreement between the accepted results and those obtained from the baked ignimbrite at site PV10 suggests that TCRM contribution is minimal and that any contribution had reduced effects on the palaeointensity estimates. Therefore, results from PV10 likely represent the palaeomagnetic field during the time of the intrusion of the sill. Taking the more cautious approach, the Q_{TRM} criterion of the Q_{PI} criteria was failed for site PV10, however (Table C.9). Site PV10 was also the sole site where Q_{DIR} failed due to the failure of the $k \geq 50$ requirement (Table 4.4; Kulakov et al., 2019) but successful results from both the thermal Thellier and Shaw-DHT method resulted in it also being the sole site where Q_{TECH} passed (Table C.9). Final accepted VDM estimates ranged between 1.6×10^{22} and 2.1×10^{22} Am^2. Assigned Q_{PI} scores ranged between 5 and 7 with both a median and mean value of 6 (Table 4.4; Table C.9).

Discussion

Suitability of Ancient Ignimbrites as Palaeointensity Recorders

There was deemed to be a consistent presence of titanomagnetite grains, in specimens of ancient ignimbrites, representing a primary magnetic phase that formed as a result of

nucleation and growth during the initial cooling of the volcanic deposit, and that are likely to carry a TRM. These cubic grains are found in unaltered portions of the vitric matrix, suggesting that the matrix is able to offer protection against alteration even when exposed to a hydrothermally active environment across prolonged time scales. Palaeointensity estimates from such magnetic carriers would provide a reliable description of the palaeomagnetic field in which they formed, but in the specimens analysed for this study, they are often accompanied by secondary magnetic phases that have the potential to produce biased estimates. Thermally unstable maghaemite produces distinctive behaviour during rock magnetic experiments, making it easily recognisable, and due to the nature of its formation it must be interpreted as secondary. The presence of secondary haematite and magnetite, formed through devitrification processes such as chloritisation, is much more difficult to identify but could have significant biasing effects on palaeointensity estimates. Such phases were identified through SEM microscopy, successfully identifying secondary textures, and analyses of susceptibility and density profiles, within the context of ignimbrite formation and alteration processes, was found to be particularly advantageous. It has been demonstrated that the ignimbrite sampled at site PV10 produced reliable palaeointensity results despite the likelihood that it contained a proportion of TCRM carrying grains, likely due to its reduced contribution to the ChRM. More generally, the agreement between palaeointensity estimates obtained from ignimbrites and the more traditionally used basalt sills from Puesto Viejo strengthens the reliability of the estimates obtained and demonstrates that ancient ignimbrites can be reliable palaeointensity recorders. The extensional tectonic setting associated with the Puesto Viejo Group, gave rise to bimodal volcanism (Kleiman & Salvarredi, 2001; Monti & Franzese, 2019). As such, emplacement of rhyolitic ignimbrites and basaltic sills, within the San Rafael depocenter, was occurring concurrently without a progressive evolution of magma composition. This is supported by the overlapping dates previously obtained from samples of the ignimbrites and sills (Domeier et al., 2011; Valencio et al., 1975). Palaeointensity estimates were successfully obtained from localities across the depocenter (Figure 4.1b) and throughout the stratigraphic profile of the Puesto Viejo Group. As a result, the range of palaeointensity estimates obtained from the more traditionally used basaltic sills are expected to be representative of the variation in the strength of the palaeomagnetic field across the duration of the emplacement of the Puesto Viejo Group. Furthermore, there would be no reason to suggest that the strength of the palaeomagnetic field should have displayed greater variation during the emplacement of any ignimbrite units. With the estimates obtained from ignimbrite units displaying agreement with the range of estimates obtained from the basaltic sills, they are interpreted as being representative of the palaeomagnetic field at the time of their formation and not significantly biased through TCRM acquisition.

Ignimbrites sampled from Los Menucos contained secondary magnetic phases, and without results from a more traditional, similarly aged lithology, any biasing effects on the final palaeointensity estimates are unknown. For this reason, results from Los Menucos are not considered to be reliable. Ancient ignimbrites are capable of being reliable palaeointensity recorders, but, without the corroboration of results from another lithology, it is difficult to confidently attribute any palaeointensity estimates as being representative of the palaeomagnetic field during the time of the lithology formation. From this study, the recommendation would be to avoid carrying out palaeointensity studies that rely solely on results obtained from ignimbrites, due to their complex thermal

histories and the difficulty in ascertaining the formation of magnetic phases in relation to this. The bimodal nature of volcanism in the San Rafael depocenter, was paramount in assessing the reliability of estimates obtained from the rhyolitic ignimbrites and would be required to conduct future investigations in a similar manner. The association of bimodal volcanism with extensional tectonics (Frost & Frost, 2019), emphasises the potential that other extensional basins along the western margin of southern South America have to further our understanding of palaeointensity in the Post-PCRS. For example, the Rincón Blanco sub-basin of NW Argentina (Barredo et al., 2012) contains alkaline basalts and Rhyolitic ignimbrite units (Barredo et al., 2012) associated with a range of dates, obtained via U-Pb SHRIMP geochronology, between 246.4 ± 1.1 Ma and 230.3 ± 1.5 Ma. Alternatively, a more traditional investigation could be facilitated by the more numerous lava flows with assigned Triassic dates of the Peruvian Mitu Rift (Spikings et al., 2016).

The sole example of a palaeointensity estimate in the PINT database, from ignimbrite units of comparable age to those of this study, come from the study of Krs. (1967), who calculated a VDM of 12.9 x 10^{22} Am^2. This estimate has an assigned age of 275.5 Ma and was obtained from ignimbrite specimens that were part of the Bohemian Massif, sampled near Broumov, Czech Republic. The palaeointensity estimate of Krs. (1967) is of interest as it lies within the interval of the PCRS, for which palaeointensity behaviour is disputed (Tarduno & Cotrrell, 2005; Hawkins et al., 2021). Applying the findings of this study, the palaeointensity estimate presented by Krs. (1967) has been re-evaluated, in an attempt to assess its reliability. Thermal demagnetisation of the studied ignimbrite suggests that the majority of the remanence was held by haematite. Approximately 80% of the NRM remained after heating up to 580°C, and the majority of demagnetisation occurred between 600°C and 650°C. Evidence to suggest a lack of CRM within the specimens came from agreement of the direction of remanent magnetisation between partially demagnetised specimens and that across the full ChRM (Krs, 1967). In this study, it has been discussed how haematite can replace magnetite as a secondary magnetic phase, and that in such cases the TCRM acquired would not be expected to display a different direction to the initial TRM acquired (Dunlop & Özdemir, 1997). This study also discussed how haematite within ignimbrites is unlikely to be a primary phase unless present in the pyroclastic material as detrital grains. These observations raise doubts over the reliability of the estimates and further highlight the requirement for detailed assessment of the likely origin of magnetic carriers with regards to the thermal history of ignimbrites.

Implications of Palaeointensity Estimates for the Strength of the Post-PCRS

As discussed, specimens of the Los Menucos Complex that displayed LMIB type behaviour, were interpreted as having experienced (titano)magnetite replacement by (titano)haematite due to VPA. Avery et al. (2018) arrived at a similar conclusion to explain the behaviour of specimens from the Bishop Tuff, that they termed as having 'Group A' properties. Estimates obtained from these Group A specimens were significantly higher than those obtained from specimens displaying 'Group B' properties, which were interpreted as the most likely specimens to carry a TRM, and thus produce a more reliable estimate of palaeointensity. The overestimated palaeointensity values of specimens that displayed Group A properties (Avery et al., 2018) was explained by the models of TCRM acquisition proposed by Fabian. (2009). The process of magnetite replacement by haematite, within a hydrothermal environment, occurs through a combination of leaching

and low-temperature oxidation (Ohmoto, 2003; Otake et al., 2010; Zhao et al., 2019). TCRM acquisition via both leaching and low-temperature oxidation, after TRM acquisition, were demonstrated separately to be capable of producing statistically acceptable Arai plots that resulted in overestimated palaeointensity values (Fabian, 2009). If one were to assume that palaeointensity estimates obtained in this study from specimens displaying LMIB type behaviour are similarly biased, then the estimated values (2.9 - 4.6 x 10^{22} Am^2) would represent overestimates and suggest that the true palaeointensity was much weaker. This interpretation is in keeping with the weak field strength suggested by estimates from the Siberian Traps for the PTB. A more recent model exploring the effects of TCRM acquisition on palaeointensity estimates, did so for the more general case of TCRM acquisition through T_C increase (Shcherbakov et al., 2021). This model is also applicable to (titano)haematite replacement of (titano)magnetite as the product has a higher T_C (Dunlop & Özdemir, 1997). The model of Shcherbakov et al. (2021), predicts that palaeointensity estimates obtained from a TCRM acquired in this way will display limited biasing effects. If this were to be the case then the palaeointensity estimates from LMIB type specimens would suggest a geomagnetic field strength broadly in keeping with the long-term geomagnetic field behaviour (**Chapter 3**).

The models of both Fabian. (2009) and Shcherbakov et al. (2021) explain the behaviour of ensembles of single domain particles. In reality, whole rock specimens contain a range of interacting magnetic grains of different domain states, making direct application difficult. Despite this, and the contrasting interpretations of the two models discussed, the implications highlight the importance of exploring the physical processes that have affected remanence carriers. Through continued improvement to our understanding of the effects of these processes on palaeointensity estimates, such results still have the potential to provide important information.

Successful palaeointensity results were obtained from the basaltic sills and rhyolitic ignimbrites of the Puesto Viejo Group. Site mean VDM estimates ranged between 0.9 x 10^{22} and 2.1 x 10^{22} Am^2 with an average Q_{PI} value of 6. The sills and ignimbrites of the Puesto Viejo Group were targeted as their assigned age (ca. 236 Ma, Domeier et al., 2011; Ottone et al., 2014) is proximal to that of the pillow lavas of the Fernazza Fm (ca. 238.2 Ma), that were previously studied in **Chapter 3**. Palaeointensity estimates from the Fernazza volcanics seemed to suggest that geomagnetic field strength during the Post-PCRS was comparable to that of the long-term median, and that the weak field strength associated with the PTB was a time-limited feature (**Chapter 3**). The estimates from the Puesto Viejo specimens are lower than those obtained from the Fernazza volcanics, that ranged between 3.0 x 10^{22} and 4.8 x 10^{22} Am^2 (**Chapter 3**), and there is no crossover in the range of the estimated V(A)DMs from the two sampling localities (Figure 4.14). When the global V(A)DM record over the last 320 Ma is analysed, the combined distribution of the V(A)DM values from the Puesto Viejo Group and the Fernazza Fm, appears similar to the distribution of V(A)DM values around the PTB (Figure 4.14). This is further highlighted by the position of the median V(A)DM value for the PTB (2.3 x 10^{22} Am^2; **Chapter 3**) lying almost exactly in between the median V(A)DM values for the Puesto Viejo Group (1.4 x 10^{22} Am^2) and the Fernazza Fm (3.6 x 10^{22} Am^2; **Chapter 3**). Similarity between V(A)DM distributions around the PTB and ca. 236 Ma could suggest that the presence of a weaker geomagnetic field was not time-limited. This could also suggest it

to be more likely that the palaeointensity results obtained from Los Menucos specimens are overestimates, following the model of Fabian. (2009).

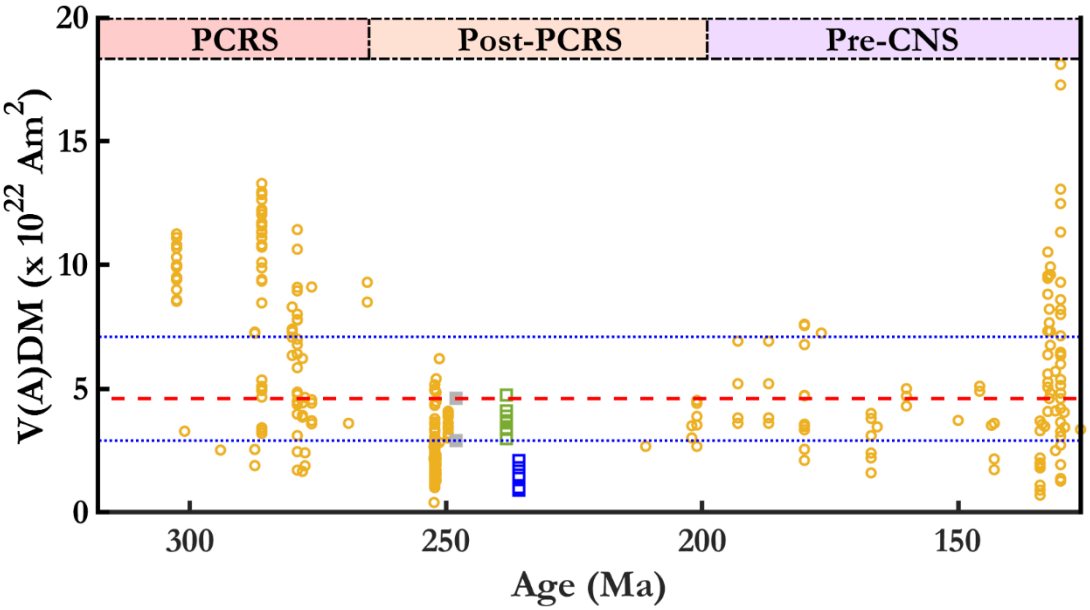

*Figure 4.14: The virtual (axial) dipole moment (V(A)DM) record between 320 Ma and 100 Ma. V(A)DM values, with $Q_{PI} \geq 3$, from v8.0.0 of the PINT database (Bono et al., 2021, yellow circle) plotted alongside site-level V(A)DM estimates from **Chapter 3** (green square) and Puesto Viejo (this study, blue square). Estimates obtained from Los Menucos specimens, that were ultimately deemed to be unreliable, are also presented for comparative purposes (grey square). The long-term average V(A)DM value (**Chapter 3**) is given by the dashed line (red) alongside the interquartile range, dotted lines (blue).*

Conclusions

Ancient ignimbrite units are capable of recording reliable palaeointensity information but, due to their complex thermal history and therefore the difficulty in ascertaining the nature of the ChRM, it is recommended that palaeointensity estimates are obtained alongside those from similarly aged lava flows and/or rapidly cooled intrusives. This approach is likely applicable to other Triassic basins of southern South America, in which ignimbrite units are often more numerous than those of more traditionally studied lithologies and bimodal volcanism has occurred as a result of the extensional tectonic setting. The Rincón Blanco sub-basin has been highlighted as one such potential study area, where palaeointensity estimates from ignimbrite units could increase palaeointensity coverage. Alongside estimates from basins more abundant in more traditionally studied units, such as the Mitu Rift, the basins of southern South America have great potential to provide much needed palaeointensity data throughout the Triassic.

The five new VDM estimates from the Puesto Viejo Group (0.9×10^{22} - 2.1×10^{22} Am^2) are slightly lower than those previously obtained from the similarly dated pillow lavas of the Fernazza Fm, Italy. When viewed together, the distribution of the palaeointensity values from these two sampling localities displays similarity to those within the PINT database that define the PTB. This would appear to suggest that the weaker geomagnetic

field strength associated with the PTB was not a time limited feature and may instead be characteristic of the geomagnetic field throughout the Post-PCRS.

Acknowledgments

All data from Shaw-DHT experiments was analysed using a Jupyter notebook developed by Daniele Thallner at the University of Liverpool. The Author would like to thank Dr Matt Bilton, Dr Heath Bagshaw, and the SEM Shared Research Facility at the University of Liverpool for the support received for the acquisition of high-resolution BSE images and EDX analyses. In addition, the author wishes to acknowledge the insightful petrological discussions with Janine L. Kavanagh that contributed to this chapter. Palaeomagnetic sampling was undertaken alongside colleagues from the University of Buenos Aires (Augusto E. Rapalini, Mónica G. López de Luchi, & Pablo Franceschinis), the National University of La Plata (Mariana Monti), and the University of Liverpool (Annique van der Boon).

Chapter 5. Evolution of long-term geomagnetic field behaviour since the Permo-Carboniferous Reversed Superchron

Abstract

Giant Gaussian process (GGP) models provide a statistical description of the geomagnetic field, under the assumption that the field can be described by a suite of independently, normally distributed Gauss coefficients. The resulting Gaussian framework facilitates predictions of any palaeomagnetic observable. Optimised models can be generated that represent a plausible description of the palaeomagnetic field across a given interval, by minimising to palaeomagnetic observations. Previously, GGP models have primarily been used as a tool to describe the recent palaeomagnetic field, for the last 5 or 10 million years. This study utilised recent improvements to palaeomagnetic databases that are representative of behaviour for the last 320 million years, to generate optimised statistical models for time intervals of distinct reversal frequency across this time. Comparison of the different models, and the observations on which each was constructed, appeared to suggest that the palaeointensity record is highly discriminatory, when characterising changes in long-term geomagnetic field behaviour. As a result, unique statistical models were required to describe palaeointensity observations associated with each studied time interval. The β parameter defining the preferred model representing the PCRS was approximately twice that of the preferred models representing other studied time intervals. This indicated that the relationship between symmetric and antisymmetric families was somewhat unique during the PCRS. The PCRS was also the only studied time interval for which the selection criteria chosen for filtering of the palaeointensity observations resulted in distributions with markedly different average values. Statistical models constructed around these two distributions suggested that the existence of increased average geomagnetic field intensity, and an average strength more in keeping with the long-term average, were both plausible for the PCRS. Through evaluation of the palaeointensity data, and their associated studies, this study favours the existence of high average intensity during the PCRS.

Introduction

Statistical models of the palaeomagnetic field are a powerful tool due to their predictive nature. Their development represents vast improvement over phenomenological models, such as Model G (McFadden et al., 1988; Handford et al., 2021), whose value lies in their descriptive capabilities (Doubrovine et al., 2019). The most commonly utilised statistical field models attempt to describe variations in the palaeomagnetic field through a giant Gaussian process (GGP; Constable & Parker, 1988), in which the field is modelled by distributions of spherical harmonic Gauss coefficients (Bono et al., 2020). Predictions can be made from a given GGP model about any measured characteristic of the palaeomagnetic field that it describes, this includes the distribution of virtual geomagnetic pole (VGP) dispersion (Handford et al., 2021), VGP inclination anomalies, field strength, and palaeomagnetic directional distributions (Brandt et al., 2020; Brandt et al., 2021; Tauxe & Kent, 2004). GGP models provide a plausible description of the palaeomagnetic field across a given time interval, by comparing and minimising the modelled distributions against corresponding palaeomagnetic observations. The parameters defining the GGP model provide potential insight into the behaviour of the palaeomagnetic field and the geodynamo processes behind its production.

Since their original proposal (Constable & Parker, 1988), the process of constructing GGP models has been refined by multiple contributors (e.g. Bono et al., 2020; Tauxe & Kent, 2004). The first GGP model provided a statistical description of geomagnetic secular variation for the last 5 Ma (Constable & Parker, 1988). The non-dipole components, and the non-axial components of the dipole (g_1^1 and h_1^1), were modelled as independently, normally distributed Gauss coefficients. Each was assigned a zero mean and a distribution of standard deviations corresponding with that associated with a white-noise source at the core-mantle boundary (CMB). The resulting spatial power spectra provided an accurate description of the non-dipolar part of the modern geomagnetic field (Constable & Parker, 1988). This simplistic description is what is referred to as the GGP and can be described by just one free parameter, its variance (α^2). As it is known that the axial dipole component ($\overline{g_1^0}$) has been dominant throughout geological time (Cox, 1970), during times not associated with reversals a steady axial part of the dipole was superimposed. This introduced a second free parameter, $\overline{g_1^0}$. Under these assumptions, the palaeomagnetic observations of behaviour across the past 5 Ma could not be described. Predicted directional palaeosecular variation (PSV) distributions, determined from the model, failed to replicate observed distributions from palaeomagnetic data or differ in a manner that may be realistically expected when considering sources of bias (Constable & Parker, 1988). The differences in the observed and modelled behaviour were overcome by allowing the standard deviation of the dipole term ($\overline{g_1^0}$, g_1^1 and h_1^1) to deviate from that predicted by the GGP, and through the inclusion of a non-zero mean quadrupole term ($\overline{g_2^0}$). Subsequent construction of GGP models continued to modify the variance and/or power of asymmetric terms to better fit palaeomagnetic observations (e.g. Quidelleur & Courtillot, 1996; Constable & Johnson, 1999), until the introduction of a new parameter (Tauxe & Kent, 2004). This parameter, termed β, accounted for the larger variance in asymmetric Gauss coefficients than in the symmetric ones, simplifying the approach of previous studies (e.g. Quidelleur & Courtillot, 1996; Constable & Parker, 1988). Despite this improvement to the process, GGP models failed to simultaneously

reproduce the observed distributions of both field strength and PSV. This issue was addressed through, amongst other things, the incorporation of covariance between the Gauss coefficients, substantially improving the simultaneous reproduction of field strength and PSV distributions for the past 10 Ma (Bono et al., 2020).

Just one previous study has published parameters that describe an optimised GGP model for any interval outside of the last 10 Ma (Brandt et al., 2021). GGP models were generated for the Permo-Carboniferous Reversed Superchron (PCRS; ~318-265 Ma; Haldan et al., 2009; Opdyke & Channell., 1996) and the inclusion of the correlation coefficients of Bono et al. (2020) generated models that best described the palaeomagnetic observations. The improved misfit between the statistical models and the palaeomagnetic observations for the last 10 Ma and the PCRS, through the incorporation of the correlation coefficients, was used to suggest that the correlations between Gauss coefficients has remained unchanged throughout the geological past (Brandt et al., 2021; Bono et al., 2020). Further comparison between statistical models for the last 10 Myr and the PCRS, resulted in additional suggestions as to how aspects of the geomagnetic field may have evolved throughout geological time. It was proposed that the relationship between symmetric and antisymmetric families has remained unchanged, and that changes in total relative variability provide greater insight into changes in geomagnetic behaviour, with superchrons associated with reduced variability (Brandt et al., 2021). Recent advancements in our definitions of observed PSV behaviour have resulted in a near-complete record across the past ~320 Ma (Cromwell et al., 2018; Doubrovine et al., 2019; Engbers et al., 2022; Handford et al., 2021), providing an opportunity to generate GGP models associated with various time intervals. By generating covariant-style GGP models for these different time intervals, the suggestion that correlation coefficients have remained unchanged can be investigated further, and greater insight can be obtained into the evolution of the geomagnetic field throughout this time.

This study presents covariant-style GGP models that best describe palaeomagnetic field behaviour during the last 5 Myr, Miocene (23 - 5.3 Ma; Engbers et al., 2022; Ogg, 2012), CNS (126-84 Ma; Doubrovine et al., 2019), Pre-CNS & Post-PCRS (265-126 Ma; Handford et al., 2021; Doubrovine et al., 2019), and PCRS, utilising the VGP dispersion patterns of Handford et al. (2021) and Engbers et al. (2022), and a recent update to the PINT database (PINT v8.0.0, Bono et al., 2021). This represents the most comprehensive application of GGP models as a tool to investigate long-term geomagnetic field evolution. The robustness of these models is tested through the application of different quality filters to the palaeointensity observations and different methods of determining the cut-off angle for identifying outlying VGPs. Further discussion is then presented on the most appropriate models to describe the Pre-CNS & Post-PCRS, and the PCRS where data selection has greater effects. Finally, the implications of the preferred statistical models for the evolution of the geomagnetic field throughout geological time are discussed, with a particular focus on the consistent and contrasting aspects previously proposed by Brandt et al. (2021).

Background

The Introduction of GGP Models – CP88

Constable & Parker. (1988) overcame previous difficulties in modelling the non-dipole components of the geomagnetic field, by assuming that the non-dipole terms can be described by a zero-mean Gaussian distribution. This was an application of uniformitarianism from observations of the modern field. The power spectra across each degree was described using the form devised by Lowes. (1974) that is based on the spherical harmonic expansion of the potential gradient of the geomagnetic field, with applied weighting as a function of degree (l). The total power associated with the coefficients at each degree was known to experience continual small changes. This means that individual Gauss coefficients within each degree do not always sum to the same total, and so they were treated as being independent of one another. With the additional assumption that Gauss coefficients within the same degree were identically distributed, the variance of each Gauss coefficient could be expressed as

$$\sigma_l^2 = \frac{({}^{R_C}/_{R_E})^{2l}\alpha^2}{(l+1)(2l+1)}. \quad (5.1)$$

In which, R_C/R_E is the ratio of the core radius to that of the Earth (Constable & Parker, 1988) and α is an isotropic scaling term used to define the standard deviation for each Gauss coefficient (Bono et al., 2020; Constable & Parker, 1988).

The cumulative distribution function resulting from the description of the non-dipole terms of the geomagnetic field in Equation 5.1, was found to be consistent with that of the modern geomagnetic field by means of the Kolmogorov-Smirnov test.

The non-axial components of the dipole term (g_1^1 and h_1^1) were found to be within one standard deviation of the zero mean, and so the variation in these Gauss coefficients was ascribed to the same statistical behaviour as the non-dipole (Equation 5.1). As g_1^0 is considered to have been dominant throughout geological time, it could not be described by the same behaviour as g_1^1 and h_1^1, as was the case for coefficients of the same degree for the non-dipole field. The g_1^0 coefficient was ascribed to the giant Gaussian distribution but with a non-zero mean.

Refinement of the model was achieved by allowing deviation of specific Gauss coefficients from the GGP, in order to better describe directional PSV observations for the last 5 Ma. The preferred model (CP88), allowed departure of the standard deviation of coefficients of the first degree (σ_1) from that determined by the GGP. This was done under the reasoning that it was not a requirement to ascribe Gauss coefficients of the dipole term to the GGP for the ancient field, despite this approach being appropriate for the modern field (Constable & Parker, 1988).

A non-zero axial quadrupole term ($\overline{g_2^0}$) was also introduced (Constable & Parker, 1988), a deviation from the geocentric axial dipole (GAD) hypothesis (Tauxe, 2005).

CP88 then, was described by four free parameters

- $\overline{g_1^0}$ Mean magnitude of the axial dipole

- $\overline{g_2^0}$ Mean magnitude of the axial quadrupole
- σ_1^2 Variance of each of the dipole terms
- α^2 Variance of the GGP

A Major Refinement on GGP Models – TK03

A major limitation of CP88 was its inability to reproduce the observed increase in VGP dispersion with latitude for the last 5 Ma. Early proposed solutions, separately manipulated the variance of the dipole and quadrupole coefficients so that, for most coefficients, their behaviour was no longer described by the GGP (Constable & Johnson, 1999; Quidelleur & Courtillot, 1996). The resulting preferred models provided greater variance to the Gauss coefficients of the non-axial quadrupole relative to other terms. This was a targeted approach as it was known that asymmetric Gauss coefficients contributed more strongly to VGP dispersion at high latitudes than symmetric Gauss coefficients (McFadden et al., 1988).

In order to simplify this process, and remove the need for separate manipulation of the variance of individual Gauss coefficients, Tauxe & Kent. (2004) introduced a scaling term to incorporate into Equation 5.1 for the determination of the variance of asymmetric Gauss coefficients. This provided the greater variance required in the asymmetric terms in order to better reproduce the observed dependence of VGP dispersion on latitude.

$$(\sigma_l^m)^2 = \frac{({}^{R_C}/_{R_E})^{2l}\alpha^2\beta^2}{(l+1)(2l+1)}\ l-m:odd \tag{5.2}$$

Here, β is defined as the ratio of the variance in the asymmetric terms to that of the symmetric terms for a given degree.

$$\beta = \frac{\sigma_l^m(l-m:odd)}{\sigma_l^m(l-m:even)} \tag{5.3}$$

Again, the optimised model (TK03) aimed to describe secular variation for the last 5 Ma (Tauxe & Kent, 2004). Unlike the approach outlined for CP88, apart from having a non-zero mean, $\overline{g_1^0}$ was treated in the same manner as all other asymmetric Gauss coefficients, with its variance determined by Equation 5.2.

Covariant-style GGP Models – BB18 & BB18.Z3

More recently, Bono et al. (2020) incorporated the expected spatial correlations between Gauss coefficients that are of the same order and also belong to the same family of spherical harmonics (i.e. symmetric or asymmetric), into the GGP (Hulot & Gallet, 1996; Hulot & Bouligand, 2005). Previous geodynamo simulations (Bouligand et al., 2005; Sanchez et al., 2019) had revealed the covariance structure, as predicted by Hulot & Bouligand. (2005). Bono et al. (2020) determined the Pearson correlation coefficients of all pairs of Gauss coefficients from 21 high quality (Sprain et al., 2019) geodynamo simulations and used them to define a mean correlation matrix. They found that Gauss coefficients displayed covariance according to the previously observed structure (Bouligand et al., 2005; Sanchez et al., 2019), and that Gauss coefficients outside of this

structure appeared independent. This resulted in the following mean correlation coefficients (ϱ).

Table 5.1 :Mean correlation coefficients for select terms determined form dynamo simulations.

	(g_1^0, g_3^0)	(g_1^1, g_3^1)	(h_1^1, h_3^1)	(g_2^0, g_4^0)	(g_2^1, g_4^1)	(h_2^1, h_4^1)	(g_2^2, g_4^2)	(h_2^2, h_4^2)
$\boldsymbol{\rho}$	0.51	0.55	0.53	0.14	0.60	0.58	0.42	0.37

Note 5.1: Mean correlation matrix (ρ) used to define covariance matrix used in the covariant style models of Bono et al. (2020).

The mean correlation matrix was then used to define a covariance matrix (∑) using the following equation

$$\sum_{ij} = \sigma_i \sigma_j \rho_{ij} \tag{5.4}$$

in which the standard deviation of individual Gauss coefficients (i and j) were determined through the GGP in a similar manner to TK03 (Equations 5.1 & 5.2). The standard deviation of $\overline{g_1^0}$ was not determined by this process and was instead estimated from palaeointensity observations, introducing σ_1^0 as an additional parameter defining the statistical model.

The preferred model to describe PSV observations for the last 10 Ma, termed BB18, resulted in improved fits to the observed VGP dispersion pattern when compared with previous GGP models, with particular improvement at the highest latitudes (Bono et al., 2020). The model was also capable of simultaneously reproducing the observed VGP pattern and the observed field strength distribution for the last 10 Ma, something that previous GGP models had not successfully done. This was interpreted as a clear demonstration that covariance is a fundamental statistical property of the geodynamo, lending support to the inclusion of covariance in future GGP models (Bono et al., 2020).

A separate preferred model was presented in which zonal terms (m = 0) were assigned a non-zero mean. This was an attempt to better explain the PSV observations for the last 10 Ma through a deviation from GAD, in line with the original proposal of Constable & Parker. (1988). This model was termed BB18.Z3 and the introduction of non-zero mean $\overline{g_2^0}$ and $\overline{g_3^0}$ Gauss coefficients yielded improved fits to the observations when compared with BB18.

GGP Models of More Ancient Time Intervals – KRSM & KRSCovM

The previously described GGP models (CP88, TK03, BB18, BB18.Z3) all attempted to replicate PSV observations for the last 5 or 10 Ma. As the majority of the VGPs analysed for the last 10 Ma come from the last 5 Ma, for example 93% of the directional data within PSV10 (Cromwell et al., 2018) comes from the last 5 Ma, the models are essentially describing the same observations. At present, the only study to publish a GGP model that described PSV observations for a more ancient time interval, was that of Brandt et al. (2021), which focused on the PCRS.

Two preferred models for the PCRS were generated. The first was a simplified GGP model, termed KRSM, generated in accordance with the construction process of TK03. The second model utilised the correlation matrix of Bono et al. (2020) (Table 5.1) to generate a covariant-style GGP model that was termed KRSCovM. Both preferred models were selected based on the minimum residual sum of squares (RSS) misfit to the PSV statistic proposed by Brandt et al. (2020). This follows the method applied to the generation of the GGP model BCE19 (Brandt et al., 2020), that was constructed as an

update on TK03. The PSV statistic proposed by Brandt et al. (2020) is the standard deviation of equal area co-ordinates of distributions of palaeomagnetic directions rotated to the vertical, expressed in both the east-west and north-south directions (σ_E and σ_N). A flexible selection criterion was applied to the palaeomagnetic directional data, associated with the PCRS, in order to maximise the available data to construct the GGP models against (Brandt et al., 2021). A similar approach was taken when selecting palaeointensity data to define mean $\overline{g_1^0}$ for the PCRS, with no quality filtering applied.

The model KRSCovM resulted in lower misfits to the observed PSV distributions for the PCRS than model KRSM. This led to the suggestion that the correlations between Gauss coefficients of the geodynamo have remained unchanged throughout geological time (Brandt et al., 2021). The β parameter for the preferred models was found to be similar for KRSM and BCE19, and for KRSCovM and BB18, suggesting that the relationship between symmetric and antisymmetric families has remained broadly unchanged. This was somewhat unexpected as it was though that β might be enhanced during superchrons (Brandt et al., 2021). Instead, it was the total relative variability of the palaeomagnetic field, measured by α/g_1^0 or σ_1^0/g_1^0, that appeared to change throughout geological time, with lower values proposed for superchrons (Brandt et al., 2021).

This Study

The consistent and contrasting aspects of the geomagnetic field across geological time-scales, proposed by Brandt et al. (2021), demonstrate the power of utilising GGP models to assess long-term variations between different aspects of the geomagnetic field. The apparent relationship between total relative variability and the average reversal frequency across a given interval, could result in a better understanding of the long-disputed nature of the relationship between palaeointensity and reversal frequency (Doubrovine et al., 2019; Gubbins, 1987; Ingham et al., 2014; Prévot et al., 1990; Tarduno & Cottrell, 2005; Tauxe & Staudigel, 2004). Combined with the differences in observed directional PSV also being associated with relative variability, it suggests a potential framework to describe the relationships between the observable characteristics of the palaeomagnetic field most commonly used to describe its behaviour. Such relationships would provide a more complete definition of the palaeomagnetic field during time intervals where current understanding of one or more of these characteristics is lacking. In turn, hypothesis testing of proposed long-term geomagnetic field variations could be achieved from fewer observations. The link between the geodynamo mechanism and long-term variations, then providing greater insight into the evolution of the Earth's deep interior.

The proposed relationships of Brandt et al. (2021), require further validation as they were based on a comparison between optimised GGP models for just two time intervals, the last 10 Myr and the PCRS. The models themselves were also constructed through different approaches. The BB18 family of models were built around the PSV10 database that applied selection criteria to remove low quality palaeomagnetic data. Mild selection criteria were also applied to the palaeointensity data (Bono et al., 2020), though need for a more thorough examination of the palaeointensity record was noted (Bono et al., 2020). Finally, model optimisation was conducted by reducing the misfit between the modelled and observed equatorial VGP dispersion. In contrast, the directional database constructed for KRSM family of models used a more flexible selection criteria, with no filtering of the palaeointensity data, and model optimisation reduced the misfit between the observed and modelled directional PSV statistic of Brandt et al. (2020).

The differences in data selection could be particularly important. Low quality directional data has the potential to bias GGP models and dominate both shape and scale in directional analyses and VGP dispersion analyses (Bono et al., 2020; Brandt et al., 2021). This is apparent in the more extreme PSV behaviour that was observed for the PCRS by Handford et al. (2021), through the application of stricter selection criteria when compared with that observed by Brandt et al. (2021). The lack of filtering of palaeointensity data is of added significance for the PCRS, as previous studies have demonstrated that the average virtual (axial) dipole moment (V(A)DM) for the PCRS, from which mean $\overline{g_1^0}$ is calculated, can vary significantly depending on the filtering applied to the compiled palaeointensity data (e.g. Hawkins et al., 2021).

This study constructs new preferred GGP models for the last 5 Myr and the PCRS through a consistent approach, in order to facilitate a more direct comparison. The same approach is also used to generate preferred GGP models for the Miocene, CNS, and combined Pre-CNS and Post-PCRS, utilising recent advances in the understanding of the evolution of PSV behaviour over the last 320 Myr. These models allow further investigation of the consistent and contrasting aspects of the geomagnetic field proposed by Brandt et al. (2021). The robustness of the optimised GGP models to the chosen palaeointensity data is investigated by utilising a range of selection criteria. The uniqueness of the GGP models for each interval is also explored to assess the need for different GGP models to explain the different range of palaeomagnetic observations associated with the studied intervals.

Method

Data Selection

The distributions of observed VGP dispersion, used to determine Model G shape parameters in Handford et al. (2021), were used to construct preferred GGP models. Again, analysis of the last 10 Myr was replaced by analysis of the last 5 Myr and the Miocene, as was the approach in **Chapter 3** when estimating axial dipole dominance values. This means that palaeomagnetic data were subject to selection criteria 1-8 of Handford et al. (2021). The preferred approach of determining outlying VGPs was through the use of the iterative Vandamme cut-off (Vandamme, 1994), but the effects of using a fixed-angle cut-off of 45° were also investigated. In contrast with studies generating GGP models for the last 5 or 10 Myr, estimates of VGP dispersion are presented for given localities, not grouped into latitudinal bins (e.g. Cromwell et al., 2018). Grouping estimates of VGP dispersion into latitudinal bins is not appropriate for more ancient time intervals due to the difficulty constraining the full extent of localised block rotations (Engbers et al., 2022) For continuity, this approach has been extended to the more recent time intervals studied. The decision was made to investigate the Pre-CNS and Post-PCRS as one continuous time interval due to the near-identical PSV behaviour observed in Handford et al. (2021) and the continued lack of palaeointensity data representing the Post-PCRS. This decision, and its implications, will be discussed at greater length.

Palaeointensity data were obtained from queries of a recent update to the PINT database (v8.0.0, Bono et al., 2021), using the previously defined dates for each studied time interval. Reliable palaeointensity estimates obtained from **Chapters 3 & 4** were also included for the Pre-CNS & Post-PCRS compilation. Palaeointensity data were subject to a range of selection criteria, with preferred GGP models generated for each. The criteria were as followed:

1. **QPI1** – Minimal selection criteria applied, all V(A)DM estimates with a Q_{PI} score ≥ 1 included.

2. **QPI3** – V(A)DM estimates with an assigned Q_{PI} score ≥ 3.

3. **NINT3** – V(A)DM estimates with a Q_{PI} score ≥ 1 based on at least 3 specimen level palaeointensity estimates.

4. **AAM –** fulfilment of the Q_{AGE}, Q_{ALT}, & Q_{MD} criteria (Biggin & Paterson, 2014; Bono et al., 2021).

QPI1 acts as a baseline for all other models to be compared against and assesses the need for quality filtering of palaeointensity data. QPI3 was chosen because it is a commonly used selection criteria, as a compromise between reducing the effects of undesirable biases from low-quality data and retaining sufficient data to perform meaningful statistical analysis (Biggin & Paterson, 2014; Kulakov et al., 2019). NINT3 uses the minimum number of specimen-level palaeointensity estimates required to provide insight into the reliability of the site-level average. The number of required estimates is variable depending on the chosen selection criteria but is always at least three specimens (e.g. Biggin et al., 2009). Whilst recognising that this minimum number is often five specimens, it has previously been shown that the majority of multi-specimen palaeointensity estimates from fewer than five specimens pass Q_{STAT} (Biggin et al., 2015). Therefore, the decision was made to filter the data by the lower cut-off. Finally, the requirement to pass Q_{AGE}, Q_{ALT}, & Q_{MD} reflects one of two prioritised QPI criteria when assessing long-term variations in geomagnetic field strength (Kulakov et al., 2019). The other requires that Q_{AGE}, Q_{ALT}, & Q_{STAT} are fulfilled but through this, the total number of palaeointensity data available for analysis drops significantly (Hawkins et al., 2021; Kulakov et al., 2019).

Model Construction

Preferred statistical models were constructed as covariant-style GGP models, due to the consistent improvement that they produce to the palaeomagnetic observations (Bono et al., 2020; Brandt et al., 2021). As the majority of the time intervals that are the subject of this study cover tens of millions of years, models were constructed with zero-mean quadrupole terms under the reasonable assumption that the GAD hypothesis is maintained. This also aids model simplicity. The variance of the symmetric terms was determined by Equation 5.1, and antisymmetric terms Equation 5.2. The mean correlation matrix of Bono et al. (2020) (Table 5.1) defined the covariance matrix that scaled the determined variance values (Equation 5.4).

Determination of optimised model parameters was done in accordance with the approach of Bono et al., (2021). Estimates of $\overline{g_1^0}$ were determined directly from the palaeointensity observations using the following equation

$$g_1^0 = \frac{\mu_0 V(A)DM}{4\pi {R_E}^3} \quad (5.5)$$

where the g_1^0 Gauss coefficient is that which would result in the observed median V(A)DM, and μ_0 is the permeability of free space. This assumes that the VDM is entirely described by the dipole field and that time-averaged equatorial terms have means of zero (Bono et al., 2021).

The latitudinal dependence of VGP dispersion is used to minimise the misfit between the statistical model and the palaeomagnetic observations, by utilising an observed relationship between $\overline{g_1^0}$ and α for a given value of β (Bono et al., 2021). As g_1^0 is predefined by palaeointensity observations, β can be varied and the corresponding α value easily determined. Therefore, β is systematically varied between 1 and 5 and the Chi-squared misfit (χ^2) between the modelled and the observed VGP dispersion is minimised.

The preferred standard deviation of $\overline{g_1^0}$ is estimated by varying σ_1^0 and minimising the maximum absolute difference between the empirical cumulative distribution function (ECDF) of the predicted VDM distribution and that of the observed VDM distribution. This maximum absolute difference is referred to as the Kolmogorov-Smirnov statistic (D_{KS}). The noise present in the palaeointensity dataset is accounted for in the form of the median percentage error, assuming a Gaussian distribution. Determination of the standard deviation during this process accounts for sample size, following the approach of Paterson et al. (2010).

Comparing Models with Observations

In order to determine the goodness of fit between the latitudinal dependence of VGP dispersion associated with the preferred model and that of the palaeomagnetic observations, values of the χ^2 statistic were calculated (Pearson, 1900). Treating the estimates of observed VGP dispersion as absolute values, the χ^2 statistic can be calculated following the traditional approach

$$\chi^2 = \sum_{i=1}^{N} \frac{(O_i - E_i)^2}{E_i} \quad (5.6)$$

in which O_i represents the ith of N number of observations, in this case VGP dispersion, and E_i is the corresponding model prediction.

The observed values of VGP dispersion are in fact estimated values, and so a statistic is required that allows for weighting by observed variance (Equation 5.7; Bono et al., 2021; Doubrovine et al., 2019). As outlined in Handford et al. (2021), 95% confidence intervals of estimated VGP dispersion values were determined through use of a non-parametric bootstrap. The variance of S_B is estimated from the 95% confidence limits, assuming normally distributed uncertainties (Bono et al., 2021).

$$\sigma_i^2 = \left(\frac{U95_i - L95_i}{2}\right)^2 \quad (5.7)$$

A weighted Chi-squared test statistic (χ^2_w) can then be calculated following the approach of Doubrovine et al. (2019)

$$\chi_w^2 = \sum_{i=1}^{N} \frac{(O_i - E_i)^2}{\sigma_i^2} \quad (5.8)$$

In this study, both χ^2 statistics were calculated in order to explore the significant differences that occur through the choice of statistic used. Both statistics were normalised (L), according to the number of S_B observations, to facilitate greater ease of comparison between the statistics generated to describe the goodness of fit for the different time intervals studied. This follows the approach of Parker. (1994)

$$L = \sqrt{\frac{\chi^2}{N}} \tag{5.9}$$

where a value of $L \sim 1$ would be expected for a model that provides a good description of the observations.

The comparison between the predicted VDM distribution from the models and the observed VDM distribution makes use of the two-sample Kolmogorov-Smirnov test. This is a non-parametric test that evaluates the difference between the cumulative distribution functions of two samples, to assess the likelihood of them originating from the same distribution. Results are reported in the form of two test statistics, D_{KS} and P_{KS}. Determination of D_{KS} has been outlined, taking noise of the distribution into consideration. The second statistic, P_{KS}, reports the probability of the occurrence of a D_{KS} value, with a magnitude greater than or equal to the observed D_{KS} value, occurring between two samples from the same distribution. A greater P_{KS} value represents an increased probability that the samples originated from the same distribution. A complete overview of the construction process of preferred statistical models can be found in the supporting information (Figure D.1).

The ability for a model constructed around palaeomagnetic observations from a given time interval to reproduce the palaeomagnetic observations associated with each other studied time interval was also assessed. In this way, attempts were made to quantify the need for unique GGP models for each studied time interval. The methods outlined above were also used in this assessment.

Results

Preferred Model Construction

The optimised values of the free parameters, defining each statistical model (α, β, $\overline{g_1^0}$, and σ_1^0), are presented in Tables 5.2 to 5.6, alongside the Chi-squared and Kolmogorov-Smirnov test statistics used to assess the goodness of fit between the modelled and observed palaeomagnetic distributions. Chi-squared values were also calculated to determine the goodness of fit of the corresponding Model G description (Tables 5.2-5.6). Model G fits were generated as a visual comparison with the predictions from GGP models as, despite their lack of statistical significance (Doubrovine et al., 2019), such descriptions are still widely used to model the palaeomagnetic observations (de Oliveira et al., 2021; Engbers et al., 2022).

For each studied time interval, estimates of VGP dispersion, through the application of the Vandamme cut-off (Vandamme, 1994), are plotted against palaeolatitude (Figure 5.1). Alongside these are the best-fitting models following the Model G description (McFadden et al., 1988), and predictions of the latitudinal dependence of VGP dispersion

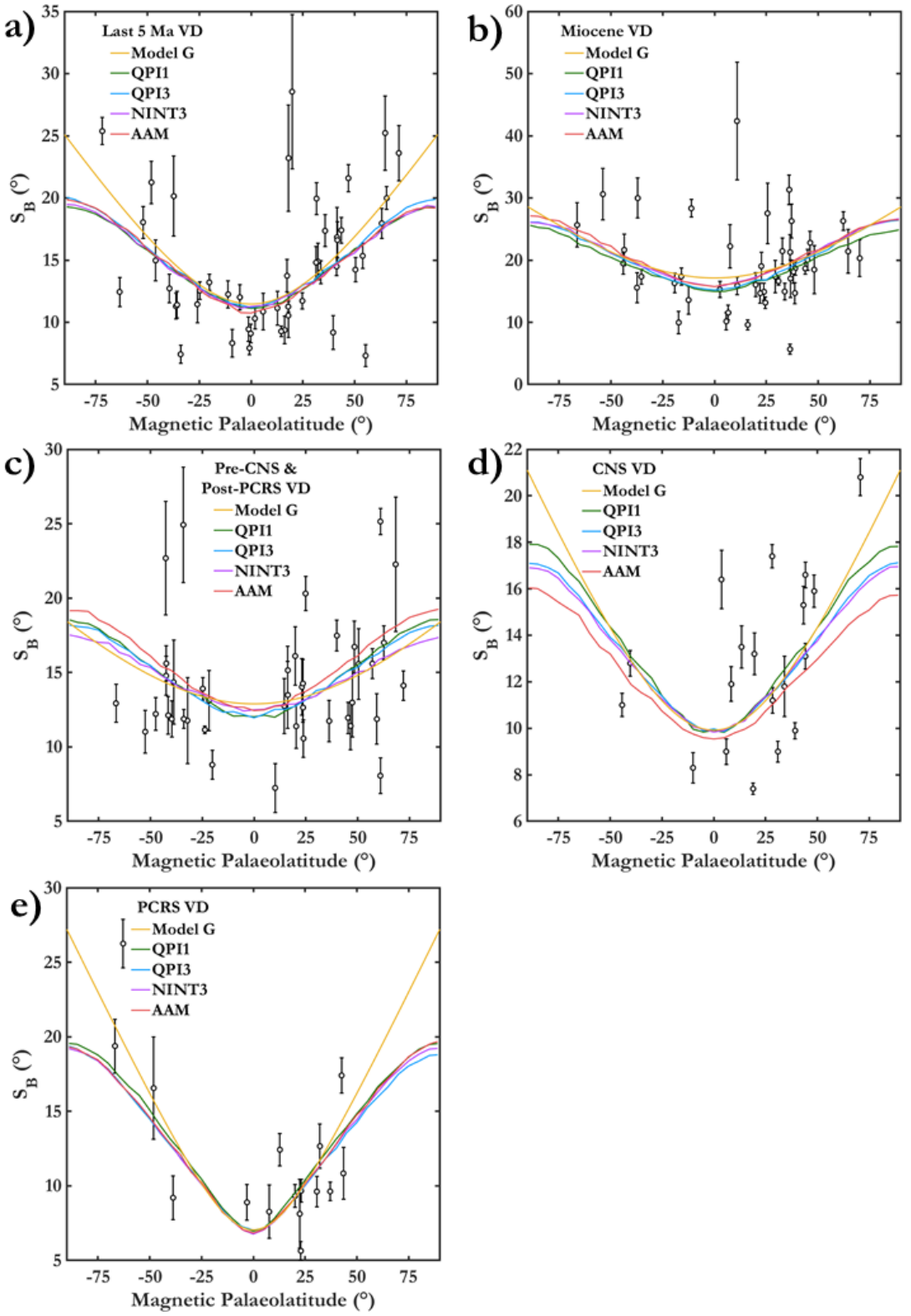

Figure 5.1: Estimates of VGP dispersion versus estimated magnetic palaeolatitude. Determined from palaeomagnetic data after the application of selection criteria 1-8 of Handford et al. (2021) and the Vandamme cut-off. Model G fit to the distribution is plotted alongside predicted VGP dispersion distributions from statistical models constructed with each of the palaeointensity filtering criteria outlined in the main text. This is done for each of the studied time intervals a) last 5 Ma, b) Miocene, c) CNS, d) Pre-CNS & Post-PCRS, e) PCRS.

from the optimised GGP models, generated using each of the outlined palaeointensity selection criteria (Figure 5.1). There were two main categorisations when describing the differences between the Model G fit to the observations and the predicted latitudinal dependence of VGP dispersion, as suggested by the statistical models. The first can be characterised by an agreement in the equatorial S_B values of the model prediction and the Model G fit, with increasing deviation between the two with increasing latitude (Figure 5.1a, d, e). The second observed behaviour is characterised by a lower prediction of equatorial S_B from the statistical models, and improved agreement with Model G predictions at high latitudes (Figure 5.1b, c).

The general shape of the VGP dispersion curves predicted by the GGP models remains the same, regardless of the palaeointensity selection criteria used. Variability primarily comes from their predicted equatorial S_B values (Figure 5.1). Agreement between the different predicted distributions of VGP dispersion varies between the studied time intervals (Figure 5.1, Tables 5.2-5.6) but it is their ability to describe the palaeomagnetic observations that is of greater importance. Weighted Chi-squared (L_W) values are consistent within each studied time interval (Figure 5.2a, Tables 5.2-5.6), suggesting that the choice of palaeointensity selection criteria has little bearing on the optimised GGP models' ability to describe the VGP dispersion observations. A much greater difference was observed in the models' ability to simultaneously describe the observed palaeointensity distribution. This is reflected in the P_{KS} statistics (Figure 5.2b, Tables 5.2-5.6).

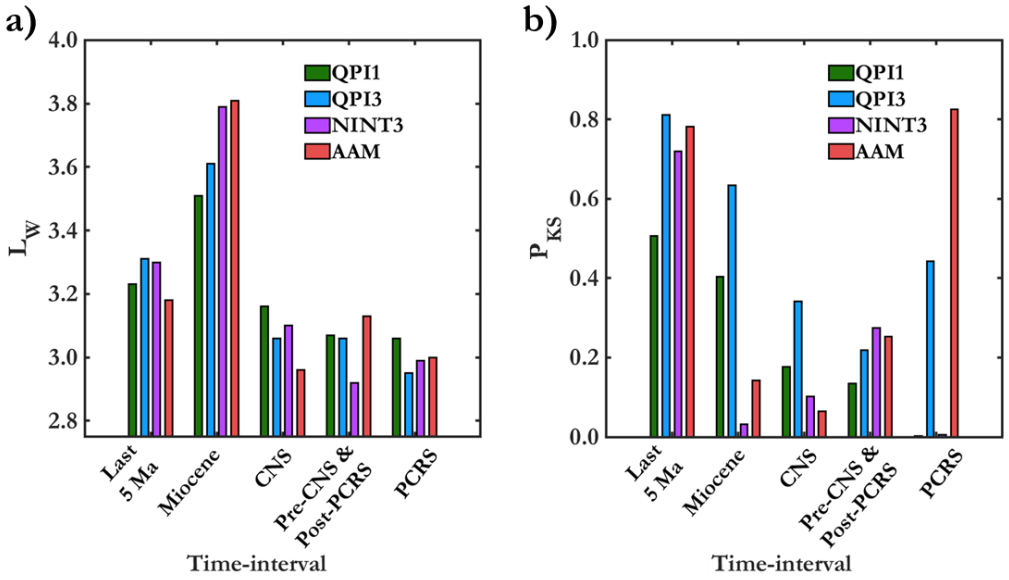

Figure 5.2: Goodness of fit statistics plotted for the statistical models generated for each time interval following the application of each of the palaeointensity criteria outlined in the main text. a) L_W b) P_{KS}.

A low P_{KS} statistic could suggest that the GGP model is not an accurate representation of the geomagnetic field during the time interval being studied, or that filtering of the palaeointensity data has resulted in an observed palaeointensity distribution that is not a true representation of the palaeomagnetic field. There is a wide range of P_{KS} values associated with optimised models within each time interval, with the exception of the last 5 Ma and the Pre-CNS & Post-PCRS (Figure 5.2b, Tables 5.2-5.6). For the CNS, predictions from models constructed using palaeointensity data filtered through NINT3

and AAM can both be rejected at 90% significance (Table 5.4), for the PCRS this is true after the application of QPI1 and NINT3 (Table 5.6). For both time intervals, the observed distributions that result in low P_{KS} values, appear very different to the observed distributions within the same time interval that result in higher P_{KS} values (Figure 5.2b, Figure 5.3c, e, Table 5.4, & Table 5.6). This would suggest that low P_{KS} values are a result of a non-representative observed palaeointensity distribution.

For the Miocene, the observed palaeointensity distributions show greater consistency between one another than displayed by the predicted distributions (Figure 5.3b). This suggests that, where P_{KS} values are low, the modelled distribution does not accurately represent Miocene behaviour. The primary difference in the construction of these models appears to be an increased estimated $\overline{g_1^0}$ term (Table 5.3), as the observed VGP dispersion distributions are identical and palaeointensity distributions are similar (Figure 5.3b). Incidentally, the filtering criteria that produced the worst fitting palaeointensity distributions (NINT3 & AAM, Figure 5.2b) also produced the worst fitting VGP dispersion distributions (Table 5.3). It may be that higher estimated $\overline{g_1^0}$ terms produce GGP models less capable of reproducing palaeomagnetic observations, indicating a preference for a weak field to best describe palaeomagnetic observations of the Miocene.

Regardless of the reasoning behind poor agreement between the observed and predicted palaeointensity distributions, constructing statistical models around palaeointensity data filtered by QPI3 appeared to most consistently result in improved fits. In general, the choice of palaeointensity selection criteria had little effect on the ability for statistical models to replicate observed distributions of VGP dispersion (Figure 5.2a). The exception to this was the use of NINT3 and AAM data in the construction of a statistical model for the Miocene (Figure 5.2a). Greater differences were observed in the models' ability to predict the palaeointensity distributions (Figure 5.2b). QPI3 filtering resulted in the best goodness of fit, between predictions and observations, for the last 5 Ma, Miocene, and CNS (Figure 5.2b). For the Pre-CNS & Post-PCRS, the choice of selection criteria had little effect on the goodness of fit statistic (Figure 5.2b), and for the PCRS the application of QPI3 was one of just two criteria that resulted in statistically meaningful predictions of palaeointensity distribution (Figure 5.2b, Table 5.6). The ability of these statistical models to simultaneously reproduce observed palaeointensity and VGP dispersion distributions, suggests that the incorporation of the covariance matrix was appropriate for all studied time intervals. Due to its consistently high goodness of fit (Figure 5.2b), GGP models constructed with palaeointensity data filtered by QPI3 were selected to assess relationships between the studied time intervals.

Following this, statistical models were generated after the application of QPI3 to palaeointensity observations, and the application of a fixed 45° cut-off angle to the VGP observations. Through this process, the robustness of the statistical models to the choice of cut-off angle was assessed. Model parameters for the last 5 Ma and the Miocene were almost unchanged (Tables 5.2 & 5.3). This could be due to the greater tectonic control associated with younger units, and suggest that some of the VGP dispersion not removed by the Vandamme cut-off is artificial for older intervals. Of the remaining time intervals, the superchrons experience the greatest change in model parameters between the use of the two cut-off approaches (Tables 5.4-5.6). The differences between parameters are still

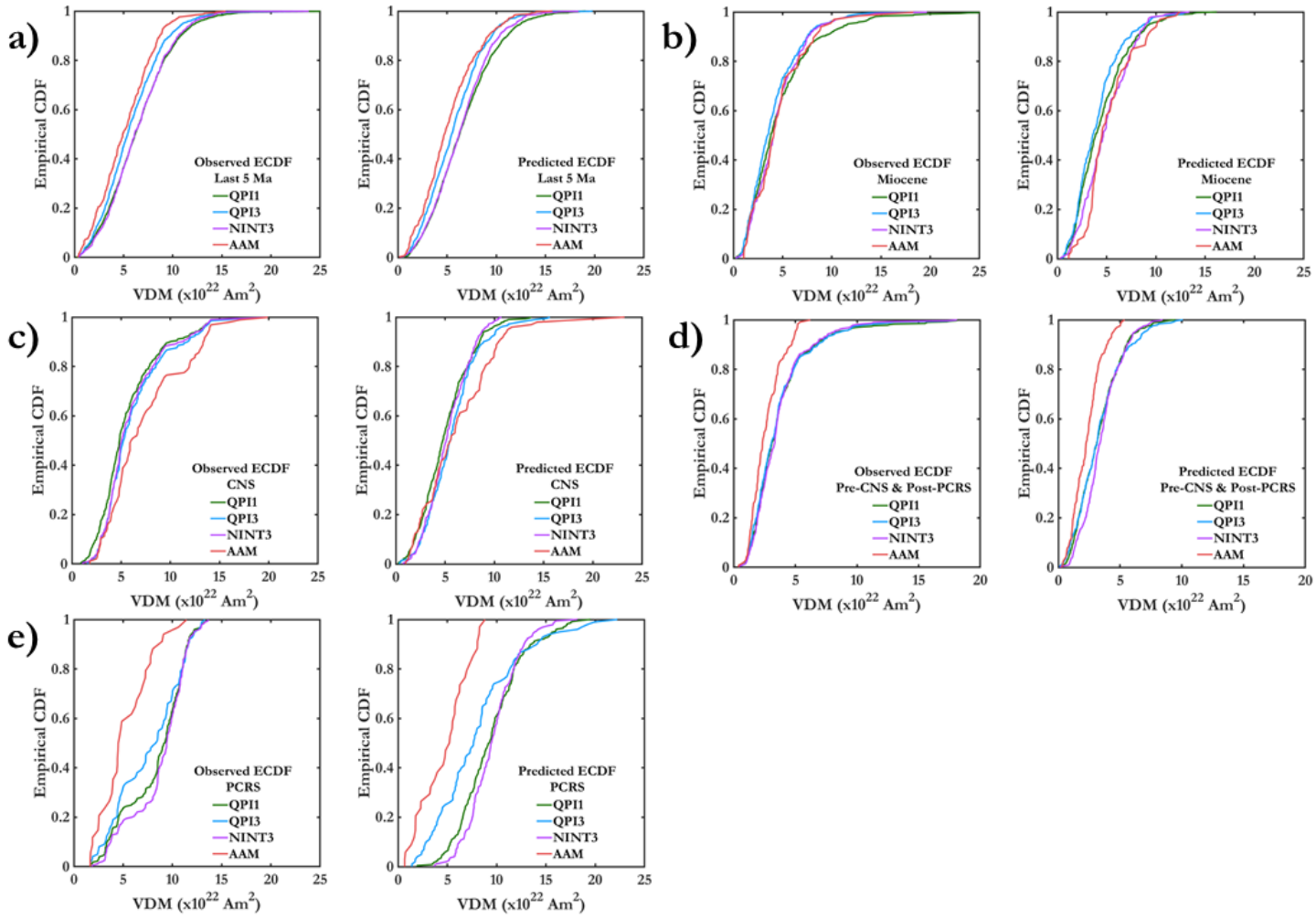

Figure 5.3: Observed empirical CDF and predicted empirical CDF of palaeointensity distributions. Displayed for models generated after the application of the Vandamme cut-off, in VGP dispersion calculations, and each of the palaeointensity criteria outlined in the main text. a) last 5 Ma, b) Miocene, c) CNS, d) Pre-CNS, e) PCRS.

Table 5.2: Model parameters and goodness of fit statistics for optimised statistical models representing the Last 5 Ma.

Model	NINT	α	β	g_1^0	σ_1^0	χ^2	L	χ_w^2	L_w	D_{KS}	P_{KS}	α/g_1^0	RSD
Model G	-	-	-	-	-	64.2	1.16	557.3	3.41	-	-	-	-
QPI1-VD	1711	13.34	2.35	-23.90	12.08	69.8	1.21	500.1	3.23	0.028	0.506	-0.56	-0.51
QPI3-VD	908	11.70	2.47	-20.89	11.12	68.1	1.19	524.7	3.31	0.030	0.811	-0.56	-0.53
NINT3-VD	941	13.18	2.37	-23.63	11.38	69.8	1.21	521.2	3.30	0.032	0.719	-0.56	-0.48
AAM-VD	342	10.58	2.51	-18.99	11.30	70.5	1.21	484.9	3.18	0.050	0.782	-0.56	-0.60
QPI3-45°	908	11.66	2.69	-20.89	11.02	41.6	0.94	347.4	2.72	0.030	0.698	-0.56	-0.53

Note 5.2: Model parameters α, β, g_1^0, (σ_1^0) defining the statistical models that were optimised to palaeomagnetic observations assigned to the Last 5 Ma, where σ_1^0 represents the standard deviation of g_1^0. VD denotes that virtual geomagnetic pole (VGP) dispersion was calculated with the application of the Vandamme cut-off (Vandamme. 1994), 45° indicates the use of a fixed angle cut-off of 45°. The first part of the model name denotes the filtering of palaeointensity data utilised in model construction, as defined within the main text. Chi squared values (χ^2) measure the misfit between the VGP dispersion pattern predicted by the corresponding statistical model, and that observed from palaeomagnetic data used in the model construction. L represents normalised χ^2 values. χ_w^2 denotes the weighted chi-squared value, and L_w the corresponding normalised value. P_{KS} and D_{KS} display the Kolmogorov-Smirnov test statistics measuring the goodness of fit between the empirical cumulative distribution function (ECDF) of virtual (axial) dipole moment (V(A)DM) predicted by the corresponding statistical model, and that observed from palaeointensity data used in the model construction. NINT denotes the number of V(A)DM values used in the model construction. RSD (σ_1^0/g_1^0).

Table 5.3: Model parameters and goodness of fit statistics for optimised statistical models representing the Miocene.

Model	NINT	α	β	g_1^0	σ_1^0	χ^2	L	χ_w^2	L_w	D_{KS}	P_{KS}	α/g_1^0	RSD
Model G	-	-	-	-	-	100.3	1.51	668.4	3.90	-	-	-	-
QPI1-VD	399	12.91	2.07	-14.69	11.89	115.9	1.62	542.9	3.51	0.063	0.403	-0.88	-0.81
QPI3-VD	265	11.77	2.14	-13.53	9.96	111.4	1.59	572.4	3.61	0.064	0.633	-0.87	-0.74
NINT3-VD	196	14.32	2.10	-15.86	9.71	104.4	1.54	630.4	3.79	0.143	0.032	-0.90	-0.61
AAM-VD	67	14.31	2.15	-15.93	9.67	104.7	1.54	637.9	3.81	0.194	0.142	-0.90	-0.61
QPI3-45°	265	11.71	2.40	-13.53	9.87	30.3	0.83	137.2	1.77	0.136	0.014	-0.87	-0.73

Note 5.3: See note of Table 5.2 for description.

Table 5.4: Model parameters and goodness of fit statistics for optimised statistical models representing the Cretaceous Normal Superchron (CNS).

Model	NINT	α	β	g_1^0	σ_1^0	χ^2	L	χ_w^2	L_w	D_{KS}	P_{KS}	α/g_1^0	RSD
Model G	-	-	-	-	-	13.1	0.83	178.3	3.06	-	-	-	-
QPI1-VD	307	8.87	2.60	-18.72	8.97	13.5	0.84	189.4	3.16	0.088	0.177	-0.47	-0.48
QPI3-VD	210	9.64	2.33	-20.29	8.45	13.7	0.85	178.5	3.06	0.090	0.341	-0.48	-0.42
NINT3-VD	215	9.35	2.29	-19.72	7.67	14.0	0.86	182.7	3.10	0.116	0.102	-0.47	-0.39
AAM-VD	98	11.19	2.30	-23.59	14.95	16.0	0.92	166.2	2.96	0.184	0.064	-0.47	-0.63
QPI3-45°	210	10.87	1.92	-20.29	8.44	17.3	0.95	180.6	3.08	0.100	0.232	-0.54	-0.42

Note 5.4: See note of Table 5.2 for description.

Table 5.5: Model parameters and goodness of fit statistics for optimised statistical models representing the combined Pre-Cretaceous Normal Superchron (CNS) & Post Permo-Carboniferous Reversed Superchron (PCRS).

Model	NINT	α	β	g_1^0	σ_1^0	χ^2	L	χ_w^2	L_w	D_{KS}	P_{KS}	α/g_1^0	RSD
Model G	-	-	-	-	-	42.9	1.02	396.2	3.11	-	-	-	-
QPI1-VD	435	7.53	1.87	-11.99	6.62	42.2	1.01	385.6	3.07	0.078	0.134	-0.63	-0.55
QPI3-VD	245	7.49	1.79	-11.84	6.97	42.8	1.02	383.6	3.06	0.094	0.219	-0.63	-0.59
NINT3-VD	321	8.22	1.48	-12.89	6.48	56.7	1.18	349.4	2.92	0.078	0.274	-0.64	-0.50
AAM-VD	128	5.72	1.84	-9.05	4.46	69.6	1.30	402.6	3.13	0.125	0.253	-0.63	-0.49
QPI3-45°	245	8.20	1.78	-11.84	7.24	31.4	0.88	260.2	2.52	0.078	0.438	-0.69	-0.61

Note 5.5: See note of Table 5.2 for description.

Table 5.6: Model parameters and goodness of fit statistics for optimised statistical models representing the Permo-Carboniferous Reversed Superchron (PCRS).

Model	NINT	α	β	g_1^0	σ_1^0	χ^2	L	χ_w^2	L_w	D_{KS}	P_{KS}	α/g_1^0	RSD
Model G	-	-	-	-	-	11.4	0.84	133.0	2.88	-	-	-	-
QPI1-VD	229	11.49	4.66	-35.80	8.75	14.1	0.94	149.7	3.06	0.175	0.002	-0.32	-0.24
QPI3-VD	100	10.34	4.51	-32.43	13.99	14.6	0.96	139.5	2.95	0.120	0.443	-0.32	-0.43
NINT3-VD	195	11.67	4.54	-36.40	4.90	15.0	0.97	143.0	2.99	0.169	0.006	-0.32	-0.13
AAM-VD	34	5.68	4.84	-17.68	9.83	14.8	0.96	143.8	3.00	0.147	0.825	-0.32	-0.56
QPI3-45°	100	12.39	4.01	-32.43	13.82	10.8	0.82	74.3	2.16	0.140	0.261	-0.38	-0.43

Note 5.6: See note of Table 5.2 for description.

Table 5.7: Model parameters and goodness of fit statistics for optimised statistical models representing the time interval between 265 and 143 Ma.

Model	NINT	α	β	g_1^0	σ_1^0	χ^2	L	χ_w^2	L_w	D_{KS}	P_{KS}	α/g_1^0	RSD
265-143 Ma VD	184	6.66	2.16	-10.38	4.88	45.3	1.12	41.1	3.50	0.098	0.326	-0.64	-0.47

Note 5.7: See note of Table 5.2 for description.

Table 5.8: Comparison of model parameters defining the different statistical models proposed for the Permo-Carboniferous Reversed Superchron (PCRS).

Model	NINT	α	β	g_1^0	σ_1^0	χ^2	L	χ_w^2	L_w	D_{KS}	P_{KS}	α/g_1^0	RSD
QPI3-VD	100	10.34	4.51	-32.43	13.99	14.6	0.96	139.5	2.95	0.120	0.443	-0.32	-0.43
KRSCovM*	-	10.60	3.10	28.90	8.10	166.6	1.69	355.3	2.48	-	-	0.37	0.28
KRSCovM-VGP	-	14.70	1.68	28.90	8.10	95.1	1.28	365.2	2.51	-	-	0.51	0.28
KRSCovM-VGP-QPI3	100	16.53	1.81	-32.43	14.37	94.7	1.28	369.4	2.52	0.190	0.047	-0.51	-0.44

*Note 5.8: See note of Table 5.2 for description. *Parameters obtained from Brandt et al., (2021).*

relatively small, however. For all time intervals, the goodness of fit to the predicted VGP dispersion distribution is improved (Tables 5.2-5.6). This is to be expected as there is less extreme outlying data for the modelled distribution to be compared against (Figure D.2). The use of the Vandamme cut-off is preferred going forward as a more cautious approach against the removal of VGP dispersion due to secular variation (Biggin et al., 2008).

Comparison Between Time intervals

A comparison of $\alpha/\overline{g_1^0}$ and the relative standard deviation of $\overline{g_1^0}$ ($RSD = \sigma_1^0/\overline{g_1^0}$), between QPI3-VD models, suggests that total relative variability of the geomagnetic field has varied across geological time, and that reduced variability occurred during superchrons (Figure 5.4; Tables 5.2-5.6). Models optimised for a given VGP dispersion distribution produced consistent estimates of $\alpha/\overline{g_1^0}$, regardless of the utilised palaeointensity observations (Tables 5.2-5.6). This was because $\alpha/\overline{g_1^0}$ displays a very strong relationship with equatorial VGP dispersion, which in this study was approximated by the Model G *a* parameter (Figure 5.5). This is not the case for estimates of RSD and, depending on the palaeointensity selection used, RSD values are not always lower during superchrons than for times of reversals (e.g. for the AAM criteria, Tables 5.2-5.6). This was not observed by Brandt et al. (2021), when $\overline{g_1^0}$ was varied, because preferred models were not minimised to palaeointensity distributions, instead σ_1^0 was predicted from the GGP.

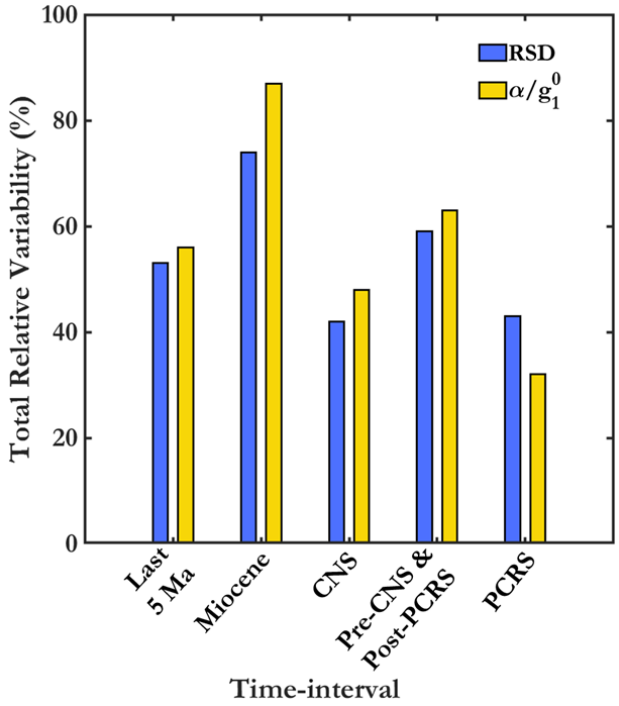

Figure 5.4: Estimates of total relative variability presented for each studied time interval, RSD (σ_1^0/g_1^0) and α/g_1^0. Estimates utilise model parameters of QPI3-VD statistical models.

Estimated values of the β parameter are broadly consistent throughout the last 5 Ma, Miocene, CNS, and Pre-CNS & Post-PCRS (2.47, 2.14, 2.33, 1.87, Tables 5.2-5.5), with a much higher value estimated for the PCRS (4.51, Table 5.6). This would suggest that the relationship between symmetric and antisymmetric families was different during the

PCRS, more so than for any other time interval over the last 320 Ma. The β parameter displays little variation for models optimised against palaeointensity observations subjected to the range of different selection criteria. Therefore, the choice of palaeointensity criteria does not change the observed trend in β throughout geological time. Likewise, the preference of using the Vandamme cut-off over a fixed 45° cut-off when estimating VGP dispersion, does not change any of the long-term trends identified.

In the absence of errors associated with the parameters defining statistical models (Tables 5.2-5.6), the goodness of fit was assessed between palaeomagnetic observations from a given time interval and predictions from optimised GGP models for each other time interval. This process assessed the need for different statistical models to describe the different palaeomagnetic observations associated with each studied time interval. This facilitated an assessment of the likelihood of the previously discussed differences between the parameters defining each statistical model, being representative of differences in aspects of palaeomagnetic field behaviour. Often, the different GGP models could predict VGP dispersion distributions as well as models optimised to the observations but predictions of palaeointensity distributions were significantly worse, as indicated by similar L_W values and vanishingly small P_{KS} values, respectively (Tables D.2-D.6). This further highlights the lack of statistical significance in predicted models of variation in VGP dispersion with latitude, and demonstrates that palaeointensity dispersions display much greater variability across geological times. This also suggests that unique statistical models are required to most accurately describe palaeomagnetic observations for each studied time interval, strengthening the corresponding implications regarding geomagnetic field evolution.

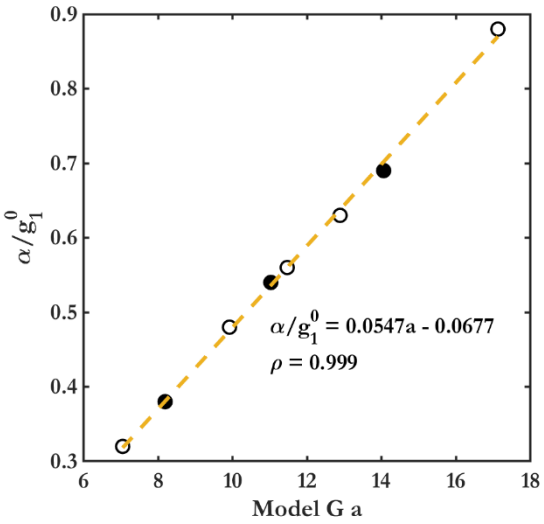

Figure 5.5: Relationship between Model G a parameter and α/g_1^0 from the time intervals analysed in this study. Model G a parameter, defining Model G fits to VGP dispersions, versus α/g_1^0 that defines the corresponding optimised statistical model. Application of the Vandamme cut-off (open circle) and 45° cut-off where values differed (filled circle). ρ is the Pearson correlation coefficient.

Statistical models not constructed around PCRS observations did struggle to predict the observed VGP dispersion distribution of the PCRS. The closest to matching the goodness of fit of the PCRS model was that of the CNS but L_W was still greater by ~0.5 (Table D.5), further emphasising the unique VGP dispersion distribution of the PCRS (Handford et al., 2021). That being said, the model optimised to PCRS observations predicted the observed VGP dispersion distribution of the CNS closer than the model

optimised to CNS observations. This could suggest that directional PSV during the two superchrons was not as different as suggested by Model G fits, again highlighting the limits of Model G.

Discussion

Prior to greater discussion on the implications of these findings within the context of the evolution of the geomagnetic field across the last 320 Ma, the robustness and appropriateness of the preferred models is explored for the Pre-CNS & Post-PCRS, and for the PCRS. The construction of models that describe the Pre-CNS & Post-PCRS assumed that behaviour of the geomagnetic field was comparable during the two time intervals. The suitability of this assumption is first explored and an alternative model is proposed. Secondly, the preferred model for the PCRS is compared with KRSCovM (Brandt et al., 2021), and the effects of the chosen palaeointensity filtering is explored. The discussed similarities and differences between models of different time intervals was based on comparison on QPI3-VD GGP models. For most time intervals, the different palaeointensity filtering criteria resulted in small enough changes to the GGP model parameters that the variations throughout geological time remain broadly unchanged. For the PCRS, application of AAM has significant consequences, however (Table 5.6).

Combined Analysis of Pre-CNS & Post-PCRS

The decision to generate optimised GGP models for the Pre-CNS & Post-PCRS as one discrete time interval, was based on previous results in **Chapters 2**, **3**, and **4**. Treated separately, the two intervals displayed near-identical VGP dispersion distributions as described by Model G shape parameters (Handford et al., 2021). Palaeointensity estimates for the Post-PCRS are still at a premium, despite previous success in taking steps towards addressing this issue (**Chapters 3, & 4**). When the 17 new palaeointensity estimates from prior studies were included (**Chapters 3, & 4**), still just 163 palaeointensity estimates defined the Post-PCRS after the application of QPI1. The greater issue was that 76% of this data described the strength of the field as recorded by the Siberian Traps at the PTB. The combined analysis of the Pre-CNS & Post-PCRS was designed to reduce the weighting of this data.

The palaeointensity estimates obtained from the Post-PCRS Fernazza Formation of the Dolomites (median, 3.6 x 10^{22} Am^2, **Chapter 3**) support this approach, as they lie close to the median strength of the Pre-CNS (4.6 x 10^{22} Am^2, **Chapter 3**). Palaeointensity estimates obtained from the Puesto Viejo Group of Argentina were much lower, however (median, 1.5 x 10^{22} Am^2, **Chapter 4**). This led to the suggestion that the weak field strength associated with the PTB (median, 2.3 x 10^{22} Am^2) could extend further into the Post-PCRS. Looking back at the palaeointensity record, just two palaeointensity estimates between ca. 252-143 Ma lie above the upper quartile of the long-term median (Figure 4.14, **Chapter 4**). This is in contrast with the rest of the palaeointensity record where estimates above this range are common (Figure 4.14, **Chapter 4**), and it opens the possibility that the lower range of palaeointensity estimates of the PTB, corroborated by estimates from **Chapter 4**, are in fact more representative of a longer time interval. The majority of VGPs analysed for the Pre-CNS & Post-PCRS (85%) were from lithologies associated with dates between 252 Ma and 143 Ma (Doubrovine et al., 2019; Handford et

al., 2021), but most of the palaeointensity data analysed (62%) represented geomagnetic field behaviour between 143 Ma and 127 Ma. It is possible that this could explain the consistently lower P_{KS} values than for other time intervals, regardless of the chosen palaeointensity selection criteria (Figure 5.2b; Table 5.4), as the directions and intensities may not represent the geomagnetic field across the same time interval.

To investigate this, an additional optimised GGP model was generated that exclusively used palaeomagnetic observations representing the geomagnetic field between 265 Ma and 143 Ma, as opposed to that within the entirety of the Post-PCRS and Pre-CNS. The parameters of this model are presented in Table 5.7, alongside goodness of fit statistics, following the format of Tables 5.2 to 5.6. The model's ability to describe the VGP dispersion distribution is slightly reduced compared to the original GGP model for the Pre-CNS & Post-PCRS, demonstrated by L_W values of 3.50 and 3.06, respectively. This appears to be a trade-off with the model's ability to describe the palaeointensity observations as the P_{KS} value increased from 0.219 (Table 5.5) to 0.326 (Table 5.7). Overall, the statistical model's ability to simultaneously describe VGP dispersion and palaeointensity observations is not much changed. There is an improved agreement between the optimised model's β parameter (2.16, Table 5.7) with those of other studied time intervals prior to the PCRS, however (Tables 5.2-5.5). If the relationship between the antisymmetric families and symmetric families has remained broadly unchanged, at least since the end of the PCRS, then this would suggest that a palaeointensity distribution of consistently lower strength was present between ca. 265 Ma and 143 Ma, increasing prior to the CNS. A similar change in the geodynamo regime was previously proposed by Kulakov et al. (2019) when analysing the palaeointensity record between 200 Ma and 65 Ma. The better agreement of the β parameter with those of subsequent time intervals, also further highlights the PCRS as an outlying time interval (Table 5.6).

PCRS GGP Model & KRSCovM

The apparent outlying nature of the β parameter of the optimised model for the PCRS is of interest, as it was the similarity between the β parameters for optimised statistical models of the last 10 Ma and the PCRS that led to the proposal of an unchanged relationship between symmetric and antisymmetric families throughout geological time (Brandt et al., 2021). The parameters that describe the optimised PCRS model of this study, differ to those of KRSCovM (Table 5.8), from which the proposal was made (Brandt et al., 2021). The primary difference between the two models is a lower β parameter defining KRSCovM (β = 3.1), though slightly higher than those defining statistical models of other time intervals in this study (Tables 5.2-5.5). When searching for an optimised model that best describes the palaeomagnetic observations, a range of models, described by a variety of model parameters, will produce similarly small misfits to those of the optimised model. There is the potential for this to produce local minima solutions, which was explored for the PCRS. It was clear that there were no local minima solutions with a β parameter more in keeping with that of KRSCovM (Figure 5.6). Interestingly, it is also apparent, from Figure 5.6, that there were no local minima solutions with a β parameter similar to that of the optimised models for the other time intervals. This suggests that a higher β parameter is required to best describe the palaeomagnetic observations during the PCRS, that were utilised in this study.

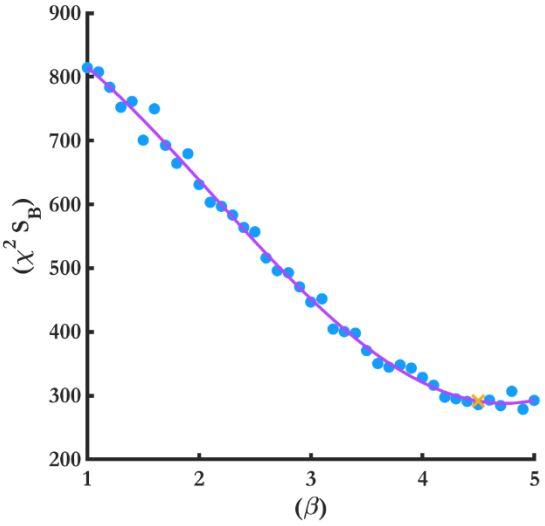

Figure 5.6: Chi squared values (χ^2) measure the misfit between the VGP dispersion (S_B) pattern predicted by the corresponding statistical model, and that observed from palaeomagnetic data used in the PCRS-QPI3-VD model construction. χ^2 determined as β was systematically varied between 1 and 5 (blue circles), as outlined in the method of model construction. Optimised solution indicated by yellow cross. Purple line represents the best-fit trend.

There are two primary differences in the processes by which the statistical models for the PCRS were constructed in this study and that of KRSCovM (Brandt et al., 2021). Firstly, optimised parameters for KRSCovM were determined by minimising to the observed distribution of the directional PSV statistic proposed by Brandt et al. (2020). In this study however, minimisation occurred against VGP dispersion and palaeointensity distributions. Secondly, the palaeomagnetic observations used to construct KRSCovM were subjected to more lenient selection criteria (Brandt et al., 2021). To investigate possible effects associated with these differences, an additional optimised GGP model was constructed for the PCRS using the palaeomagnetic data involved in the construction of KRSCovM, but expressed as locality level VGP dispersion. This model was termed KRSCovM-VGP. Observations are from extrusive units within the palaeomagnetic database of Kiaman Reversed Superchron (PDKRS, Brandt et al., 2021). Values for $\overline{g_1^0}$ and σ_1^0 were taken directly from the parameters defining KRSCovM (Table 5.8).

The newly determined β parameter of KRSCovM-VGP (β = 1.68) is almost half that of KRSCovM, and $\alpha/\overline{g_1^0}$ displays a marked increase (Table 5.8). Comparing these values with those of BB18 (Bono et al., 2020), or the optimised model for the last 5 Ma of this study, the trends proposed by Brandt et al. (2021) are no longer observed, as $\alpha/\overline{g_1^0}$ appears approximately unchanged and β displays variation between the two studied time intervals. These results demonstrate that the process by which the GGP model is constructed, potentially including the type of observations to which they are minimised, can affect the parameters defining the optimised model. Out of the four parameters defining KRSCovM-VGP, $\overline{g_1^0}$ and σ_1^0 are identical to those defining KRSCovM (Brandt et al., 2021). The remaining two, α and β, were determined by minimising to the same palaeomagnetic data as was the case during the construction of KRSCovM (Brandt et al., 2021) but, crucially, this data was expressed differently in the construction of the two statistical models. Data was expressed in the form of VGP dispersions for the construction of KRSCovM-VGP, and σ_E and σ_N (Brandt et al., 2020) for the construction

of KRSCovM (Brand et al., 2021). There are clear differences in the α and β parameters defining the two models (Table 5.8) despite them being constructed around the same palaeomagnetic observations. This has potential implications when attempting to evaluate the evolution of the geomagnetic field by comparing the parameters of GGP model's representative of different time intervals, but constructed around palaeomagnetic data expressed in the two ways that have been outlined.

Interestingly, despite the differences in their defining parameters, KRSCovM and KRSCovM-VGP describe the observed VGP dispersion distribution equally well, statistically speaking, as indicated by estimates of L_W (Table 5.8). Visibly, differences are apparent in their predicted distributions of VGP dispersion, however (Figure 5.7). KRSCovM shows much greater deviation from the associated Model-G fit, particularly at equatorial latitudes. This is reflected in the lower estimated L value of KRSCovM than KRSCovM-VGP (Table 5.8), when VGP scatter values are treated as absolute values (Doubrovine et al., 2019; Parker, 1994).

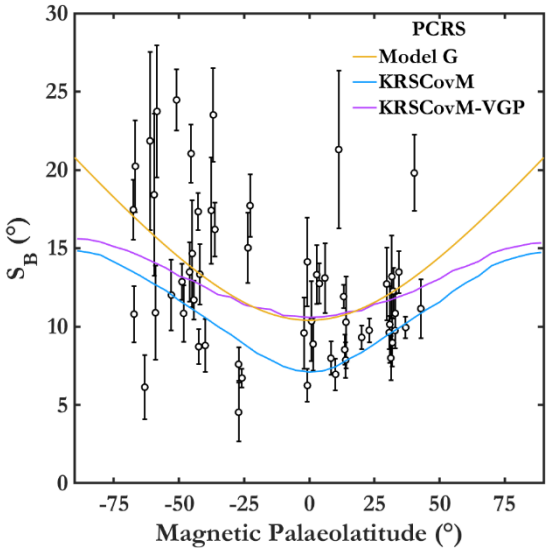

Figure 5.7: Site-level VGP dispersion versus magnetic palaeolatitude for the palaeomagnetic data utilised in the construction of KRSCovM (open circles, Brandt et al., 2021). Error bars represent associated uncertainties in VGP dispersion. Predicted VGP dispersion distributions displayed for Model G fit to presented data, KRSCovM, and KRSCovM-VGP.

After highlighting the issues of comparing KRSCovM (Brandt et al., 2021) with models constructed utilising different PSV statistics, an optimised GGP model was constructed for the PCRS based around KRSCovM-VGP but with addition of minimising to the palaeointensity distribution after the application of QPI3 (KRSCoVM-VGP-QPI3, Table 5.8). This allowed for a more direct comparison between statistical models representing the different possible palaeomagnetic observations for the PCRS, these being the reduced latitudinal VGP dispersion proposed by Handford et al. (2021) and the greater latitudinal VGP dispersion suggested by analysis of extrusive units within PDKRS (Figure 5.7). As expected, the parameters were similar to those of KRSCovM-VGP (Table 5.8). There was a slight increase in the β parameter (β = 1.68), and increased variance of $\overline{g_1^0}$ (σ_1^0 = 14.37). Acceptance of this new model would better align the β parameter associated with the PCRS with that of the other time intervals over the last 320 Ma. It would also suggest that the relative stability of the geomagnetic field ($\alpha/\overline{g_1^0}$ = 0.51, Table 5.8) was similar to

that during the CNS, suggestive of a potential characteristic of superchrons. The difficulty in accepting this model is in the uncertainty around the quality of the data used in its construction. Precursory filtering for high-quality data is used in the compilations around which the GGP models of this study have been constructed (Cromwell et al., 2018; de Oliveira et al., 2018; Doubrovine et al., 2019; Engbers et al., 2022; Handford et al., 2021). The PDKRS database (Brandt et al., 2021), utilised in the construction of KRSCovM, applied lenient selection criteria. A potentially significant issue with this is that effects associated with local block rotations are not accounted for, this can cause further problems when data are analysed in latitudinal bins. The P_{KS} value associated with KRSCovM-VGP-QPI3 was < 0.05 (Table 5.8), suggesting that the statistical model is not able to simultaneously reproduce the VGP dispersion distribution observed after the application of lenient selection criteria, and the palaeointensity distribution after the application of QPI3. It would appear that low quality directional data have biased the resulting GGP model.

In being able to better simultaneously reproduce observations of VGP distribution and palaeointensity distribution, it is believed that the model of this study, constructed around the Group 1 datasets compiled by Handford et al. (2021), better represents the palaeomagnetic field during the PCRS than KRSCovM (Brandt et al., 2021), or any variations of this model (Table 5.8). It is also the belief that this demonstrates the need for a more robust assessment of the quality of the palaeomagnetic data being analysed by ensuring that sufficient spot-readings have been captured to average out secular variation (N ≥ 9, Handford et al., 2021), assessing the reliability of palaeomagnetic data through Q scores (Meert et al., 2020; Van der Voo, 1990), and assessing the tectonic relationships between sampling sites (e.g. Doubrovine et al., 2019; Handford et al., 2021). The application of intra-site statistics to data from extrusive units in the PDKRS database by Brandt et al. (2021), resulted in a very similar Model G fit to the fit to Group 2 data of Handford et al. (2021) for which intra-site statistics were also applied (n ≥ 4 k ≥ 50 DC ≥ 4 a = 7.9 b = 0.29, Brandt et al., 2021; n ≥ 5 k ≥ 50 DC ≥ 3 a = 7.2 b = 0.30, Handford et al., 2021). This resemblance further highlights low equatorial VGP dispersion and a strong latitudinal dependence as being characteristic of the PCRS palaeomagnetic field. Following discussion of Handford et al. (2021), the use of Group 1 data in the construction of statistical models for the PCRS is favoured due to the wider confidence limits associated with Group 2 data.

Effects of Palaeointensity Filtering For the PCRS

Previous studies have highlighted the wide range of published palaeointensity values associated with the PCRS (Cottrell et al., 2008; Hawkins et al., 2021), and have questioned the reliability of estimates at both the upper and the lower end of this range. Cottrell et al. (2008), obtained VDM estimates of around 9 x 10^{22} Am^2 for the PCRS, from single feldspar crystals. They deemed these estimates to be more reliable than those obtained from whole rock specimens, and suggested that alteration of the latter may have resulted in estimates of minimum palaeointensity only. It was proposed, therefore, that the large temporal changes in palaeointensity during the PCRS could be an artefact. Conversely, Hawkins et al. (2021) suggested that the higher palaeointensity values associated with the PCRS may be unreliable, with MD effects resulting in overestimates. This idea was the result of a much lower average strength of the palaeomagnetic field during the PCRS, after the application of the AAM criteria.

The incompatibility between high and low palaeointensity estimates of the PCRS is clear in the observed palaeointensity distributions that have been subject to the most flexible selection criteria (QPI1 and NINT3, Figure 5.3e). Both of these criteria resulted in bimodal distributions of ECDF, with peaks around 5 x 10^{22} and 8 x 10^{22} Am^2 (Figure 5.3e). Such an observed distribution cannot be simultaneously reproduced alongside that of the VGP dispersion, under the model assumptions of a Gaussian palaeointensity distribution (Bono et al., 2021), with P_{KS} values << 0.05 (Table 5.6). Filtering through QPI3 resulted in a much improved P_{KS} value (0.443, Table 5.6) and visual improvement of the observed distribution with suppression of the lower peak around 5 x 10^{22} Am^2 (Figure 5.3e). The range of the palaeointensity distribution remained similar but, interestingly, all of the remaining weak palaeointensity estimates passed Q_{ALT} of the Q_{PI} criteria (Biggin & Paterson, 2014). This would seem to suggest that alteration effects have resulted in estimates of minimum palaeointensity, as suggested by Cottrell et al. (2008), but not to the extent where all weak palaeointensity estimates are artefacts. Finally, the median V(A)DM for the PCRS after the application of AAM was 4.6 x 10^{22} Am^2, around half the size of the median values obtained after the application of the other palaeointensity criteria (9.4 x 10^{22} - 8.4 x 10^{22} Am^2, Table 5.6), and in keeping with the observations of Hawkins et al. (2021). The resulting statistical model predicted a similar dispersion (P_{KS} = 0.825, Table 5.6), with no reduction in the ability to predict the observed VGP dispersion distribution (Table 5.6). With this finding, the suggestion that the high palaeointensity estimates of the PCRS are biased by MD effects (Hawkins et al., 2021) cannot be entirely rejected.

Estimates of $\overline{g_1^0}$ vary considerably between the two viable statistical models for the PCRS (QPI3 $\overline{g_1^0}$ = 32.43, AAM $\overline{g_1^0}$ = 17.68, Table 5.6). To maintain the ratio of $\alpha/\overline{g_1^0}$, as determined by the palaeomagnetic observations, the model built around AAM palaeointensity data displays much reduced variance of the GGP (QPI3 α = 10.34, AAM α = 5.68, Table 5.6). This would represent the lowest variance across the last 320 Ma and suggest a gradual increase in variance throughout this time (Table 5.6; Figure 5.8). The statistical model constructed around data filtered by QPI3 is favoured, however.

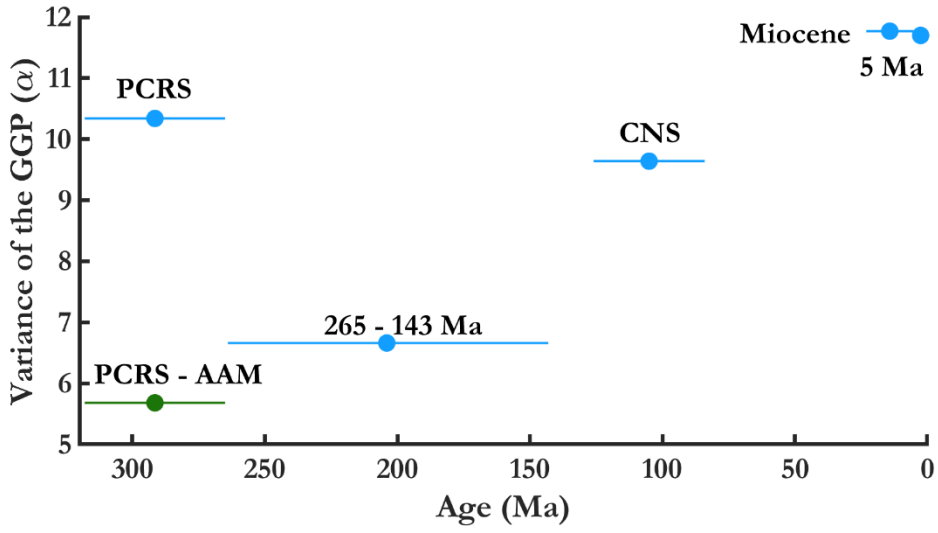

Figure 5.8: Plot of the variance of the GGP (α) for optimised models (QPI3) representing each of the studied time intervals (blue), and the model constructed around AAM filtering of palaeointensity data, for the PCRS (green).

Palaeointensity estimates obtained from middle Carboniferous sections in Uzbekistan and early Permian sections in the northern Caucasus account for the majority of the high palaeointensity values associated with the PCRS. Released in a series of publications by the same author (Solodovnikov, 1992a; 1992b; 1992c), results were obtained via the same approach. Estimates were primarily obtained from baked contacts of tuffs and ignimbrites, with little evidence of detailed microscopy and rock magnetic investigation to assess the nature of the remanence carriers and the process by which their remanence was likely acquired. As previously demonstrated, this is of particular importance when studying re-heated and ignimbritic rocks (**Chapter 4**). The reliability of estimates obtained from such rocks were strengthened by very good agreement with estimates obtained from associated lava flows, however. This was even observed within a sampling site, on occasion, fulfilling the requirements of Q_{LITH} of the Q_{PI} criteria (Biggin & Paterson, 2014; Bono et al., 2021; Solodovnikov, 1992b; 1992c). Consistent results from different lithologies representing the same palaeomagnetic field would suggest that specimens were not affected by laboratory alteration. Experimental results do not oppose this suggestion, as failure of Q_{ALT} was due to a lack of alteration checks and not due to failure of such measures (Solodovnikov, 1992a; 1992b; 1992c). Successful palaeointensity estimates were also obtained via two experimental methods, thermal Thellier and the Wilson method (Wilson, 1961). As specimens acquire a laboratory remanence via a single cooling stage from above a Curie temperature, the Wilson method is considered to be domain-state independent and so passes the Q_{MD} criteria (Biggin & Paterson, 2014). Results via this method demonstrated good agreement with those obtained via the thermal Thellier method (Solodovnikov, 1992a; 1992b; 1992c). For these reasons, it is believed that these high palaeointensity estimates are unlikely to be biased by alteration or MD effects, despite their near-consistent failure of Q_{ALT} and Q_{MD}. Combined with other high palaeointensity estimates for the PCRS (Schwarz & Symons, 1969; Senanyake & McElhinny, 1983; Usui & Tan, 2017), it is believed that the statistical model that utilises QPI3 data best represents the PCRS. This decision is further validated by the study of Usui & Tan. (2017) that provides additional reasoning to believe that the lower estimates within the QPI3 range are not solely due to alteration of whole rock specimens, as single crystal and whole-rock analysis result in low palaeointensity estimates.

Geomagnetic Field Evolution

A comparison of the preferred models of this study, representing the studied time intervals across the last 320 Ma (Table 5.9), suggests that total relative variability of the geomagnetic field displays some correlation with average reversal frequency. It would also suggest that the relationship between antisymmetric and symmetric family harmonics has remained relatively unchanged since the PCRS, but that a different relationship was present during the PCRS that was responsible for the observed strong latitudinal dependence of VGP dispersion.

Expressed as $\alpha/\overline{g_1^0}$, relative variability is lowest during the two superchrons studied. A higher estimate was obtained for the Miocene than that for the field between 265 Ma and 143 Ma, which is suggestive of a positive relationship with reversal frequency (Table 5.9; Figure 5.9). This relationship does not extend to behaviour during the last 5 Ma, during which average reversal frequency was comparable to that of the Miocene but relative variability was lower than that estimated for the field between 265 Ma and 143 Ma (Table

Table 5.9: Preferred statistical models representing each of the studied time intervals.

Model	NINT	α	β	g_1^0	σ_1^0	χ^2	L	χ_w^2	L_w	D_{KS}	P_{KS}	α/g_1^0	RSD	ARF (Myr^{-1})
5Ma-QPI3-VD	908	11.70	2.47	-20.89	11.12	68.1	1.19	524.7	3.31	0.030	0.811	-0.56	-0.53	4.40
Miocene-QPI3-VD	265	11.77	2.14	-13.53	9.96	111.4	1.59	572.4	3.61	0.064	0.633	-0.87	-0.74	4.80
CNS-QPI3-VD	210	9.64	2.33	-20.29	8.45	13.7	0.85	178.5	3.06	0.090	0.341	-0.48	-0.42	0.09
265-143Ma-QPI3-VD	184	6.66	2.16	-10.38	4.88	45.3	1.12	41.1	3.50	0.098	0.326	-0.64	-0.47	3.20
PCRS-QPI3-VD	100	10.34	4.51	-32.43	13.99	14.6	0.96	139.5	2.95	0.120	0.443	-0.32	-0.43	0.08

Note 5.9: Model parameters defining the preferred statistical models, of this study, representing time intervals of distinct average reversal frequency (ARF) across the last ca. 320 Ma. See note of Table 5.2 for description.

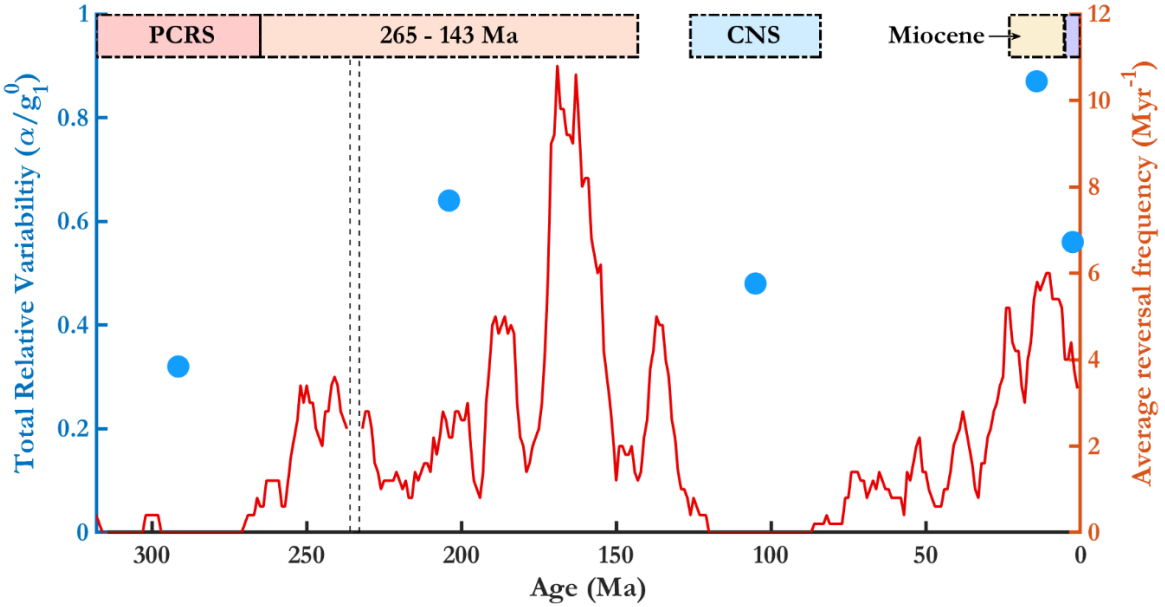

Figure 5.9: Variations in total relative variability (α/g_1^0) for preferred statistical models representing each of the studied time intervals (blue). Red line displays reversal frequency model for the last 320 Ma (Handford et al., 2021).

5.9; Figure 5.9). For the last 5 Ma, average geomagnetic field behaviour was quantified over a much shorter time interval, however. Direct comparison of behaviour between time intervals with such varying lengths should be done cautiously. The observed relationship between $\alpha/\overline{g_1^0}$ and average reversal frequency is not unexpected, as it has long been proposed that reversals would occur less frequently during time intervals associated with greater dominance of the axial dipole to the non-axial dipole (Coe & Glatzmaier, 2006; Cox, 1969; 1975). Model G *a* parameter displays a power law relationship with axial dipole dominance (Biggin et al., 2020), and $\alpha/\overline{g_1^0}$ displays a very strong, positive correlation with Model G *a* (Figure 5.5). Therefore, reduced relative variability correlates with increased axial dipole dominance. From this, increased axial dipole dominance appears to reduce the likelihood of the geomagnetic field undergoing a reversal, this could also explain the increased length of the PCRS when compared with that of the CNS, as relative variability of the PCRS model is much lower (Table 5.9).

As part of their assessment of the history of dipole moment, Kulakov et al. (2019) tested the hypothesis of an inverse correlation between field stability and reversal rate by assessing changes in field variability. For this they used the ratio of the interquartile range to the median value, a metric termed *V%* (Kulakov et al., 2019). The process of estimating V(A)DM values clearly separates contributions from the non-dipole and the dipole (Constable, 2007). All Gauss coefficients associated with the dipole term contribute equally to the V(A)DM, and so variation in these values (*V%*) is assumed to result from variations in the axial dipole and non-axial dipole Gauss coefficients. In this scenario, *V%*, RSD, and $\alpha/\overline{g_1^0}$ might be expected to covary. In contrast to this, Kulakov et al. (2019) revealed a positive relationship between field stability and average polarity reversal frequency. With *V%* greatest during times of reduced reversal frequency (Kulakov et al., 2019).

As discussed, lower $\alpha/\overline{g_1^0}$ values were observed during the superchrons. RSD trends likewise but displays a reduced difference between time intervals (Figure 5.10). *V%* was calculated from the observed palaeointensity distribution of each studied time interval, and the same relationship did not hold. *V%* was lower during the interval of 265-143 Ma than during either studied superchron (Figure 5.10). Furthermore, out of these three time intervals *V%* was highest during the PCRS, despite much reduced relative variability, and thus increased axial dipole dominance (Figure 5.10). As RSD and $\alpha/\overline{g_1^0}$ utilise model parameters, and because the preferred models do not identically reproduce observed palaeomagnetic observations, *V%* was also determined for the predicted palaeointensity distributions (Figure 5.10). Generally, there was little difference between the observed and predicted values. The greatest difference between the two was observed for the CNS (Figure 5.10). Predicted *V%* is lowest for the CNS, which suggests that the VGP dispersion distribution observed for the CNS was more likely to have resulted from a geomagnetic field displaying reduced variability than that suggested from palaeointensity observations. This interpretation follows the discussion of Kulakov et al. (2019), who highlighted the reduced *V%* for the CNS when analysing single crystal data, and suggested that this could indicate an observed *V%* that is amplified by differences in carriers' abilities to record and preserve palaeointensity signal. This is similar to the discussions surrounding the PCRS (Cottrell et al., 2008; Hawkins et al., 2021). Predicted *V%* is also lower than observed *V%* for the PCRS but still greater than that of 265-143 Ma

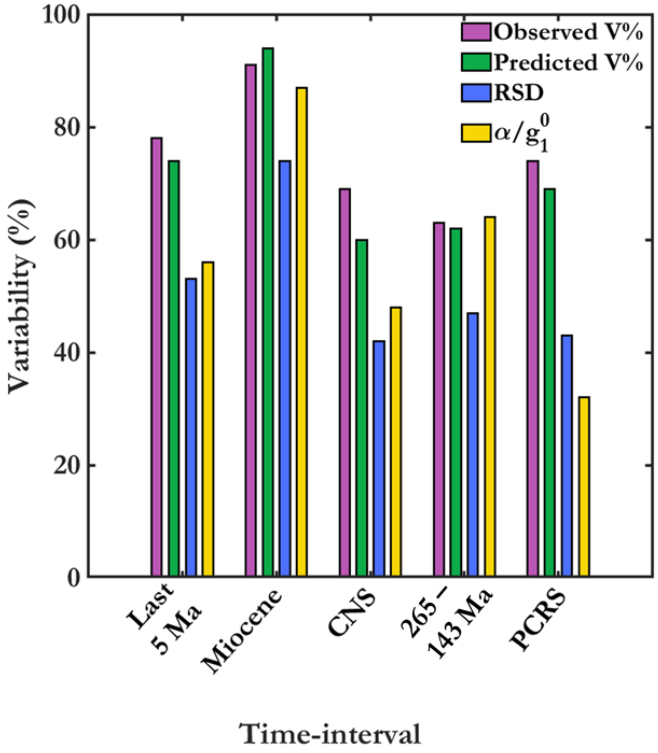

Figure 5.10: Estimates of total relative variability (RSD (σ_1^0/g_1^0) and α/g_1^0) presented alongside predicted and observed variability of VDMs (V%) for preferred statistical models from each studied time interval.

again, much higher than might be expected considering the much lower $\alpha/\overline{g_1^0}$ value (Figure 5.10). The variance of the predicted VDM distribution was also analysed via parametric means ($\sigma_{VDM}/\overline{VDM}$), facilitating a more direct comparison with $\alpha/\overline{g_1^0}$ and RSD. The same general trend was observed to that described for *V%* (Figure D.3), validating the discussed behaviour under the assumptions of the statistical models.

With reduced variance of the Gauss coefficients of the dipole term but a relatively high predicted *V%*, variation in V(A)DM values must have an alternative source. The first three harmonic terms were previously demonstrated to have been the greatest contributors to V(A)DM estimates across the last century (Campuzano et al., 2014). The inclusion of the quadrupole and octupole terms in the computation of synthetic V(A)DM estimates from a statistical field model (IGRF-11, Campuzano et al., 2014), resulted in increased values. It is assumed that such contributions are averaged out, but greater variability of the non-dipole terms could result in greater observed variability of V(A)DM. Greater variance of antisymmetric terms during the PCRS, as suggested by the increased β parameter, appears to result in sufficient variability of the quadrupole and octupole terms to produce increased variability in V(A)DM values, despite the much-increased axial dipole dominance.

The predicted geomagnetic field behaviour during the PCRS shows great similarity to that of the most stable geodynamo simulations of Coe & Glatzmaier (2006). The most stable simulations, those exhibiting less reversals and excursion events, had a greater contribution from antisymmetric Gauss coefficients relative to symmetric Gauss coefficients, and displayed an increased axial dipole dominance. This is observed for the PCRS with a much greater axial dipole dominance and much greater variance of the

antisymmetric families relative to the symmetric, as represented by β. A similar relationship is observed for the CNS but here axial dipole dominance is not markedly different from that of the Miocene and the geomagnetic field between 265 Ma and 143 Ma, and so the increased β parameter is subtler (Table 5.9). This increase does appear sufficient to maintain a higher $V\%$ than expected from $\alpha/\overline{g_1^0}$, however.

The behaviour of the geomagnetic field modelled in this study, offers an alternative explanation as to why the traditionally expected inverse relationship between field stability, $V\%$, and average polarity reversal frequency is not observed in the palaeomagnetic record. Previously, this has been attributed to intrinsic differences in different palaeomagnetic carriers' abilities to record and preserve palaeomagnetic information (Kulakov et al., 2019; Tarduno & Cottrell, 2005). With the expectation that such a relationship might be observed if sufficient palaeointensity data could be obtained from single crystal specimens (Tarduno & Cottrell, 2005).

Here, a scenario has been presented in which there is no obvious relationship between $V\%$ and average polarity reversal frequency, because of the contrasting ways in which the variances of the symmetric and antisymmetric families appear to differ between times of different reversal frequency. By considering the appropriateness of different filtering criteria, such behaviour is favoured over that proposed by Kulakov et al., (2019). The positive relationship between field stability and average polarity reversal frequency, observed by Kulakov et al., (2019), was most evident when palaeointensity data were subject to the strictest filtering criteria; i.e. when data were analysed that fulfilled the requirements of Q_{AGE}, Q_{ALT}, & Q_{STAT} and Q_{AGE}, Q_{ALT}, & Q_{MD} (Biggin & Paterson, 2014), respectively (Kulakov et al., 2019). In fact, these were the only analysed subsets for which $V\%$ was greatest during the CNS (Kulakov et al., 2019), and a clear relationship was observed. As previously discussed, requiring data to fulfil the Q_{AGE}, Q_{ALT}, & Q_{STAT} criteria, significantly reduces the amount of palaeointensity data available for analysis (Hawkins et al., 2021; Kulakov et al., 2019). This study has demonstrated that applying the AAM criteria to palaeointensity data is not appropriate when studying the CNS, with the associated GGP model unable to simultaneously reproduce both sets of palaeomagnetic observations (Table 5.4). For these reasons, it is believed that the less coherent relationship between $V\%$ and average reversal frequency observed by Kulakov et al. (2019), through the application of total QPI score based filtering, to be more representative of true geomagnetic field behaviour.

Conclusions

1. Application of the QPI3 criteria to the palaeointensity observations, most consistently and reliably resulted in GGP models capable of simultaneously describing VGP dispersion and palaeointensity observations. The robustness of GGP models was tested against a range of palaeointensity filtering criteria that found that, for each studied time interval, the observed VGP dispersion distribution could be equally well explained regardless of the chosen palaeointensity selection criteria. Differences occurred in the models' abilities to simultaneously reproduce the observed palaeointensity distributions. If the VGP dispersion is well-defined and fit well by the model, but the same model shows a poor fit to the palaeointensity distribution from

the same interval, then this reduces confidence in the accuracy of the palaeointensity distribution. The consistent construction of GGP models capable of best describing palaeomagnetic observations, when utilising data subject to QPI3 filtering, would appear to support the use of QPI3 filtering over the other selection criteria investigated. On the evidence of this study, it is recommended to filter palaeointensity data by QPI3 in order to maximise the likelihood that the resulting data is representative of the geomagnetic field during the time interval being studied, unless there is reason to believe that the use of some other filtering criteria would prove more appropriate.

2. The palaeointensity record provides much greater discriminatory power than the PSV record, when assessing differences in palaeomagnetic field behaviour between distinct time intervals. Unique statistical models were required in order to explain the different V(A)DM distributions observed for each time interval. This was demonstrated when assessing the goodness of fit of predicted distributions from a GGP model representing the geomagnetic field across a given time interval, to palaeomagnetic observations from each other studied time interval. The model predictions were generally as capable of describing VGP dispersion distributions as those of the model constructed around the palaeomagnetic observations. This was not so for the palaeointensity distributions, with almost all predicted distributions rejected at the 95% significance level. Greater difficulties around obtaining reliable palaeointensity estimates over palaeomagnetic information should be considered, but these findings could suggest that changes in relative variability and dipole moment are the optimal tool for documenting changes in geodynamo regime.

3. When attempting to evaluate long-term evolution of the geomagnetic field, it is unsuitable to compare parameters of GGP models that were constructed via different means. In particular, models that were minimised to different observed PSV statistics. Under consistent model construction, the relationship between antisymmetric and symmetric families appears to have remained approximately unchanged since the cessation of the PCRS ca. 265 Ma, as indicated by the β parameters of preferred statistical models. Consistency in this aspect of geomagnetic field behaviour, favours the existence of a slightly weaker field ca. 265 Ma to 143 Ma before a change in the geodynamo ca. 20 Myr prior to the onset of the CNS. In contrast to the time following the PCRS, variance of antisymmetric Gauss coefficients relative to that of symmetric Gauss coefficients, appears to have been approximately twice as great during the PCRS. The observed strong latitudinal dependence of VGP dispersion, that is revealed when the quality of the palaeomagnetic data is assessed through intra-site statistics, can be explained by this enhanced variance in the antisymmetric Gauss coefficients.

4. Dipole moment variability does not appear to display a relationship with reversal frequency. This is despite superchrons demonstrating increased axial dipole dominance, and thus reduced relative variability of the geomagnetic field during superchrons. This could be explained by greater variability of the non-dipole terms, in particular the quadrupole and octupole terms, contributing to greater variability of dipole moment than suggested by variability of the dipole terms. This is suggested by

the predicted increase in the variance of antisymmetric Gauss coefficients during superchrons. Such an increase, as indicated by a greater β parameter, also indicates an increased likelihood of reduced equatorial symmetry of the geomagnetic field during a superchron. This supports previous suggestions that, during time intervals defined by a reduced tendency for geomagnetic reversals and excursion events, equatorial symmetry is reduced and axial dipole dominance is increased. Such behaviour is most evident during PCRS, with axial dipole dominance during the CNS more in keeping with that estimated for times of reversals. This would account for the near constant β parameter since the cessation of the PCRS, when compared with the much higher value associated with the PCRS.

5. Under the assumption that the distribution of palaeointensities during the PCRS was Gaussian in nature, the PCRS palaeointensity record in its entirety cannot be an accurate representation of geomagnetic field behaviour. Statistical models for the PCRS that were built around palaeointensity observations subject to overly lenient selection criteria, were incapable of reproducing the observed palaeointensity distribution. This study favours a strong average field strength during the PCRS but the alternative model of a PCRS with a geomagnetic field strength in keeping with that of the long-term average, cannot be confidently rejected. Such a model would have important implications for long-term geomagnetic field evolution with regards to its variance and average strength. A more consistent strength of the geomagnetic field throughout geological time would suggest that the occurrence of superchrons is almost solely due to variations in relative variability, and that any relationship between reversal frequency and field strength is more complicated than an entirely inverse relationship. High quality palaeointensity estimates indicative of a strong geomagnetic field during the PCRS would provide greater clarity around this situation.

Acknowledgements

Covariant-style GGP models were constructed using the MATLAB code developed by Bono et al. (2020), and the associated Graphical User Interface, that were previously made openly available at the EarthRef Digital Archive (ERDA/2420).

Chapter 6. Summary & Implications

Summary of Results

Through comparison with the results of previous palaeosecular variation (PSV) studies on time intervals across the last 320 Ma, analysis of PSV during the PCRS and the time immediately following, revealed extreme behaviour during the PCRS and near-constant, almost latitudinal invariance of VGP dispersion until the onset of the CNS. Despite being characterised by different apparent average polarity reversal frequencies, the latitudinal dependencies of VGP dispersion during the Post-PCRS and the Pre-CNS were defined by similar Model G shape parameters (Figure 6.1a, b). The *b*/*a* ratios of the respective models were near identical, with Model G *a* slightly lower for the Pre-CNS, the higher reversal frequency regime of the two. Despite showing similarities in their shape and overall trend, VGP dispersion patterns representing the PCRS and the CNS, respectively, demonstrated greater differences than suggested by previous studies (Biggin et al., 2008; de Oliveira et al., 2018; Doubrovine et al., 2019; Handford et al., 2021). Equatorial VGP dispersion appeared much reduced for the PCRS (Figure 6.1c, d), an indication that the palaeomagnetic field displayed enhanced axial dipole dominance.

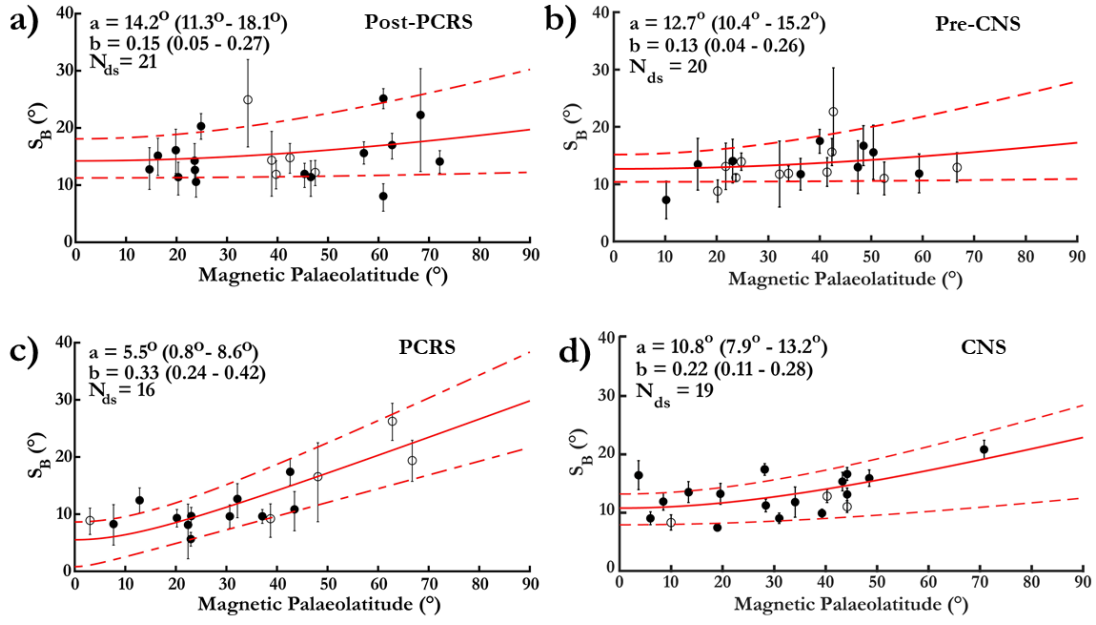

Figure 6.1: One hemisphere projection showing latitude dependence of virtual geomagnetic pole dispersion in the a) Post-PCRS (Handford et al., 2021), b) Pre-CNS (Doubrovine et al., 2019), c) PCRS (Handford et al., 2021), d) CNS (Doubrovine et al., 2019). S_B values for northern and southern palaeolatitudes given by filled and empty circles respectively, determined through application of the Vandamme cut-off (Vandamme, 1994); error bars show their 95% confidence intervals. The solid red curve displays the best fit of Model G to the S_B values, dashed line represents the 95% confidence intervals given by the jack-knife method for 5,000 replications. Estimates of Model G a and b shape parameters are displayed alongside their associated uncertainties and the number of datasets analysed (N_{ds}).

Reliable palaeointensity results were successfully obtained from a wide range of lithologies and rock units, though none from subaerial basaltic lavas, the most commonly utilised material for palaeointensity analysis. Reliable estimates came from two sampling localities for which similar dates have previously been obtained (**Chapters 3 & 4**), but likely separated by over 60° latitude across Pangaea at the times of their formations (Torsvik et al., 2012; van Hinsbergen et al., 2015).

Submarine pillow lavas from the Fernazza Fm of the Dolomites, NE Italy, produced 12 independent V(A)DM estimates between 3.0 x 10^{22} and 4.8 x 10^{22} Am^2 (Figure 6.2b), with associated Q_{PI} scores between 4 and 7 (**Chapter 3**). Of the 12 sites from which palaeointensity estimates were obtained, 10 of the final V(A)DM values were estimated from a combination of results from thermal Thellier and Shaw-DHT experiments. There was good agreement between the results obtained via these two methods and those obtained via the calibrated pseudo-Thellier approach, especially when the large associated uncertainty of the latter was considered. Although not included in final site mean V(A)DM calculations, these calibrated pseudo-Thellier results suggested that palaeointensity estimates were not biased by laboratory induced alteration. The Ti-poor titanomagnetites that were identified as remanence carriers are somewhat atypical of submarine lavas; fast cooling rates and quenching generally favour the formation of more Ti-rich titanomagnetites. Relatively slow cooling rates, evident by the large volume of individual pillows, and higher oxygen fugacity associated with arc/back-arc settings when compared with mid-ocean ridge basalts, at which previously studied submarine lavas have formed, provide a possible explanation for this curiosity. Similarly, samples generally lacked the widespread, extensive low-temperature oxidation products that are typical of submarine lavas.

Additional palaeointensity results were obtained from approximately coeval basalt sills and rhyolitic ignimbrites of the Puesto Viejo Group, located in the Rafael depocenter of the Mendoza province, Argentina (**Chapter 4**). After detailed rock magnetic and microscopy analysis, palaeointensity estimates from 3 basaltic sill sites and 2 rhyolitic ignimbrite sites were interpreted to be representative of the palaeomagnetic field during the time of their formation. Estimated VDM values ranged between 0.9 x 10^{22} and 2.1 x 10^{22} Am^2 (Figure 6.2b), with associated Q_{PI} scores between 5 and 7. Basalt sills were characterised by ChRM carrying grains that covered a broad range of titanomagnetite compositions. These grains were susceptible to laboratory induced oxyexsolution during heating. As such, no results were obtained via the thermal Thellier method, due to the continuous alteration of the remanence carriers throughout the stepwise heating experiments. Success was achieved with the Shaw-DHT method where the alteration correction appeared to account for the effects of laboratory induced alteration, supported by the agreement with results from the non-heating calibrated pseudo-Thellier method. Difficulty was also encountered in obtaining results from thermal Thellier experiments on specimens of the Rhyolitic ignimbrites. Results were obtained from one site, at which there was good agreement with the results obtained via the Shaw-DHT method. Q_{TRM} was cautiously failed at this site due to its complex thermal history. General agreement with the range of estimates obtained from more traditionally used basaltic sills was interpreted as an indicator of reliability, when considering the bimodal nature of the extensional tectonic setting in which the studied units formed.

Finally, GGP models that represented time intervals of distinct reversal frequency regimes across the last 320 Ma were constructed (**Chapter 5**). This process utilised the improvements made to our understanding of palaeomagnetic field behaviour during the PCRS and the Triassic, in combination with the pre-existing understanding of palaeomagnetic field behaviour across this time (PINT v8.0.0, Bono et al., 2021; Cromwell et al., 2018; Doubrovine et al., 2019; Engbers et al., 2022). These statistical models were constructed using the recently proposed covariance approach (Bono et al., 2020), which is derived from relationships between Gauss coefficients that were previously observed during geodynamo simulations (Bouligand et al., 2005; Sanchez et al., 2019). Preferred models were generated for each studied time interval through an optimisation process using PSV and palaeointensity observations. Generating these optimised models for different reversal regimes, resulted in a framework by which interactions between the most commonly described characteristics of the palaeomagnetic field could be investigated.

A range of models were generated for each time interval using palaeointensity data subjected to a range of selection criteria. The use of QPI3 criteria was the most consistent and reliable in generating GGP models that were capable of simultaneously explaining both sets of palaeomagnetic observations. Between time intervals, the observed distributions of palaeointensity behaviour demonstrated greater variability than VGP dispersion distributions and this observation ultimately required unique GGP models to be generated for each studied time interval.

The previous proposal of a largely unchanged relationship between symmetric and antisymmetric families (Brandt et al., 2021) was supported but only since the cessation of the PCRS. Support came from the similarity between β parameters defining the GGP models representing the different time intervals since the PCRS. This behaviour would favour a slight reduction in palaeointensity between ca. 265 Ma and 143 Ma. The inability of a previously analysed VGP dispersion distribution to produce an optimised GGP model that can simultaneously describe the palaeointensity observations for the PCRS, suggested that it is unlikely to be representative of the palaeomagnetic field across this time. To address this, filtering of the data was required via an assessment of intra-site statistics. In full, the palaeointensity data associated with the PCRS also appeared non-representative of actual palaeomagnetic field behaviour. Application of the most lenient Q_{PI}-based selection criteria utilised in this study, QPI1 and NINT3, resulted in a bimodal empirical cumulative distribution function of V(A)DM, and corresponding GGP models could not simultaneously describe observed palaeomagnetic distributions. Q_{PI}-based filtering, QPI3 and AAM, did result in optimised GGP models that could simultaneously describe the observed palaeointensity and VGP dispersion distributions but with differing consequences for the strength of the palaeomagnetic field during the PCRS. Through evaluation of the palaeointensity data representing the PCRS, the statistical model representative of increased field strength was favoured.

Implications & Future Work

Geodynamics

In evaluating geomagnetic field evolution across the last 320 Ma, long-term variations were also assessed across a full period of the hypothesised 200 Myr cyclicity. With the full cycle encompassing the PCRS through to the CNS. The relatively consistent palaeointensities and PSV behaviour observed for the Post-PCRS and the Pre-CNS (**Chapters 3, 4, & 5**), is somewhat reminiscent of the plateau in palaeointensity evolution observed in the mantle forced model of Driscoll & Olson. (2011), across a complete 200 Myr cycle (Figure 6.2a, b). With the average field strength across this time interval likely closer to the long-term average than was initially suggested by Prévot et al. (1990), any reduction in CMB heat flux appears to be more likely attributable to mantle convection processes than some anomalous event. The mantle forced simulation of Driscoll & Olson. (2011) displayed greatest dipole moment during superchrons, but also near-symmetrical behaviour when transitioning out of one superchron into the next. This study suggests that the PCRS displayed much increased axial dipole dominance, and almost unique palaeomagnetic field behaviour, when compared with the CNS. The increase associated with the PCRS is greater than that suggested by the effects of mantle forcing (Driscoll & Olson, 2011), and could suggest some additional contribution to decreased CMB heat flux.

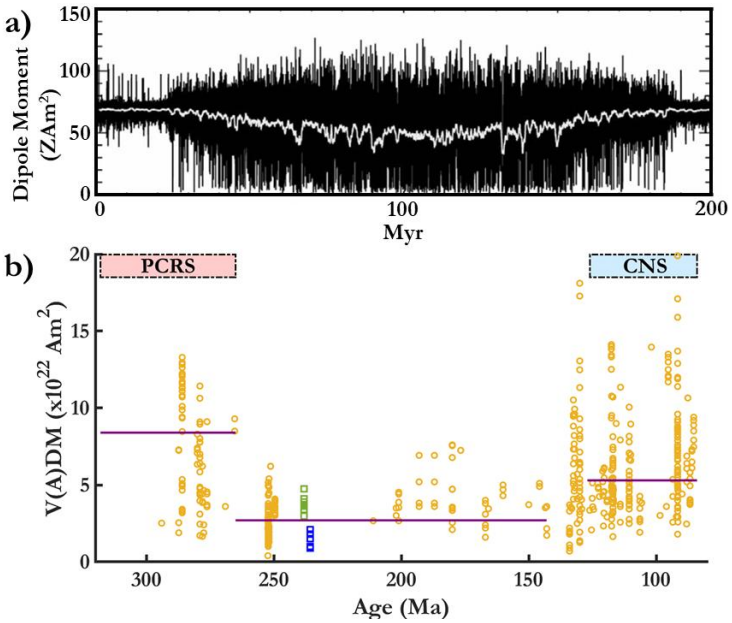

*Figure 6.2: Comparison of predicted palaeointensity behaviour across a 200 Myr cycle with palaeointensity observations across the corresponding time interval. a) Variations of dipole moment (black) with 1 Myr smoothing (white) of predictions from numerical dynamo model of Driscoll & Olson, 2011). Figure modified from Driscoll & Olson (2011). b) V(A)DM record associated with preferred statistical models (**Chapter 5**) for distinct time intervals across a complete cycle of the proposed 200 Myr variations. V(A)DM data from PINT V8.0.0 (Bono et al., 2021) with a Q_{PI} score ≥ 3 (yellow). Palaeointensity estimates included from this thesis (green squares: **Chapter 3**, blue squares: **Chapter 4**) Median V(A)DM values around which optimised statistical models were constructed (purple).*

The collapse of large low-shear velocity provinces (LLSVPs), that are characteristic structures of parts of the lowermost mantle (Figure 6.3; McNamara, 2019), has been proposed to result in reduced CMB heat flux (Olson & Amit, 2015). It is suggested that

these regions are relatively hot and so CMB heat flux is dominated by the relatively cold regions outside of these structures (Zhang & Zhong, 2011). Collapses cause the footprint of the LLSVPs on the CMB to increase, and thus CMB heat flux to decrease. Following the assumption that mantle plumes are generated at the edges of these LLSVPs (Figure 6.3; Burke et al., 2008; Burke & Torsvik; 2004; Torsvik et al., 2006), this collapse is

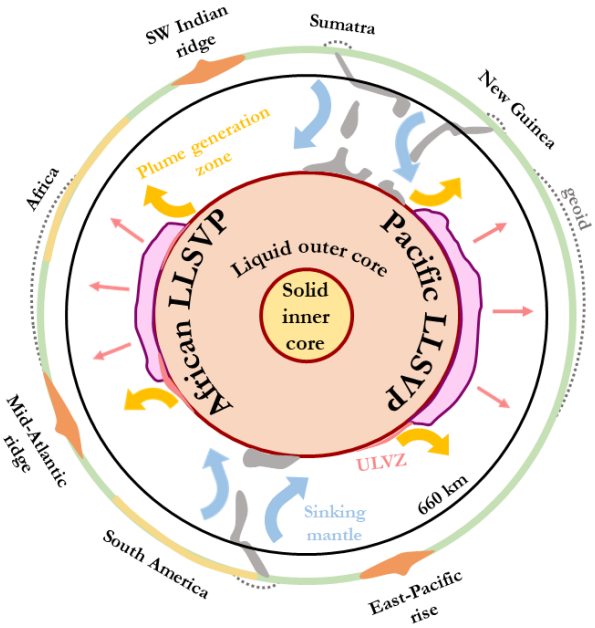

Figure 6.3: Modified from Torsvik et al. (2014). Schematic cross-section of the Earth, as seen from the South Pole, displaying the position of the large low shear-wave velocity zones (LLSVPs) and their proposed relationship with the wider tectonic and mantle processes. The edges of the LLSVPs are indicated as being the principle plume generation zones. Ultra-low velocity zones (ULVZs), indicated at the margins of the LLSVPs, are localised patches with extreme physical properties (e.g. Brown et al., 2015). Buoyant upwelling associated with the LLSVPs is indicated by surface facing arrows (red) and is presented as dominating the elevated region of the residual geoid (dashed lines).

proposed to result in an increase in the production of large igneous provinces (LIPs) 30-60 Myr after the collapse of an LLSVP (Biggin et al., 2012; Olson & Amit, 2015). Such a scenario is plausible for the PCRS with the identification of the Siberian Traps (ca. 250 Ma, Courtillot & Renne, 2003), Emeishan large igneous province (ELIP, ca. 260 Ma, Chung & Jahn, 1995; Courtillot & Renne, 2003), and the Tarim large igneous province (ca. 290 - 288 Ma, Yang et al., 2013) (Figure 6.4). These LIPs of overlapping eruption date, have been proposed to originate from two different lowermost mantle anomalies (Figure 6.4). The palaeogeographic position of the ELIP has been correlated with the edge of the Pacific LLSVP (Torsvik & Domeier, 2017), and that of the Siberian Traps and TLIP proposed to be associated with the edges of the smaller deep mantle structure termed the Perm anomaly (Torsvik et al., 2014; Wei et al., 2020; Wu et al., 2017). Overlapping eruption dates of the associated LIPs (Figure 6.4) could suggest that collapse of these structures occurred near-simultaneously, within the geological timeframe, which could explain the much reduced CMB heat flux observed for the PCRS. This would be in contrast with the proposed collapse events of the Pacific LLSVP and the African LLSVP associated with the CNS, for which evidence from LIP formations (Figure 6.4) suggests collapse of the Pacific LLSVP occurred 40-45 Myr prior to that of the African LLSVP (Olson & Amit, 2015).

Gaining further insight into such events that could explain the decreased CMB heat flux during the PCRS, and subsequent enhanced axial dipole dominance, will require further investigation. Uncertainty still surrounds the likely CMB source regions of the LIPs that are potentially linked to the onset of the PCRS (Flament et al., 2017; Torsvik & Domeier, 2017). In addition, there have been alternative proposals for mantle plume and LIP formation that do not rely on origination at LLSVP edges (Foulger, 2007; Ivanov, 2007; Klausen, 2020). Regardless of the direction in which our understanding around these processes takes, this study has demonstrated the important contribution that palaeomagnetic observations can have to these ongoing discussions. Greater refinement of the kinematics and effects of mantle forcing across the 200 Myr cycle, would help to further establish the cause of the palaeomagnetic field behaviour during the PCRS as being something other than typical mantle convection.

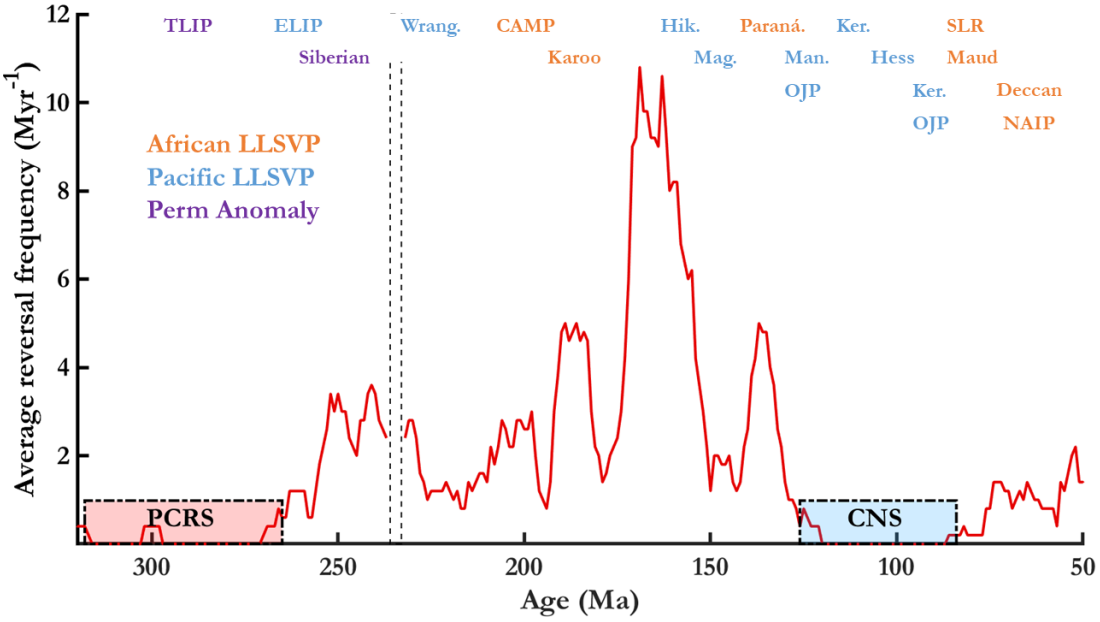

Figure 6.4: Modified from Olson & Amit (2015). Composite showing the relationship between average polarity reversal frequency and the formation of large igneous provinces (LIPs) between 320 and 50 Ma. Proposed associated large low shear velocity provinces (LLSVPs), or other lowermost mantle anomaly, are indicated by a colour code (orange: African LLSVP, blue: Pacific LLSVP, purple: Perm). TLIP: Tarim LIP, ELIP: Emeishan LIP, Siberian: Siberian Traps, Wrang.: Wrangelia Terrane, CAMP: Central Atlantic Magmatic Province, Karoo: Karoo Basin, Hik.: Hikurangi Plateau, Mag.: Magellan Rise, Paraná: Paraná-Etendeka Traps, Man.: Manihiki Plateau, OJP: Ontong-Java Plateau, Ker.: Kerguelen Plateau, Hess: Hess Rise, SLR: Sierra Leone Rise, Maud: Maud Rise, Deccan: Deccan Traps, NAIP: North Atlantic Igneous Province.

The last 5 Myr represents approximately the half way point of the current 200 Myr cycle. Modelled behaviour would suggest that dipole moment should be reduced in comparison to the most recent superchron, the CNS. In fact, observed median V(A)DM is comparable to that of the CNS (**Chapter 5**). The last 5 Myr provides further discrepancies, with the general relationship between relative variability and reversal frequency not holding (**Chapter 5**), and providing the greatest deviation from an inverse correlation between Model G shape parameters (**Chapters 2 & 5**). The repetitive breakdown of relationships and trends during the last 5 Myr, that are otherwise observed for the last 320 Myr, could be due to the significantly shorter timescale that is being represented. Palaeomagnetic observations are present at a much greater density than for any of the other studied time intervals, providing a detailed description of a relatively

short-lived feature. The high density of data makes incorporating the data from the last 5 Myr into a longer time-scale challenging, without introducing a temporal bias to the dataset selected for analysis.

Palaeointensity Methods & Recorders

During this study, palaeointensity experiments were conducted on geological material that are less typically utilised than subaerial basalt lavas, due to a lack of the latter having been previously identified and attributed to the Triassic. Of the rock units and lithologies that were interpreted as providing reliable palaeointensity estimates, ignimbrites and submarine basalts are the most historically underrepresented in the palaeointensity record, likely due to the high rate at which alteration occurs in their formation environments. Obtaining reliable estimates has demonstrated that by considering the geological setting in which a unit formed, the geological history since its formation, and the implications for magnetic remanence acquisition and changes in the remanence carriers, a more diverse range of geological material can provide palaeointensity information than is often used. From this study, massive pillow lavas appear to have greater potential in providing reliable palaeointensity estimates that can be associated with some high level of certainty, with the complex thermal histories of ignimbrites proving a barrier to this when results are obtained in isolation. Nonetheless, palaeointensity estimates determined from ignimbrite specimens could be utilised in conjunction with estimates obtained from different lithology types, from which similar dates have been obtained, to support results and better populate the palaeointensity record. Diversifying the lithologies and rock units from which palaeointensity estimates are obtained has the potential to provide crucial information where gaps in the palaeointensity record are primarily a result of more traditionally utilised palaeointensity recorders being at a premium.

It could be foreseen that future uptake of such an approach would be limited because of the time-consuming nature of thermal Thellier methods, widely regarded as the method from which the most reliable palaeointensity estimates are obtained, and the already high failure rates of palaeointensity experiments on materials that are more similar to ideal recorders. An approach to address this would be to impart greater value on the element of palaeointensity experiments that aims to ascertain the reliability of any palaeointensity estimates obtained, and investigate probable magnetic remanence carriers within studied specimens. Such investigations could be conducted prior to any palaeointensity experiments, and published in isolation, a practice that could encourage greater variety in the nature of lithologies targeted for palaeointensity analysis.

This study has demonstrated the proficiency of rock magnetism techniques and microscopy analysis in assessing the extent of alteration experienced by specimens. It has also demonstrated the proficiency of less utilised palaeointensity techniques such as the Shaw-DHT and calibrated pseudo-Thellier method. Imparting full TRMs and comparing stepwise demagnetisation trends provided greater insight into the nature of non-multidomain grains that most likely carry a large proportion of the remanence. Furthermore, the agreement of Shaw-DHT results associated with minor alteration corrections, with estimates from non-heating methods, was interpreted as an indicator of thermal stability. Crucially, such methods are significantly quicker than conducting thermal Thellier experiments when completed with an automated alternating field demgnetisation system, such as the RAPID-2G. More detailed petrological analysis of

specimens than has been typical of palaeointensity studies, was also crucial in determining the likelihood of magnetic grains carrying a TRM. It would be recommended from this study, that similar methods be employed to any future investigations into the suitability and reliability of potential palaeointensity estimates.

Greater uptake of such methods will allow us to develop a greater understanding around the types of lithologies that may be appropriate for palaeointensity analysis and targets that should perhaps be avoided on account of their geological history. Wider application to all palaeointensity experiments will provide better evaluations around the likelihood of specimens carrying a TRM, a fundamental assumption of palaeointensity experiments. Often, this is currently assessed on the frequency of alteration textures, but with little thought to the likelihood of grains having formed below their Curie temperature. Misinterpretation of TRM acquisition can result in biased palaeointensity estimates being incorrectly interpreted as representative of geomagnetic field behaviour across a given time. This further impedes attempts to define palaeointensity across a given time interval, as appears likely to have been the case for the PCRS, and leads to greater difficulty in assessing long-term variations in the geomagnetic field.

Evaluating the Potential of Statistical Models

Assessing long-term variations in the geomagnetic field by generating and comparing optimised GGP models for distinct reversal regimes across a near-continuous time frame, was a novel approach used within this study. This has demonstrated how the use of palaeomagnetic observations alongside statistical models can provide greater insight into palaeomagnetic field behaviour than observations alone. Critical evaluation of the two in unison, allows the validity of palaeomagnetic observations and model assumptions to be tested and verified. If a future study were to investigate PSV between ca. 84 Ma and 25 Ma, the only time interval studied by McFadden et al. (1991) not to have been reanalysed, an optimised GGP model could be generated following the same approach as in this study, and the relative wealth of palaeointensity data that is available. The GGP models generated to represent the palaeomagnetic field during the time intervals analysed in this study, generally resulted in palaeomagnetic predictions that displayed a similar goodness of fit to the observed data. They were also approximately equal in their ability to simultaneously reproduce both PSV and palaeointensity observations. Failure of covariant-style GGP models to comparably predict palaeomagnetic observations across different time intervals, such as ca. 84 Ma to 25 Ma, would suggest either biases and inaccuracies in the palaeomagnetic observations, or inadequacy of the model assumptions across that time interval. Improving confidence in one of these by, for example, obtaining new palaeomagnetic data with modern techniques and methods, conducting an in-depth review of all palaeomagnetic observations across the studied time interval, or developing a more robust theoretical understanding of model assumptions and the opportunities for deviation from these, would reveal insight into the nature of the unique palaeomagnetic field behaviour.

The potential of the approach detailed above has been demonstrated within this study when assessing the potential reliability of data through observed trends in constructed GGP models. Constructing a GGP model around the VGP dispersion pattern that resulted from analysis of all extrusive data in the PDKRS database (Brandt et al., 2021), did not result in a statistical model that was capable of simultaneously describing both

PSV and palaeointensity observations. Improvement in this respect, when filtering through the use of intra-site statistics, was interpreted as evidence that the resulting, more extreme, PSV was in fact more representative of palaeomagnetic field behaviour during the PCRS. In a similar way, a slight reduction in the overall strength of the geomagnetic was inferred between ca. 265 Ma and 146 Ma. This was concluded under the assumption that the relationship between symmetric and antisymmetric terms, expressed as β, had remained broadly unchanged since the PCRS and that a reduction in palaeointensity across this time favoured such behaviour. In both instances, the conclusions reached were based on assumptions about consistent and contrasting aspects of geomagnetic field behaviour derived from observed trends in the parameters defining the different statistical models generated. Assuming that covariance-style models are valid in describing palaeomagnetic field behaviour for all studied time intervals, and that the relationship between families has remained approximately unchanged since the PCRS. Only with further investigation can the validity of these assumptions be better assessed. This will require more high-quality palaeomagnetic data, in particular palaeointensity estimates, and the development of geodynamo models that aim to simulate the inferred behaviour for given time intervals, and the more long-term evolution process. The latter would provide a better understanding as to the fundamental viability of the assumptions, and the consequences for deep Earth processes.

Appendix A. Supporting information for Chapter 2

Supporting information for: ***Analyzing Triassic and Permian Geomagnetic Paleosecular Variation and the Implications for Ancient Field Morphology*** *in Geochemistry, Geophysics, Geosystems.*

B. T. Handford, A. J. Biggin, M. M. Haldan, C. G Langereis

Introduction

The following supporting information describes the investigation into the effects of encompassing serial correlation and removing great circle derived directional data on the observed VGP dispersion pattern. These results are displayed in Figures A.1 and A.2 respectively, alongside accompanying descriptions (A.1. and A.2.). A description of Table A.2 is provided in which a commentary on source material is detailed, including on the use of analysis identifying serial correlation. Descriptions of datasets are also provided. These datasets are available through EarthRef Digital Archive (**ERDA/2481**, ERDA) and contain the full Post-PCRS and PCRS directional compilations after selection criteria 1-8 have been applied, as well as a breakdown of Van der Voo scoring of the source material.

Serial correlation & VGP dispersion

Combining site-mean directions into directional groups for the Post-PCRS, reduced just two datasets to an insufficient amount of data (PT13 & PT14). After a thorough review of all source material, only 3 datasets were found to contain data where there had been no consideration regarding serial correlation where it would have been relevant (Table A.2). The final database then, consists of 19 datasets, 16 of which, it can be confidently said, contain data that represent a unique geomagnetic field. As with the use of the other additional selection criteria, the general trend of VGP dispersion is very similar to that observed when all data is used (Figure A.1). It would appear that, at least for this study, the use of serially correlated data had little bearing on the result when taking the initial aims into consideration. An equivalent investigation was not possible for the PCRS as only 3 studies found reason to create directional groups (K01, K04, & K05, Table A.1), with K01 finding effects to be minor.

Great Circle Analysis & VGP Dispersion

A separate database was analysed for Group 1 Post-PCRS datasets in which all directions determined from great circle analysis were removed. This affected 7 datasets (K02, K03, K06, K07, K16, K20, & K21) but only K03 was left with an $N < 9$. With very similar datasets to the original database, VGP dispersion and the Model G fit were almost unchanged (Figure A.2). As expected, estimates of scatter remained relatively unchanged when datasets contained a small amount of great circle derived data (Table A.2). Greater differences in scatter estimates were observed when great circle data made up over 25% of the original data (K07, K16, K20; Table A.2). The inclusion of great circle data can lead to both overestimates and underestimates of scatter, and a greater percentage of great circle derived data does not necessarily mean a greater over/underestimate. K16 shows a greater discrepancy between the two estimates than K07, despite the proportion of great

circle data being half that of the latter. The effects can also be very large as demonstrated by K20 where the estimates differ by over 35%. It is worth noting that, as was the case when addressing serial correlation, the PCRS did not contain enough relevant datasets to allow the effects of great circle derived data to be assessed.

For this study the overall effects are minimal and so the removal of great circle site-mean data was not included as a selection criterion. This study has shown that the effects can be significant, however. These effects should be explored, especially if using a database where a majority of the datasets contain a large amount of great circle data.

Supporting Figures

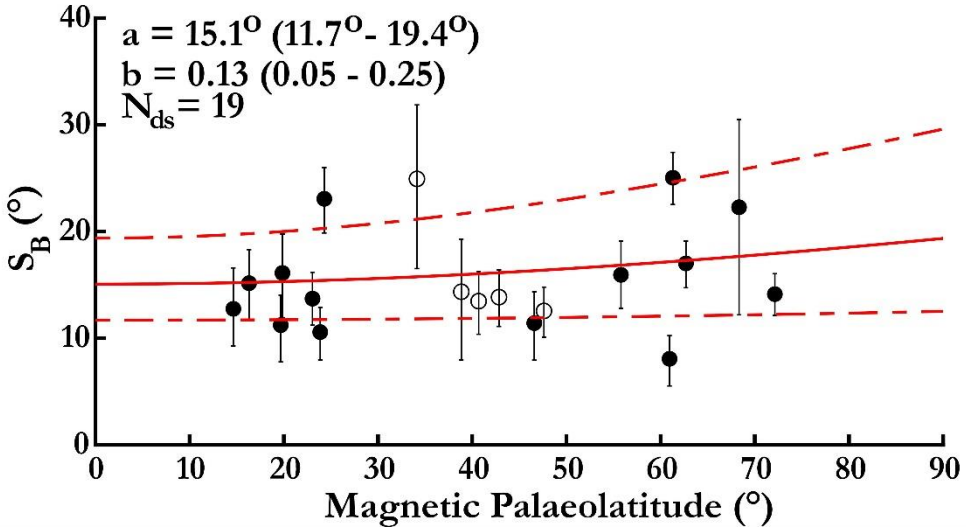

Figure A.1: Latitude dependence of virtual geomagnetic pole dispersion and Model G curves for the Post-PCRS (265-200 Ma), using Group 1 datasets and applying serial correlation according to information in Table A.1. For full description see the caption of Figure 2.1.

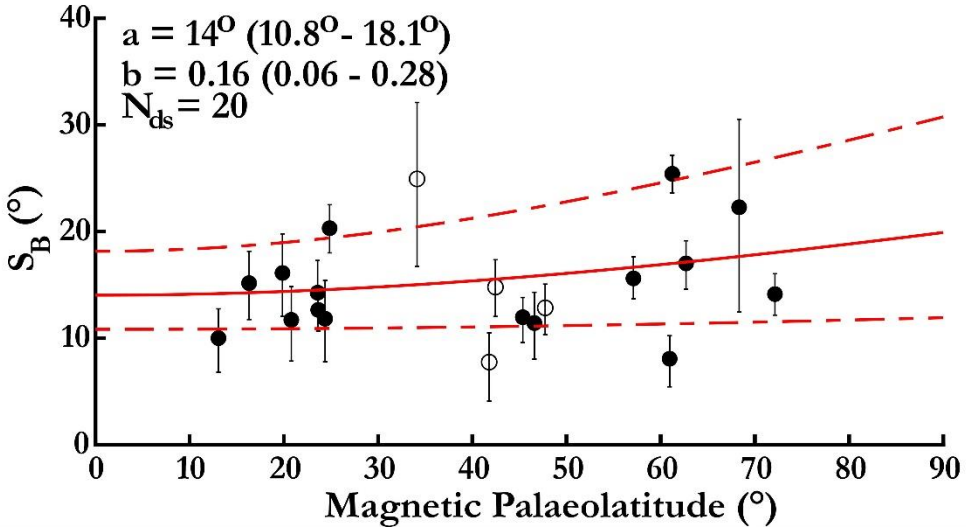

Figure A.2: Latitude dependence of virtual geomagnetic pole dispersion and Model G curves for the Post-PCRS (265-200 Ma), using Group 2 datasets and removing site-mean directions that use great circle data. For full description see the caption of Figure 2.1.

Supporting Datasets

Dataset A.1. Post-PCRS database.

Dataset A.2. PCRS database.

Dataset A.3. Van der Voo Q-scores for Post-PCRS and PCRS datasets.

The above datasets are openly available through the EarthRef Digital Archive (https://earthref.org/ERDA/2481, ERDA).

Supporting Tables

Table A.1: Effects of great circles on estimates of virtual geomagnetic pole (VGP) dispersion.

Code	**S_B original** (°)	**S_B NGC** (°)	**GC data** (%)
K02	25.2	25.4	2.5
K06	11.4	11.7	15.4
K07	10.6	11.8	50.0
K16	12.7	10.0	25.0
K20	11.9	7.7	50.0
K21	12.2	12.8	14.6

Note A.1: VGP dispersion (S_B) no great circles (NGC) shows the estimated scatter values with no great circle data included. Great circle (GC) Data gives the percentage of data in the original dataset that came from great circle analysis.

Table A.2: Commentary for PCRS and Post-PCRS datasets.

Code	Rock formation	References	Tectonic Correction	Serial Correlation
PT01	Qiangtang Block Middle Triassic Lavas	Song et al. (2020)	Bedding-tilt correction applied to lavas taken from both section A and section B, the two sections sampled in Song et al. 2020. Lavas from section A dip 25° SE and those from section B dip 36° NE. Tilt corrected group-mean directions show an improvement when compared to those from in situ measurements. Potential for a very slight tectonic effect between section A and section B however as there is no appreciable difference when either fold or rotation corrections were applied the dataset was still selected for this study.	Of the 28 site-mean directions presented, 13 were found to be indistinguishable to at least one other and as such they were split into 5 directional groups. This resulted in 20 mean directions. The approach used to identify sites followed that described by McFadden & Lowes. 1981, the grouping of directions followed the approach of Chenet et al. 2008.
PT02	Norilsk Region Volcanics	Pavlov & Fluteau. (2019), Pavlov et al. (2007), Gurevitch et al. (2004)	Bedding-tilt correction applied to all sites in both Pavlov & Fluteau. 2019 and Gurevitch et al. 2004, the later using average bedding dip for a given sampling region. No regional tilt could be determined for the Moyero River region (Pavlov et al. 2007), as such, no bedding-tilt correction was applied for these samples. Those taken from Kulumbe River were however subject to tectonic correction. The potential for unaccounted primary tilts of the Moyero River region could potentially cause higher scatter values however they make up a relatively small fraction of the overall dataset, reducing this effect if present.	Site mean directions belonging to the same "volcanic pulse" were attributed to the same directional group by Pavlov et al. 2019 following the approach used by Chenet et al. 2008. High Non-Random Ordering values among consecutive lava flows further indicate brief time gaps between their eruptions. There is no indication of this approach being used by Pavlov et al. 2007.
PT03	Los Menucos acidic dykes	Luppo et al. (2019)	No tectonic correction is applied. The dykes sampled are described as "sub-vertical" overlying "sub-horizontal" strata. As the underlying strata is the same for all of the acidic dykes there appears to be little need for a bedding-tilt correction, any variation in dip angle should be minimum and have very little effect on the final outcome.	No mention is made of exploring the possibility of serial correlation. The slower cooling rate of dykes should mitigate the occurrence however it does bring other potential issues with it.
PT04	Gezira & Bir Umhebal dyke complex	Lotfy & Elaal. (2018)	No bedding-tilt correction has been applied to the samples in this dataset and there is no mention of tectonic control.	No mention is made of exploring the possibility of serial correlation. The slower cooling rate of dykes should mitigate the occurrence however it does bring other potential issues with it.

PT05	Alto Paraguay Province	Ernesto et al. (2015)	No bedding tilt-correction has been applied due to difficulties identifying reference planes to estimate tilting. Sub-horizontal foliation planes given by AMS measurements were used to indicate the palaeohorizontal. Applying the bedding correction given by this placed the pole much closer to the Jurassic segment of the apparent polar wander path for the area, suggesting complete re-magnetisation for which it is argued there is no evidence. The lack of tectonic control could have resulted in higher scatter values.	The possibility of serial correlation is not addressed. Sampling sites are referred to as "independent", suggesting that the author did not appear to believe that serial correlation was occurring. It is not clear whether this was a conscious conclusion or something that was overlooked
PT06	Tasguint & Alezmi formations	Ruiz-Martinez et al. (2012)	Bedding tilt-correction applied to all samples. A bedding-tilt test was not found to be significant at the 95% confidence level however the correction does decrease ChRM scatter.	Consecutive flows were studied for serial correlation using the approach of McFadden & Lowes. 1981 resulting in 3 couples of grouped flows. The resulting difference was found to be minimal and as such the directional group statistics are not given.
PT07	Zguid & Ighrem dykes	Palencia-Ortas et al. (2011)	No bedding-tilt correction applied, the area has remained tectonically stable for the last 300 Myr (Palencia-Ortas et al. 2011), as such no correction should be necessary.	The possibility of directional groups is acknowledged however as only dykes were sampled no directional groups are given and instead issues regarding under sampling PSV are discussed.
PT08	Ukrainian Shield intrusions	Yuan et al. (2011)	No bedding tilt correction has been applied with the justification that the Ukrainian Shield has remained tectonically stable since the Permian. The dykes sampled intrude this shield.	There is no mention of serial correlation and it has not been explored, presumably as dykes have been sampled.
PT09	Puesto Viejo Group	Domeier et al. (2011b), Valencio et al. (1975)	Anisotropy of magnetic susceptibility (AMS) used to discriminate between primary and secondary bedding attitudes. Bedding-tilt correction applied accordingly (Domeier et al. 2011b). No bedding-tilt correction applied to sites taken from Valencio et al. (1975), few sites used from this study so the impact is likely very small if tilt correction would have been relevant.	Statistical checks were done for thick ignimbrite sequences. In some cases, a group of site-mean directions were indistinguishable at 95% confidence level, these sites were averaged at sample level (Domeier et al. 2011b).
PT10	South Taimyr Igneous Complex Intrusives	Walderhaug et al. (2005)	The sills sampled show variation in their dip, 8°-28° with the exception of one sill with a dip of 62°. A positive fold test demonstrated that the sills were flat lying during magnetisation, as such the correction was applied.	No statistical approach has been done to address the possibility of serial correlation. Intrusives were sampled at these sites where serial correlation is less likely to have occurred.

PT11	South Taimyr Igneous Complex Extrusives	Walderhaug et al. (2005)	A bedding-tilt correction has been applied to all samples depending on the dip of the strata. All flows show consistent dips of approximately 30° SSE.	No statistical approach has been done to address the possibility of serial correlation and as such no directional groups are given. The author uses the much greater scatter of the lava flows over the dykes to conclude that they give spot readings.
PT12	CAMP volcanics	Knight et al. (2004)	Bedding-tilt corrections were applied using the dips measured on bedding structures for each lava flow sampled.	Directional groups have been defined where the variation of the directional group is less than A_{95} of the mean group direction, and the jump in direction is greater than A_{95} of the previous group. Statistics of these directional groups is not presented.
PT13	Semeitau igneous series	Lyons et al. (2002)	No bedding-tilt corrections applied on the basis that the SIS has not been tilted significantly at site level or that of the entire complex. This was concluded from the shallow dips recorded from boreholes and the inconsistencies of these dips between different lithologies.	Serial correlation addressed for samples from the same "cooling unit". Any sites that were indistinguishable at the 95% confidence level (Watson. 1956) were interpreted as the same cooling unit to mitigate the effects from sampling the same unit at different localities. The author believed this to be a particular issue for ignimbrite and vitrophyre sites as the bodies would have likely cooled over huge areas.
PT14	Issaldain & Ait-Aadel dolorites	Hailwood. (1975)	No bedding-tilt corrections were applied to any of the volcanics. A tectonic correction was applied to the underlying sedimentary rocks which did reduce between-site scatter but was not significant at the 95% confidence level. The lack of correction could therefore have resulted in higher scatter however it does not appear that this would be significant.	The possibility of serial correlation was not explored, potentially due to the fact that dykes were sampled.
PT15	Dolomites Volcanics	Manzoni. (1970)	No bedding-tilt corrections applied for pillow basalts. Described as "flat-lying flows" in the literature so it was concluded that no correction was required.	Serial correlation was not taken into consideration likely due to the age of the paper. As lava flows have been sampled this should have been explored.
PT16	Niuhetang Formation	Zhao et al. (2015)	Bedding-tilt correction applied to all samples. Two-step unfolding procedure applied whereby general tilt correction first applied to declination values followed by a tilt correction with folding plunge axis (N148.9°, E29.7°). This was found to provide optimal concentration of ChRMs.	There is no direct mention of serial correlation. The author does conclude that the time-averaged field has been adequately sampled due to the comparable VGP dispersion with the last 5 Myr.

PT17	Tunguska Basin Intrusives	Latyshev et al. (2018), Konstantinov et al. (2014)	No bedding-tilt corrections applied to samples from either study. Basalt flows are described as "sub-horizontal" (Latyshev et al. 2018) and "usually residing on nearly flat-lying beds" (Konstantinov et al. 2014). Evidence that no tilt correction is required so there should be no effect on final scatter values.	Latyshev et al. 2018 explores the possibility of serial correlation but finds no evidence to support its existence in their samples from the Tunguska Basin.
PT18	Angara-Tasevva Intrusives	Latyshev et al. (2018)	No bedding-tilt corrections applied as flows sampled described as "sub-horizontal".	Two directional groups were presented for the Angara-Tasevva samples, Chuna and Uda. It is unclear whether or not the site mean directions in these groups are statistically indistinguishable.
PT19	East Siberian Traps	Kravchinsky et al. (2002)	No bedding tilt corrections applied as "most rocks have horizontal bedding". The only exceptions to this being a small number of sills in the original study which were not included in this final dataset.	There appears to be no mention of the possibility of serial correlation between site mean directions despite lava flows being sampled.
PT20	Sierra Chica Complex	Domeier et al. (2011a), Tomezzoli et al. (2009)	The uppermost sections of the Domeier et al. 2011b study were deemed to be unaffected by tectonic activity and so no correction was applied to the corresponding sites. The sites from the lower sections have been subjected to a tilt correction of approximately 25° to restore them to palaeohorizontal.	The possibility of serial correlation has not been directly addressed by Domeier et al 2011b but the possibility of oversampling volcanic events is discussed. Tight clustering of VGPs from the upper unit could suggest it represents one eruptive event, further suggested by a lack of features and cooling contacts. Conversely the middle and lower units are thinner with distinctive features and cooling contacts so are likely to represent a prolonged series of eruptions.
PT21	Upper Choiyoi Group	Domeier et al. (2011b)	Anisotropy of magnetic susceptibility (AMS) used to discriminate between primary and secondary bedding attitudes. Bedding-tilt correction applied accordingly (Domeier et al. 2011b).	Statistical checks were done for thick ignimbrite sequences. In some cases, a group of site-mean directions were indistinguishable at 95% confidence level, these sites were averaged at sample level (Domeier et al. 2011b).
K01	Bakaly formation	Bazhenov et al. (2016)	Tilt correction has been applied which sees a slight increase in data grouping but does not constitute a positive tilt test. Pre-folding age of ChRM has been previously established.	The possibility of serial correlation has been explored with the conclusion that any effects are likely minor. This has been determined by use of the NRO factor (Biggin et al., 2008), identifying loops and swathes, and testing for statistical similarity of studied flows.
K02	Koldar formation	Abrajevitch et al. (2008)	Calculated VGP agrees well with those of the same age range when the tilt correction has been applied to the directional data. This age range is the same as that assigned to the formation based on fossil content and stratigraphic relationships.	Cannot find any mention of serial correlation or possible directional groups.

K03	Lunner dykes	Dominguez et al. (2011)	No tilt correction has been applied as the sampling area has remained a stable part of the Baltic Shield since the Permian activity ceased. It is believed that no regional tilting has occurred since the intrusion of the studied dykes.	Serial correlation is less likely to occur when intrusives are sampled and so has not been considered.
K04	Vestfold Volcanic Plateau	Haldan et al. (2014)	Tilt corrections applied according to bedding orientation at each site.	Serial correlation has been explored and 2 directional groups created.
K05	Krokskogen Volcanic Plateau	Haldan et al. (2014)	Tilt corrections applied according to bedding orientation at each site.	Serial correlation has been explored and 6 directional groups created.
K06	Ukrainian Shield trachytes	Yuan et al. (2011)	Since the Ukrainian Shield has been deemed to have remained tectonically stable since the Permian no correction has been applied.	As only dykes have been sampled serial correlation has not been considered.
K07	Baoshan formation	Huang & Opdyke. (1991)	Tilt corrections have been applied according to orientation of the two syncline limbs sampled. In-situ site mean directions from the two limbs are well away from each other but form a well-defined group after the respective corrections.	Although flows have been sampled it does not appear that the possibility of serial correlation has been explored.
K08	Punta del Aua formation	Geuna & Escosteguy. (2004)	Tectonic correction has been applied to accommodate for folding associated with Andean orogeny. Corrections constitute a positive fold test.	Serial correlation has been mentioned but not thoroughly explored. The author believes that the wide distribution and thickness of the Rincón Blanco sites makes serial correlation unlikely.
K09	New England orogen	Opdyke et al. (2000)	Tilt correction has been used resulting in maximum k-values when unfolding is at 95-104%.	No mention of serial correlation.
K10	Gerringong Volcanics	Belica et al. (2017)	No bedding tilt correction applied as the sites sampled are within the southern Sydney Basin which is "largely flat-lying and undeformed". Agreement of calculated palaeopole with others of a similar age and location appear to suggest that the lack of tectonic correction is justified.	No mention regarding the possibility of serial correlation between sites despite flows being sampled and multiple sites representing the same units.
K11	Junggar Block dykes	Li et al. (1989)	No tilt correction applied as the sampled dykes are vertically dipping and the intruded pluton is believed to have remained stable. This conclusion was reached due to the varied orientation of the dykes and the slight tilting of the surrounding Mesozoic lithology due to the uplift of the pluton.	Serial correlation has not been investigated as dykes have been sampled.

K12	Biyoulitie super formation	Sharps et al. (1989)	Tilt correction has been applied and leads to the convergence of separate sections.	No mention of serial correlation despite lava flows being sampled.
K13	Bohemian Massif	Soffel & Harzer. (1991)	Bedding correction applied but was only necessary for 4 sites. As such it was not feasible to conduct a fold test.	No investigation into serial correlation as dykes were sampled.
K14	Sardo-Corso Massif intrusives	Vigliotti et al. (1990)	The vertical orientation of the dykes has led to the assumption that they have remained undisturbed from their original position, and so no tectonic correction has been applied.	Dykes have been sampled so an investigation into serial correlation was not required.
K15	Esayoo formation	Wynne et al. (1983)	Separate tilt corrections applied to the two different localities sampled. Correction of 63° at 163° applied at sites 12-20, and 29° at 225° at sites 21-25. The site mean directions from the two localities are in excellent agreement	No investigation into the possibility of serial correlation.
K16	Tabla formation	Jesinkey et al. (1987)	Samples were taken from the western limb of an upright syncline. Tilt correction was applied accordingly, 010°, 53°.	Cannot find any mention of serial correlation or possible directional groups.

Note A.2: Commentary discusses tectonic corrections applied to data in the original studies and the extent to which serial correlation was considered.

Appendix B. Supporting information for Chapter 3

Introduction

The following supporting information provides additional rock magnetic and microscopy data (Figures B.1 & B.5) that complement those presented and analysed within the main text of **Chapter 3**, alongside energy dispersive X-ray spectroscopy (EDX) data that provide additional support to the final interpretations (Figures B.2, B.3, & B.4). Results are presented that represent the investigation into the magnetic properties and remanence acquisition potential of secondary amygdales that is referred to in the main text (Figures B.6, B.7, & B.8; Table B.2).

The directional statistics determined from stepwise demagnetisations of specimens acquired from clasts of the Marmolada Conglomerate are presented in Table B.1. Palaeointensity statistics are also presented, according to each palaeointensity method utilised (Tables B.3, B.4, & B.5). The corresponding critical values are highlighted following the selection criteria outlined in the main text. A complete breakdown of the Q_{PI} score associated with each accepted site-level VDM estimate is also presented, alongside accompanying comments where appropriate (Table B.6).

Magnetic properties of amygdales

Individual amygdales were removed from bulk specimens (Figure B.6a) using a diamond drill bit that produced cores 5 mm in diameter. EDX analysis identified these as being calcite in composition (Figure B.4). Amygdales rarely exhibited a diameter much greater than that of the drill bit. Similarly, 5 mm cores were extracted from bulk specimens that constituted both bulk matrix material and amygdale. Such specimens are referred to as mixed micro-specimens, with each constituent part typically making up an equal proportion of the specimen. This approach was taken to investigate the influence of the secondary calcite material on the magnetic properties of a bulk specimen, in which it represented a relatively high proportion, in comparison to traditional 1-inch diameter cores.

The NRM of micro-specimens was measured with the SQUID magnetometers of a RAPID-2G system. For this, specimens were enclosed within non-magnetic sample holders reminiscent of the traditionally used 1-inch core (Figure B.6b). The electromagnetic unit (EMU) measured by the 2G system was normalised by the mass of each micro-specimen. Typically, the NRM of amygdale specimens was two orders of magnitude weaker than that of mixed micro-specimens (Figure B.7a; Table B.2). The weaker nature of amygdale specimens was also reflected in AF demagnetisation behaviour. Although amygdale specimens displayed a strong enough magnetisation to result in observable demagnetisation, resulting Zijderveld plots were noisy and no ChRM could be isolated (Figure B.8a, b). Conversely, demagnetisation of mixed specimens consistently resulted in Zijderveld plots in which two components of magnetisation could

be identified (Figure B.8c, d). IRM saturation values were determined from IRM acquisition curves acquired using a Variable Field Translation Balance (VFTB). Whole micro-specimens were used with no external holder required. The resulting EMU differs from that in which specimen NRM was expressed, but no direct comparison of the two values was required. Again, magnetisation values were mass normalised. Saturated IRM values were consistently much weaker for amygdale specimens (Figure B.7b), commonly differing by at least an order of magnitude (Figure B.7b; Table B.2).

In addition to the investigations into the magnetisation strength and acquisition potential of micro-specimens, estimates of Curie temperature were also determined from thermomagnetic curves. Curie temperatures obtained from mixed specimens were consistently lower than those obtained from mixed specimens, with the exception of one result (Table B.2). These estimated Curie temperatures lie within the temperature range in which significant demagnetisation of 1-inch bulk specimens occurred. In contrast, the typical Curie temperatures determined from amygdale specimens corresponded with temperatures by which the NRM of 1-inch bulk specimens had typically demagnetised by over 90%.

Overall, the seemingly insignificant contribution to the NRM from iron oxides hosted within calcite amygdales (Figure B.7a), and their reduced ability to acquire a remanent magnetisation when compared with iron-oxides hosted within the bulk matrix (Figure B.7b), suggests that these secondary iron-oxides would have negligible effects on any palaeointensity experiments. Estimates of Curie-temperatures associated with amygdale hosted iron-oxides, further demonstrate the minimal contribution of these grains to the magnetic properties of bulk specimens of the Fernazza Fm pillow lavas, when compared with bulk specimen demagnetisation behaviour.

Supporting Figures

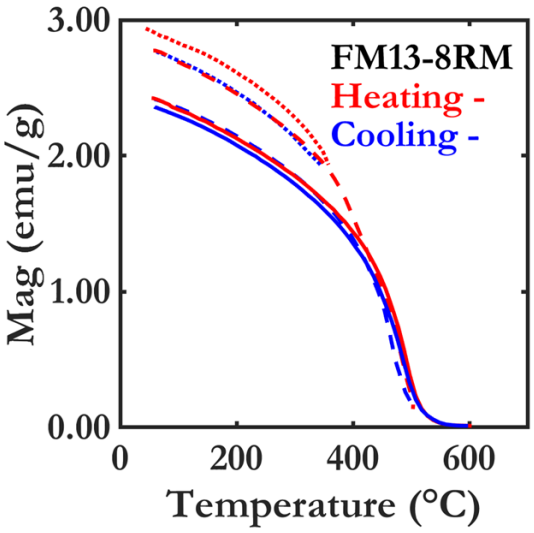

Figure B.1: Thermomagnetic curve resulting from cyclic heating steps. Heating up to temperatures of 350°C (dotted line), 500°C (dashed line), and 600°C (solid line). Broadly reversible behaviour is exhibited after the initial heating up to a temperature of 350°C. The cooling curve after heating up to 500°C displays reduced magnetisation when compared to the corresponding heating curve. Further heating up to 600°C reveals reversible behaviour.

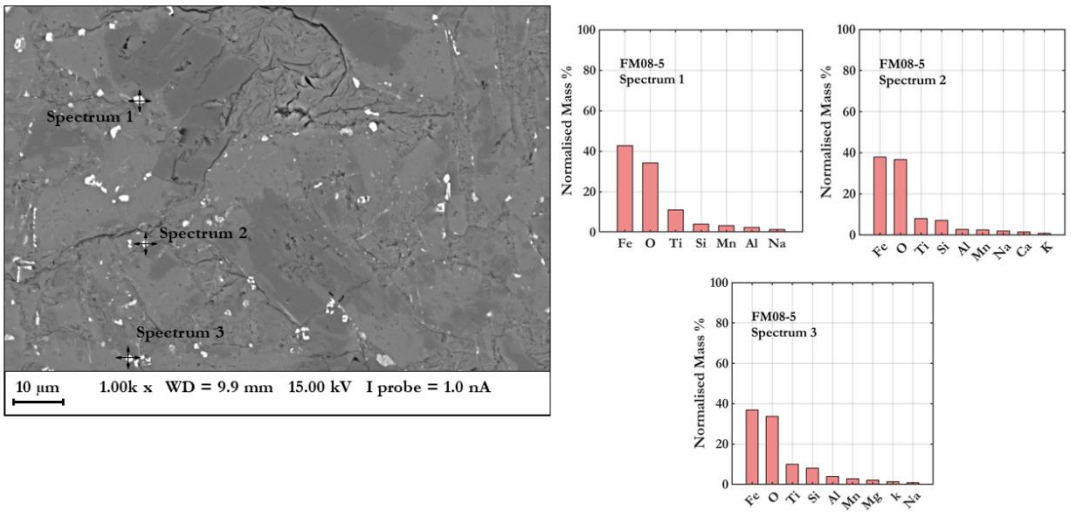

Figure B.2: SEM BSE image obtained from a thin section of specimen FM08-5 and corresponding EDX spectra representative of the highlighted areas. The normalised mass percentage of the most abundant elements are presented for each EDX spectra obtained.

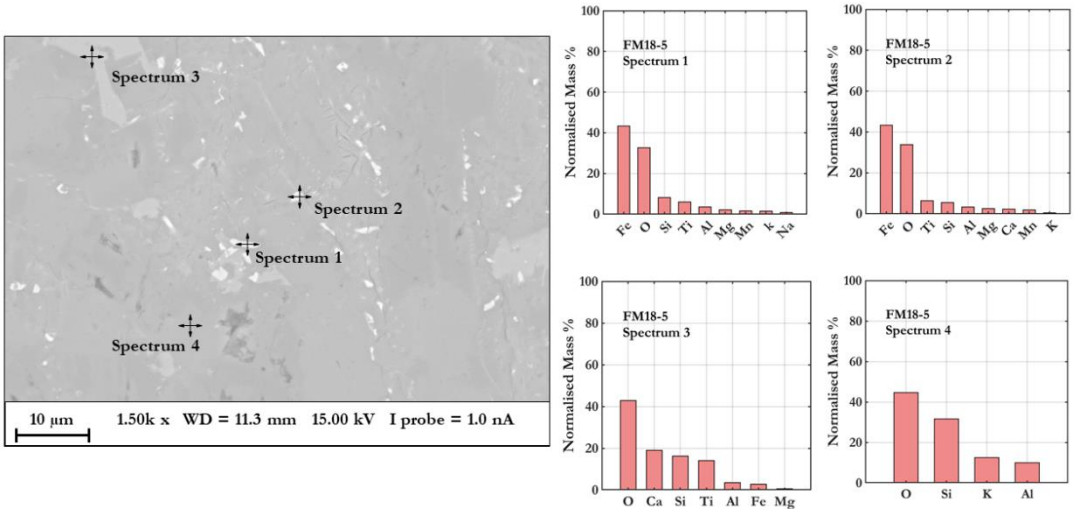

Figure B.3: SEM BSE image from a thin section of specimen FM18-5 and corresponding EDX spectra representative of the highlighted areas. The normalised mass percentage of the most abundant elements are presented for each EDX spectra obtained.

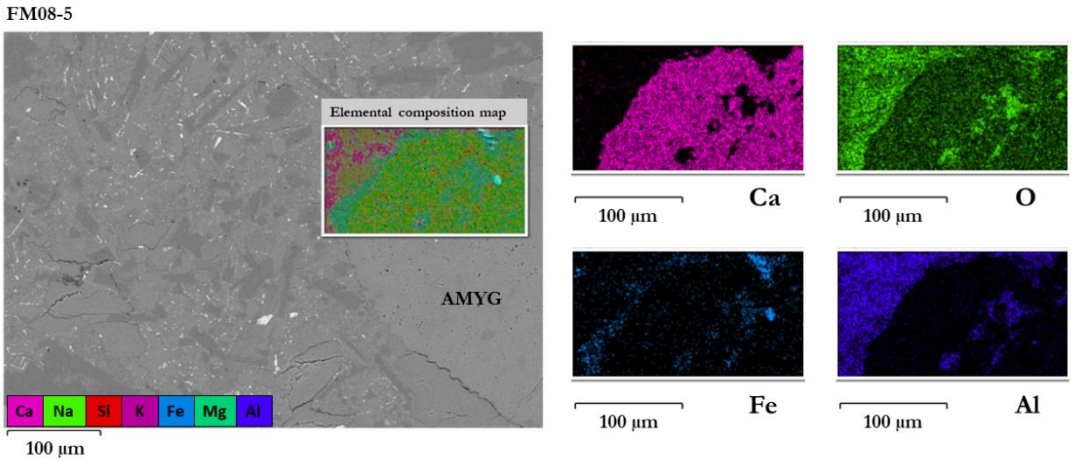

Figure B.4: SEM BSE image obtained from a thin section of specimen FM08-5. Image displays groundmass features and a secondary amygdale (AMYG). Layered elemental composition map overlays the SEM image. Separate elemental composition maps are presented for calcium (Ca, pink), oxygen (O, green), iron (Fe, blue), and aluminium (Al, purple).

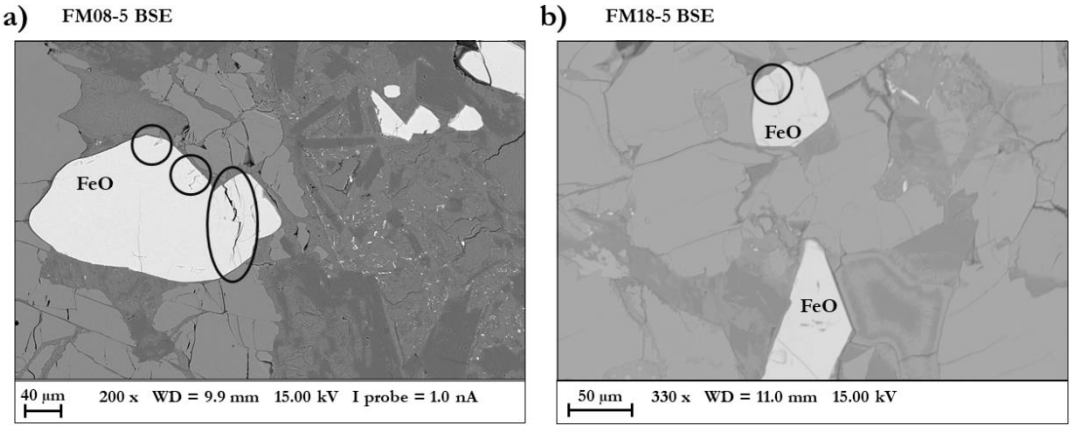

Figure B.5: SEM BSE image obtained from thin section of specimen a) FM08-5 and b) FM18-5. Iron oxides (FeO) highlighted in each that display some evidence of cracking around grain edges.

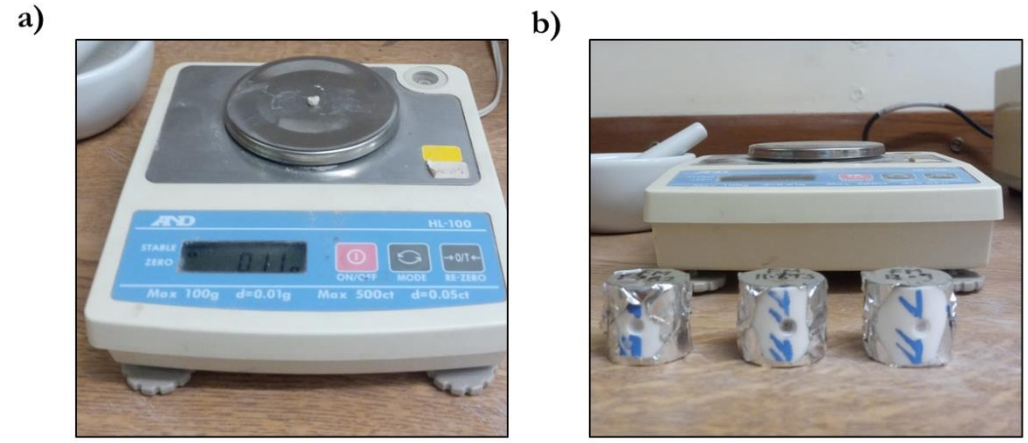

Figure B.6: Images that depict the process of sample preparation in order to conduct experiments on amygdales situated within specimens of the Fernazza Fm pillow lavas. a) An example amygdale situated on a mass balance, b) non-magnetic specimen holders in which amygdales were emplaced to allow measurement on the RAPID-2G system. Secured with aluminium tape.

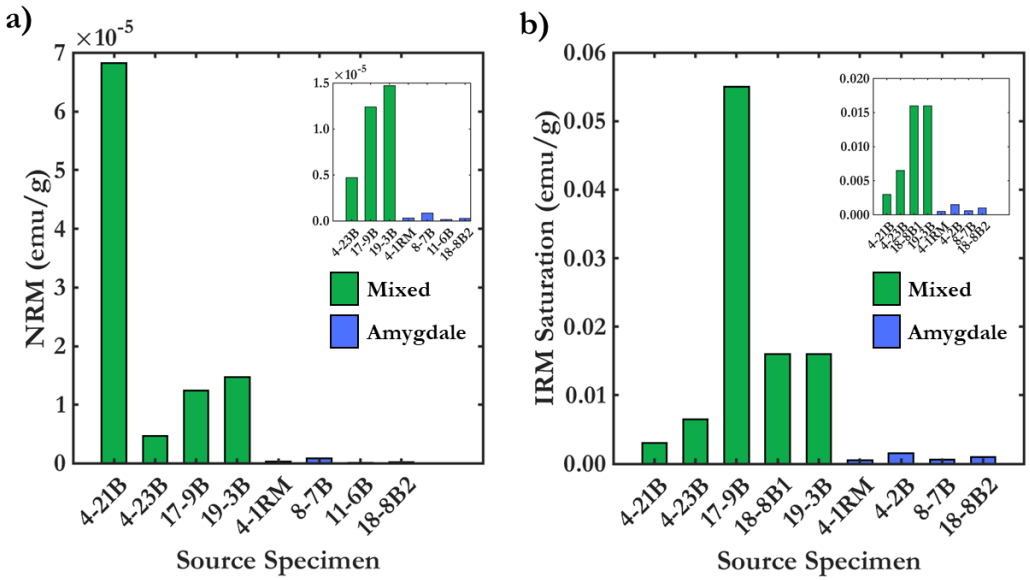

Figure B.7: Mass normalised magnetisation values of amygdales (blue) and mixed (green) micro-specimens. a) Natural remanent magnetisation (NRM), b) saturated isothermal remanent magnetisation (IRM). Inserted Figures represent the same data but with outlying values removed. This serves to facilitate easier visual comparison between typical magnetisation values of amygdale and mixed micro-specimens.

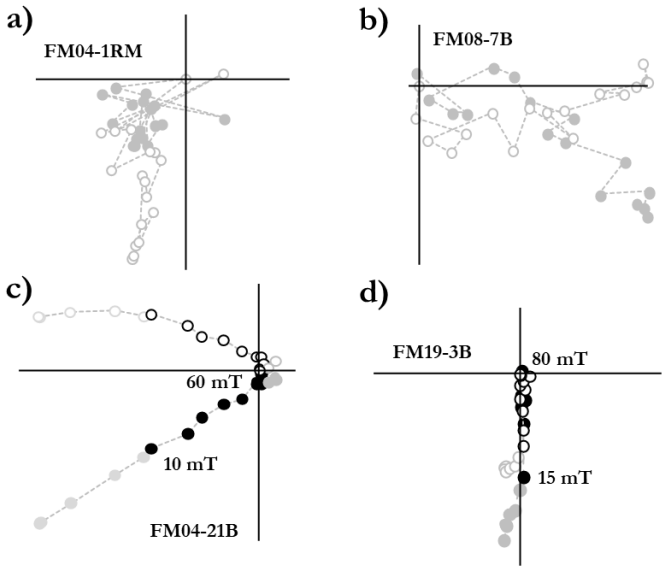

Figure B.8: Zijderveld plots representative of the AF demagnetisation behaviour of a, b) amygdale specimens, c, d) mixed micro-specimens. Black points represent an isolated characteristic remanent magnetisation (ChRM) component, and grey points represent overprints or undeterminable components.

Supporting Tables

Table B.1: Directional statistics of conglomerate test specimens.

Specimen(s)	Dec	Inc
FM01-1A	353.8	30.8
FM01-2A	216.4	10.5
FM01-3A	9.6	38.9
FM01-4B	57.2	32.4
FM01-5B	39.4	21.8
FM21-1A	222.1	-34.9
FM21-2A	255.6	62.5
FM21-3A	153.3	-11.8
FM21-4A	290.2	55.3
FM21-5A-6A	290.7	48
FM21-7B	333.6	32.8
FM21-8A	345.5	31.2
FM21-9A-10	135.9	-11.9
FM21-11-12	326.8	56.5
FM21-13-14	275.2	-8.2
FM21-17-18	43.6	-3.4
FM21-20	62.9	-52.6
FM21-21	56	-33
FM21-22	87.1	15.5
FM21-23	202	60.8
FM21-24	74.6	-7.2

Note B.1: Declination and inclination of isolated ChRM components obtained from clasts of the Marmolada Conglomerate. Mean statistics calculated when multiple specimens were obtained from the same clast. Such statistics are accompanied by all specimen level identifiers.

Table B.2: Overview of results from amygdale investigation.

Specimen	Specimen Type	NRM (emu/g)	Saturated IRM (emu/g)	T_C (°C)
FM04-21B	Mixed	6.83E-05	3.00E-03	512
FM04-23B	Mixed	4.71E-06	6.50E-03	591
FM17-9B	Mixed	1.24E-05	5.50E-02	513
FM18-8B1	Mixed	n/a	1.60E-02	531
FM19-3B	Mixed	1.47E-05	1.60E-02	542
FM04-1RM	Amygdale	3.24E-07	5.00E-04	563
FM04-2B	Amygdale	n/a	1.50E-03	591
FM08-7B	Amygdale	8.46E-07	6.00E-04	608
FM11-6B	Amygdale	1.54E-07	n/a	n/a
FM18-8B2	Amygdale	2.58E-07	2.58E-08	583

Note B.2: Specimen type indicates nature of micro-specimen as being either entirely amygdale or a mixture of amygdale and bulk matrix. Micro-specimen NRM and saturated IRM expressed as mass normalised values. T_C gives Curie temperatures estimated by application of the differential method to thermomagnetic curves.

Table B.3: Thermal Thellier results and critical values according to selection criteria outlined in the main text.

Specimen	B_{anc} (μT)	B_{lab} (μT)	T_{min} (°C)	T_{max} (°C)	n	α	MAD_{Anc}	f	β	q	k'	DRAT	CDRAT
FM04-1B	17.2	15	300	540	8	5.7	4.4	0.77	0.098	5.8	0.413	6.6	7.1
FM04-3A	10.9	15	450	570	9	1.8	3.9	0.96	0.038	18.4	0.057	11.7	15.2
FM04-4B	9.4	15	450	550	7	14.5	4.5	0.52	0.121	3.2	0.183	24.0	1.8
FM04-8B	7.5	15	450	570	9	14.7	11.9	0.89	0.097	7.5	0.448	25.3	39.9
FM04-10B	7.7	15	450	550	7	9.9	4.7	0.65	0.125	4.0	0.488	20.6	6.9
FM04-13C	8.1	30	450	620	11	15.1	12.9	0.82	0.084	7.9	0.670	26.9	11.2
FM04-16B	8.5	15	500	550	6	12.9	8.3	0.31	0.277	0.8	1.357	46.0	82.4
FM04-21C	17.3	30	400	620	13	6.9	4.9	0.81	0.075	9.0	0.165	14.3	3.0
FM05-1A	10.8	15	450	550	7	12.1	8.8	0.64	0.285	1.0	1.890	17.3	14.3
FM05-2A	7.6	15	450	570	9	26.7	15.9	0.85	0.173	4.0	0.950	19.7	39.4
FM05-3A	12.0	30	450	620	11	24.3	8.3	0.57	0.076	6.3	-0.337	15.3	18.8
FM05-5A	8.5	15	400	550	8	23.6	13.8	0.66	0.168	2.1	-1.353	13.8	4.4
FM05-6B	5.9	15	400	570	10	29.1	15.0	0.87	0.155	4.4	0.903	20.8	39.4
FM05-7B	8.6	30	400	620	13	17.6	8.6	0.80	0.055	12.4	0.256	7.9	1.2
FM05-8A	7.2	15	400	550	8	11.0	3.7	0.60	0.175	2.6	0.966	29.5	19.5
FM06-1A	18.5	15	400	550	8	6.5	7.0	0.78	0.241	1.9	1.911	19.1	15.8
FM06-2B	18.0	30	425	620	12	6.6	4.6	0.87	0.069	11.0	0.036	10.6	19.5
FM06-4A	5.5	15	400	570	10	4.9	15.9	0.84	0.253	1.2	2.201	31.7	43.8
FM06-5B	23.8	30	550	620	7	2.8	3.1	0.14	0.529	0.0	0.745	69.8	150.0
FM06-7A	13.8	15	400	550	8	6.8	4.8	0.91	0.237	2.9	1.338	40.4	35.1
FM06-8A	19.9	15	400	570	10	5.5	5.7	1.11	0.187	5.0	1.101	13.0	9.7
FM07-1A	5.2	15	510	550	5	13.7	6.4	0.31	0.172	1.3	-0.112	50.7	67.2
FM07-6A	11.2	15	450	570	9	0.5	1.1	0.89	0.098	6.6	-0.263	16.6	6.0
FM07-6B	32.1	30	550	620	7	0.6	0.5	0.69	0.014	41.8	-0.033	22.7	51.2
FM07-7B	8.2	30	500	620	9	2.9	5.7	0.70	0.159	3.7	-0.938	8.9	5.1
FM08-1B	5.9	15	450	570	9	4.7	10.0	0.85	0.136	3.8	-0.593	17.0	34.5
FM08-3A	8.6	15	400	570	10	2.0	3.8	0.89	0.060	10.6	-0.136	19.7	7.1

FM08-5B	13.8	30	450	620	11	6.7	4.9	0.78	0.098	6.9	-0.625	7.9	16.3	
FM08-6A	8.1	15	300	550	9	6.2	2.6	0.67	0.190	2.7	1.290	37.1	22.0	
FM08-7A	7.3	15	450	570	9	1.6	2.4	0.77	0.141	4.4	-0.734	10.9	19.2	
FM08-8B	10.3	15	400	570	10	3.8	4.0	0.92	0.095	7.8	0.055	13.9	23.3	
FM08-9B	16.8	30	350	600	13	5.8	2.7	0.73	0.070	9.0	0.145	5.7	2.9	
FM09-1A	3.6	15	400	550	8	20.1	7.9	0.67	0.253	1.9	1.319	44.9	16.6	
FM09-2B	24.8	30	560	620	6	1.8	2.9	0.15	0.314	0.4	0.792	48.6	66.7	
FM09-4A	29.8	15	510	550	5	10.7	5.9	0.12	0.302	0.3	0.492	128.0	113.7	
FM09-5B	-													
FM09-6A	5.1	15	400	550	8	9.2	2.2	0.45	0.201	1.7	0.979	37.2	20.9	
FM09-7A														
FM09-8B	10.2	30	350	600	13	6.0	3.0	0.74	0.100	6.4	-0.383	8.5	5.5	*
FM10-1B	10.4	30	425	620	12	5.7	6.0	0.84	0.101	7.3	-0.703	6.6	14.8	
FM10-2A	8.3	15	450	570	9	2.3	4.0	0.85	0.048	14.5	-0.176	13.2	8.0	
FM10-4B	9.7	15	300	570	11	4.2	3.5	0.91	0.111	6.9	0.357	17.9	31.0	
FM10-5A	5.9	15	450	550	7	3.2	2.4	0.35	0.120	2.1	0.032	24.8	2.0	
FM10-6A	7.7	15	300	570	11	3.7	4.1	0.93	0.061	12.8	-0.037	14.9	5.6	
FM10-6B	7.9	30	300	590	13	13.5	3.8	0.47	0.096	4.2	0.080	6.6	11.4	
FM10-7A	7.4	15	450	550	7	11.4	2.7	0.36	0.117	2.4	0.212	39.1	37.4	
FM10-8A	12.8	15	400	570	10	6.8	4.0	0.79	0.090	7.2	-0.069	15.8	33.5	
FM11-1A	-													
FM11-1B	46.9	30	475	620	10	2.4	4.0	0.88	0.215	2.6	1.806	28.0	22.6	
FM11-6B	21.9	30	400	620	13	4.8	5.8	0.90	0.079	9.6	-0.454	11.3	7.7	
FM13-1A	14.6	15	400	570	10	4.9	4.1	0.96	0.096	8.4	0.463	12.5	22.1	
FM13-2A	15.3	15	300	570	11	1.5	4.1	0.94	0.063	12.4	0.203	4.2	12.4	
FM13-2B	15.2	30	425	580	9	7.2	3.4	0.66	0.099	5.7	0.126	7.8	11.6	
FM13-3A	11.2	15	450	550	7	3.5	2.4	0.56	0.093	4.8	0.341	17.1	4.7	
FM13-6A	11.2	15	400	570	10	3.5	4.3	0.96	0.087	9.4	0.380	9.9	22.5	
FM13-7A	5.9	15	450	550	7	25.2	5.1	0.33	0.236	1.0	-0.856	19.2	16.1	
FM13-8A	4.1	15	400	550	8	12.0	2.1	0.25	0.129	1.6	-0.227	18.0	7.1	

FM13-9B	10.4	30	400	620	13	4.1	4.8	0.78	0.140	4.9	-1.053	12.0	12.4	
FM14-4A	2.8	15	450	550	7	13.9	14.0	0.55	0.352	1.0	-1.827	15.4	5.3	
FM14-4B	5.3	30	425	620	12	11.6	13.7	0.93	0.078	10.3	-0.156	4.0	0.1	**
FM14-6A	5.0	15	400	550	8	19.5	14.4	0.84	0.192	3.3	0.586	17.9	10.8	
FM14-8B	7.0	30	300	620	15	12.7	13.6	0.92	0.092	8.7	-0.291	3.0	3.2	**
FM15-1A	4.3	15	400	550	8	13.2	5.4	0.69	0.170	3.3	0.835	32.0	38.9	
FM15-4A	11.8	15	400	570	10	4.3	4.9	0.62	0.098	4.8	-0.519	86.4	104.1	
FM15-7B	13.3	15	520	550	4	40.6	2.9	0.11	0.312	0.2	-0.953	43.7	32.4	
FM16-2B	11.6	15	300	570	11	6.7	4.1	0.82	0.056	11.5	-0.186	7.6	21.8	
FM16-3A	13.1	15	500	550	6	3.3	1.3	0.51	0.056	6.4	0.076	9.9	11.5	
FM16-3B	11.7	30	500	620	9	0.2	0.8	0.78	0.052	12.5	-0.265	2.4	1.1	
FM16-4B	8.0	30	450	580	8	4.1	2.5	0.48	0.081	5.0	-0.423	6.5	9.0	
FM16-7A	10.7	15	450	570	9	8.5	9.3	0.88	0.079	8.6	0.278	15.3	17.0	
FM16-9A	16.4	15	510	550	5	18.2	5.7	0.34	0.113	2.2	0.620	26.4	47.6	
FM17-2A	10.7	15	450	570	9	7.6	8.5	0.87	0.087	8.0	-0.103	10.5	15.0	**
FM17-3A	10.0	15	400	570	10	3.0	7.5	0.93	0.129	6.1	0.417	11.3	17.3	
FM17-3B	11.0	15	400	550	8	16.0	7.4	0.62	0.109	4.5	-0.330	15.6	10.7	
FM17-4A	13.1	15	510	550	5	31.5	8.3	0.34	0.052	4.8	0.144	19.3	10.7	
FM17-5A	22.0	15	400	560	9	3.7	2.4	0.63	0.067	7.6	-0.216	7.6	12.4	
FM17-6A	16.0	15	450	570	9	0.4	3.4	0.94	0.055	14.0	-0.101	4.6	4.8	
FM17-7B	29.9	30	425	600	11	3.0	3.6	0.90	0.067	11.8	-0.472	3.8	10.1	
FM17-8B	26.7	30	400	580	10	4.2	3.4	0.79	0.096	7.0	-0.388	6.0	12.4	
FM18-1A	15.1	15	300	560	10	12.5	4.4	0.57	0.091	5.3	-0.327	5.5	10.9	
FM18-2A	14.5	15	450	570	9	0.3	2.7	0.90	0.045	17.0	0.076	6.2	10.3	
FM18-3A	17.9	15	300	550	9	28.9	15.3	0.75	0.087	7.3	0.432	3.9	8.3	
FM18-3B	15.5	15	400	550	8	8.3	2.9	0.60	0.090	5.6	0.335	9.7	14.9	
FM18-5A	8.1	15	450	570	9	7.6	7.0	0.85	0.073	10.1	0.193	10.2	13.7	***
FM18-6A	6.5	15	450	550	7	11.0	5.1	0.65	0.102	5.2	0.379	9.6	5.7	***
FM18-7B	5.7	30	425	620	12	3.9	6.2	0.97	0.068	12.4	-0.140	23.0	23.2	
FM18-8A	5.1	15	450	550	7	2.5	12.3	0.87	0.144	2.7	-0.417	14.1	10.7	

FM18-9B	5.7	30	400	570	9	14.4	9.9	0.72	0.087	6.7	-0.381	3.6	0.6	***
FM19-1A	6.2	15	450	550	7	3.0	5.3	0.91	0.110	6.0	0.100	7.0	11.0	***
FM19-3A	15.2	15	400	570	10	3.9	3.3	1.00	0.096	9.1	0.417	5.6	10.0	
FM19-5A	19.9	15	450	550	7	4.4	6.7	0.71	0.190	2.4	-0.968	15.8	6.6	
FM19-6B	22.9	15	450	550	7	9.4	5.0	0.55	0.156	2.8	-0.929	20.4	27.7	
FM19-7A	9.1	15	300	570	11	1.9	3.7	0.89	0.107	6.9	-0.679	9.9	10.6	
FM19-9A	9.2	15	450	550	7	3.2	2.7	0.61	0.058	8.0	-0.207	5.9	14.5	
FM19-9B	10.8	30	425	570	8	4.9	3.5	0.69	0.090	6.2	-0.415	5.1	5.9	
FM23-2A	6.7	15	450	550	7	2.5	10.9	0.97	0.109	6.6	0.453	21.6	32.3	
FM23-4B	-													
FM23-6A	11.2	15	400	550	8	3.1	4.8	1.00	0.183	4.3	0.639	27.7	50.1	
FM23-7A	-													
FM23-8B	-													

*Note B.3: Accepted palaeointensity estimates (B_{anc}) highlighted in green, estimates otherwise rejected due to failure of one of the selection criteria outlined in the main text. Where statistical parameters violate the critical limit, this is indicated (red) as is violation of the stricter critical limit but within the limits of the relaxed critical limit (amber). On occasion, selection criteria are fulfilled but final palaeointensity estimate if interpreted as being unreliable due to: *outlying nature, **evidence of multi-domain effects (highly zigzagging), ***2-slope behaviour.*

Table B.4: Shaw double heating technique (DHT) results and critical values according to selection criteria outlined in the main text.

Specimen	B_{anc} (μT)	B_{lab} (μT)	AF_{min} (mT)	AF_{max} (mT)	n	α	MAD_{Anc}	MAD_{Free}	β	f	k'_A	k'_N	k'_T	r^2_N	r^2_T	Slope-T
FM04-5C	10.6	30	10	100	13	0.6	1.5	1.5	0.048	0.81	0.153	0.354	0.024	0.974	0.998	1.09
FM04-10A	11.8	15	7	35	7	2.3	1.6	1.4	0.016	0.74	0.503	0.057	0.188	0.999	0.997	0.95
FM04-11A	11.2	15	10	80	9	0.8	1.0	1.0	0.083	0.55	0.123	0.475	0.211	0.952	0.991	1.21
FM04-11C	13.4	30	10	80	11	179.1	1.6	1.9	0.085	0.94	0.088	0.608	0.030	0.937	0.998	1.02
FM04-12A	13.3	15	5	30	7	2.4	2.1	3.3	0.024	0.76	0.545	0.163	0.189	0.997	0.997	0.97
FM04-13A	14.5	15	9	45	7	1.3	1.1	1.3	0.049	0.64	0.069	0.087	0.191	0.988	0.994	0.94
FM04-14A	13.9	15	7	60	10	0.8	1.5	2.0	0.038	0.81	0.235	0.019	0.194	0.988	0.994	0.98
FM04-15A	10.9	15	7	35	7	1.1	1.3	1.7	0.030	0.71	0.318	0.117	0.207	0.996	0.995	0.97
FM04-16A	13.4	15	5	80	12	0.6	1.2	1.6	0.028	0.93	0.185	0.030	0.076	0.992	0.999	0.99
FM04-17A	14.9	15	9	30	5	0.8	0.7	0.8	0.024	0.53	0.340	0.105	0.185	0.998	0.996	0.99
FM04-18A	11.7	15	9	50	8	0.6	1.2	1.5	0.051	0.62	0.019	0.092	0.155	0.985	0.995	1.01
FM04-19A	9.8	15	7	45	8	0.7	1.1	1.3	0.021	0.67	0.443	0.129	0.189	0.997	0.996	1.01
FM04-20A	13.2	15	9	40	7	0.9	1.0	0.9	0.029	0.56	0.406	0.120	0.157	0.996	0.995	1.09
FM04-21A	14.1	15	5	40	9	0.9	1.3	1.7	0.009	0.86	0.591	0.030	0.082	0.999	0.999	1.04
FM04-22A	13.9	15	5	45	9	0.8	1.2	1.4	0.008	0.85	0.792	0.056	0.061	1.000	0.999	1.05
FM04-23A	14.4	15	5	80	12	0.5	1.5	1.8	0.012	0.88	0.935	0.096	0.063	0.999	1.000	1.05
FM04-23C	18.5	30	5	80	12	0.4	1.5	1.6	0.056	0.95	0.231	0.455	0.234	0.969	0.985	0.99
FM05-1B	22.1	30	10	100	13	0.3	1.0	1.1	0.106	0.52	0.149	0.687	0.049	0.881	0.998	1.13
FM05-2B	17.7	15	7	50	11	0.6	1.4	1.9	0.030	0.61	0.608	0.024	0.077	0.992	0.996	1.00
FM05-3C	12.1	30	10	80	11	0.7	1.4	1.6	0.079	0.59	0.099	0.521	0.092	0.944	0.997	1.21
FM05-4B	18.1	15	13	80	11	0.8	1.3	1.1	0.155	0.34	0.005	1.010	0.015	0.794	0.983	1.09
FM05-5B	10.5	15	20	80	9	2.6	4.6	6.0	0.118	0.20	0.058	0.691	0.102	0.906	0.998	1.07
FM05-7A	17.0	15	9	80	13	0.2	1.4	1.9	0.067	0.50	0.071	0.005	0.069	0.952	0.999	1.03

FM05-7C	16.0	30	10	100	13	0.4	1.5	1.8	0.123	0.53	0.447	0.799	0.097	0.840	0.990	1.00
FM05-9C	18.4	15	9	40	9	0.1	0.8	1.4	0.036	0.48	0.116	0.157	0.069	0.991	0.988	1.09
FM06-2A	17.9	15	9	80	13	0.3	0.6	0.8	0.035	0.73	0.078	0.208	0.091	0.986	0.983	0.96
FM06-2B	23.8	30	7	45	7	1.1	1.3	1.4	0.041	0.58	0.209	0.106	0.098	0.991	0.998	0.97
FM06-6A	25.8	15	9	80	13	5.4	10.8	7.7	0.081	0.47	0.266	0.669	0.071	0.929	0.997	0.94
FM06-8B	13.5	30	15	80	10	0.6	1.2	1.3	0.060	0.61	0.167	0.404	0.301	0.971	0.630	5.30
FM06-9A	19.9	30	10	40	7	1.7	1.9	2.2	0.033	0.34	0.165	0.044	0.086	0.995	0.998	1.04
FM07-3B	13.5	30	13	80	10	6.0	13.4	9.4	0.170	0.30	0.457	0.998	0.053	0.783	0.998	1.19
FM07-8B	11.8	30	10	100	13	2.9	4.1	2.4	0.099	0.48	0.009	0.633	0.135	0.896	0.994	1.07
FM08-1C	14.7	30	10	100	13	0.5	2.0	2.3	0.097	0.87	0.209	0.713	0.116	0.899	0.996	0.96
FM08-1C	14.0	15	13	80	11	0.8	2.0	2.5	0.083	0.50	0.125	0.558	0.448	0.939	0.839	0.94
FM08-2B	12.0	15	7	80	14	0.8	1.7	2.1	0.018	0.81	0.304	0.080	0.073	0.996	0.999	0.99
FM08-3C	12.4	15	7	80	14	0.8	1.6	1.9	0.024	0.81	0.283	0.191	0.059	0.993	0.999	0.99
FM08-4B	12.9	15	7	80	14	0.4	1.4	1.8	0.024	0.85	0.468	0.131	0.086	0.993	0.999	0.98
FM08-5C	13.8	15	7	35	9	2.1	2.0	2.6	0.026	0.77	0.303	0.174	0.191	0.995	0.996	0.97
FM08-6C	13.1	15	7	80	14	0.5	1.1	1.5	0.041	0.90	0.225	0.319	0.052	0.980	0.999	0.87
FM08-7V	17.8	15	10	50	9	1.2	0.9	0.9	0.034	0.86	0.319	0.110	0.057	0.992	0.998	1.04
FM08-8C	-1.9	30	2	20	5	87.0	17.2	25.4	0.395	0.01	0.178	5.794	0.112	0.587	0.988	0.84
FM08-9C	23.2	30	5	100	14	0.2	0.9	1.1	0.062	0.97	0.397	0.553	0.209	0.954	0.994	0.97
FM09-3B	14.4	15	9	40	9	1.7	1.2	0.9	0.028	0.44	0.603	0.190	0.189	0.995	0.996	0.92
FM09-4C	15.7	30	5	100	14	0.6	2.6	2.9	0.028	0.94	0.587	0.031	0.140	0.991	0.996	0.96
FM09-6C	15.2	30	15	45	6	0.9	1.0	1.2	0.045	0.50	0.049	0.206	0.099	0.992	0.996	1.01
FM09-7D	19.2	30	10	35	6	1.2	1.1	1.2	0.049	0.73	0.285	0.018	0.014	0.990	1.000	0.94
FM10-1A	15.7	15	10	45	8	1.2	1.0	1.2	0.039	0.60	0.129	0.114	0.113	0.991	0.998	0.91
FM10-2B	20.0	15	13	45	7	1.3	1.2	1.6	0.035	0.45	0.146	0.079	0.027	0.994	0.999	0.91
FM10-3B	-635.7	30	15	60	8	0.6	0.9	1.4	0.411	1.22	0.198	1.708	2.148	0.243	0.064	-0.09

FM10-5B	10.5	15	5	80	15	0.6	1.2	1.7	0.009	0.94	0.229	0.012	0.110	0.999	0.999	1.08
FM10-7B	16.5	30	15	100	12	0.6	1.0	1.0	0.029	0.73	0.384	0.167	0.070	0.992	0.999	0.98
FM10-8B	16.9	15	5	80	15	0.5	0.9	1.1	0.038	0.99	0.007	0.365	0.093	0.981	0.998	0.88
FM10-9B	16.9	30	10	100	13	0.4	0.9	0.9	0.069	0.89	0.332	0.551	0.182	0.949	0.995	1.01
FM11-2B	16.0	30	15	100	12	0.1	0.5	0.6	0.009	0.56	0.187	0.003	0.165	0.999	0.993	1.03
FM11-3C	18.2	30	20	100	11	0.1	0.4	0.5	0.026	0.37	0.172	0.189	0.105	0.994	0.994	1.05
FM11-4C	8.2	30	20	100	11	2.1	5.3	5.8	0.078	0.34	0.239	0.560	0.091	0.945	0.995	1.11
FM11-5B	15.4	15	7	60	12	0.2	0.4	0.5	0.017	0.59	1.022	0.002	0.085	0.997	0.997	0.98
FM11-7A	13.9	15	13	80	11	0.7	0.9	1.3	0.156	0.92	0.748	0.905	0.178	0.794	0.984	0.88
FM11-8A	16.7	15	13	80	11	0.8	1.2	1.4	0.079	0.74	0.317	0.560	0.113	0.945	0.996	0.97
FM11-9A	11.2	15	25	80	8	0.6	0.5	0.5	0.031	0.52	0.334	0.178	0.066	0.994	0.999	1.03
FM11-11B	29.6	15	15	50	7	0.2	0.2	0.4	0.035	0.63	0.007	0.177	0.119	0.994	0.998	0.90
FM11-13B	20.8	15	20	60	7	0.3	0.3	0.4	0.022	0.58	0.143	0.092	0.037	0.998	0.999	0.91
FM13-1C	18.0	15	9	45	9	0.3	0.3	0.5	0.032	0.68	0.037	0.200	0.115	0.993	0.997	0.89
FM13-2C	21.1	30	5	100	14	0.1	0.8	0.9	0.097	1.04	0.171	0.792	0.042	0.889	0.998	1.00
FM13-6B	5.8	30	25	100	10	0.8	1.5	1.7	0.067	0.41	0.021	0.457	0.165	0.965	0.993	0.93
FM14-1A	17.2	15	9	80	13	0.9	1.7	1.9	0.070	0.52	0.378	0.502	0.467	0.947	0.878	1.02
FM14-2B	14.2	15	5	80	15	0.5	0.9	1.0	0.033	0.89	0.584	0.198	0.087	0.986	0.998	0.95
FM14-3B	12.6	30	7	100	13	1.8	2.7	1.8	0.065	0.46	0.037	0.263	0.129	0.954	0.996	0.87
FM14-5B	17.9	30	5	50	9	1.0	2.7	3.3	0.035	0.94	0.214	0.090	0.107	0.991	0.997	0.99
FM14-6B	13.5	15	9	45	9	1.4	1.2	0.8	0.037	0.47	0.234	0.087	0.006	0.990	0.998	0.99
FM15-1B	21.5	15	7	50	11	0.5	0.9	1.1	0.028	0.61	0.817	0.146	0.129	0.993	0.998	1.03
FM15-1C	14.4	30	7	80	11	0.3	1.2	1.4	0.104	0.79	0.090	0.701	0.054	0.905	0.997	1.15
FM15-2B	24.0	15	7	40	10	0.8	1.1	1.5	0.025	0.66	0.758	0.150	0.179	0.995	0.998	0.95
FM15-3C	15.3	30	7	80	11	0.8	1.2	1.2	0.141	1.03	0.197	0.984	0.101	0.828	0.998	1.05
FM15-5B	12.9	30	10	100	13	0.8	1.5	1.5	0.099	1.10	0.327	0.768	0.042	0.896	0.999	1.09

FM15-6A	9.3	15	15	80	10	6.3	3.7	1.2	0.103	0.76	0.439	0.679	0.208	0.917	0.957	0.03
FM15-7C	13.9	30	10	100	13	0.7	1.5	1.6	0.136	1.02	0.027	1.003	0.126	0.806	0.997	1.03
FM16-1B	14.5	15	15	60	8	1.4	1.2	0.6	0.037	0.57	0.210	0.193	0.175	0.992	0.995	0.98
FM16-2C	15.7	30	7	80	11	0.5	0.7	0.6	0.017	0.96	0.295	0.104	0.052	0.997	1.000	0.95
FM16-3C	18.4	30	10	100	13	0.2	0.4	0.4	0.054	0.67	0.413	0.299	0.076	0.968	0.998	1.05
FM16-5B	19.9	15	9	50	10	0.3	0.5	0.7	0.032	0.70	0.057	0.126	0.134	0.992	0.996	0.93
FM16-8A	16.1	15	9	80	13	0.7	1.2	1.4	0.041	0.83	0.307	0.294	0.229	0.982	0.992	0.96
FM17-1B	12.4	15	9	40	9	1.3	1.4	1.5	0.026	0.46	1.217	0.179	0.190	0.995	0.997	1.02
FM17-2B	0.6	15	7	80	14	0.7	1.6	1.9	0.061	0.55	1.614	0.548	1.963	0.956	0.019	15.62
FM17-4B	29.3	30	5	80	12	0.1	0.3	0.4	0.117	1.12	0.150	0.874	0.184	0.867	0.991	1.01
FM17-6B	15.1	30	10	100	13	0.1	0.7	0.8	0.125	0.76	0.255	0.917	0.179	0.836	0.993	1.05
FM17-7A	17.2	15	9	80	13	0.7	1.2	1.1	0.062	0.61	0.593	0.475	0.161	0.958	0.991	1.02
FM18-2B	20.6	15	10	80	12	0.8	1.4	1.4	0.065	0.63	0.325	0.394	0.275	0.958	0.989	1.22
FM18-5B	18.1	30	15	60	8	0.5	0.8	1.4	0.036	0.57	0.652	0.158	0.063	0.992	0.999	0.94
FM18-6B	16.5	30	10	80	11	0.3	0.6	0.9	0.008	0.98	0.684	0.003	0.023	0.999	0.998	0.98
FM18-7C	14.3	30	10	80	11	0.9	1.4	1.9	0.036	0.71	0.780	0.045	0.005	0.989	1.000	0.96
FM18-8C	10.0	15	9	40	9	1.0	0.9	0.8	0.030	0.57	0.308	0.175	0.151	0.994	0.997	1.04
FM18-9A	13.9	15	9	45	9	0.8	0.9	1.0	0.022	0.50	0.410	0.072	0.198	0.997	0.996	0.96
FM19-2A	11.9	15	7	70	13	0.5	0.5	0.6	0.029	0.89	0.000	0.119	0.099	0.991	0.998	0.99
FM19-3B	21.0	30	15	50	7	1.2	0.9	1.1	0.038	0.79	0.397	0.163	0.079	0.993	0.999	0.92
FM19-5B	20.5	15	7	45	10	0.3	0.7	1.1	0.022	0.59	1.411	0.166	0.061	0.996	0.997	1.03
FM19-7B	14.2	30	10	40	7	1.5	1.8	1.8	0.041	0.51	0.260	0.045	0.183	0.991	0.995	0.98
FM19-8A	17.8	15	9	80	13	0.4	1.1	1.3	0.035	0.64	0.663	0.118	0.487	0.986	0.965	1.09
FM23-1C	16.2	15	9	80	13	0.2	1.1	1.5	0.069	0.28	1.126	0.173	0.277	0.948	0.988	1.15
FM23-2C	11.2	15	9	80	13	0.5	1.7	2.1	0.027	0.30	1.076	0.157	0.258	0.992	0.987	1.17
FM23-3C	12.4	15	7	80	14	0.6	1.6	2.0	0.041	0.51	1.155	0.336	0.464	0.980	0.969	1.00

FM23-4C	30.7	30	7	80	11	0.9	1.3	0.9	0.103	0.22	0.927	0.036	0.358	0.907	0.987	1.06
FM23-5B	22.3	15	10	80	12	0.5	0.9	1.1	0.041	0.35	1.024	0.021	0.131	0.983	0.998	1.17
FM23-6B	22.8	30	10	100	13	0.8	1.6	1.4	0.111	0.33	0.760	0.390	0.090	0.870	0.996	1.13
FM23-7B	36.4	30	10	100	13	0.8	1.4	0.7	0.076	0.27	1.065	0.262	0.377	0.937	0.980	1.10

Note B.4: Accepted palaeointensity estimates (B_{anc}) highlighted in green, estimates otherwise rejected due to failure of one of the selection criteria outlined in the main text. Violation of the stricter critical limit but within the limits of the relaxed critical limit is highlighted (amber). k' and r^2 presented for NRM-TRM1 (N) and TRM1-TRM2* (T).*

Table B.5: Pseudo- Thellier results and critical values according to selection criteria outlined in the main text.

Specimen	B_{anc} (μT)	B_{lab} (μT)	AF_{min} (mT)	AF_{max} (mT)	b	σb	$B_{1/2ARM}$	n	α	MAD_{Anc}	β	R^2	R^2_{AA}	R^2_{DD}	k'	k'_{AA}	k'_{DD}	b_{AA}	f	f_{resid}
FM4-5C	11.9	35	10	40	-1.111	0.026	14.3	7	1.2	1.4	0.024	0.997	0.999	0.998	-0.083	0.000	0.077	-0.981	0.61	0.04
FM4-10A	12.8	35	10	40	-1.204	0.032	17.6	8	1.1	0.9	0.026	0.996	0.998	0.998	0.190	0.032	0.142	-0.987	0.67	0.10
FM4-11A	16.3	35	13	40	-1.530	0.024	15.6	7	1.1	0.9	0.016	0.999	0.999	1.000	0.030	0.004	0.026	-1.045	0.46	0.06
FM4-11C	15.7	35	10	60	-1.474	0.035	16.4	9	1.0	1.5	0.024	0.996	0.999	0.997	0.067	-0.031	0.096	-0.956	0.70	0.06
FM4-12A	13.8	35	9	60	-1.297	0.030	14.7	11	0.5	1.0	0.023	0.995	0.997	0.999	0.125	0.076	0.044	-0.954	0.74	0.02
FM4-13A	14.3	35	13	50	-1.344	0.034	17.1	8	0.9	0.7	0.025	0.996	0.999	0.998	0.153	0.059	0.092	-0.998	0.56	0.05
FM4-14A	16.1	35	13	50	-1.513	0.042	16.6	8	0.6	0.5	0.028	0.995	0.998	0.999	0.186	0.088	0.092	-1.017	0.53	0.06
FM4-15A	11.3	35	10	40	-1.056	0.027	13.7	8	0.9	0.9	0.026	0.996	0.996	0.998	0.058	0.113	0.052	-0.983	0.62	0.03
FM4-16A	17.8	35	7	60	-1.664	0.035	16.5	12	0.3	0.7	0.021	0.996	0.998	0.999	0.152	0.115	0.032	-1.045	0.81	0.02
FM4-17A	14.5	35	10	50	-1.359	0.030	12.9	9	0.5	0.6	0.022	0.997	0.999	0.998	0.068	0.004	0.064	-0.952	0.64	0.04
FM4-18A	11.1	35	10	40	-1.040	0.025	13.0	8	0.8	1.2	0.024	0.997	0.998	0.999	0.076	0.039	0.039	-0.966	0.59	0.06
FM4-19A	10.0	35	7	50	-0.937	0.018	11.9	11	0.6	1.0	0.019	0.997	0.997	0.999	0.085	0.128	0.044	-0.956	0.77	0.02
FM4-20A	12.9	35	9	70	-1.213	0.026	12.2	12	0.2	0.7	0.021	0.996	0.998	0.999	0.090	0.053	0.037	-0.920	0.68	0.01
FM4-21A	15.0	35	7	50	-1.403	0.030	12.8	11	0.7	1.0	0.021	0.996	0.998	0.999	0.173	0.092	0.077	-0.924	0.83	0.02
FM4-22A	15.8	35	7	60	-1.479	0.032	11.8	12	0.7	1.2	0.022	0.995	0.997	0.999	0.179	0.134	0.042	-0.938	0.81	0.02
FM4-23A	14.3	35	9	70	-1.340	0.029	10.9	12	0.5	1.0	0.022	0.995	0.996	0.999	0.176	0.161	0.011	-0.900	0.62	0.01
FM4-23C	16.4	35	10	60	-1.539	0.040	12.2	9	1.1	1.5	0.026	0.995	0.998	0.999	0.058	0.055	0.003	-0.851	0.61	0.02
FM5-1B	18.9	35	10	40	-1.770	0.041	10.8	7	0.5	0.8	0.023	0.997	0.999	0.998	0.136	0.039	0.100	-0.875	0.47	0.12
FM5-2B	14.5	35	9	80	-1.362	0.025	9.6	13	0.6	1.4	0.018	0.996	0.999	0.997	0.122	0.030	0.090	-0.882	0.54	0.03
FM5-3C	13.9	35	5	100	-1.298	0.015	9.4	14	0.4	1.4	0.012	0.998	0.998	0.998	-0.017	0.037	0.052	-0.897	0.83	0.00
FM5-4B	16.6	35	10	80	-1.560	0.079	8.8	12	0.2	0.9	0.051	0.975	0.994	0.950	0.259	-0.148	0.451	-0.860	0.47	0.07
FM5-5B	13.7	35	13	80	-1.285	0.048	8.5	11	1.4	2.6	0.037	0.988	0.996	0.990	0.178	0.011	0.219	-0.839	0.31	0.04
FM5-7A	13.6	35	10	80	-1.279	0.019	9.8	12	0.5	1.6	0.015	0.998	0.970	0.976	0.078	0.139	0.093	-0.899	0.49	0.01

FM5-7C	15.5	35	10	60	-1.455	0.035	11.8	9	0.3	1.3	0.024	0.996	0.999	0.997	0.092	0.014	0.078	-0.919	0.55	0.05
FM5-9C	13.5	35	10	80	-1.264	0.044	12.4	12	0.6	1.0	0.034	0.988	0.997	0.996	0.164	0.069	0.093	-0.895	0.62	0.03
FM6-2B	18.5	35	10	100	-1.734	0.079	14.8	13	0.6	1.5	0.046	0.977	0.992	0.995	0.356	0.181	0.166	-0.912	0.74	0.02
FM6-8B	17.2	35	10	60	-1.609	0.043	14.6	9	1.0	1.9	0.026	0.995	0.998	0.999	0.122	0.074	0.049	-0.924	0.71	0.03
FM6-9A	12.5	35	10	100	-1.168	0.015	9.7	13	0.6	2.0	0.013	0.998	0.999	1.000	0.077	0.045	0.031	-0.865	0.48	0.00
FM7-1B	13.2	35	15	100	-1.235	0.086	9.0	12	5.4	11.5	0.070	0.952	0.987	0.954	0.353	-0.022	0.468	-0.789	0.29	0.10
FM7-3B	10.3	35	20	100	-0.967	0.056	10.2	11	7.1	10.5	0.058	0.970	0.991	0.985	0.129	0.048	0.183	-0.874	0.22	0.01
FM7-8B	9.8	35	10	100	-0.914	0.024	10.1	13	0.8	2.2	0.026	0.993	0.997	0.987	0.163	-0.065	0.226	-0.820	0.51	0.04
FM8-1C	17.6	35	10	50	-1.651	0.049	14.6	8	1.7	2.2	0.030	0.995	0.996	0.996	0.164	0.004	0.142	-0.927	0.64	0.07
FM8-1C	14.9	35	9	80	-1.396	0.031	14.0	13	1.9	3.8	0.022	0.995	0.999	0.998	0.152	0.040	0.106	-0.912	0.76	0.03
FM8-2B	14.6	35	9	60	-1.370	0.029	13.9	11	0.9	1.3	0.021	0.996	0.996	0.999	0.134	0.105	0.022	-0.970	0.72	0.01
FM8-3C	14.9	35	9	70	-1.398	0.029	13.6	12	0.9	1.4	0.021	0.996	0.998	0.999	0.189	0.115	0.070	-0.953	0.73	0.01
FM8-4B	14.9	35	9	60	-1.397	0.033	13.7	11	0.8	1.5	0.023	0.995	0.997	0.999	0.164	0.084	0.078	-0.947	0.75	0.02
FM8-5C	15.7	35	10	30	-1.467	0.032	14.1	6	2.2	1.5	0.022	0.998	0.999	0.998	0.124	-0.006	0.126	-0.981	0.58	0.09
FM8-6C	17.9	35	9	60	-1.678	0.033	18.7	11	0.9	1.1	0.020	0.996	0.999	0.997	0.154	0.007	0.137	-1.026	0.78	0.05
FM8-7C	29.7	35	10	60	-2.784	0.060	23.5	10	0.9	0.9	0.022	0.996	0.998	0.999	0.139	0.106	0.030	-1.025	0.85	0.03
FM8-8C		35			-															
FM8-9C	24.6	35	10	35	-2.306	0.077	16.8	6	1.2	1.1	0.033	0.996	0.998	0.999	0.194	0.115	0.080	-0.980	0.69	0.09
FM9-3B	12.0	35	7	80	-1.129	0.014	10.3	14	0.9	1.3	0.012	0.998	0.997	0.999	0.021	0.112	0.081	-0.861	0.70	0.00
FM9-4C	14.5	35	10	100	-1.362	0.026	9.3	13	0.8	1.8	0.019	0.996	0.997	0.997	0.117	0.083	0.030	-0.860	0.45	0.01
FM9-6C	17.1	35	10	40	-1.600	0.046	13.3	7	1.3	1.6	0.029	0.996	0.998	0.999	0.155	0.094	0.062	-0.931	0.61	0.05
FM9-7D	19.2	35	5	40	-1.800	0.049	15.0	8	1.3	1.7	0.027	0.996	1.000	0.996	0.154	0.012	0.144	-0.968	0.90	0.10
FM10-1A	16.8	35	10	35	-1.579	0.036	16.1	7	0.8	0.8	0.023	0.997	0.999	0.998	0.120	-0.007	0.119	-1.004	0.61	0.10
FM10-2B	21.9	35	7	60	-2.056	0.045	15.7	12	1.3	1.7	0.022	0.995	0.998	0.998	0.177	0.070	0.104	-1.005	0.85	0.04
FM10-3B	19.7	35	10	50	-1.845	0.049	20.7	8	1.2	1.2	0.027	0.996	0.999	0.998	0.135	0.034	0.098	-1.020	0.70	0.08
FM10-5B	17.3	35	9	50	-1.623	0.035	19.9	10	1.2	1.1	0.022	0.996	0.998	0.999	0.179	0.120	0.055	-1.005	0.81	0.02

FM10-7B	19.4	35	5	100	-1.822	0.065	18.4	14	0.4	0.9	0.036	0.985	0.988	0.996	0.250	0.079	0.151	-0.970	0.98	0.03
FM10-8B	22.7	35	2	80	-2.123	0.064	19.4	16	0.4	0.8	0.030	0.987	0.999	0.993	0.290	0.078	0.212	-0.980	1.03	0.04
FM10-9B	19.5	35	10	50	-1.825	0.049	18.2	8	0.7	0.7	0.027	0.996	0.998	0.999	0.133	0.069	0.062	-0.967	0.77	0.05
FM11-2B	20.5	35	10	50	-1.922	0.047	14.1	8	0.5	0.9	0.024	0.996	0.998	0.999	0.105	0.112	0.007	-0.937	0.70	0.03
FM11-3C	26.1	35	10	60	-2.445	0.063	14.2	9	0.3	0.7	0.026	0.995	0.996	0.997	0.111	0.163	0.054	-0.890	0.72	0.01
FM11-4C	12.6	35	20	100	-1.178	0.048	10.8	11	2.2	5.5	0.041	0.985	0.996	0.990	0.147	0.016	0.243	-0.783	0.20	0.03
FM11-5B	16.9	35	7	20	-1.583	0.051	8.5	6	0.6	0.4	0.032	0.996	0.999	0.998	-0.175	-0.069	0.099	-0.850	0.56	0.00
FM11-7A	16.2	35	7	80	-1.516	0.079	31.7	14	0.9	1.1	0.052	0.967	0.995	0.985	0.478	0.159	0.331	-1.017	0.97	0.07
FM11-8A	25.2	35	7	40	-2.357	0.049	21.0	10	1.6	1.2	0.021	0.997	0.999	0.997	0.152	0.004	0.153	-1.047	0.81	0.12
FM11-9A	15.7	35	13	40	-1.475	0.025	29.3	7	3.0	2.1	0.017	0.999	0.999	0.999	-0.006	0.014	0.019	-1.114	0.57	0.14
FM11-11B	34.9	35	7	70	-3.269	0.068	22.7	13	0.2	0.3	0.021	0.995	0.999	0.999	0.094	0.085	0.004	-1.026	0.92	0.03
FM11-12A	30.1	35	9	80	-2.824	0.054	25.0	13	0.1	0.2	0.019	0.996	0.996	1.000	0.146	0.180	0.038	-1.009	0.92	0.00
FM11-13B	29.0	35	9	70	-2.719	0.060	24.1	12	0.3	0.5	0.022	0.995	0.997	0.999	0.089	0.101	0.014	-1.025	0.90	0.01
FM13-1C	20.0	35	7	80	-1.872	0.085	16.2	14	0.3	0.5	0.045	0.975	0.997	0.986	0.442	0.100	0.330	-0.993	0.91	0.05
FM13-2C	22.6	35	10	35	-2.114	0.062	15.4	6	0.4	0.3	0.029	0.997	0.999	0.996	0.128	-0.056	0.172	-0.972	0.62	0.14
FM13-6B	13.7	35	5	30	-1.286	0.045	15.0	6	1.4	1.5	0.035	0.995	0.999	0.997	0.200	0.067	0.138	-0.996	0.82	0.14
FM14-1A	18.5	35	7	30	-1.737	0.047	9.8	8	2.2	1.7	0.027	0.996	0.997	0.998	0.089	-0.044	0.120	-0.869	0.58	0.13
FM14-2B	12.1	35	2	80	-1.135	0.012	11.4	16	0.2	0.7	0.010	0.999	0.996	0.996	-0.033	0.135	0.164	-0.941	1.00	0.01
FM14-3B	10.2	35	10	100	-0.960	0.010	11.3	13	0.2	1.5	0.011	0.999	0.997	0.999	0.070	0.128	0.056	-0.912	0.56	0.00
FM14-5B	15.2	35	5	100	-1.422	0.029	11.5	14	0.5	2.7	0.020	0.995	0.997	0.998	0.169	0.107	0.054	-0.921	0.92	0.01
FM14-6B	12.0	35	7	60	-1.129	0.023	10.8	12	1.3	1.6	0.020	0.996	0.997	0.999	0.175	0.135	0.034	-0.907	0.72	0.03
FM14-8A	11.6	35	7	80	-1.089	0.009	10.5	14	0.9	1.6	0.009	0.999	0.997	0.999	0.075	0.124	0.048	-0.882	0.73	0.01
FM15-1B	17.8	35	7	80	-1.666	0.035	10.1	14	0.3	0.9	0.021	0.995	0.998	0.996	0.101	-0.047	0.148	-0.869	0.70	0.04
FM15-1C	16.0	35	10	40	-1.504	0.027	12.7	7	1.0	1.2	0.018	0.998	0.999	0.996	0.060	-0.060	0.111	-0.970	0.56	0.02
FM15-2B	20.6	35	7	40	-1.926	0.045	11.6	10	0.8	1.1	0.023	0.996	1.000	0.997	0.190	0.036	0.147	-0.921	0.71	0.08
FM15-3C	20.4	35	10	40	-1.908	0.058	18.9	7	1.9	1.4	0.030	0.995	0.999	0.998	0.178	0.069	0.107	-1.011	0.66	0.14

FM15-5B	20.8	35	5	40	-1.945	0.046	20.8	8	1.9	1.4	0.024	0.997	1.000	0.996	0.152	-0.022	0.184	-1.028	0.85	0.15
FM15-6A	14.1	35	9	40	-1.323	0.024	21.9	9	0.4	0.9	0.018	0.998	0.999	0.997	0.118	-0.061	0.183	-1.024	0.66	0.13
FM15-7C	20.2	35	0	40	-1.892	0.044	18.7	10	1.4	1.6	0.023	0.996	0.999	0.995	0.135	0.051	0.086	-1.044	0.95	0.13
FM16-1B	18.4	35	9	80	-1.726	0.036	18.6	13	0.4	0.7	0.021	0.995	0.997	0.999	0.137	0.113	0.022	-0.977	0.83	0.02
FM16-2C	18.1	35	5	100	-1.699	0.032	19.1	14	0.3	0.7	0.019	0.996	0.996	0.997	0.057	0.150	0.103	-0.980	0.96	0.00
FM16-3C	22.3	35	5	40	-2.087	0.049	17.9	8	0.9	1.1	0.023	0.997	1.000	0.996	0.007	0.045	0.044	-1.000	0.87	0.15
FM16-5B	18.7	35	7	80	-1.751	0.086	15.5	14	0.6	0.9	0.049	0.972	0.996	0.985	0.471	0.136	0.315	-0.955	0.90	0.06
FM16-8A	17.4	35	5	70	-1.629	0.032	14.8	14	1.2	1.5	0.020	0.995	0.998	0.999	0.151	0.103	0.046	-0.968	0.95	0.03
FM17-1B	12.1	35	9	80	-1.133	0.017	9.2	13	0.3	1.1	0.015	0.997	0.997	0.995	-0.108	0.076	0.177	-0.764	0.51	0.01
FM17-2B	13.0	35	10	80	-1.218	0.056	8.8	12	0.2	1.0	0.046	0.979	0.996	0.987	-0.337	-0.070	0.270	-0.752	0.44	0.02
FM17-4B	27.4	35	5	50	-2.571	0.060	18.9	9	0.2	0.3	0.024	0.996	0.998	0.999	0.114	0.092	0.020	-1.028	0.93	0.07
FM17-6B	21.3	35	5	40	-1.999	0.046	13.6	8	1.1	1.5	0.023	0.997	0.999	0.998	0.115	0.010	0.108	-0.986	0.90	0.09
FM17-7A	19.8	35	5	50	-1.858	0.038	11.4	12	1.2	1.4	0.020	0.996	0.998	0.997	0.103	0.094	0.005	-0.889	0.91	0.06
FM18-2B	22.0	35	9	60	-2.059	0.033	12.3	11	1.3	1.5	0.016	0.998	0.998	0.998	0.092	0.008	0.078	-0.900	0.66	0.05
FM18-5B	14.8	35	15	100	-1.383	0.108	28.2	12	0.2	0.8	0.078	0.940	0.994	0.968	0.623	0.186	0.433	-0.984	0.83	0.07
FM18-6B	18.3	35	10	100	-1.715	0.109	31.1	13	0.4	0.7	0.063	0.956	0.995	0.978	0.527	0.161	0.371	-1.018	0.98	0.06
FM18-7C	12.6	35	15	100	-1.177	0.079	27.2	12	0.7	1.2	0.067	0.955	0.994	0.979	0.550	0.178	0.356	-1.026	0.79	0.05
FM18-8C	11.0	35	10	80	-1.027	0.021	12.2	12	0.5	0.8	0.021	0.996	0.996	0.999	0.138	0.157	0.025	-0.870	0.62	0.01
FM19-3B	26.6	35	10	50	-2.497	0.047	25.5	8	1.4	1.4	0.019	0.998	0.999	0.998	0.014	-0.059	0.074	-1.023	0.75	0.03
FM19-7B	9.8	35	15	100	-0.920	0.055	11.9	12	1.6	2.9	0.060	0.964	0.994	0.978	0.338	0.058	0.337	-0.893	0.37	0.04
FM19-8A	15.1	35	10	50	-1.415	0.039	11.5	9	1.1	1.4	0.027	0.995	0.997	0.999	0.170	0.137	0.035	-0.900	0.56	0.05
FM23-1C	12.4	35	7	80	-1.163	0.036	6.7	14	0.9	1.4	0.031	0.988	0.991	0.986	-0.206	0.130	0.295	-0.800	0.46	0.02
FM23-2C	9.4	35	9	80	-0.880	0.025	7.6	13	1.0	2.0	0.029	0.991	0.996	0.994	-0.186	-0.007	0.202	-0.787	0.34	0.02
FM23-3C	10.5	35	7	80	-0.981	0.029	7.7	14	1.0	1.9	0.029	0.990	0.995	0.987	-0.237	0.105	0.293	-0.861	0.54	0.03
FM23-4C	15.0	35	5	100	-1.405	0.041	8.4	14	0.1	0.4	0.029	0.990	0.995	0.978	-0.272	0.138	0.366	-0.852	0.77	0.02
FM23-5B	17.2	35	7	80	-1.614	0.034	8.5	14	0.2	0.6	0.021	0.995	0.997	0.994	-0.189	0.017	0.182	-0.801	0.61	0.01

FM23-6B	18.6	35	10	100	-1.741	0.029	8.2	13	0.9	1.7	0.017	0.997	0.991	0.996	-0.099	-0.155	0.068	-0.780	0.34	0.03
FM23-7B	21.1	35	5	100	-1.975	0.057	7.9	14	0.2	1.2	0.029	0.990	0.994	0.976	-0.272	0.199	0.413	-0.858	0.76	0.01

Note B.5: Accepted palaeointensity estimates (B_{anc}) highlighted in green, estimates otherwise rejected due to failure of one of the selection criteria outlined in the main text. Where statistical parameters violate the critical limit, this is indicated (red). k' and r^2 presented for pseudo-Arai plot (k', r^2), ARM-ARM (k'_{AA}, r^2_{AA}), and demag-demag (k'_{DD}, r^2_{DD}).

Table B.6: Breakdown of Q_{PI} scores.

Site	Q_{AGE}	Q_{STAT}	Q_{TRM}	Q_{ALT}	Q_{MD}	Q_{ACN}	Q_{TECH}	Q_{LITH}	Q_{MAG}	Q_{DIR}	Q_{PI}	Additional Comments
FM03	1	1	0	1	1	0	1	0	1	1	7	FM04-21C was affected by the specimen not reaching temperature at higher temperatures. This has resulted in change in slope at 'high temperatures' which is unlikely to be a real feature as it is not observed in any other sets of experiments. Strong agreement with all other results suggests palaeointensity estimate has not been affected and so estimate has been included.
FM04											0	
FM05	1	1	0	1	1	0	1	0	1	0	6	Similar scenario to FM04-21C regarding maximum temperatures. In this case IZZI result shows general agreement with other results and so is combined with Shaw to present final estimate.
FM06											0	
FM08	1	0	0	1	1	0	1	0	1	1	6	
FM09	1	1	0	1	1	0	0	0		1	5	FM09-8B passes IZZI criteria but experienced experimental error. Only Shaw results were included in final VDM estimate.
FM10	1	0	0	1	1	0	1	0	1	1	6	Agreement between IZZI results even though FM10-6B affected by the ongoing temperature issue. Sister specimen in 15 μT field produces almost identical result suggesting that the intensity estimate was not affected. Agreement between different methods is worse than for previous sites, this will be reflected in larger σ.
FM11	1	0	0	1	1	0	1	0	1	0	5	General agreement suggestive of stronger field. IZZI result is well within range of results from other methods but slope behaviour is far from ideal.
FM13	1	1	0	1	1	0	1	0	1	0	6	IZZI results from sister specimens but with different applied fields. There is good agreement with results that marginally fail however (FM13-1A, FM13-3A, FM13-6A), suggesting the value to be representative. Also, good agreement with other methods from different specimens. Results are very limited from this site but strengthened by overall general agreement with other sites

FM14	1	0	0	1	1	0	0	0		1	4	Two IZZI specimens pass but are affected by temperature issue. As there are no other results for comparison and they do not agree with results from other methods they are deemed unreliable. This is further strengthened by the similarity of Shaw & P-T results with other sites
FM15											0	Insufficient results for VDM estimate but results show general agreement with those from other sites.
FM16	1	0	0	1	0	0	1	0	1	0	4	Passing Arai plots show two-slope behaviour not associated with directional change -- MD effects likely. One specimen (FM16-2B) does much more ideal Arai plot (like previous) and estimated PINT is very similar but marginally fails CDRAT. Estimates from P-T & Shaw higher which could suggest underestimate from IZZI due to MD effects. Combined but failed Q_{MD}.
FM17	1	0	0	1	1	0	1	0	1	0	5	Another IZZI result marginally passes but is highly zigzagging and produces lower estimate (than IZZ and other methods) therefore was not included in final estimate. P-T agrees relatively well but Shaw less so -- only n of 1 so maybe not so reliable but also would expect better agreement (domain independent). Perhaps Shaw often has a range and works better with multiple? Look int Shaw for this
FM18	1	1	0	1	1	0	1	0	1	0	6	Rest of passing Arai plots (18-5a, 18-6a, 18-9b) show two-slope behaviour and appear to underestimate - likely due to MD. Sister specimens from Shaw do not underestimate in this way demonstrating domain state independence of the method.
FM19	1	0	0	1	0	0	1	0	1	0	4	Maybe a couple of Arai plots slightly 2-slope (19-9A, 19-9B) which could have led to underestimates from IZZI, associated with change in direction so maybe not MD effects? Cautiously failed Q_{MD}. Agreement with other methods improves if these estimates are not included.

Note B.6: Indication of pass or fail of each Q_{PI} category according to the corresponding criteria. Value of 1 indicates a pass and 0 a fail, final Q_{PI} score reflects the sum of these values. Additional comments provide rationale behind more complicated decisions and additional information on accepted palaeointensity estimates.

Appendix C. Supporting information for Chapter 4

Introduction

The following supporting information provides additional rock magnetic and microscopy (Figure C.9) data that complement those presented and analysed within the main text of **Chapter 4**, including isothermal remanent magnetisation (IRM) acquisition curves (Figures C.2 & C.6). Thermomagnetic and susceptibility versus temperature curves demonstrate the combinations and variations of rock magnetic behaviour from the broad classifications outlined in the main text (Figures C.2 & C.5). Energy dispersive X-ray spectroscopy (EDX) data provide additional support to the final interpretations (Figures C.3, C.7, C.8). Pseudo-Arai plots are presented (Figure C.4) and additional insight is provided into specimen behaviour of basalt sills of Puesto Viejo during thermal Thellier experiments (Figure C.10).

Estimates of Curie temperature (T_C) are presented from specimens of Los Menucos and Puesto Viejo (Tables C.1 & C.5), determined from thermomagnetic curves using the differential method (Tauxe, 1998). Specimen level palaeointensity statistics are presented, according to each utilised palaeointensity method (Tables C.2, C.3, C.4, C.6, C.7, & C.8). The corresponding critical values are highlighted following the selection criteria outlined in the main text. A complete breakdown of the Q_{PI} score associated with each accepted site-level V(A)DM estimate is also presented Table (C.7).

Supporting Figures

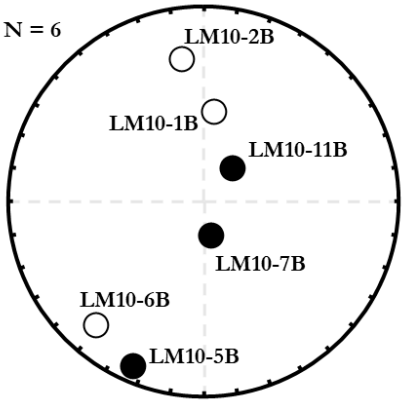

Figure C.1: Example of a dyke sampling site (LM10) at which the ChRM directions that were isolated demonstrated poor internal consistency. Closed/open circles define positive/negative inclinations.

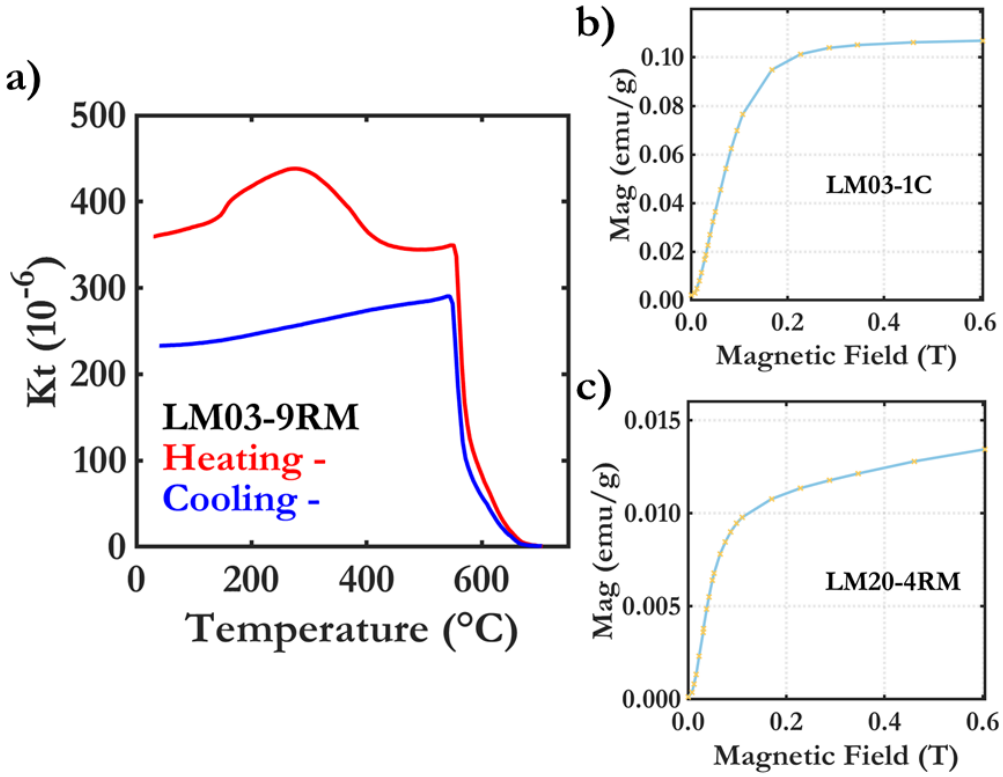

Figure C.2: Additional rock magnetic results from Los Menucos specimens. a) Example of a susceptibility versus temperature curve from a specimen displaying LMIA type behaviour, with the addition of a second phase at higher unblocking temperatures as indicated by the continual decrease above ~600°C. (b & c) Typical isothermal remanent magnetisation (IRM) acquisition curve for specimens displaying a) LMIA type behaviour b) LMIB type behaviour.

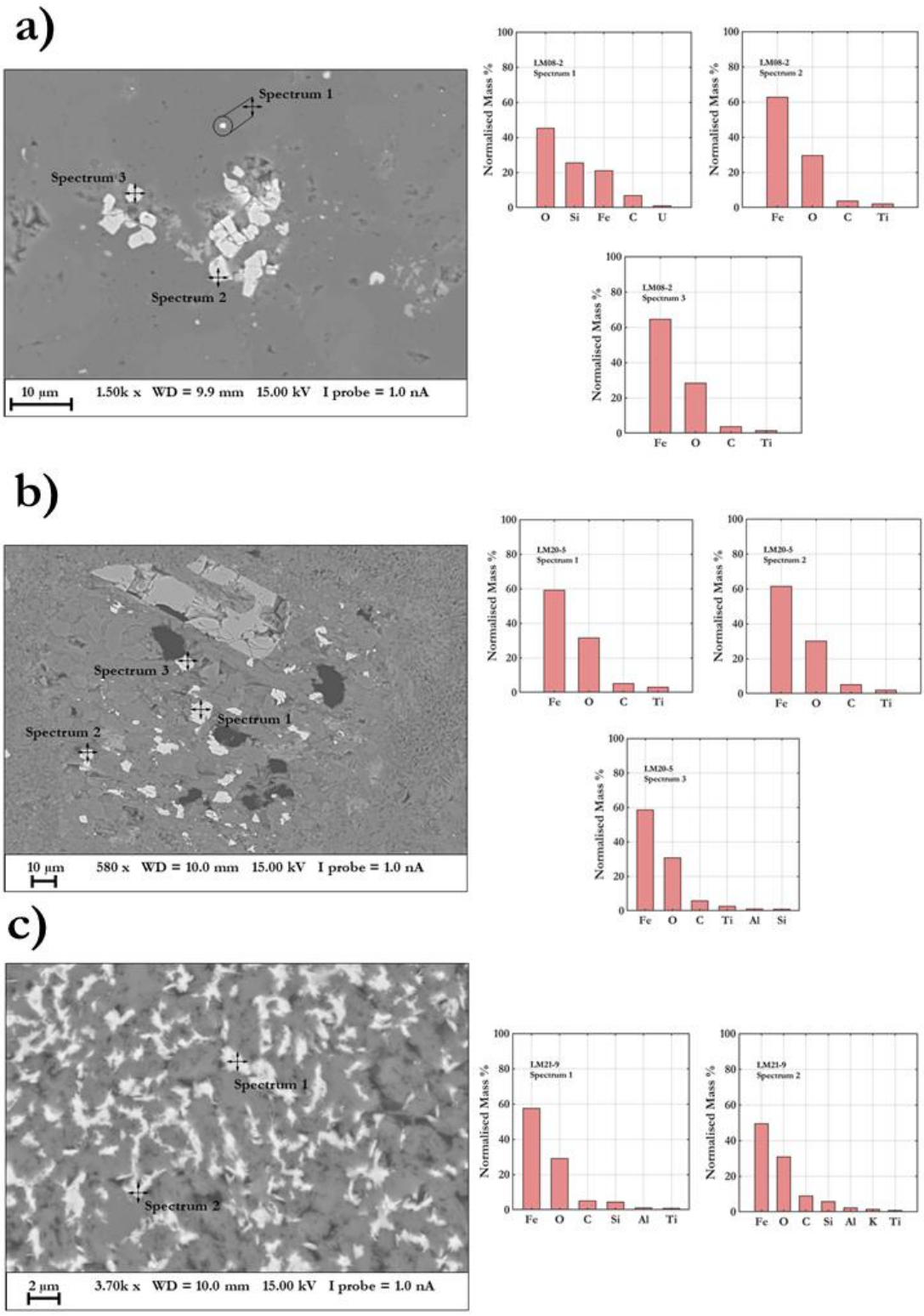

Figure C.3: Additional scanning electron microscope (SEM) images of specimens from Los Menucos, obtained from backscattered electrons, and associated energy-dispersive X-ray spectroscopy (EDX) results. Areas at which EDX spectra were acquired are indicated, and associated elemental compositions are expressed as normalised mass percentage.

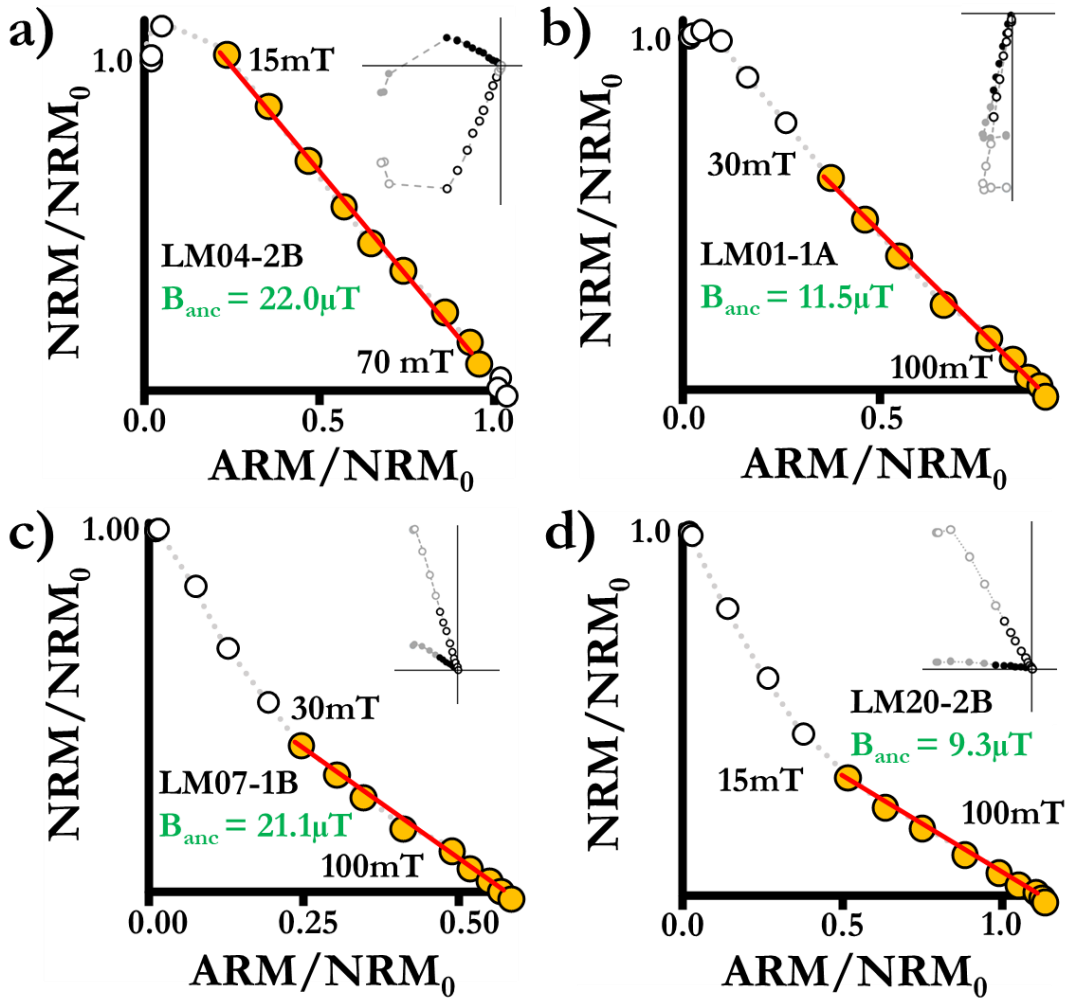

Figure C.4: Representative pseudo-Arai plots and Zijderveld plots for Los Menucos specimens. Filled circles (orange) represent the maximum intensity of the applied alternating field (AF) steps selected for the palaeointensity estimates, with a best-fit line to these points (red). The start and end AF steps are provided. Black circles of the Zijderveld plot correspond to the same AF steps as those chosen for palaeointensity analysis. Zijderveld plots presented in specimen coordinates.

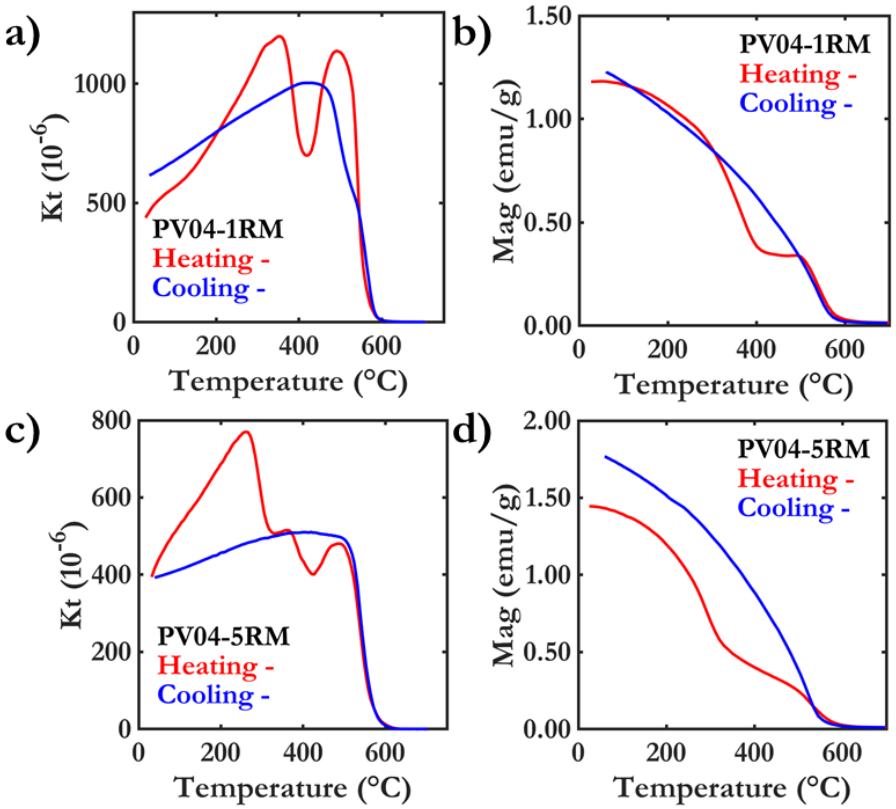

Figure C.5: Additional rock magnetic results from basaltic sill specimens of the Puesto Viejo Group. Selected specimens display behaviour intermediate to that of PVSA and PVSB, interpreted as continuous oxyexsolution of a range of titanomagnetite compositions.

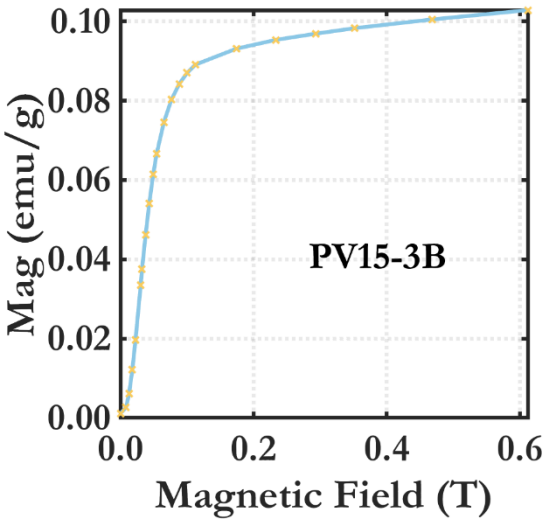

Figure C.6: Typical isothermal remanent magnetisation acquisition plot for basalt lava specimens of the Puesto Viejo Group. Non-saturated after a maximum applied field of 0.6 T.

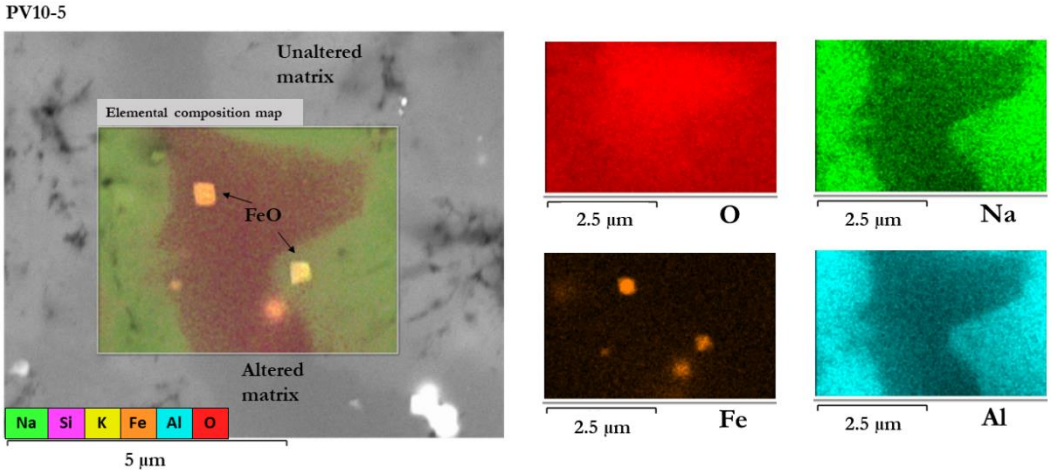

Figure C.7: Additional scanning electron microscope (SEM) images of specimen PV10-5, obtained from backscattered electrons, and elemental composition map obtained by energy-dispersive X-ray spectroscopy (EDX). Individual elemental composition maps also displayed for the most abundant elements. Oxidised banding structure evident through the coloured map, with iron-oxide grains present within both the altered and unaltered portions of the matrix.

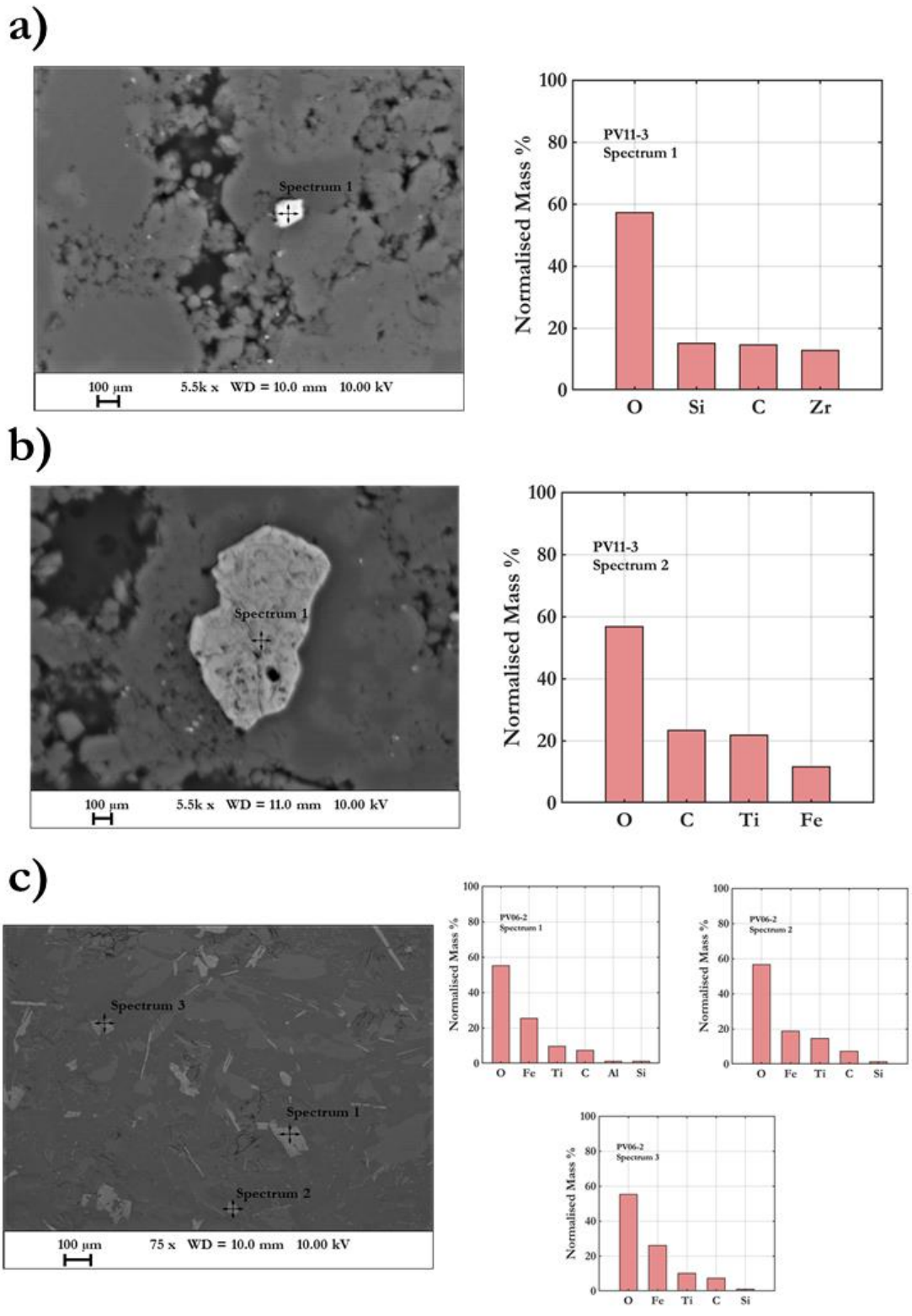

Figure C.8: Additional scanning electron microscope (SEM) images of specimens from Puesto Viejo, obtained from backscattered electrons, and associated energy-dispersive X-ray spectroscopy (EDX) results. Areas at which EDX spectra were acquired are indicated, and associated elemental compositions are expressed as normalised mass percentage.

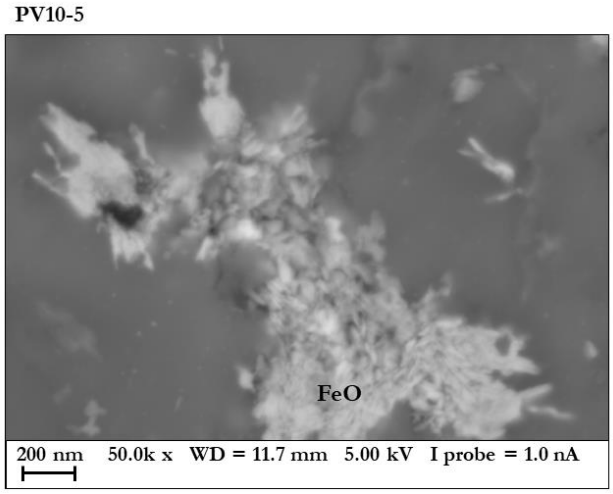

Figure C.9: Additional scanning electron microscope (SEM) image of specimen PV10-5 that displayed assemblages of platy iron-oxides.

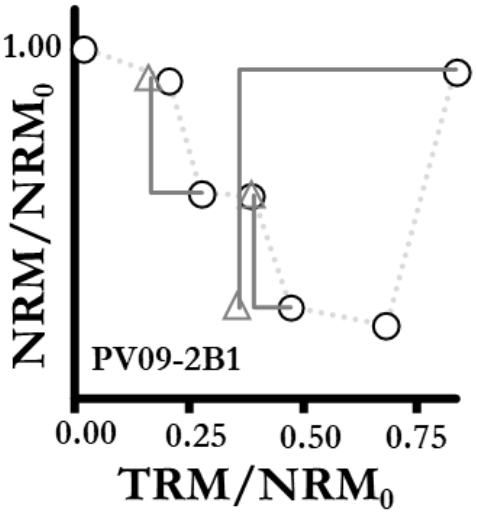

Figure C.10: Resulting Arai plot from thermal Thellier experiment on specimen PV09-2B. No palaeointensity estimate could be obtained due to the continuous slope change associated with increased temperature steps. Representative behaviour of all basalt sills specimens subjected to the thermal Thellier approach.

Supporting Tables

Table C.1: Estimated Curie temperatures from Los Menucos specimens.

Sample	RM Type	T_C (1)	T_C (2)	T_C (3)
LM01-4RM	LMIB	654	577	-
LM01-7RM	LMIB	364	571	-
LM03-1C	LMIA	581	361	-
LM03-6RM	LMIA	579	397	-
LM04-2B1	LMIA	571	381	-
LM04-4C	LMIA	577	386	-
LM04-6RM	LMIA	574	402	-
LM05-2RM	LMIA	563	371	-
LM05-4RM	LMIA	563	361	-
LM06-6A2	LMIA	567	-	-
LM07-1RM	LMIB	560	660	371
LM07-2RM	LMIB	651	561	399
LM08-7RM	LMIA	561	341	431
LM08-8RM	LMIA	562	380	-
LM18-4RM	LMIA	545	-	-
LM18-6RM	LMIA	571	-	-
LM20-4RM	LMIB	396	649	567
LM20-7RM	LMIB	571	367	420
LM21-4C	LMIB	572	669	420
LM21-8RM	LMIB	574	676	357

Note C.1: Estimated Curie temperatures (T_C) obtained from thermomagnetic curves, using the differential method (Tauxe, 1998). Tc (1) indicates the Curie temperature of the primary phase, i.e. the temperature associated with the greatest decrease in magnetisation. Additional unblocking temperatures associated with notable reductions in magnetisation highlighted where appropriate in decreasing order (T_c (2), T_c (3)).

Table C.2: Los Menucos thermal Thellier results and critical values according to selection criteria outlined in the main text.

Specimen	B_{anc} (μT)	B_{lab} (μT)	T_{min} (°C)	T_{max} (°C)	n	α	MAD_{Anc}	f	β	q	k'	DRAT	CDRAT
LM01-2A2	40.0	30	400	680	6	0.2	1.5	0.888	0.052	11.2	-0.116	5.4	6.3
LM01-3A2	31.9	30	400	660	7	0.2	1.1	0.913	0.061	9.6	0.088	7.4	5.9
LM01-4A2	34.9	30	400	680	8	0.3	1.5	0.886	0.026	23.6	0.007	8.6	12.0
LM01-5A2	28.4	30	500	660	6	1.0	1.5	0.874	0.057	11.4	0.207	3.2	3.2
LM01-7A2	22.8	30	500	660	6	1.9	1.7	0.87	0.093	7.0	0.393	2.2	1.0
LM01-8A2	27.0	30	350	680	9	0.6	1.3	0.831	0.023	28.1	0.022	4.7	4.1
LM01-9A2	32.7	30	400	680	8	0.5	1.5	0.903	0.035	19.2	0.064	5.7	0.9
LM07-1A2	67.1	30	300	680	9	0.1	0.9	0.986	0.308	1.9	1.916	12.6	14.6
LM07-2A2	43.2	30	500	680	7	1.2	1.8	0.886	0.334	1.7	1.814	21.5	18.4
LM07-3A2	48.5	30	500	680	7	0.7	1.9	0.924	0.356	1.7	1.841	17.5	20.2
LM07-4A2	33.8	30	600	680	5	0.6	1.3	0.614	0.431	0.8	2.244	31.4	26.2
LM07-5A2	32.6	30	600	680	5	0.3	1	0.695	0.484	0.7	2.049	60.9	61.5
LM07-6A2	67.8	30	500	680	7	4.3	6.2	0.944	0.459	1.4	1.974	12.0	8.8
LM07-7A2	67.8	30	550	680	6	1.9	3.6	0.67	0.504	0.9	2.175	20.0	24.4
LM20-2A2	156.7	30	0	500	7	1.2	1.7	0.407	0.623	0.2	2.231	7.9	9.6
LM20-3A2	255.7	30	0	500	7	9.5	4.6	0.609	0.545	0.6	-2.284	5.8	9.5
LM20-4A2	165.9	30	0	500	7	5.9	2.6	0.491	0.587	0.4	1.393	7.7	8.9
LM20-6A2	93.4	30	300	500	3	10.9	4	0.584	0.222	-0.2	0.748	22.6	46.0
LM20-7A2	169.2	30	250	500	5	9.8	3.7	1.375	0.685	-0.2	2.061	8.8	9.1
LM20-8A2	379.7	30	100	500	6	13.6	11.2	17.459	0.483	22.5	1.847	8.6	18.6
LM20-9A2	119.2	30	250	500	5	19.8	15	0.294	0.816	0.1	2.288	11.2	5.3
LM21-1A2	27.3	30	500	660	6	1.0	2.5	0.778	0.095	5.4	0.110	7.3	9.2
LM21-2A2	28.8	30	500	660	6	1.3	2.6	0.797	0.107	4.8	0.290	9.7	10.0

LM21-3A2	31.0	30	500	680	7	3.5	8.3	0.815	0.105	5.3	0.532	10.5	21.8
LM21-4A2	27.3	30	500	680	7	2.0	3.6	0.808	0.097	5.0	0.452	14.9	17.9
LM21-7A2	26.2	30	500	680	7	2.2	4.2	0.783	0.13	3.4	0.707	17.8	23.6
LM21-8A2	34.1	30	500	680	7	1.0	2	0.772	0.142	2.8	0.638	21.9	23.0
LM21-9A2	30.5	30	550	680	6	3.4	4.4	0.685	0.259	0.3	1.229	40.2	52.8

Note C.2: Accepted palaeointensity estimates (B_{anc}) highlighted in green, estimates otherwise rejected due to failure of one of the selection criteria outlined in the main text. Where statistical parameters violate the critical limit, this is indicated (red) as is violation of the stricter critical limit but within the limits of the relaxed critical limit (amber).

Table C.3: Los Menucos Shaw double heating technique (DHT) results and critical values according to selection criteria outlined in the main text.

Specimen	B_{anc} (μT)	B_{lab} (μT)	AF_{min} (mT)	AF_{max} (mT)	n	α	MAD_{Anc}	MAD_{Free}	β	f	k'_A	k'_N	k'_T	r^2_N	r^2_T	Slope-T
LM01-1A2	50.3	30	15	100	12	0.4	0.7	1.4	0.016	0.83	0.044	0.010	0.252	0.998	0.990	0.59
LM01-2B1	32.8	30	15	100	12	0.6	1.0	1.8	0.014	0.81	0.122	0.066	0.108	0.998	0.998	0.62
LM01-3B	13.1	30	15	100	12	0.8	0.9	1.3	0.022	0.85	0.522	0.146	0.027	0.995	1.000	1.03
LM01-4B	6.7	30	10	100	13	0.0	0.3	0.6	0.018	0.94	0.452	0.131	0.002	0.997	1.000	1.50
LM01-6A2	37.4	30	15	100	12	2.3	1.4	1.2	0.031	0.75	0.291	0.222	0.145	0.991	0.997	0.69
LM01-9B1	29.4	20	0	100	16	1.4	3.1	5.6	0.043	0.94	0.597	0.437	0.241	0.975	0.992	0.03
LM07-1B	41.5	30	15	100	12	0.7	0.6	0.4	0.023	0.79	0.310	0.159	0.663	0.995	0.936	0.61
LM07-3B1	46.9	20	15	100	12	0.6	0.6	0.7	0.011	0.75	0.236	0.010	0.074	0.999	0.999	1.19
LM07-4	43.0	30	10	100	13	1.3	1.0	0.6	0.018	0.90	0.431	0.133	0.034	0.996	0.999	0.98
LM07-5B	41.2	30	15	100	12	1.5	1.2	0.8	0.025	0.80	0.383	0.167	0.030	0.994	1.000	1.09
LM07-7B	35.6	30	10	100	13	1.0	1.0	0.7	0.028	0.93	0.345	0.232	0.024	0.992	1.000	1.16
LM20-2B	17.6	30	15	100	12	1.0	0.8	0.7	0.024	0.80	0.408	0.163	0.021	0.994	1.000	1.10
LM20-4C2	22.8	30	25	80	8	0.7	0.4	0.6	0.031	0.39	0.199	0.159	0.072	0.994	0.999	1.10
LM20-5B	15.2	30	10	100	12	3.1	2.2	1.3	0.013	0.72	0.437	0.017	0.029	0.998	1.000	1.09
LM20-6B	15.1	30	10	100	12	2.1	1.3	0.5	0.013	0.76	0.462	0.007	0.172	0.998	0.994	1.20
LM21-1C2	34.6	30	5	100	14	2.3	1.4	1.7	0.104	0.87	0.016	0.905	0.157	0.874	0.996	1.07
LM21-2B	34.0	30	10	100	12	2.1	1.4	1.7	0.068	0.82	0.037	0.576	0.140	0.954	0.993	0.07
LM21-3B	27.8	30	10	100	12	2.2	1.3	1.4	0.084	0.78	0.064	0.691	0.003	0.931	1.000	0.79
LM21-4B	23.3	30	5	100	13	1.7	0.9	0.5	0.094	0.89	0.041	0.802	0.214	0.905	0.992	1.16
LM21-5A2	31.5	30	5	100	14	1.4	0.8	1.1	0.107	0.88	0.097	0.930	0.072	0.867	0.999	1.22
LM21-6A2	93.7	30	50	100	6	6.2	2.7	0.7	0.049	0.18	0.041	0.031	0.006	0.990	1.000	0.95
LM21-7B	23.7	30	25	100	10	2.0	1.2	1.7	0.065	0.62	0.059	0.495	0.013	0.967	1.000	1.12
LM21-8C2	61.7	30	35	100	8	2.2	1.2	0.8	0.035	0.39	0.069	0.136	0.057	0.992	0.998	1.04

LM21-9B2	41.9	30	30	60	5	1.2	0.4	0.7	0.037	0.33	0.165	0.199	0.011	0.996	0.998	1.00

Note C.3: Accepted palaeointensity estimates (B_{anc}) highlighted in green, estimates otherwise rejected due to failure of one of the selection criteria outlined in the main text. Violation of the stricter critical limit but within the limits of the relaxed critical limit is highlighted (amber). k' and r^2 presented for NRM-TRM1 (N) and TRM1-TRM2* (T).*

Table C.4: Los Menucos pseudo- Thellier results and critical values according to selection criteria outlined in the main text.

Specimen	B_{anc} (μT)	B_{lab} (μT)	AF_{min} (mT)	AF_{max} (mT)	b	σb	$B_{1/2ARM}$	n	α	MAD_{Anc}	β	R^2	R^2_{AA}	R^2_{DD}	k'	k'_{AA}	k'_{DD}	b_{AA}	f
LM01-1A2	11.5	35	30	100	-1.080	0.026	35.4	9	0.7	1.2	0.024	0.996	0.996	0.997	0.127	0.159	0.020	-0.872	0.62
LM01-2B1		35	10	100	-0.791	0.036	35.0	13	1.7	1.8	0.046	0.977	0.992	0.993	0.389	0.203	0.199	-0.988	1.04
LM01-3B	4.5	35	30	70	-0.426	0.013	31.7	6	1.2	0.9	0.030	0.996	0.998	0.999	0.169	0.134	0.032	-0.898	0.49
LM01-4B	4.5	35	30	100	-0.424	0.011	32.6	9	0.3	0.8	0.025	0.996	0.996	0.998	-0.008	0.030	0.034	-0.874	0.57
LM01-9B1	12.7	58	30	70	-0.717	0.025	31.7	6	0.4	0.4	0.035	0.995	0.996	0.999	0.189	0.165	0.017	-0.910	0.48
LM7-1B	21.1	58	30	100	-1.196	0.031	34.7	9	0.2	0.3	0.026	0.995	0.996	0.998	0.087	0.126	0.030	-0.879	0.60
LM7-2B	16.2	35	35	100	-1.519	0.019	33.1	8	0.1	0.2	0.012	0.999	0.997	0.999	0.075	0.128	0.055	-0.856	0.47
LM7-3B1	18.7	35	35	100	-1.757	0.047	32.7	8	0.1	0.4	0.027	0.996	0.995	0.999	0.134	0.130	0.006	-0.862	0.47
LM7-4		58	2	35	-2.387	0.075	33.8	7	0.3	0.7	0.031	0.995	0.999	0.997	0.154	0.080	0.096	-1.156	0.69
LM7-5B	21.6	58	30	90	-1.221	0.028	32.9	8	0.4	0.3	0.023	0.997	0.998	0.999	0.119	0.097	0.021	-0.862	0.56
LM7-7B	17.6	58	35	90	-0.993	0.031	35.8	7	0.6	0.5	0.031	0.995	0.996	0.999	0.118	0.033	0.080	-0.920	0.48
LM20-2B	9.3	58	30	100	-0.526	0.013	32.6	9	1.3	1.6	0.024	0.996	0.995	0.996	0.119	0.178	0.048	-0.871	0.56
LM20-4C2		35	15	100	-0.984	0.051	30.9	12	0.1	0.4	0.052	0.973	0.994	0.989	0.426	0.209	0.228	-0.938	0.93
LM20-5B	9.1	58	30	100	-0.513	0.010	29.7	9	0.7	0.9	0.020	0.997	0.997	0.997	0.042	0.124	0.076	-0.873	0.50
LM20-6B	8.7	58	30	80	-0.494	0.011	31.1	7	0.8	0.6	0.022	0.998	0.998	0.999	-0.036	0.035	0.066	-0.890	0.49
LM21-2B		58	20	100	-1.580	0.052	39.6	11	0.9	1.2	0.033	0.990	0.995	0.977	-0.262	0.184	0.435	-0.963	0.83
LM21-1C2		35	20	100	-2.109	0.059	37.7	11	1.0	1.3	0.028	0.993	0.997	0.985	-0.232	0.125	0.350	-0.974	0.82
LM21-3B		58	30	100	-1.436	0.049	38.8	9	0.5	0.8	0.034	0.992	0.994	0.985	-0.190	0.161	0.347	-0.951	0.66
LM21-4B		58	20	100	-1.203	0.050	39.7	11	0.3	0.4	0.041	0.985	0.994	0.966	-0.355	0.209	0.523	-0.972	0.82
LM21-5A2		35	25	100	-1.928	0.084	39.7	10	0.5	0.9	0.044	0.985	0.996	0.975	-0.348	0.136	0.445	-0.975	0.75
LM21-6A2		35	20	100	-2.467	0.086	38.3	11	0.5	0.7	0.035	0.989	0.995	0.984	-0.243	0.113	0.361	-1.009	0.84
LM21-7B		58	30	100	-0.979	0.040	40.7	9	1.1	1.3	0.041	0.988	0.992	0.982	-0.227	0.157	0.382	-0.935	0.68
LM21-8C2		35	25	100	-2.063	0.024	38.9	10	0.5	0.7	0.012	0.999	0.991	0.989	-0.038	0.270	0.291	-0.947	0.77

LM21-9B2	15.9	35	15	60	-1.487	0.028	36.1	8	1.6	0.8	0.019	0.998	0.997	0.997	0.000	0.123	0.138	-1.022	0.73

Note C. 4: Accepted palaeointensity estimates (B_{anc}) highlighted in green, estimates otherwise rejected due to failure of one of the selection criteria outlined in the main text. Where statistical parameters violate the critical limit, this is indicated (red). k' and r^2 presented for pseudo-Arai plot (k', r^2), ARM-ARM (k'_{AA}, r^2_{AA}), and demag-demag (k'_{DD}, r^2_{DD}).

Table C.5: Estimated Curie temperatures from Puesto Viejo specimens.

Sample	T_C (1)	T_C (2)	T_C (3)
PV01-5RM	633	401	-
PV01-7B	620	-	-
PV04-1RM	403	573	-
PV04-3B	233	558	478
PV04-5RM	329	572	
PV04-8RM	235	578	467
PV04-10RM	426	580	-
PV05-2UO	164	392	-
PV05-8B	203	401	590
PV06-1B	413	572	-
PV06-4UO	408	578	-
PV09-4UO	396	571	-
PV09-9B	387	507	627
PV10-3A	589	110	265
PV10-7RM	582	410	-
PV10-8B	582	410	-
PV11-1B	402	587	-
PV11-8UO	513	421	-
PV13-3RM	638	397	-
PV13-6C	643	383	-
PV14-5C	633	421	-
PV14-6UO	393	633	-
PV15-3	634	432	-
PV15-3B	633	571	432
PV15-5C2	583	410	-
PV16-5RM	642	409	-
PV16-6C	643	391	-
PV17-7	646	423	572
PV17-3RM	640	421	103
PV17-7RM	641	403	571
PV17-9UO	530	391	610

Note C. 5: See note of Table C.1 for description.

Table C.6: Puesto Viejo thermal Thellier results and critical values according to selection criteria outlined in the main text.

Specimen	B_{anc} (μT)	B_{lab} (μT)	T_{min} (°C)	T_{max} (°C)	n	α	MAD_{Anc}	f	β	q	k'	DRAT	CDRAT
PV01-3B	283.7	30	100	450	6	15.3	4.9	0.46	0.362	0.6	-2.895	4.9	7.0
PV01-5B	24.7	30	0	450	7	62.1	9.8	0.21	0.345	0.5	0.566	10.4	24.9
PV01-7B	116.1	30	250	450	4	11.9	2.1	0.30	0.250	0.8	-0.237	11.7	14.8
PV04-4B1	2.4	30	0	450	7	3.3	29.1	1.46	0.566	-0.6	1.703	5.1	1.5
PV04-5B1	22.8	30	0	450	7	4.2	6.5	1.03	0.325	2.1	1.635	25.9	3.6
PV05-5B1	4.5	30	0	600	13	3.6	14.8	1.39	0.243	4.3	1.330	58.2	66.8
PV05-7B1	4.4	30	0	600	13	6.8	18.5	1.43	0.206	5.8	1.221	19.4	38.6
PV05-9B1	4.7	30	0	600	13	7.2	17.6	1.41	0.216	5.4	1.258	39.4	54.7
PV06-1B1	2.0	30	0	450	7	24.5	19.5	0.46	0.191	-0.5	0.511	10.1	9.4
PV06-4B1	8.3	30	0	450	7	52.1	25.4	0.45	0.563	0.5	2.043	40.5	38.3
PV06-8B1	40.1	30	0	450	7	13.6	15.4	0.64	0.333	0.7	-1.085	7.4	7.5
PV09-2B1	41.4	30	0	400	6	9.0	9.1	0.82	0.172	3.8	0.139	3.7	3.7
PV09-6B1	24.5	30	0	450	7	26.6	35.3	1.59	0.632	0.6	2.189	17.7	26.9
PV09-9B1	9.0	30	100	400	5	14.3	14.7	0.86	0.481	1.2	1.624	3.0	2.1
PV10-1A1	12.2	15	0	600	13	12.6	4.0	0.61	0.099	5.1	0.454	22.9	24.5
PV10-1B1	4.9	30	0	600	13	14.7	11.6	1.08	0.134	5.9	0.946	0.7	1.3
PV10-2A2	9.7	15	0	600	13	10.3	3.2	0.65	0.093	5.9	0.386	22.5	21.3
PV10-3A2	10.0	15	0	600	13	9.0	3.5	0.77	0.118	5.4	0.654	23.0	24.1
PV10-4A2	2.0	15	250	640	13	12.6	22.9	0.78	0.211	3.1	1.422	26.6	42.7
PV10-5A2	10.4	15	250	580	10	4.1	2.5	0.95	0.098	7.5	0.397	4.2	4.7
PV10-5B1	13.6	30	200	525	8	19.0	10.4	0.79	0.084	7.4	0.447	3.7	4.4
PV10-6A2	8.6	15	200	580	11	3.0	2.0	0.98	0.101	7.5	0.284	2.6	0.1
PV10-7A2	8.7	15	200	600	12	10.6	6.9	0.84	0.180	3.3	0.479	23.3	21.2

PV10-8A2	7.3	15	200	580	11	7.0	3.0	0.85	0.090	6.2	0.302	2.5	0.9
PV10-8B1	6.4	30	0	600	13	13.2	16.5	0.98	0.274	1.5	1.749	1.5	2.1
PV11-1A2	16.4	15	450	580	7	2.5	1.7	0.41	0.084	3.4	-0.273	6.4	9.5
PV11-1B1	16.4	30	400	600	8	1.4	2.8	0.73	0.054	10.7	-0.282	8.0	25.9
PV11-2A2	9.7	15	450	600	8	0.6	3.4	0.62	0.058	8.4	0.229	26.0	6.6
PV11-3A1	2.5	15	475	600	7	13.2	7.5	0.52	0.089	4.4	-0.460	66.1	57.1
PV11-4A2	4.8	15	400	600	9	6.4	7.7	0.86	0.156	4.4	0.893	21.6	42.0
PV11-4B1	45.6	30	100	450	6	5.6	4.7	0.78	0.059	8.1	0.329	25.4	24.5
PV11-5A2	3.2	15	450	600	8	12.4	10.5	0.62	0.076	6.7	0.495	33.2	17.0
PV11-6B1	7.2	30	400	600	8	4.6	6.2	0.70	0.063	9.3	0.254	29.7	81.7
PV11-7A2	3.1	15	475	600	7	16.7	11.2	0.61	0.080	5.9	-0.575	61.9	24.6
PV11-8A2	8.5	15	475	600	7	2.6	2.6	0.61	0.081	5.9	-0.461	28.6	70.0

Note C.6: See note of Table C.2 for description.

Table C.7: Puesto Viejo Shaw double heating technique (DHT) results and critical values according to selection criteria outlined in the main text.

Specimen	B_{anc} (μT)	B_{lab} (μT)	AF_{min} (mT)	AF_{max} (mT)	n	α	MAD_{Anc}	MAD_{Free}	β	f	k'_A	k'_N	k'_T	r^2_N	r^2_T	Slope-T
PV01-1A2	6.6	15	20	100	11	1.3	1.8	2.1	0.027	0.60	0.447	0.184	0.021	0.993	0.999	1.05
PV01-2A2	6.8	15	20	100	11	0.2	1.2	1.8	0.108	0.60	0.436	0.551	0.307	0.898	0.887	0.89
PV01-3C1	6.7	30	25	100	10	1.0	2.7	3.8	0.024	0.44	0.089	0.153	0.018	0.996	1.000	0.98
PV01-3C2	5.7	15	25	100	10	0.4	3.3	5.0	0.083	0.50	0.364	0.484	0.482	0.946	0.940	0.94
PV01-4A2	5.1	15	25	70	7	2.7	4.5	7.7	0.028	0.50	0.265	0.155	0.031	0.996	1.000	0.95
PV01-4B1	6.4	30	25	100	10	0.9	2.8	3.9	0.027	0.45	0.184	0.200	0.006	0.994	1.000	0.97
PV01-5	8.5	30	20	100	11	1.2	1.7	1.8	0.010	0.63	0.006	0.073	0.006	0.999	1.000	0.97
PV01-5A2	8.1	15	15	100	12	0.9	2.6	3.5	0.027	0.81	0.369	0.186	0.077	0.993	0.999	1.00
PV01-6	8.6	30	20	100	11	0.9	1.5	1.8	0.015	0.66	0.041	0.103	0.006	0.998	1.000	0.98
PV01-6A2	7.9	15	20	100	11	0.6	1.5	1.9	0.020	0.71	0.290	0.050	0.090	0.997	0.999	1.04
PV01-7C1	8.0	30	20	100	11	0.3	1.5	2.1	0.021	0.58	0.276	0.164	0.041	0.996	1.000	0.97
PV01-7C2	8.2	15	20	100	11	0.2	1.8	2.5	0.020	0.59	0.402	0.141	0.084	0.996	0.998	0.98
PV04-1	4.5	30	5	80	12	0.7	1.4	1.5	0.023	0.80	1.293	0.109	0.092	0.995	0.997	0.98
PV04-1A2	4.6	10	5	100	14	1.4	2.6	1.9	0.022	0.83	1.280	0.105	0.050	0.994	0.999	1.07
PV04-2B1	15.0	30	15	100	12	4.2	5.4	7.5	0.186	0.08	1.013	0.635	0.299	0.683	0.976	0.89
PV04-3	7.9	30	10	100	13	8.1	9.6	12.9	0.122	0.12	1.118	0.763	0.453	0.842	0.923	0.93
PV04-5A	10.5	30	5	80	12	1.9	3.9	3.7	0.020	0.49	1.404	0.046	0.013	0.996	1.000	0.91
PV04-6	5.7	30	20	100	11	4.5	5.2	5.3	0.096	0.16	0.990	0.585	0.105	0.919	0.988	0.92
PV04-6A2	3.7	10	10	100	13	3.4	4.7	5.1	0.074	0.38	1.176	0.554	0.027	0.941	0.999	0.90
PV04-6C2	5.7	30	15	100	12	3.1	4.6	5.3	0.073	0.24	1.112	0.440	0.136	0.947	0.993	0.87
PV04-7B1	6.6	30	10	100	13	5.4	7.3	9.8	0.292	0.08	0.939	1.926	1.953	0.283	0.069	1.20
PV04-8B	12.6	30	10	100	13	6.4	7.2	7.7	0.119	0.09	1.204	0.507	0.089	0.849	0.566	1.64
PV04-9B	20.4	30	15	100	12	3.2	4.4	5.6	0.252	0.07	1.241	2.047	0.524	0.466	0.906	0.88
PV04-10B1	5.2	30	25	100	10	4.8	6.0	6.9	0.152	0.09	1.050	0.967	0.097	0.824	0.997	0.96

PV05-2B1	18.2	30	10	100	13	2.2	3.4	4.0	0.103	0.13	0.891	0.086	0.640	0.887	0.940	1.15
PV05-3B	19.2	30	20	100	11	3.9	4.1	4.6	0.155	0.08	0.670	0.398	0.402	0.796	0.978	1.08
PV05-5	13.9	30	15	100	12	2.7	4.0	5.1	0.289	0.12	0.816	2.087	0.638	0.338	0.884	1.29
PV05-6B1	14.6	30	5	100	14	1.1	2.0	2.2	0.062	0.39	1.308	0.410	0.339	0.954	0.981	0.96
PV05-8A2	8.6	10	10	100	13	3.0	4.3	4.9	0.279	0.16	1.321	0.625	1.506	0.326	0.552	1.99
PV05-8B1	9.2	30	5	100	14	3.5	9.4	11.3	0.120	0.34	1.297	0.638	0.506	0.834	0.959	1.01
PV05-9	18.0	30	10	100	13	1.5	2.6	2.9	0.044	0.17	1.141	0.315	0.006	0.978	1.000	0.92
PV05-9A2	9.8	10	10	100	13	3.6	3.6	2.5	0.272	0.19	1.061	0.532	1.019	0.352	0.817	1.63
PV06-1	7.2	30	10	50	8	1.5	2.1	2.1	0.030	0.38	1.420	0.117	0.186	0.995	0.999	0.97
PV06-2C	10.1	30	10	50	8	0.7	1.3	1.4	0.024	0.45	1.221	0.148	0.086	0.997	1.000	1.02
PV06-3B	7.7	30	10	50	8	1.4	1.7	1.0	0.010	0.46	1.359	0.002	0.123	0.999	0.999	1.09
PV06-3B1	9.2	10	10	40	7	1.6	1.5	1.1	0.014	0.49	1.072	0.007	0.111	0.999	1.000	1.04
PV06-4	6.4	30	15	60	8	5.2	5.5	4.4	0.047	0.48	1.032	0.300	0.018	0.987	1.000	0.95
PV06-5B1	5.6	30	15	100	12	1.1	8.4	9.3	0.044	0.16	1.356	0.263	0.057	0.981	0.999	0.87
PV06-6B	5.4	30	10	100	13	7.0	11.5	6.1	0.020	0.83	0.938	0.105	0.004	0.996	1.000	0.92
PV06-6B1	4.3	10	15	60	8	5.8	6.9	5.1	0.023	0.69	0.698	0.096	0.178	0.997	0.997	0.97
PV06-8C	11.9	30	10	100	13	1.2	1.8	1.5	0.032	0.59	0.950	0.126	2.247	0.989	0.359	3.88
PV06-9B1	9.1	30	10	100	13	0.3	1.1	1.3	0.010	0.60	1.252	0.028	0.101	0.999	0.998	1.02
PV09-1A2	9.5	10	20	60	7	1.2	0.9	1.0	0.036	0.48	0.760	0.148	0.108	0.994	0.999	0.98
PV09-1B1	10.7	30	20	70	8	0.8	0.8	1.1	0.016	0.55	0.685	0.095	0.064	0.998	0.999	1.00
PV09-3B1	5.8	30	10	100	13	2.6	3.3	3.3	0.030	0.42	1.144	0.145	0.018	0.990	0.999	1.05
PV09-4B1	5.8	30	10	60	9	4.0	3.1	3.3	0.007	0.38	1.226	0.020	0.034	1.000	1.000	1.01
PV09-4B2	6.4	10	10	60	9	2.5	2.1	1.5	0.013	0.36	1.340	0.068	0.100	0.999	0.998	1.01
PV09-5B1	6.0	30	10	100	13	5.6	5.8	3.5	0.068	0.29	1.297	0.494	0.112	0.950	0.996	1.02
PV09-6C	6.2	30	10	70	10	3.9	2.6	2.0	0.030	0.34	1.235	0.191	0.001	0.993	1.000	1.03
PV09-7B1	6.0	30	15	70	9	1.4	1.2	1.2	0.023	0.40	0.959	0.135	0.010	0.996	1.000	0.99
PV09-8C	8.6	30	20	100	11	5.7	4.8	3.7	0.078	0.10	1.032	0.326	0.001	0.947	0.999	1.13

PV09-9B1	9.0	30	15	100	12	1.1	1.9	2.3	0.078	0.15	1.210	0.249	0.024	0.940	0.999	1.03
PV10-2A	10.7	10	15	35	5	0.4	0.6	1.2	0.028	0.59	0.279	0.165	0.057	0.998	1.000	0.95
PV10-2B2	7.5	30	15	100	12	1.0	1.3	1.6	0.002	0.83	0.375	0.012	0.043	1.000	1.000	1.03
PV10-3A	16.0	10	35	100	8	2.0	2.0	1.1	0.033	0.40	0.064	0.070	0.130	0.993	0.997	0.93
PV10-4A	13.5	10	20	100	11	1.1	2.5	2.9	0.090	0.51	0.320	0.560	0.338	0.928	0.865	0.81
PV10-6A	27.0	10	15	100	12	0.2	0.7	0.9	0.061	0.86	0.702	0.141	0.232	0.964	0.988	0.68
PV10-7A	10.1	10	15	100	12	0.3	0.7	0.8	0.094	1.03	0.603	0.637	0.372	0.914	0.970	1.84
PV10-8	9.8	30	15	100	12	0.8	1.1	1.2	0.006	0.77	0.407	0.036	0.101	1.000	0.998	1.05
PV10-8A	47.4	10	15	100	12	0.2	0.7	0.8	0.097	0.89	1.860	0.379	0.103	0.908	0.956	1.00
PV11-2B1	16.8	30	40	80	5	8.3	3.0	4.1	0.046	0.35	0.191	0.160	0.098	0.994	0.998	1.05
PV11-3B1	32.6	15	40	100	7	6.5	3.1	2.3	0.040	0.41	0.135	0.121	0.085	0.992	0.997	1.01
PV11-3B2	21.0	30	40	100	7	6.1	3.2	1.9	0.035	0.41	0.198	0.126	0.008	0.994	1.000	0.97
PV11-4C	13.4	30	25	100	10	8.2	5.5	3.1	0.028	0.72	0.125	0.198	0.036	0.994	1.000	1.05
PV11-5B2	15.2	30	20	100	11	8.0	5.6	2.2	0.017	0.80	0.221	0.061	0.037	0.997	0.999	0.99
PV11-6C	23.0	30	0	100	16	18.0	9.3	9.0	0.029	0.93	0.368	0.279	0.018	0.988	1.000	1.07
PV11-7A	20.0	15	40	100	7	2.2	1.3	1.5	0.055	0.42	0.221	0.255	0.077	0.985	0.997	1.04
PV11-7B	33.1	30	20	100	11	1.2	0.8	0.9	0.020	0.79	0.399	0.152	0.031	0.996	1.000	1.03
PV11-8B	28.1	30	35	100	8	4.0	2.4	3.8	0.032	0.42	0.210	0.179	0.066	0.994	0.999	1.00

Note C.7: See note of Table C.3 for description.

Table C.8: Puesto Viejo pseudo- Thellier results and critical values according to selection criteria outlined in the main text.

Specimen	B_{anc} (μT)	B_{lab} (μT)	AF_{min} (mT)	AF_{max} (mT)	b	σb	$B_{1/2ARM}$	n	α	MAD_{Anc}	β	R^2	R^2_{AA}	R^2_{DD}	k'	k'_{AA}	k'_{DD}	b_{AA}	f
PV01-1A2		35	30	80	-0.341	0.011	30.2	7	0.9	2.6	0.031	0.995	0.995	0.998	0.104	0.177	0.071	-0.834	0.49
PV01-2A2	4.7	35	10	50	-0.439	0.007	31.1	8	3.9	5.2	0.015	0.999	0.998	0.999	0.075	0.127	0.055	-1.115	0.87
PV01-3C1		35	25	100	-0.302	0.016	32.3	10	1.1	3.0	0.052	0.978	0.987	0.998	0.403	0.318	0.081	-0.864	0.71
PV01-3C2		35	30	100	-0.286	0.032	33.1	9	2.0	4.1	0.110	0.916	0.981	0.974	0.652	0.368	0.300	-0.830	0.60
PV01-4A2		35	30	100	-0.310	0.032	31.7	9	0.5	2.7	0.102	0.928	0.932	0.995	0.070	0.000	0.092	-1.005	0.58
PV01-4B1	3.3	35	25	100	-0.307	0.015	32.7	10	1.4	3.3	0.048	0.982	0.984	1.000	0.355	0.333	0.017	-0.902	0.72
PV01-5A2		35	20	100	-0.573	0.034	33.6	11	0.2	1.3	0.059	0.969	0.972	0.995	0.480	0.420	0.065	-0.932	0.88
PV01-5		35	20	100	-0.536	0.033	33.4	11	0.4	1.4	0.061	0.966	0.990	0.992	0.499	0.269	0.236	-0.944	0.87
PV01-6A2	5.4	35	25	100	-0.504	0.046	34.6	10	0.3	1.5	0.090	0.936	0.986	0.974	0.701	0.322	0.389	-0.906	0.79
PV01-6		35	20	100	-0.531	0.032	33.9	11	1.6	2.2	0.059	0.969	0.990	0.993	0.491	0.282	0.209	-0.943	0.88
PV01-7C1		35	20	100	-0.429	0.020	30.3	11	0.7	1.8	0.046	0.981	0.991	0.998	0.379	0.262	0.116	-0.911	0.81
PV01-7C2		35	20	100	-0.473	0.026	30.5	11	1.9	2.8	0.055	0.973	0.986	0.997	0.427	0.283	0.136	-0.892	0.82
PV04-1		35	10	100	-0.280	0.009	11.3	13	1.4	2.2	0.032	0.989	0.993	0.978	-0.112	0.174	0.253	-0.700	0.55
PV04-1A2		12	10	100	-1.063	0.041	11.5	13	1.6	2.9	0.039	0.984	0.986	0.992	-0.005	0.083	0.075	-0.667	0.58
PV04-2B1		35	30	100	-1.105	0.163	4.9	9	6.4	8.5	0.147	0.854	0.695	0.942	-0.034	-0.088	0.069	-0.619	0.04
PV04-3		35	10	100	-0.376	0.048	4.9	13	1.8	8.4	0.127	0.832	0.987	0.861	-0.492	-0.063	0.786	-0.543	0.20
PV04-5A		35	5	100	-0.592	0.025	6.8	14	1.7	4.3	0.042	0.979	0.985	0.996	0.335	0.334	0.014	-0.798	0.62
PV04-6		35	15	100	-0.281	0.016	10.0	12	2.2	4.1	0.057	0.968	0.991	0.932	-0.329	0.148	0.602	-0.701	0.31
PV04-6A2		12	15	100	-1.133	0.129	9.8	12	1.0	4.3	0.114	0.874	0.943	0.956	-0.482	-0.185	0.502	-0.762	0.30
PV04-6C2		35	20	100	-0.359	0.012	9.8	11	2.3	4.5	0.033	0.990	0.987	0.967	-0.119	0.112	0.417	-0.645	0.21
PV04-7B1		35	15	100	-0.931	0.135	4.1	12	7.6	9.4	0.145	0.801	0.923	0.921	-0.202	-0.094	0.599	-0.591	0.07
PV04-8B		35	20	100	-1.295	0.169	4.6	11	1.1	4.5	0.130	0.853	0.845	0.894	-0.122	-0.107	0.356	-0.515	0.05
PV04-9B		35	40	100	-1.771	0.636	4.9	7	3.2	6.6	0.359	0.459	0.437	0.980	-0.076	-0.075	0.012	-0.621	0.02
PV04-10B1		35	25	100	-0.290	0.031	11.7	10	1.8	5.5	0.108	0.909	0.972	0.861	-0.274	0.049	0.914	-0.053	0.14

PV05-2B1		35	15	100	-1.003	0.045	4.6	12	1.3	3.6	0.045	0.980	0.991	0.988	-0.077	-0.016	0.224	-0.648	0.12
PV05-3B		35	25	100	-1.177	0.071	4.8	10	4.0	4.9	0.060	0.971	0.979	0.978	-0.064	-0.025	0.200	-0.689	0.07
PV05-5		35	5	60	-0.823	0.011	4.9	10	3.9	4.3	0.014	0.999	0.999	0.996	-0.087	0.080	0.162	-0.722	0.47
PV05-6B1		35	5	100	-0.784	0.019	5.0	14	1.9	3.0	0.024	0.993	0.988	0.973	-0.260	0.244	0.371	-0.737	0.49
PV05-8A2		12	15	100	-2.615	0.219	5.1	12	2.7	4.1	0.084	0.931	0.738	0.690	-0.053	-0.113	0.521	-0.426	0.15
PV05-8B1		35	25	100	-0.993	0.046	4.8	10	1.9	6.7	0.046	0.983	0.834	0.885	0.015	0.103	0.662	-0.521	0.05
PV05-9A2		12	10	100	-2.443	0.153	5.1	13	2.0	2.7	0.063	0.957	0.966	0.934	-0.218	0.095	0.477	-0.612	0.25
PV05-9		35	10	100	-0.866	0.030	5.6	13	1.7	3.1	0.034	0.987	0.996	0.986	-0.156	0.015	0.270	-0.623	0.26
PV06-1	7.5	35	5	40	-0.706	0.016	9.5	8	1.5	2.6	0.023	0.997	0.996	0.999	0.151	0.176	0.021	-0.887	0.82
PV06-2C		35	10	35	-1.005	0.026	10.9	6	3.0	2.6	0.026	0.997	0.999	0.998	0.125	0.014	0.109	-0.799	0.50
PV06-3B	10.0	35	10	40	-0.938	0.026	10.3	7	1.4	1.4	0.028	0.996	0.996	0.999	0.145	0.174	0.029	-0.894	0.48
PV06-3B1		12	10	100	-2.946	0.094	13.2	13	1.6	2.7	0.032	0.989	0.976	0.976	0.159	-0.188	0.289	-0.841	0.66
PV06-4		35	15	40	-0.576	0.009	17.4	6	14.4	7.2	0.016	0.999	0.996	0.996	-0.050	0.154	0.195	-0.844	0.46
PV06-5B1		35	25	100	-0.447	0.034	8.1	10	5.7	13.1	0.075	0.955	0.972	0.963	-0.090	0.013	0.423	-0.637	0.08
PV06-6B	5.1	35	10	80	-0.475	0.007	20.5	11	5.6	6.7	0.014	0.998	0.995	0.996	0.036	0.193	0.143	-0.915	0.82
PV06-6B1		12	10	100	-1.572	0.082	24.4	13	4.7	7.5	0.052	0.970	0.975	0.995	0.349	0.211	0.114	-1.000	0.95
PV06-7B1		35	20	100	-1.130	0.024	15.2	11	1.8	2.6	0.021	0.996	0.996	0.995	-0.073	0.065	0.162	-0.846	0.37
PV06-8C	10.3	35	10	35	-0.966	0.028	13.5	6	2.3	1.1	0.029	0.997	0.998	1.000	0.011	0.058	0.047	-0.852	0.49
PV06-9B1	10.6	35	10	100	-0.998	0.017	13.5	13	0.9	1.5	0.017	0.997	0.995	1.000	0.107	0.147	0.038	-0.888	0.65
PV09-1A2	11.4	12	10	60	-3.264	0.068	24.0	9	2.0	1.6	0.021	0.997	0.995	0.995	-0.049	0.115	0.167	-1.050	0.76
PV09-1B1	10.5	35	10	80	-0.985	0.012	26.2	11	0.8	1.0	0.012	0.999	0.996	0.998	0.032	0.163	0.132	-0.971	0.84
PV09-3B1		35	10	60	-0.476	0.013	11.0	9	3.6	3.0	0.026	0.995	0.999	0.998	-0.153	-0.074	0.067	-0.753	0.50
PV09-4B1		35	10	80	-0.521	0.010	10.5	11	2.2	2.8	0.018	0.997	0.999	0.990	-0.091	-0.034	0.052	-0.782	0.51
PV09-4B2		12	25	100	-2.302	0.260	9.9	10	1.7	2.4	0.113	0.901	0.938	0.970	-0.101	0.078	0.296	-0.695	0.14
PV09-5B1		35	30	100	-0.961	0.092	9.3	9	3.8	4.8	0.096	0.936	0.973	0.951	-0.090	-0.014	0.576	-0.661	0.06
PV09-6C		35	10	100	-0.542	0.026	9.8	13	0.9	1.7	0.048	0.975	0.998	0.981	-0.343	-0.073	0.281	-0.751	0.46
PV09-7B1	5.7	35	10	60	-0.532	0.009	14.7	9	2.3	2.1	0.018	0.998	0.999	0.996	-0.185	0.066	0.156	-0.893	0.60

PV09-8C		35	20	100	-0.694	0.048	9.6	11	3.2	3.8	0.069	0.958	0.994	0.972	-0.159	0.002	0.369	-0.643	0.13
PV09-9B1		35	15	100	-0.695	0.027	9.3	12	0.9	1.9	0.040	0.984	0.993	0.986	-0.126	0.035	0.254	-0.603	0.23
PV10-2A		12	15	100	-32.506	2.588	28.8	12	0.4	1.0	0.080	0.938	0.878	0.787	0.503	-0.701	0.936	-0.880	1.02
PV10-2B2	4.6	35	5	100	-0.430	0.009	30.5	14	0.8	1.3	0.021	0.995	0.998	0.999	0.192	0.130	0.062	-0.990	1.01
PV10-3A		12	20	100	-21.059	3.528	67.5	11	0.6	0.9	0.168	0.763	0.819	0.990	1.046	0.930	0.062	-1.158	1.29
PV10-3B1	7.1	35	5	60	-0.670	0.015	34.5	10	0.6	0.6	0.023	0.996	0.999	0.996	0.018	0.092	0.087	-1.060	0.90
PV10-4A		12	25	100	7.460	3.523	35.6	10	2.5	4.0	0.472	0.012	0.064	0.203	2.117	1.941	1.548	0.227	1.93
PV10-6A		12	10	100	-93.585	5.708	26.7	13	0.3	0.6	0.061	0.960	0.828	0.798	0.134	-0.276	0.416	-0.815	1.01
PV10-7A		12	15	100	-16.591	5.719	19.9	12	0.0	0.6	0.345	0.165	0.022	0.343	1.639	1.883	1.483	0.094	1.66
PV10-8A		12	0	100	-34.773	8.408	27.3	16	0.1	0.5	0.242	0.349	0.284	0.673	1.343	1.538	1.685	-0.338	1.97
PV10-8B		12	10	40	-0.619	0.012	27.1	7	1.5	0.9	0.019	0.998	1.000	0.999	0.075	0.043	0.033	-1.053	0.80
PV11-2B1		35	60	100	-0.538	0.026	39.1	5	2.7	3.7	0.048	0.993	0.990	1.000	0.105	0.128	0.039	-0.794	0.26
PV11-3B1		35	15	100	-0.894	0.013	39.5	12	0.8	1.0	0.015	0.998	0.997	0.990	-0.133	0.156	0.274	-0.973	0.87
PV11-3B2	5.3	35	20	70	-0.493	0.012	38.9	8	1.2	0.8	0.025	0.996	0.999	0.995	-0.173	0.033	0.199	-1.014	0.66
PV11-4C	4.0	35	35	100	-0.377	0.009	39.2	8	1.6	2.1	0.025	0.996	0.997	0.999	0.118	0.118	0.003	-0.918	0.57
PV11-5B2	5.4	35	2	100	-0.503	0.010	37.7	15	1.4	1.5	0.019	0.995	0.997	0.999	0.150	0.113	0.037	-0.996	1.02
PV11-6C	7.6	35	40	100	-0.710	0.009	40.3	7	4.3	4.8	0.012	0.999	0.998	0.995	-0.048	0.114	0.159	-0.876	0.50
PV11-7A		35	25	100	-0.532	0.015	39.4	10	1.5	1.6	0.028	0.994	0.997	0.983	-0.224	0.160	0.350	-0.942	0.72
PV11-7B	11.0	35	15	70	-1.034	0.009	37.0	9	1.0	0.6	0.009	0.999	0.998	0.995	-0.056	0.137	0.193	-0.992	0.71
PV11-8B		35	35	100	-0.711	0.036	32.1	8	2.2	2.9	0.050	0.985	0.995	0.991	-0.265	-0.013	0.240	-0.856	0.46

Note C.8: See note of Table C.4 for description.

Table C.9: Puesto Viejo breakdown of Q_{PI} scores.

Site	Q_{AGE}	Q_{STAT}	Q_{ALT}	Q_{MD}	Q_{ACN}	Q_{TECH}	Q_{LITH}	Q_{MAG}	Q_{DIR}	Q_{PI}	Q_{PI}
PV01	1	1	1	1	1	0	0	0	1	1	7
PV04	1	0	1	1	1	0	0	0	1	1	6
PV06	1	0	1	1	1	0	0	0	1	0	5
PV09	1	0	1	1	1	0	0	0	1	1	6
PV10	1	0	0	1	1	0	1	0	1	0	5

Note C.9: Indication of pass or fail of each Q_{PI} category according to the corresponding criteria. Value of 1 indicates a pass and 0 a fail, final Q_{PI} score reflects the sum of these values. Q_{TRM} not included as this was cautiously failed for all sites.

Appendix D. Supporting information for Chapter 5

Introduction

The following supporting information provides a graphical overview of the steps involved in the construction of optimised statistical models, and of the construction process itself which was outlined in the main text (Figure D.1). Visual representation is also presented of the predicted distributions of virtual geomagnetic pole (VGP) dispersion, from statistical models constructed around observations subjected to a fixed 45° cut-off angle during the S_B determination process (Figure D.2).

Results of the investigation into the ability of statistical models constructed around palaeomagnetic observations from one time interval to predict observations from each other studied time interval are provided (Tables D.1-D.5). These take the form of goodness of fit statistics consistent with those used throughout **Chapter 5**. Finally, an overview of the data, data source, and processes used in the construction of the different statistical models that were evaluated for the Permo-Carboniferous Reversed Superchron are provided (Table D.6).

Supporting Figures

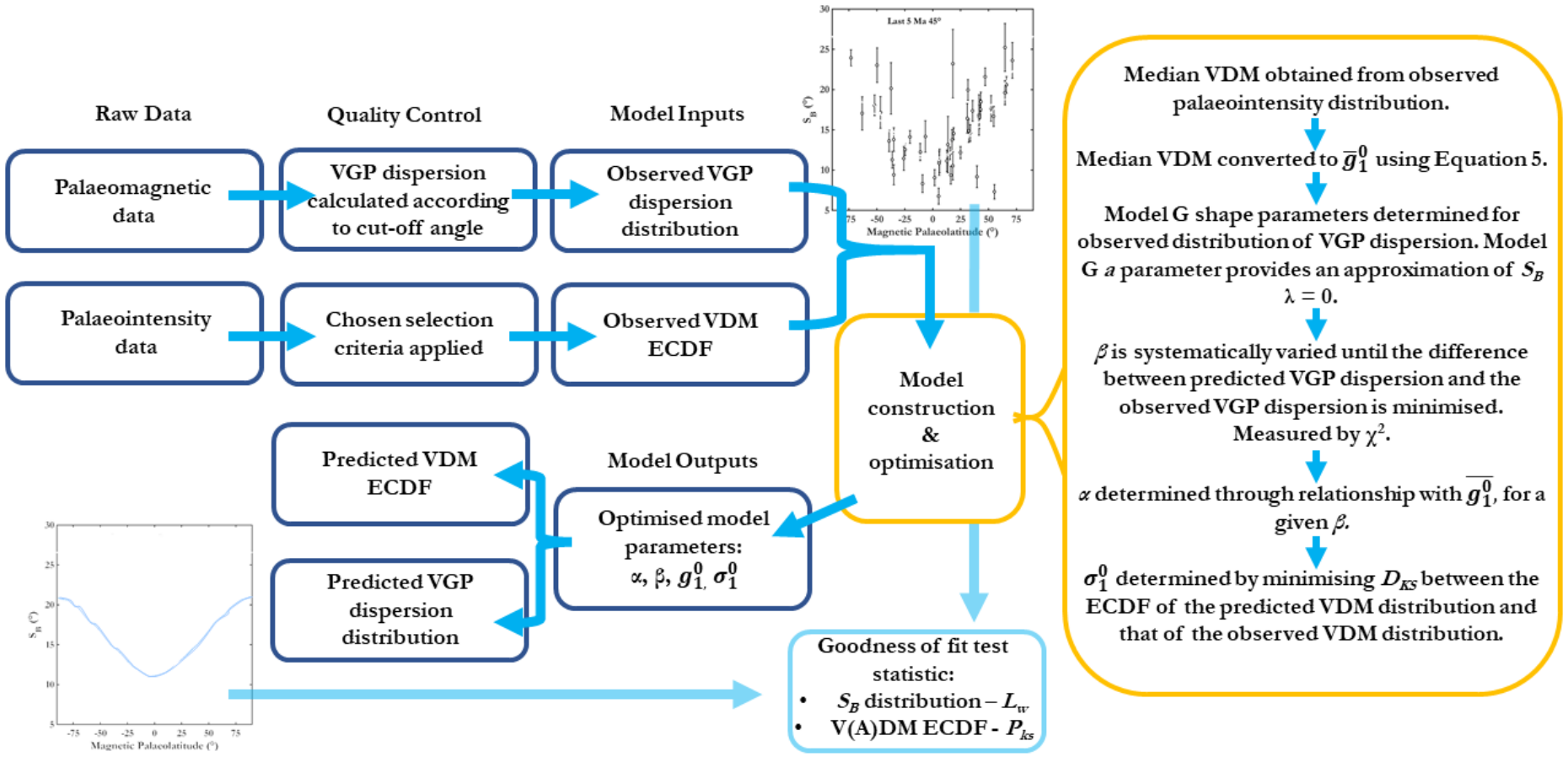

Figure D.1: Flowchart highlighting the steps involved in the construction of the statistical models and the way in which goodness of fit statistics were determined. Steps highlighted by the yellow box outline the specific method in which this study determined optimised model parameters, following the approach of Bono et al., (2020).

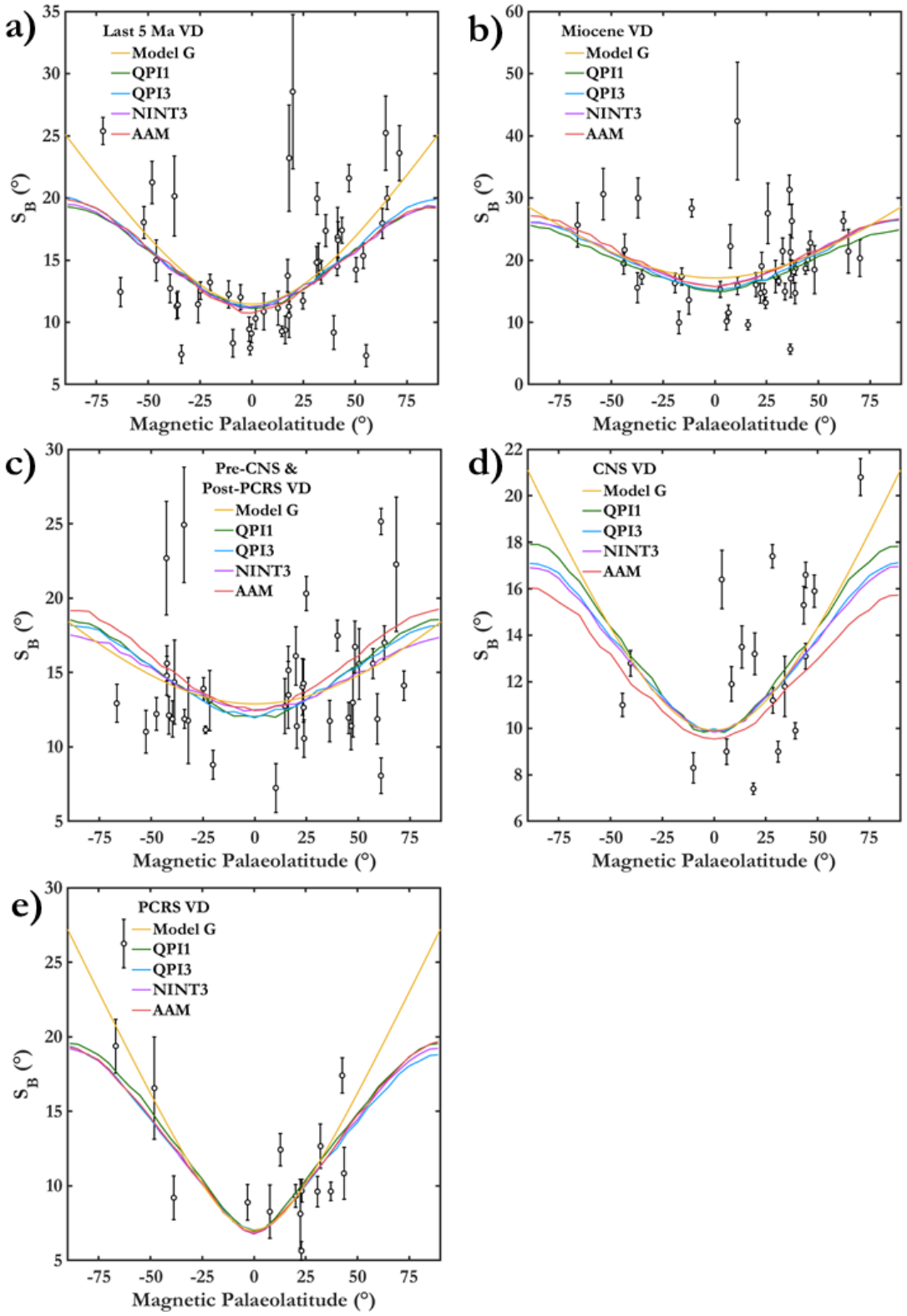

Figure D.2: Estimates of VGP dispersion versus estimated magnetic palaeolatitude. Determined from palaeomagnetic data after the application of selection criteria 1-8 in Handford et al. (2021) and a 45° fixed-angle cut-off. Model G fit to the distribution is plotted alongside predicted VGP dispersion distributions from statistical models constructed with each of the palaeointensity filtering criteria outlined in the main text. This is done for each of the studied time intervals a) last 5 Ma, b) Miocene, c) CNS, d) Pre-CNS & Post-PCRS, e) PCRS.

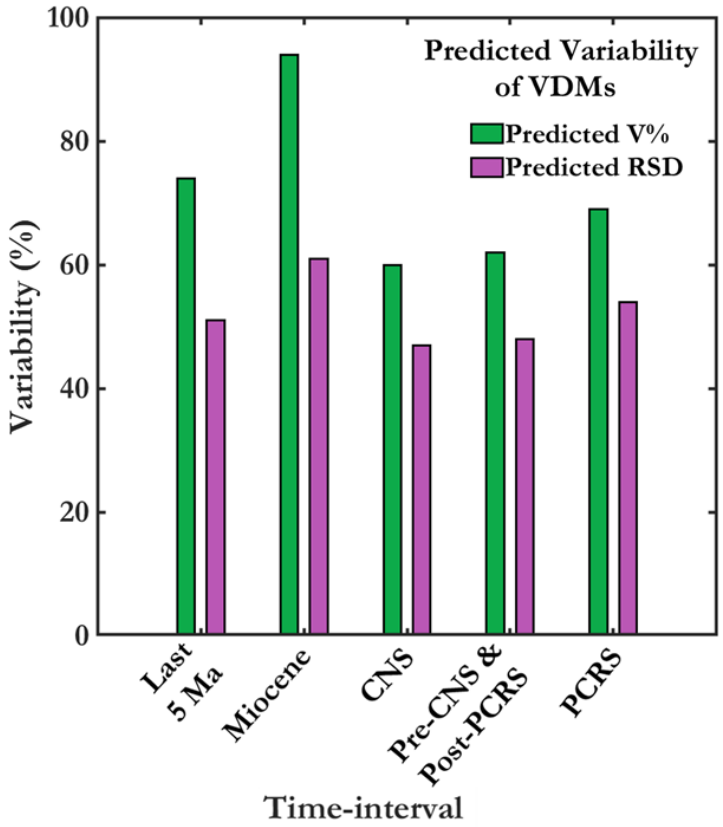

Figure D.3: Variance of the predicted virtual dipole moment (VDM) distribution for preferred statistical models for each studied time interval. Expressed as V% and $\sigma_{VDM}/\overline{VDM}$ (RSD).

Supporting Tables

Table D.1: Goodness of fit between optimised statistical models and palaeomagnetic observations from the last 5 Ma.

Data	Model	χ^2	L	χ_w^2	L_w	D_{KS}	P_{KS}
Last 5 Ma-QPI3-VD	Last 5 Ma-QPI3-VD	68.1	1.19	524.7	3.31	0.030	0.811
Last 5 Ma-QPI3-VD	Miocene-QPI3-VD	93.1	1.39	2094.8	6.61	0.291	$x10^{-16}$
Last 5 Ma-QPI3-VD	CNS-QPI3-VD	98.6	1.43	507.3	3.25	0.077	0.257
Last 5 Ma-QPI3-VD	Pre-CNS & Post-PCRS-QPI3-VD	16.3	0.93	593.6	3.52	0.401	$x10^{-28}$
Last 5 Ma-QPI3-VD	PCRS-QPI3-VD	21.3	1.06	617.4	3.59	0.263	$x10^{-6}$

Note D.1: Chi-squared (χ^2), weighted chi-squared (χ_w^2) and associated normalised values (L & L_w) assessing the goodness of fit between the observed palaeomagnetic data and the predicted distribution by the indicated statistical model. Kolmogorov-Smirnov test statistics (D_{KS} & P_{KS}) assessing the goodness of fit between the observed empirical cumulative distribution of palaeointensity observations and that predicted by the indicated statistical model.

Table D.2: Goodness of fit between optimised statistical models and palaeomagnetic observations from the Miocene.

Data	Model	χ^2	L	χ_w^2	L_w	D_{KS}	P_{KS}
Miocene-QPI3-VD	Miocene-QPI3-VD	111.4	1.59	572.4	3.61	0.064	0.633
Miocene-QPI3-VD	Last 5 Ma-QPI3-VD	240.6	2.34	617.4	3.75	0.299	$x10^{-16}$
Miocene-QPI3-VD	CNS-QPI3-VD	357.7	2.85	839.7	4.37	0.331	$x10^{-12}$
Miocene-QPI3-VD	Pre-CNS & Post-PCRS-QPI3-VD	16.3	0.93	609.0	3.72	0.120	0.046
Miocene-QPI3-VD	PCRS-QPI3-VD	21.3	1.06	1023.3	4.82	0.510	$x10^{-17}$

Note D.2: See note of Table D.1 for description.

Table D.3: Goodness of fit between optimised statistical models and palaeomagnetic observations from the Cretaceous Normal Superchron (CNS).

Data	Model	χ^2	L	χ_w^2	L_w	D_{KS}	P_{KS}
CNS-QPI3-VD	CNS-QPI3-VD	13.7	0.85	178.5	3.06	0.090	0.341
CNS-QPI3-VD	Last 5 Ma-QPI3-VD	15.4	0.90	300.9	3.98	0.115	0.021
CNS-QPI3-VD	Miocene-QPI3-VD	48.9	1.60	1186.9	7.91	0.335	$x10^{-12}$
CNS-QPI3-VD	Pre-CNS & Post-PCRS-QPI3-VD	16.3	0.93	323.6	4.13	0.454	$x10^{-21}$
CNS-QPI3-VD	PCRS-QPI3-VD	21.3	1.06	160.7	2.91	0.288	$x10^{-5}$

Note D.3: See not of Table D.1 for description.

Table D.4: Goodness of fit between optimised statistical models and palaeomagnetic observations from the combined Pre-Cretaceous Normal Superchron (Pre-CNS) and Post-Permo-Carboniferous Reversed Superchron (Post-PCRS).

Data	Model	χ^2	L	χ_w^2	L_w	D_{KS}	P_{KS}
Pre-CNS & Post-PCRS-QPI3-VD	Pre-CNS & Post-PCRS-QPI3-VD	42.8	1.02	383.6	3.06	0.094	0.219
Pre-CNS & Post-PCRS-QPI3-VD	Last 5 Ma-QPI3-VD	43.6	1.03	393.0	3.10	0.400	$x10^{-28}$
Pre-CNS & Post-PCRS-QPI3-VD	Miocene-QPI3-VD	89.3	1.48	1635.9	6.32	0.167	0.001
Pre-CNS & Post-PCRS-QPI3-VD	CNS-QPI3-VD	56.9	1.18	349.5	2.92	0.440	$x10^{-20}$
Pre-CNS & Post-PCRS-QPI3-VD	PCRS-QPI3-VD	75.4	1.36	447.6	3.30	0.593	$x10^{-23}$

Note D.4: See note of Table D.1 for description.

Table D.5: Goodness of fit between optimised statistical models and palaeomagnetic observations from the Post-Permo-Carboniferous Reversed Superchron (Post-PCRS).

Data	Model	χ^2	L	χ_w^2	L_w	D_{KS}	P_{KS}
PCRS-QPI3-VD	PCRS-QPI3-VD	14.6	0.96	139.5	2.95	0.120	0.443
PCRS-QPI3-VD	Last 5 Ma-QPI3-VD	18.8	1.08	301.7	4.34	0.344	$x10^{-10}$

PCRS-QPI3-VD	Miocene-QPI3-VD	47.3	1.72	990.5	7.87	0.501	$x10^{-16}$
PCRS-QPI3-VD	CNS-QPI3-VD	17.7	1.05	191.5	3.46	0.377	$x10^{-9}$
PCRS-QPI3-VD	Pre-CNS & Post-PCRS-QPI3-VD	22.1	1.18	330.0	4.54	0.563	$x10^{-20}$

Note D.5: See note of Table D.1 for description.

Table D.6: Construction methods for statistical models utilising palaeomagnetic observations attributed to the Permo-Carboniferous Reversed Superchron (PCRS).

Model	Study	Palaeomagnetic Observations	Measure of PSV	PINT Filtering	σ_1^0 from ECDF
PCRS-QPI3	This study	PCRS Group 1 database (1)	S_B	QPI3	Yes
KRSCovM	Brandt et al., (2021)	Extrusive rocks PDKRS (2)	σ_E & σ_N (3)	None	No
KRSCovM-VGP	This study	Extrusive rocks PDKRS (2)	S_B	None	No
KRSCovM-VGP-QPI3	This study	Extrusive rocks PDKRS (2)	S_B	QPI3	Yes

Note D.6: PDKRS: paleomagnetic database of Kiaman Reversed Superchron, S_B: Virtual geomagnetic pole (VGP) dispersion, σ_E & σ_N: directional palaeosecular variation (PSV) statistic. PINT filtering denotes the filtering applied to palaeointensity observations. Standard deviation of g_1^0 (σ_1^0) from ECDF indicates if σ_1^0 was determined by minimising model parameters to the observed empirical cumulative distribution function (ECDF) of palaeointensity observations. (1) Handford et al., 2021, (2) Brandt et al., 2021, (3) Brandt et al., 2020.

References

Abrajevitch, A., Van der Voo, R., Bazhenov, M. L., Levashova, N. M., & McCausland, P. J. A. (2008). The role of Kazakhstan orocline in the late Paleozoic amalgamation of Eurasia. *Tectonophysics*, 455, 61-76. https//doi.org/10.1016/j.tecto.2008.05.006

Ahn, H. S., Kidane, T., Yamamoto, Y., & Otofuji, Y. I. (2016). Low geomagnetic field intensity in the Matuyama Chron: palaeomagnetic study of a lava sequence from Afar depression, East Africa. *Geophysical Journal International*, *204*(1), 127–146. https://doi.org/10.1093/GJI/GGV303

Aitken, M. J., Aslop, A. L., Bussel, G.D., & Winter, M. B. (1988). Determination of the intensity of the Earth's magnetic field during archaeological times: reliability of the Thellier technique. *Reviews of Geophysics, 26,* 3–12.

Anderson, B. J., Johnson, C. L., Korth, H., Winslow, R. M., Borovsky, J. E., Purucker, M. E., et al. (2012). Low-degree structure in Mercury's planetary magnetic field. *Journal of Geophysical Research: Planets*, *117*(E12), 0–12. https://doi.org/10.1029/2012JE004159

Anwar, T., Hawkins, L., Kravchinsky V. A., Biggin, A. J., & Pavlov, V. E. (2016). Microwave paleointensities indicate a low paleomagnetic dipole moment at Permo-Triassic boundary. *Physics of the Earth and Planetary Interiors*, 260, 62-73. https://doi.org/10.1016/j.pepi.2016.09.007

Arlen, T. C., Vassilev, V. V, Weisgarber, T., Wakely, S. P., & Shafi, S. Y. (2014). Intergalactic Magnetic Fields and Gamma-Ray observations of Extreme TeV Blazars. *The Astrophysical Journal*, *796*(18pp), 18. https://doi.org/10.1088/0004-637X/796/1/18

Arndt, N. (2011). Pillow Lava. In M. Gargaud (Ed.), *Encyclopedia of Astrobiology* (pp. 1260–1260). Springer, Berlin, Heidelberg. https://doi.org/10.1007/978-3-642-11274-4_1215

Aubert, J., Tarduno, J. A., & Johnson, C. L. (2010). Observations and Models of the Long-Term Evolution of Earth's Magnetic Field. *Space Science Reviews 2010 155:1*, *155*(1), 337–370. https://doi.org/10.1007/S11214-010-9684-5

Avery, M. S., Gee, J. S., Bowles, J. A., & Jackson, M. J. (2018). Paleointensity Estimates from Ignimbrites: The Bishop Tuff Revisited. *Geochemistry, Geophysics, Geosystems*, *19*(10), 3811–3831. https://doi.org/10.1029/2018GC007665

Barbara, B. (2019). Louis Néel: His multifaceted seminal work in magnetism. *Comptes Rendus Physique*, *20*(7–8), 631–649. https://doi.org/10.1016/J.CRHY.2019.07.003

Barredo, S., Chemale, F., Marsicano, C., Ávila, J. N., Ottone, E. G., & Ramos, V. A. (2012). Tectono-sequence stratigraphy and U–Pb zircon ages of the Rincón Blanco Depocenter, northern Cuyo Rift, Argentina. *Gondwana Research*, *21*(2–3), 624–636. https://doi.org/10.1016/J.GR.2011.05.016

Bazhenov, M. L., Van der Voo, R., Menzo, Z., Dominguez, A. R., Meert, J. G., & Levashova, N. M. (2016). Paleomagnetism and dating of a thick lava pile in the Permina Bakaly formation of eastern Kazakhstan: Regularities and singularities of the paleomagnetic record in thick lava series. *Physics of the Earth and Planetary Interiors*, 253, 5-20. http://dx.doi.org/10.1016/j.pepi.2016.02.001

Béguin, A., Paterson, G. A., Biggin, A. J., & de Groot, L. V. (2020). Paleointensity.org: An Online, Open Source, Application for the Interpretation of Paleointensity Data. *Geochemistry, Geophysics, Geosystems*, *21*(5), e2019GC008791. https://doi.org/10.1029/2019GC008791

Belica, M. E., Tohver, E., Pisarevsky, S. A., Jourdan, F., Denyszyn, S., & George, A. D. (2017). Middle Permian paleomagnetism of the Sydney Basin, Eastern Gondwana: Testing Pangea models and the timing of the end of the Kiaman Reverse Superchron. *Tectonophysics*, 699, 178-198. http://dx.doi.org/10.1016/j.tecto.2016.12.029

Benton, M. J. (2016). The Triassic. *Current Biology*, 26, R1205–R1225. https://doi.org/10.1016/j.cub.2016.10.060

Bernát, I. (1983). The Distribution of Iron in Nature. *Iron Metabolism*, 9–13. https://doi.org/10.1007/978-1-4615-7308-1_1

Bernoulli D., & Lemoine, M. (1980). Birth and early evolution of the Tethys: the overall situation. *Mémoires Du Bureau de Recherches Géologiques et Minières*, *115*, 168–179.

Bertotti, G. (1998). Magnetic Work and Thermodynamics. *Hysteresis in Magnetism*, 103–125. https://doi.org/10.1016/B978-012093270-2/50053-2

Bianchini, G., Natali, C., Shibata, T., & Yoshikawa, M. (2018). Basic Dykes Crosscutting the Crystalline Basement of Valsugana (Italy): New Evidence of Early Triassic Volcanism in the Southern Alps. *Tectonics*, *37*(7), 2080–2093. https://doi.org/10.1029/2017TC004950

Biggin, A. J., & Paterson, G. A. (2014). A new set of qualitative reliability criteria to aid inferences on palaeomagnetic dipole moment variations through geological time. *Frontiers in Earth Science*, *2*. https://doi.org/10.3389/feart.2014.00024

Biggin, A. J., & Thomas, D. N. (2003). Analysis of long-term variations in the geomagnetic poloidal field intensity and evaluation of their relationship with global geodynamics. *Geophysical Journal International*, *152*(2), 392–415. https://doi.org/10.1046/J.1365-246X.2003.01849.X

Biggin, A. J., Bono, R., Meduri, D. G., Sprain, C., Davies, C., Holme, R., & Doubrovine, P. V. (2020). Quantitative estimates of average geomagnetic axial dipole dominance in deep geological time. *Nature Communications*, 11, 6100. https://doi.org/10.1038/s41467-020-19794-7

Biggin, A. J., Piispa, E. J., Pesonen, L. J., Holme, R., Paterson, G. A., Veikkolainen, T., & Tauxe, L. (2015). Palaeomagnetic field intensity variations suggest Mesoproterozoic inner-core nucleation. *Nature, 526:7572*, *526*(7572), 245–248. https://doi.org/10.1038/nature15523

Biggin, A. J., Steinberger, B., Aubert, J., Suttie, N., Holme, R., Torsvik, T. H., et al. (2012). Possible links between long-term geomagnetic variations and whole-mantle convection processes. *Nature Geoscience*, 5, 526–533. https://doi.org/10.1038/ngeo1521

Biggin, A. J., Strik, G. H. M. A., & Langereis, C. G. (2009). The intensity of the geomagnetic field in the late-Archaean: New measurements and an analysis of the updated IAGA palaeointensity database. *Earth, Planets and Space*, *61*(1), 9–22. https://doi.org/10.1186/BF03352881/METRICS

Biggin, A. J., van Hinsbergen, D. J. J., Langereis, C. G., Straathof, G. B., & Deenen, M. H. L. (2008). Geomagnetic secular variation in the Cretaceous Normal Superchron and in the Jurassic. *Physics of the Earth and Planetary Interiors*, 169(1–4), 3–19. https://doi.org/10.1016/j.pepi.2008.07.004

Biggin, A.J., Sprain, C.J., Bono, R. K., Davies, C. J., Heimpel, M.H., & Holme, R. T. (2018). Detecting Externally Forced Long Term Palaeomagnetic Variations: Insight from Dynamo Simulations. *Publications of the Institute of Geophysics, Polish Academy of Sciences; Geophysical Data Bases,*

Processing and Instrumentation, *423*(C–112), 15–16. https://doi.org/10.25171/instgeoph_pas_publs-2018-009

Bleeker, W. (2004). Towards a 'natural' time scale for the Precambrian – A proposal. In F. M. Gradstein, J. G. Ogg, A. G. Smith (Eds.), *A Geologic Time Scale* (pp. 141-146). Cambridge, Uk: Cambridge University Press. https//doi.org/10.1017/CBO9780511536045

Bol'shakov, A. S., & Shcherbakova. V. V. (1979). A thermomagnetic criterion for determining the domain structure of ferrimagnetics. *Izvestiya, Solid Earth,* 111–117.

Bol'shakov, A. S., Solodovnikov, G. M., & Vinogradov, Y. K. (1989). Paleostrength of the Geomagnetic Field in the Early Permian. *Izvestiya, Earth Physics, 25(7),* 575–582.

Bonadiman, C., Coltorti, M., & Siena, F. (1994). Petrogenesis and T-fO2 estimates of Mt. Monzoni complex (Central Dolomites, Southern Alps): a Triassic shoshonitic intrusion in a transcurrent geodynamic setting. *European Journal of Mineralogy*, *6*(6), 943–966. https://doi.org/10.1127/EJM/6/6/0943

Bono, R. K., Biggin, A. J., Holme, R., Davies, C. J., Meduri, D. G., & Bestard, J. (2020). Covariant Giant Gaussian Process Models with Improved Reproduction of Palaeosecular Variation. *Geochemisty, Geophysics, Geosystems, 21(8),* e2020GC008960. https://doi.org/10.1029/2020GC008960

Bono, R. K., Paterson, G. A., van der Boon, A., Engbers, Y. A., Michael Grappone, J., Handford, B., et al. (2021). The PINT database: a definitive compilation of absolute palaeomagnetic intensity determinations since 4 billion years ago. *Geophysical Journal International*, *229*(1), 522–545. https://doi.org/10.1093/gji/ggab490

Bono, R. K., Tarduno, J. A., Nimmo, F., & Cottrell, R. D. (2019). Young inner core inferred from Ediacaran ultra-low geomagnetic field intensity. *Nature Geoscience*, *12*(2), 143–147. https://doi.org/10.1038/s41561-018-0288-0

Borlina, C. S., Weiss, B. P., Lima, E. A., Tang, F., Taylor, R. J. M., Einsle, J. F., et al. (2020). *Reevaluating the evidence for a Hadean-Eoarchean dynamo*. Retrieved from https://www.science.org

Bosellini, A. (1996). Geologia delle Dolomiti. *Athesia*, 192 pp.

Bouffard, M., Choblet, G., Labrosse, S., & Wicht, J. (2019). Chemical convection and stratification in the earth's outer core. *Frontiers in Earth Science*, *7*, 99. https://doi.org/10.3389/FEART.2019.00099/BIBTEX

Bouligand, C., Hulot, G., Khokhlov, A., & Glatzmaier, G. A. (2005). Statistical palaeomagnetic field modelling and dynamo numerical simulation. *Geophysical Journal International, 161(3),* 603–626. https://doi.org/10.1111/j.1365-246X.2005.02613.x

Bowles, J. A., Gee, J. S., Jackson, M. J., & Avery, M. S. (2015). Geomagnetic paleointensity in historical pyroclastic density currents: Testing the effects of emplacement temperature and postemplacement alteration. *Geochemistry, Geophysics, Geosystems*, *16*(10), 3607–3625. https://doi.org/10.1002/2015GC005910

Brandner, R., Gruber, A., Morelli, C., & Mair, V. (2016). *Field trip 1 Pulses of Neotethys-Rifting in the Permomesozoic of the Dolomites*. *Geo.Alp* (Vol. 13).

Brandt, D., Constable, C., & Ernesto, M. (2020). Giant Gaussian process models of geomagnetic palaeosecular variation: a directional outlook. *Geophysical journal International, 222(3),* 1526–1541. https://doi.org/10.1093/gji/ggaa258.

Brandt, D., Ernesto, M., & Constable, C. (2021). Consistent and Contrasting Aspects of the Geomagnetic Field Across Epochs with Distinct Reversal Frequencies Revealed by Modeling the Kiaman Superchron. *Geochemistry, Geophysics, Geosystems, 22(7).* https://doi.org/10.1029/2021GC009866

Breuer, D., & Spohn, T. (2006). Viscosity of the Martian mantle and its initial temperature: Constraints from crust formation history and the evolution of the magnetic field. *Planetary and Space Science*, *54*(2), 153–169. https://doi.org/10.1016/J.PSS.2005.08.008

Breuer, D., Spohn, T., van Hoolst, T., van Westrenen, W., Stanley, S., & Rambaux, N. (2021). Interiors of Earth-Like Planets and Satellites of the Solar System. *Surveys in Geophysics, 43:1*, *43*(1), 177–226. https://doi.org/10.1007/S10712-021-09677-X

Brown, M. C., Donadini, F., Korte, M., Nilsson, A., Korhonen, K., Lodge, A., et al. (2011). GEOMAGIA50.v3: 1. general structure and modifications to the archeological and volcanic database. *Earth, Planets and Space*, *67*, 83. https://doi.org/10.1186/s40623-015-0232-0

Brown, S. P., Thorne, M. S., Miyagi, L., & Rost, S. (2015). A compositional origin to ultralow-velocity zones. *Geophysical Research Letters*, *42*(4), 1039–1045. https://doi.org/10.1002/2014GL062097

Brunhes, B. (1906). Recherches sur la direction de l'aimantation des roches volcaniques. *Journal de Physique*, 705–724.

Buffett, B. A. (2010). Chemical stratification at the top of Earth's core: Constraints from observations of nutations. *Earth and Planetary Science Letters*, *296*(3–4), 367–372. https://doi.org/10.1016/J.EPSL.2010.05.020

Burgess, S. D., Muirhead, J. D., & Bowring, S. A. (2017). Initial pulse of Siberian Traps sills as the trigger of the end-Permian mass extinction. *Nature Communications,* 8, 164. https://doi.org/10.1038/s41467-017-00083-9

Burke, K., & Torsvik, T. H. (2004). Derivation of Large Igneous Provinces of the past 200 million years from long-term heterogeneities in the deep mantle. *Earth and Planetary Science Letters*, *227*(3–4), 531–538. https://doi.org/10.1016/J.EPSL.2004.09.015

Burke, K., Steinberger, B., Torsvik, T. H., & Smethurst, M. A. (2008). Plume Generation Zones at the margins of Large Low Shear Velocity Provinces on the core-mantle boundary. *Earth and Planetary Science Letters*, *265*(1–2), 49–60. https://doi.org/10.1016/J.EPSL.2007.09.042

Butler, R.F. (1992). *Paleomagnetism: Magnetic domains to Geological Terranes.* Boston, USA: Blackwell Scientific Publications.

Calvo, M., Prévot, M., Perrin, M., & Riisager, J. (2002). Investigating the reasons for the failure of palaeointensity experiments: A study on historical lava flows from Mt. Etna (Italy). *Geophysical Journal International*, *149*(1), 44–63. https://doi.org/10.1046/j.1365-246X.2002.01619.x

Calvo-Rathert, M., Bógalo, M. F., Morales, J., Goguitchaichvili, A., Lebedev, V. A., Vashakidze, G., et al. (2021). An Integrated Paleomagnetic, Multimethod-Paleointensity, and Radiometric Study on Cretaceous and Paleogene Lavas from the Lesser Caucasus: Geomagnetic and Tectonic Implications. *Journal of Geophysical Research: Solid Earth*, *126*(2), e2020JB020019. https://doi.org/10.1029/2020JB020019

Campuzano, S. A., Pavón-Carrasco, F. J., & Osete, M. L. (2014). Non-Dipole and Regional Effects on the Geomagnetic Dipole Moment Estimation. *Pure and Applied Geophysics*, *172*(1), 91–107. https://doi.org/10.1007/S00024-014-0919-3

Carlut, J., & Kent, D. V. (2002). Grain-size-dependent paleointensity results from very recent mid-oceanic ridge basalts. *Journal of Geophysical Research*, *107*(B3). https://doi.org/10.1029/2001jb000439

Carvallo, C., Roberts, A. P., Leonhardt, R., Laj, C., Kissel, C., Perrin, M., & Camps, P. (2006). Increasing the efficiency of paleointensity analyses by selection of samples using first-order reversal curve diagrams. *J. Geophys. Res*, *111*, 12103. https://doi.org/10.1029/2005JB004126

Casetta, F., Ickert, R. B., Mark, D. F., Giacomoni, P. P., Bonadiman, C., Ntaflos, T., et al. (2021). The Variscan subduction inheritance in the Southern Alps Sub-Continental Lithospheric Mantle: Clues from the Middle Triassic shoshonitic magmatism of the Dolomites (NE Italy). *Lithos*, *380–381*, 105856. https://doi.org/10.1016/j.lithos.2020.105856

Casetta, Federico, Coltorti, M., & Marrocchino, E. (2018a). Petrological evolution of the Middle Triassic Predazzo Intrusive Complex, Italian Alps. *International Geology Review*, *60*(8), 977–997. https://doi.org/10.1080/00206814.2017.1363676

Casetta, Federico, Coltorti, M., Ickert, R. B., Bonadiman, C., Giacomoni, P. P., & Ntaflos, T. (2018b). Intrusion of shoshonitic magmas at shallow crustal depth: T–P path, H_2O estimates, and AFC modeling of the Middle Triassic Predazzo Intrusive Complex (Southern Alps, Italy). *Contributions to Mineralogy and Petrology*, *173*(7), 1–27. https://doi.org/10.1007/S00410-018-1483-0

Chang, B., Kim, W., Doh, S.-J., & Yu, Y. (2013). Paleointensity determination of Late Cretaceous basalts in northwest South Korea: implications for low and stable paleofield strength in the Late Cretaceous. *Earth Planets Space*, *65*, 1501–1513. https://doi.org/10.5047/eps.2013.09.013

Chenet, A., Fluteau, F., Courtillot, V., Gérard, M., & Subbarao, K. (2008). Determination of rapid Deccan eruptions across the Cretaceous-Tertiary boundary using paleomagnetic secular variation: Results from a 1200-m-thick section in the Mahabaleshwar escarpment.*Journal of Geophysical Research*, *113*. https://doi.org/10.1029/2006JB004635

Chung, S.-L., & Jahn, B.-m. (1995). Plume-lithosphere interaction in generation of the Emeishan flood basalts at the Permian-Triassic boundary. *Geology, 23(10)*, 889-892. https://doi.org/10.1130/0091-7613(1995)023<0889:PLIIGO>2.3.CO;2

Cingolani, C., Dalla Salda, L., Hervé, F., Munizaga, F., Pankhurst, R. J., Parada, A., & Rapela, C. W. (1991). The magmatic evolution of northern Patagonia; New impressions of pre-Andean and Andean tectonics. In R.S. Harmon, C. W. Rapela (Eds.) *Andean Magmatism and Its Tectonic Setting.*

Coe, R. S. (1967). Paleo-intensities of the Earth's magnetic field determined from Tertiary and Quaternary rocks. *Journal of Geophysical Research, 72(12),* 3247–3262. https://doi.org/10.1029/jz072i012p03247

Coe, R. S., & Glatzmaier, G. A. (2006). Symmetry and stability of the geomagnetic field. *Geophysical Research Letters*, *33*(21). https://doi.org/10.1029/2006GL027903

Constable, C. (2007). Dipole Moment Variation. In: D. Gubbins, D., & E. Herrero-Bervera (Eds.) *Encyclopedia of Geomagnetism and Paleomagnetism* (pp. 159-161). Dordrecht, Springer. *Https://Doi.Org/10.1007/978-1-4020-4423-6_67*.

Constable, C. G., & Johnson, C. L. (1999). Anisotropic paleosecular variation models: implications for geomagnetic field observables. *Physics of the Earth and Planetary Interiors, 115(1),* 35–51. https://doi.org/10.1016/S0031-9201(99)00065-5

Constable, C. G., & Parker, R. L. (1988). Statistics of the geomagnetic secular variation for the past 5 m.y. *Journal of Geophysical Research: Solid Earth*, 93, 11569–11581. https://doi.org/10.1029/JB093iB10p11569

Cottrell, E., Birner, S. K., Brounce, M., Davis, F. A., Waters, L. E., & Kelley, K. A. (2021). Oxygen Fugacity Across Tectonic Settings. In R. Moretti, & D.R. Neuville (Eds.) *Magma redox Geochemistry* (pp. 33–61). https://doi.org/10.1002/9781119473206.CH3

Cottrell, R. D., & Tarduno, J. A. (1999). Geomagnetic paleointensity derived from single plagioclase crystals. *Earth and Planetary Science Letters* (Vol. 169). https://doi.org/10.1016/S0012-821X(99)00068-0

Cottrell, R. D., & Tarduno, J. A. (2000). In search of high-fidelity geomagnetic paleointensities: A comparison of single plagioclase crystal and whole rock Thellier-Thellier analyses. *Journal of Geophysical Research: Solid Earth*. https://doi.org/10.1029/2000jb900219

Cottrell, R., Tarduno. J. A., & Roberts, J. (2008). The Kiaman Reversed Polarity Superchron at Kiama: Toward a field strength estimate based on single silicate crystals. *Physics of the Earth and Planetary Interiors*, 169, 49-58. https://doi.org/10.1016/j.pepi.2008.07.041

Courtillot, V. E., & Renne, P. R. (2003). On the ages of flood basalt events. *Comptes Rendus Geoscience*, *335*(1), 113–140. https://doi.org/10.1016/S1631-0713(03)00006-3

Courtillot, V., & Olson, P. (2007). Mantle plumes link magnetic superchrons to phanerozoic mass depletion events. *Earth and Planetary Science Letters*, *260*(3–4), 495–504. https://doi.org/10.1016/J.EPSL.2007.06.003

Cox, A. (1969). Geomagnetic reversals. *Science*, *163*, 237–245.

Cox, A. (1970). Latitude dependence of the angular dispersion of the geomagnetic field. *Geophysical Journal of the Royal Astronomical Society*, 20(3), 253–269. https://doi.org/10.1111/j.1365-246X.1970.tb06069.x

Cox, A. (1975). The Frequency of Geomagnetic Reversals and the Symmetry of the Nondipole Field. *Reviews Of Geophysics And Space Physics*, *13*(3). https://doi.org/10.1029/RG013i003p00035

Cox, A., (1962). Analysis of present geomagnetic field for comparison with paleomagnetic results. *Journal of Geomagnetism and Geoelectricity, 13,* 101–112.

Creer, K. M. (1962a). The dispersion of the geomagnetic field due to secular variation and its determination for remote times from paleomagnetic data. *Journal of Geophysical Research, 67,* 3461–3476.

Creer, K. M. (1962b). An analysis of the geomagnetic field using paleomagnetic methods. *Journal of Geomagnetism and Geoelectricity, 13,* 113–119.

Cromwell, G., Johnson, C. L., Tauxe, L., Constable, C. G., & Jarboe, N. A. (2018). PSV10: A global dataset for 0–10 Ma time-averaged field and paleosecular variation studies. *Geochemistry, Geophysics, Geosystems*, 19, 1533–1558. https://doi.org/10.1002/2017GC007318

Cromwell, G., Trusdell, F., Tauxe, L., Staudigel, H., & Ron, H. (2017). Holocene Paleointensity of the Island of Hawai`i From Glassy Volcanics. *Geochemistry, Geophysics, Geosystems*, *19*(9), 3224–3245. https://doi.org/10.1002/2017GC006927

Davies, C. J., & Constable, C. (2017). Geomagnetic spikes on the core-mantle boundary. *Nature Communications*, *8*. https://doi.org/10.1038/ncomms15593

Davies, C. J., Bono, R. K., Meduri, D. G., Aubert, J., Greenwood, S., & Biggin, A. J. (2022). Dynamo constraints on the long-term evolution of Earth's magnetic field strength. *Geophysical Journal International*, *228*(1), 316–336. https://doi.org/10.1093/gji/ggab342

Davydov, V. I., Korn, D., Schmitz, M. D., Gradstein, F. M., & Hammer, O. (2012). The Carboniferous period. In F. M. Gradstein, J. G. Ogg, M. D. Schmitz, G. M. Ogg (Eds), *The Geologic Time Scale* (pp. 603-651). Elsevier. https://doi.org/10.1016/B978-0-444-59425-9.00023-8

de Groot, L. V., Biggin, A. J., Dekkers, M. J., Langereis, C. G., & Herrero-Bervera, E. (2013). Rapid regional perturbations to the recent global geomagnetic decay revealed by a new Hawaiian record, *Nature Communications, 4*. https://doi:10.1038/ncomms3727.

de Groot, L. V., Pimentel, A., & Di Chiara, A. (2016). The multi-method paleointensity approach applied to volcanics from Terceira: full-vector geomagnetic data for the past 50 kyr. *Geophysical Journal International, 206(1),* 590–604. https://doi.org/10.1093/gji/ggw095

de Groot, L.V., Béguin, A., Kosters, M. E., van Rijsingen, E. M., Struijk, E. L. M., Biggin, A. J., et al. (2015). High paleointensities for the Canary Islands constrain the Levant geomagnetic high. *Earth and Planetary Science Letters, 419(1),* 154–167. https://doi.org/10.1016/j.epsl.2015.03.020

de Min, A., Velicogna, M., Ziberna, L., Chiaradia, M., Alberti, A., & Marzoli, A. (2020). Triassic magmatism in the European Southern Alps as an early phase of Pangea break-up. *Geological Magazine*, *157*(11), 1800–1822. https://doi.org/10.1017/S0016756820000084

de Oliveira, W. P., Franco, D. R., Brandt, D., Ernesto, M., da Ponte Neto, C. F., Zhao, X., et al. (2018). Behaviour of the paleosecular variation during the Permian-Carboniferous reversed Superchron and comparisons to the low reversal frequency intervals since Precambrian times. *Geochemistry, Geophysics, Geosystems*, 19, 1035–1048. https://doi.org/10.1002/2017GC007262

de Oliveira, W. P., Hartmann, G. A., Terra-Nova, F., Brandt, D., Biggin, A. J., Engbers, Y. A., et al. (2021). Paleosecular Variation and the Time-Averaged Geomagnetic Field Since 10 Ma. *Geochemistry, Geophysics, Geosystems*, *22*(10). https://doi.org/10.1029/2021GC010063

Doglioni, C. (2007). Tectonics of the Dolomites. *Bulletin Für Angewandte Geologie*, *12*(2), 11–15. https://doi.org/10.5169/seals-226374

Domeier, M., Van der Voo, R., Tohver, E., Tomezzoli, R. N., Vizan, H., Torsvik, T. H., & Kirshner, J. (2011a). New Late Permian paleomagnetic data from Argentina: Refinement of the apparent polar wander path of Gondwana. *Geochemistry, Geophysics, Geosystems*, 12, 7. https://doi.org/10.1029/2011GC003616

Domeier, M., Van der Voo, R., Tomezzoli, R. N., Tohver, E., Hendriks, B. W. H., Torsvik, T. H., et al. (2011b). Support for an "A-type" Pangea reconstruction from high-fidelity Late Permian and Early to Middle Triassic paleomagnetic data. *Journal of Geophysical Research*, 116, B12144. https//doi.org/10.1029/2011JB008495

Dominguez, A. R., Van de Voo, R., Torsvik, T. H., Hendriks, B. W. H., Abrajevitch, A., & Domeier, M. (2011). The ~270 Ma palaeolatitude of Baltica and its significance for Pangea models. *Geophysical Journal International*, 186, 529-550. https//doi.org/10.1111/j.1365-246X.2011.05061.x

Donadini, F., Riisager, P., Korhonen, K., Kahma, K., Pesonen, L., & Snowball, I. (2007). Holocene geomagnetic paleointensities: A blind test of absolute paleointensity techniques and materials. *Physics of the Earth and planetary Interirors.* 161, 19-35. https://doi.org/10.1016/j.pepi.2006.12.002

Doubrovine, P. V., Veikkolainen, T., Pesonen, L. J., Piispa, E., Ots, S., Smirnov, A. V., et al. (2019). Latitude dependence of geomagnetic paleosecular variation and its relation to the frequency of magnetic reversals: Observations from the Cretaceous and Jurassic. *Geochemistry, Geophysics, Geosystems*, 20, 1240-1279. DOI: 10.1029/2018GC007863

Draeger, U., Prévot, M., Poidras, T., & Riisager, J. (2006). Single-domain chemical, thermochemical and thermal remanences in a basaltic rock. *Geophysical Journal International*, *166*(1), 12–32. https://doi.org/10.1111/J.1365-246X.2006.02862.X/3/M_166-1-12-EQ012.JPEG

Driscoll, P., & Olson, P. (2011). Superchron cycles driven by variable core heat flow. *Geophysical Research Letters*, *38*(9). https://doi.org/10.1029/2011GL046808

Dumoulin, C., Tobie, G., Verhoeven, O., Rosenblatt, P., & Rambaux, N. (2017). Tidal constraints on the interior of Venus. *Journal of Geophysical Research: Planets*, *122*(6), 1338–1352. https://doi.org/10.1002/2016JE005249

Dunlop, D. J. (2011). Physical basis of the Thellier–Thellier and related paleointensity methods. *Physics of the Earth and Planetary Interiors*, *187*(3–4), 118–138. https://doi.org/10.1016/J.PEPI.2011.03.006

Dunlop, D. J., & Özdemir, Ö. (1997). *Rock Magnetism Fundamentals and Frontiers*. Cambridge University Press. https://doi.org/10.1017/cbo9780511612794

Dunlop, D. J., & Özdemir, Ö. (2001). Beyond Néel's theories: thermal demagnetization of narrow-band partial thermoremanent magnetizations. *Physics of the Earth and Planetary Interiors*, *126*(1–2), 43–57. https://doi.org/10.1016/S0031-9201(01)00243-6

Dunlop, D. J., & Argyle, K. S. (1997). Thermoremanence, anhysteretic remanence and susceptibility of submicron magnetites: Nonlinear field dependence and variation with grain size. *Journal of Geophysical Research: Solid Earth, 102,* 20199–20210. https://doi.org/10.1029/97JB00957

Dunlop, D. J., Zhang, B., & Özdemir, Ö. (2005). Linear and nonlinear Thellier paleointensity behavior of natural minerals. *Journal of Geophysical Research: Solid Earth*, *110*(B1), 1–15. https://doi.org/10.1029/2004JB003095

Eid, B., Lhuillier, F., Shcherbakov, V. P., & Shcherbakova, V. V. (2022). Do changes in geomagnetic secular variation, dipole moment and polarity reversal frequency correlate over the past 155 Myr? *Geophysical Journal International*, *230*(2), 1132–1146. https://doi.org/10.1093/GJI/GGAC112

Eitel, M., Gilder, S. A., Kunzmann, T., & Pohl, J. (2014). Rochechouart impact crater melt breccias record no geomagnetic field reversal. *Earth and Planetary Science Letters*, *387*, 97–106. https://doi.org/10.1016/J.EPSL.2013.11.021

Eitel, M., Gilder, S. A., Spray, J., Thompson, L., & Pohl, J. (2016). A paleomagnetic and rock magnetic study of the Manicouagan impact structure: Implications for crater formation and geodynamo effects. *Journal of Geophysical Research: Solid Earth*, *121*(2), 436–454. https://doi.org/10.1002/2015JB012577

Engbers, Y. A., Biggin, A. J., & Bono, R. K. (2022). PSVM: A Global Database for the Miocene Indicating Elevated Paleosecular Variation Relative to the Last 10 Myrs. *Geochemistry, Geophysics, Geosystems, 23(8).* https://doi.org/10.1029/2022GC010480

Ernesto, M., Comin-Chiaramonti, P., & de Barros Gomes, C. (2015). The Early Triassic magmatism of the Alto Paraguay Province, Central South America: Paleomagnetic and ASM data. *Open Geosciences, 7(1),* 386-394. https://doi.org/10.1515/geo-2015-0022

Evans, B. W., Bruno, S., & Kuehner, S. M. (2006). Experimental determination of coexisting iron-titanium oxides in the systems FeTiAlO, FeTiAlMgO, FeTiAlMnO, and FeTiAlMgMnO at 800 and 900°C, 1-4 kbar, and relatively high oxygen fugacity. *Contributions to Mineralogy and Petrology.* https://doi.org/10.1007/s00410-006-0098-z

Fabian, K. (2009). Thermochemical remanence acquisition in single-domain particle ensembles: A case for possible overestimation of the geomagnetic paleointensity. *Geochemistry, Geophysics, Geosystems*, *10*(6). https://doi.org/10.1029/2009GC002420

Falco, J. I. (2019). Estratigrafía y evolución magmática del Grupo Los Menucos (Triásico), provincia de Río Negro, Argentina. [Doctoral thesis, Universidad Nacional del Sur]. Repositorio Digital Institucional de la Universidad Nacional del Sur (RID-UNS). handle/123456789/4717

Falco, J. I., Hauser, N., Scivetti, N., Reimold, W. U., Schmitt, R. T., & Folguera, A. (2022). Upper Triassic to Middle Jurassic magmatic evolution of northern Patagonia: Insights from the tectonic and crustal evolution of the Los Menucos area, North Patagonian Massif, Argentina. *Journal of South American Earth Sciences*, *113*, 103631. https://doi.org/10.1016/J.JSAMES.2021.103631

Flament, N., Williams, S., Müller, R. D., Gurnis, M., & Bower, D. J. (2017). Origin and evolution of the deep thermochemical structure beneath Eurasia. *Nature Communications*, *8*. https://doi.org/10.1038/ncomms14164

Foulger, G. R. (2007). The "plate" model for the genesis of melting anomalies. *Special Paper of the Geological Society of America*, *430*, 1–28. https://doi.org/10.1130/2007.2430(01)

Franco, D. R., de Oliveira, W. P., de Freitas, F. B. V., Takahashi, D., de Ponte Neto, C. S., & Peixoto, I. M. C. (2019). Paleomagnetic evidence for inverse correspondence between the relative contribution of the axial dipole field and CMB heat flux for the past 270 Myr. *Scientific Reports*, 9, 1-8. DOI:10.1038/s41598-018-36494-x

Franzese, J. R., & Spalletti, L. A. (2001). Late Triassic–early Jurassic continental extension in southwestern Gondwana: tectonic segmentation and pre-break-up rifting. *Journal of South American Earth Sciences, 14(3),* 257-270. https://doi.org/10.1016/S0895-9811(01)00029-3

Frost, B. R. (1991). Chapter 1. Introduction to Oxygen Fugacity and its Petrologic Importance. In D.H. Lindsley (Eds.), *Oxide Minerals* (pp. 1-10). https://doi.org/10.1515/9781501508684-004

Frost, B., & Frost, C. (2019). Intracontinental Volcanism. In *Essentials of Igneous and Metamorphic Petrology* (pp. 130-146). Cambridge: Cambridge University Press. doi:10.1017/9781108685047.010

Fu, R. R., Weiss, B. P., Lima, E. A., Kehayias, P., Araujo, J. F. D. F., Glenn, D. R., et al. (2017). Evaluating the paleomagnetic potential of single zircon crystals using the Bishop Tuff. *Earth and Planetary Science Letters, 458,* 1–13. https://doi.org/10.1016/j.epsl.2016.09.038

Fukuma, K., & Kono, M. (2016). A LabVIEW software for Thellier paleointensity measurements with an automated three-component spinner magnetometer TSpin 1. Geomagnetism Recent advances in environmental magnetism and paleomagnetism. *Earth, Planets and Space*, *68*(1), 1–9. https://doi.org/10.1186/S40623-016-0424-2/FIGURES/6

Fulignati, P. (2020). Clay minerals in hydrothermal systems. *Minerals*. MDPI AG. https://doi.org/10.3390/min10100919

Galán, E., & Ferrell, R. E. (2013). Genesis of Clay Minerals. *Developments in Clay Science*, *5*, 83–126. https://doi.org/10.1016/B978-0-08-098258-8.00003-1

Garcia, A. S., Thomas, D. N., Liss, D., & Shaw, J. (2006). Low geomagnetic field intensity during the Kiaman superchron: Thellier and microwave results from the Great Whin Sill intrusive complex, northern United Kingdom. *Geophysical Research Letters*, 33. https://doi.org/10.1029/2006GL026729

Gee, J. S., Yu, Y., & Bowles, J. (2010). Paleointensity estimates from ignimbrites: An evaluation of the Bishop tuff. *Geochemistry, Geophysics, Geosystems, 11(3).* https://doi.org/10.1029/2009GC002834

Geuna, S. E., & Ecosteguy, L. D. (2004). Palaeomagnetism of the Upper Carboniferous-Lower Permian transition from Paganzo basin, Argentina. *Geophysical Journal International*, 157, 1071-1089. https//doi.org/10.1111/j.1365-246X.2004.02229.x

Gimeno, D. (2003). Devitrification of natural rhyolitic obsidian glasses: petrographic and microstructural study (SEM+EDS) of recent (Lipari island) and ancient (Sarrabus, SE Sardinia) samples. *Journal of Non-Crystalline Solids*, *323*(1–3), 84–90. https://doi.org/10.1016/S0022-3093(03)00294-1

Goguitchaichvili, A., Urrutia-Fucugauchi, J., Alva-Valdivia, L. M., Morales, J., Riisager, J., & Riisager, P. (2004). Long-term variation of geomagnetic field strength: A cautionary note. *Eos, Transactions American Geophysical Union*, *85*(21), 209–212. https://doi.org/10.1029/2004EO210001

González, P. D., Giacosa, R. E., Lagorio, S., Justiniano, C. B., Sato, A. M., Cábana, M. C., et al. (2021). U–Pb geochronology of the meta-volcanic rocks from Sierra de Calcatapul: Implications for the Middle Triassic syn-rift volcanism and tectonic evolution of northern extra-Andean Patagonia. *Journal of South American Earth Sciences*, *108*, 103170. https://doi.org/10.1016/J.JSAMES.2021.103170

Govoni, F., Orrù, E., Bonafede, A., Iacobelli, M., Paladino, R., Vazza, F., et al. (2019). A radio ridge connecting two galaxy clusters in a filament of the cosmic web. *Science*, *364*(6444), 981–984. https://doi.org/10.1126/SCIENCE.AAT7500/SUPPL_FILE/AAT7500_S2.MP4

Graham, J. W. (1949). The stability and significance of magnetism in sedimentary rocks. *Journal of Geophysical Research*, *54*(2), 131–167. https://doi.org/10.1029/JZ054I002P00131

Grappone, J. M., Biggin, A. J., Barrett, T. J., Hill, M. J., & Sprain, C. J. (2020). Comparison of Thermal and Microwave Paleointensity Estimates in Specimens Displaying Non-Ideal Behavior in Thellier-Style Paleointensity Experiments. *Journal of Geophysical Research: Solid Earth*, *125*(8). https://doi.org/10.1029/2020JB019802

Gratton, M. N., Shaw, J., & Herrero-Bervera, E. (2005). An absolute palaeointensity record from SOH1 lava core, Hawaii using the microwave technique. *Physics of the Earth and Planetary Interiors, 148(2-4),* 193–214. https://doi.org/10.1016/ j.pepi.2004.09.009

Greenwood, S., Davies, C. J., & Mound, J. E. (2021). On the evolution of thermally stratified layers at the top of Earth's core. *Physics of the Earth and Planetary Interiors*, *318*, 106763. https://doi.org/10.1016/J.PEPI.2021.106763

Grommé, S., Mankinen, E. A., Marshall, M., & Coe, R. S. (1979). Geomagnetic paleointensities by the Thelliers' method from submarine pillow basalts: effects of seafloor weathering. *Journal of Geophysical Research*, *84*(B7), 3553–3575. https://doi.org/10.1029/JB084iB07p03553

Gubbins, D. (1987). Mechanism for Geomagnetic Polarity Reversals. *Nature,* 326, 167-169. https://doi.org/10.1038/326167a0

Gubbins, D. (1999). The distinction between geomagnetic excursions and reversals. *Geophysical journal International. 137*, F1–F3. https://doi.org/10.1046/j.1365-246x.1999.00810.x

Gurevitch, E. L., Heunemann, C., Rad'ko, K., Westphal, M., Bachtadse, V., Pozzi, J. P., & Feinberg, H. (2004). Palaeomagnetism and magnetostratigraphy of the Permian-Triassic

northwest central Siberian Trap Basalts. *Tectonophysics*, 379, 211-226. https//doi.org/10.1016/j.tecto.2003.11.005

Haggerty, S. E. (1991). Chapter 5. Oxide Textures - A Mini-Atlas. In D.H. Lindsley (Eds.), *Oxide Minerals* (pp. 129–220). Berlin, Boston: De Gruyter, 1991. https://doi.org/10.1515/9781501508684-008

Hailwood, E. A. (1975). The palaeomagnetism of Triassic and Cretaceous rock from Morocco. *Geophysical Journal International*, 43, 1029-1030. https://doi.org/10.1111/j.1365-246X.1975.tb04149.x

Haldan, M. M., Langereis, C. G., Biggin, A. J., Dekkers, M. J., & Evans, M. E. (2009). A comparison of detailed equatorial red bed records of secular variation during the Permo-Carboniferous Reversed Superchron. *Geophysical Journal International*, 177, 834-848. https://doi.org/10.1111/j.1365-246X.2009.04124.x

Haldan, M. M., Meijers, M. J. M., Langereis, C. G., Larsen, B. T., & Heyer, H. (2014). New palaeomagnetic results from the Oslo Graben, a Permian Superchron lava province. *Geophysical Journal International*, 199, 1554-1571. https://doi.org/10.1093/gji/ggu351

Handford, B. T., Biggin, A. J., Haldan, M. M., & Langereis, C. G. (2021). Analyzing Triassic and Permian Geomagnetic Paleosecular Variation and the Implications for Ancient Field Morphology. *Geochemistry, Geophysics, Geosystems*, *22*(11), e2021GC009930. https://doi.org/10.1029/2021GC009930

Haque, Z., Geissman, J.W., Irmis, R. B., Olsen, P. E., Lepre, C., Buhedma, H., et al. (2021). Magnetostratigraphy of the Triassic Moenkopi Formation from the continuous cores recovered in Colorado Plateau Coring Project Phase 1 (CPCP-1), Petrified Forest National Park, Arizona, USA: Correlation of the Early to Middle Triassic strata and biota in Colorado Plateau and its environs. *Journal of Geophysical Research: Solid Earth,* 126(9). https://doi.org/10.1029/2021JB021899

Hawkins, M. A., Grappone, J. M., Sprain, C. J., Saengduean, P., Sage, E. J., Thomas-Cunningham, S., et al. (2021). Intensity of the Earth's magnetic field: Evidence for a Mid-Paleozoic dipole low. *Proceedings of the National Academy of Sciences,* 118 (34). https://doi.org/10.1073/pnas.2017342118

Heiken, G. (2006). *Tuffs - Their Properties, Uses, Hydrology, and Resources*. Geological Society of America. https://doi.org/10.1130/SPE408

Henderson, C. M., Davydov, V. I., Wardlaw, B. R., Gradstein, F. M., & Hammer, O. (2012). The Permian period. In In F. M. Gradstein, J. G. Ogg, M. D. Schmitz, G. M. Ogg (Eds), *The Geologic Time Scale* (pp. 653-679). Elsevier. https://doi.org/10.1016/B978-0-444-59425-9.00024-X

Heslop, D., & Roberts, A. P. (2018a). A bayesian Approach to the Paleomagnetic Conglomerate Test. *Journal of Geophysical Research: Solid Earth, 123(2),* 1132–1142. https://doi.org/10.1002/2017JB014526

Heslop, D., & Roberts, A. P. (2018b). Revisiting the Paleomagnetic Reversal Test: A Bayesian Hypothesis Testing Framework for a Common Mean Direction. *Journal of Geophysical Research: Solid Earth*, *123*(9), 7225–7236. https://doi.org/10.1029/2018JB016081

Heunemann, C., Krása, D., Soffel, H. C., Gurevitch, E., & Bachtadse, V. (2004). Directions and intensities of the Earth's magnetic field during a reversal: results from the Permo-Triassic Siberian trap basalts, Russia. *Earth and Planetary Science Letters.* 218, 197-213. https://doi.org/10.1016/S0012-821X(03)00642-3

Hill, M. J., & Shaw, J. (1999). Palaeointensity results for historic lavas from Mt Etna using microwave demagnetization/remagnetization in a modified Thellier-type experiment. *Geophysical Journal International, 139(2),* 583–590. https://doi.org/ 10.1046/j.1365-246X.1999.00980.x

Hill, M. J., & Shaw, J. (2000). Magnetic field intensity study of the 1960 Kilauea lava flow, Hawaii, using the microwave palaeointensity technique. *Geophysical Journal International, 142(2),* 487–504. https://doi.org/10.1046/j.1365-246X.2000. 00164.x

Hounslow, M. W. (2022). A geomagnetic polarity timescale for the Carboniferous. *Geological Society Special Publication*, *512*(1), 141–195. https://doi.org/10.1144/SP512-2020-102

Hounslow, M. W., & Muttoni, G. (2010). The geomagnetic polarity timescale for the Triassic: linkage to stage boundary definitions. *Geological Society, London, Special Publications*, 334, 61-102. doi:10.1144/SP334.4

Hounslow, M. W., Domeier, M., & Biggin, A. J. (2018). Subduction flux modulates the geomagnetic polarity reversal rate. *Tectonophysics*, 742-743, 34-49. https://doi.org/10.1016/j.tecto.2018.05.018

Hounslow, M. W., Harris, S. E., Wójcik, K., Nawrocki, J., Ratcliffe, K. T., Woodcock, N. H., & Montgomery, P. (2021). A geomagnetic polarity stratigraphy for the Middle and Upper Ordovician. *Palaeogeography, Palaeoclimatology, Palaeoecology*, *567*, 110225. https://doi.org/10.1016/J.PALAEO.2021.110225

http://dx.doi.org/10.1016/j.earscirev.2006.02.001

Huang, K., & Opdyke, N. D. (1991). Paleomagentic results from the Upper Carboniferous of the Shan-Thai-Malay block of western Yunnan, China. Tectonophysics, 192, 333-334. https://doi.org/10.1016/0040-1951(91)90107-4

Hulot, G., & Bouligand, C. (2005). Statistical palaeomagnetic field modelling and symmetry considerations. *Geophysical Journal International, 161(3),* 591– 602. https://doi.org/10.1111/j.1365-246X.2005.02612.x

Hulot, G., & Gallet, Y. (1996). On the interpretation of virtual geomagnetic pole (VGP) scatter curves. *Physics of the Earth and Planetary Interiors*, 95(1–2), 37–53. https://doi.org/10.1016/0031-9201(95)03106-5

Hulot, G., & Gallet, Y. (2003). Do superchrons occur without any palaeomagnetic warning? *Earth and Planetary Science Letters*, *210*(1–2), 191–201. https://doi.org/10.1016/S0012-821X(03)00130-4

Hummel, R. E. (2011). *Electronic Properties of Materials*. New York: Springer. https://doi.org/10.1007/978-1-4419-8164-6

Humphris, S. E. (1972). *The hydrothermal alteration of oceanic basalts by seawater* [Doctoral thesis, Massachusetts Institute of Technology]. MIT Libraries. http://hdl.handle.net/1721.1/54260

Humphris, S. E., & Thompson, G. (1978). Hydrothermal alteration of oceanic basalts by seawater. *Geochimica et Cosmochimica Acta, 42(1),* 107–125. https://doi.org/10.1016/0016-7037(78)90221-1

Ingham, E., Heslop, D., Roberts, A. P., Hawkins, R., & Sambridge, M. (2014). Is there a link between geomagnetic reversal frequency and paleointensity? A Bayesian approach. *Journal of Geophysical Research: Solid Earth*, *119*(7), 5290–5304. https://doi.org/10.1002/2014JB010947

Irving, E. (1970). The Mid-Atlantic Ridge at 45° N. XIV. Oxidation and magnetic properties of basalt; review and discussion. *Canadian journal of Earth Sciences, 7*(6), 1528–1538. https://doi.org/10.1139/E70-144

Ivanov, A. V. (2007). Evaluation of different models for the origin of the Siberian Traps. *Special Paper of the Geological Society of America*, *430*, 669–691. https://doi.org/10.1130/2007.2430(31)

Jeong, J. O., Ahn, H. S., Son, M., Cho, H., & Sohn, Y. K. (2021). Eruptive and depositional processes of a low-aspect-ratio ignimbrite (the Southern Kusandong Tuff, South Korea) inferred from magnetic susceptibility variability. *Journal of Volcanology and Geothermal Research*, *419*. https://doi.org/10.1016/J.JVOLGEORES.2021.107374

Jeong, J. O., Jeon, Y. M., & Sohn, Y. K. (2005). Petrography and modal compositional variations of the Cretaceous Kusandong Tuff, Korea. *Journal of the Geological Society of Korea, 41,* 73–90.

Jesinkey, C., Forsythe, R. D., Mpodozis, C., & Davidson, J. (1987). Concordant late Paleozoic paleomagnetizations from the Atacama Desert: implications for tectonic models of the Chilean Andes. *Earth and Planetary Science Letters*, 85, 461-472. https://doi.org/10.1016/0012-821X(87)90141-5

Johnson, C. L., & McFadden, P. (2015). The Time-Averaged Field and Paleosecular Variation. In G. Schubert (Eds.) *Treatise on Geophysics: Second Edition*, (pp. 385–417). Amsterdam, The Netherlands: Elsevier. https://doi.org/10.1016/B978-0-444-53802-4.00105-6

Johnson, P. H., & Pariso, J. E. (1993). Variations in oceanic crustal magnetization: systematic changes in the last 160 million years. *Journal of Geophysical Research*, *98*(B1), 435–445. https://doi.org/10.1029/92JB01322

Johnson, P., H., & Atwater, T. (1977). Magnetic study of basalts from the Mid-Atlantic Ridge, lat 37°N. *GSA Bulletin, 88(5),* 637–647. https://doi.org/10.1130/0016-7606(1977)88%3C637:MSOBFT%3E2.0.CO;2

Jones, C. A. (2011). Planetary Magnetic Fields and Fluid Dynamos. *Annual Review of Fluid Mechanics*, *43*, 583–614. https://doi.org/10.1146/annurev-fluid-122109-160727

Joplin, G. A. (1968). The shoshonite association: A review. *Journal of the Geological Society of Australia*, *15*(2), 275–292.

Kay, S. M., Ramos, V. A., Mpodozis, C., & Sruoga, P. (1989). Late Paleozoic to Jurassic silicic magmatism at the Gondwana margin: Analogy to the Middle Proterozoic in North America? *Geology, 17,* 324-328.

Kellogg, K., Larson, E. E., & Watson, D. E. (1970). Thermochemical Remanent Magnetization and Thermal Remanent Magnetization: Comparison in a Basalt. *Science*, *170*(3958), 628–630. https://doi.org/10.1126/SCIENCE.170.3958.628

Kent, D. V, & Gee, J. (1996). Magnetic alteration of zero-age oceanic basalt. *Geology, 24(8),* 703–706. https://doi.org/10.1130/0091-7613(1996)024%3C0703:MAOZAO%3E2.3.CO;2

Kent, D. V., & Gee, J. (1994). Grain size-dependent alteration and the magnetization of oceanic basalts. *Science*, *265*(5178), 1561–1563. https://doi.org/10.1126/SCIENCE.265.5178.1561

Kent, D. V., Olsen, P. E., & Muttoni, G. (2017). Astrochronostratigraphic polarity time scale (APTS) for the Late Triassic and Early Jurassic from continental sediments and correlation with standard marine stages. *Earth-Science Reviews,* 166, 153-180. https://doi.org/10.1016/j.earscirev.2016.12.014

Kent, D. V., Olsen, P. E., Lepre, C., Rasmusen, C., Mundil, R., Gehrels, G. E., et al. (2019). Magnetochronology of the entire Chinle Formation (Norian age) in a scientific drill core from Petrified Forest National Park (Arizona, USA) and implications for regional and global

correlations in the Late Triassic. *Geochemistry, Geophysics, Geosystems,* 20(11), 4654-4664. https://doi.org/10.1029/2019GC008474

Kent, D. V., Olsen, P. E., Rasmussen, C., Lepre, C., Mundil, R., Irmis, R. B., et al. (2018). Empirical evidence for stability of the 405-kiloyear Jupiter-Venus eccentricity cycle over hundreds of millions of years. *Proceedings of the National Academy of Sciences,* 115(24), 6153-6158. https://doi.org/10.1073/pnas.1800891115

Kirschvink, J. L. (1980). The least-squares line and plane and the analysis of palaeomagnetic data. *Geophysical Journal of the Royal Astronomical Society*, *62*(3), 699–718. https://doi.org/10.1111/j.1365-246X.1980.tb02601.x

Kissel, C., & Laj, C. (2004). Improvements in procedure and paleointensity selection criteria (PICRIT-03) for Thellier and Thellier determinations: Application to Hawaiian basaltic long cores. *Physics of the Earth and Planetary Interiors*, *147*(2-3 SPEC.ISS.), 155–169. https://doi.org/10.1016/J.PEPI.2004.06.010

Klausen, M. B. (2020). Conditioned duality between supercontinental 'assembly' and 'breakup' LIPs. *Geoscience Frontiers, 11*(5), 1635–1649. https://doi.org/10.1016/J.GSF.2019.12.005

Kleiman, L. E., & Salvarredi, J. A. (2001). Petrology, geochemistry and tectonic implications of Triassic volcanism (Puesto Viejo Formation), San Rafael Massif, Mendoza. *Revista de La Asociacion Geologica Argentina*, *56*(4), 559–570.

Klein, U., & Fletcher, A. (2015). *Galactic and Intergalactic Magnetic Fields*. Springer Praxis Books, Springer, Cham. https://doi.org/10.1007/978-3-319-08942-3

Knight, K. B., Nomde, S., Renne, P. R., Marzoli, A., Bertrand, H., & Youbi, N. (2004). The Central Atlantic Magmatic Province at the Triassic-Jurassic boundary: paleomagnetic and $^{40}Ar/^{39}Ar$ evidence from Morocco for brief, episodic volcanism. *Earth and Planetary Science Letters*, 228, 143-160. https//doi.org/10.1016/j.epsl.2004.09.022

Koch, S. A., Gilder, S. A., Pohl, J., & Trepmann, C. (2012). Geomagnetic field intensity recorded after impact in the Ries meteorite crater, Germany. *Geophysical Journal International*, *189*, 383–390. https://doi.org/10.1111/j.1365-246X.2012.05399.x

Koenigsberger, J. G. (1938). Natural residual magnetism of eruptive rocks. *Terr. Magn. Atmos. Elec., 43,* 119–320.

Kono, M. (1978). Reliability of palaeointensity methods using alternating field demagnetization and anhysteretic remanence, *54*, 241–261. https://doi.org/10.1111/j.1365-246X.1978.tb04258.x

Konstantinov, K. M., Bazhenov, M. L., Fetisova, A. M., & Khutorskoy, M. D. (2014). Paleomagnetism of trap intrusions, East Siberia: Implications to flood basalt emplacement and the Permo–Triassic crisis of biosphere. *Earth and Planetary Science Letters*, 394, 242-253. http://dx.doi.org/10.1016/j.epsl.2014.03.029

Korte, M., & Mandea, M. (2019). Geomagnetism: From Alexander von Humboldt to Current Challenges. *Geochemistry, Geophysics, Geosystems, 20(8),* 3801–3820. https://doi.org/10.1029/2019GC008324

Kravchinsky, V. A., Konstantinov, K. M., Courtillot, V., Savrasov, J. I., Valet, J., Cherniy, S. D., et al. Palaeomagnetism of East Siberian traps and kimberlites: two new poles and palaeogeographic reconstructions at about 360 and 250 Ma. *Geophysical Journal International*, 148, 1-33. https://doi.org/10.1046/j.0956-540x.2001.01548.x

Kroner, U., & Romer, R. L. (2014). Forum Comment Anatomy of a diffuse cryptic suture zone: An example from the Bohemian Massif, European Variscides. *Geology, 42(4),* 275–278. https://doi.org/10.1130/G35782C.1

Krs, M. (1967). Intensity of the Earth's Magnetic Field in the Geological Past. *Nature*, *215*, 697–699. https://doi.org/10.1038/215697a0

Kulakov, E. V., Sprain, C. J., Doubrovine, P. V., Smirnov, A. V., Paterson, G. A., Hawkins, L., et al. (2019). Analysis of an updated paleointensity database (Q_{PI}-PINT) for 65-200 Ma: Implications for the long-term history of dipole moment through the Mesozoic. *Journal of Geophysical Research: Solid Earth*, 124, 9999-10022. https://doi.org/10.1029/2018JB017287

Labrosse, S., & Macouin, M. (2003). The inner core and the geodynamo. *Comptes Rendus Geoscience*, *335*(1), 37–50. https://doi.org/10.1016/S1631-0713(03)00013-0

Landeau, M., Fournier, A., Nataf, H-C., Cébron. D., & Schaeffer, N. (2022). Sustaining Earth's magnetic dynamo. *Nature Reviews Earth & Environment, 3*, 255–269. https://doi.org/10.1038/s43017-022-00264-1

Larson, R. L., & Olson, P. (1991). Mantle plumes control magnetic reversal frequency. *Earth and Planetary Science Letters*, *107*(3–4), 437–447. https://doi.org/10.1016/0012-821X(91)90091-U

Lattard, D., Engelmann, R., Kontny, A., & Sauerzapf, U. (2006). Curie temperatures of synthetic titanomagnetites in the Fe-Ti-O system: Effects of composition, crystal chemistry, and thermomagnetic methods. *Journal of Geophysical Research: Solid Earth*, *111*(12). https://doi.org/10.1029/2006JB004591

Latyshev, A. V., Veselovskiy, R. V., & Ivanov, A. V. (2018). Paleomagentism of Permian-Triassic intrusions from the Tunguska syncline and the Angara-Taseeva depresiion, Siberian Traps Large Igneous Province: Evidence of contrasting styles of magmatism. *Tectonophysics*, 723, 41-55. https://doi.org/10.1016/j.tecto.2017.11.03

Lay, T., Hernlund, J. W., & Buffet, B. A. (2008). Core-mantle boundary heat flow. *Nature Geoscience*, *1(1),* 25–32. https://doi.org/10.1038/ngeo.2007.44

Lema, H., Busteros, A., Giacosa, R., & Cucchi, R. (2008). Geología del complejo volcánico Los Menucos en el área tipo: Río Negro. *Revista de la Asociación Geológica Argentina 63 (1),* 3–13.

Leonhardt, R. (2006). Analyzing rock magnetic measurements: The RockMagAnalyzer 1.0 software. *Computers & Geosciences*, *32*(9), 1420–1431. https://doi.org/10.1016/J.CAGEO.2006.01.006

Lerner, G. A., Smirnov, A. v., Surovitckii, L. v., & Piispa, E. J. (2017). Nonheating methods for absolute paleointensity determination: Comparison and calibration using synthetic and natural magnetite-bearing samples. *Journal of Geophysical Research: Solid Earth*, *122*(3), 1614–1633. https://doi.org/10.1002/2016JB013777

Levi, S. (1977). The Effect of Magnetite Particle Size on Paleointensity Determinations of The Geomagnetic Field. *Physics of the Earth and Planetary Interiors*, *13*.

Li, M., Ogg J., Zhang, Y., Huang, C., Hinnov, L., Chen, Z., & Zou, Z. (2016). Astronomical tuning of the end-Permian extinction and the Early Triassic Epoch of South China and Germany. *Earth and Planetary Science Letters.* 441, 10-25. http://dx.doi.org/10.1016/j.epsl.2016.02.017

Li, M., Zhong, S., & Olson, P. (2018). Linking lowermost mantle structure, core-mantle boundary heat flux and mantle plume formation. *Physics of the Earth and Planetary Interiors*, *277*, 10–29. https://doi.org/10.1016/J.PEPI.2018.01.010

Li, Y., Sharps, R., McWilliams, M., Nur, A., Li, Y., Li, Q., & Zhang, W. (1989). Paleomagnetic results from Late Paleozoic dikes from the northwestern Junggar Block, northwestern China. *Earth and Planetary Science Letters*, 94, 123-130. https://doi.org/10.1016/0012-821X(89)90088-5

Lloyd, S. J., Biggin, A. J., Halls, H., & Hill, M. J. (2021b). First palaeointensity data from the cryogenian and their potential implications for inner core nucleation age. *Geophysical Journal International*, *226*, 66–77. https://doi.org/10.1093/gji/ggab090

Lloyd, S. J., Paterson, G. A., Thallner, D., & Biggin, A. J. (2021a). Improvements to the Shaw-Type Absolute Palaeointensity Method. *Frontiers in Earth Science*, *9*. https://doi.org/10.3389/feart.2021.701863

Loader, C. (1999). *Local Regression and Likelihood*. New York: Springer. https://doi.org/10.1007/0-387-22732-6_1

Loper, D. (2003). Earth's Core. *Encyclopedia of Physical Science and Technology*, 775–781. https://doi.org/10.1016/B0-12-227410-5/00192-7

Lopes, R. W., Renac, C., Mexias, A. S., Nardi, L. V. S., Fontana, E., Gomes, M. E. B., & Barats, A. (2019). Mineral assemblages and temperature associated with Cu enrichment in the Seival area (Neoproterozoic Camaquã Basin of Southern Brazil). *Journal of Geochemical Exploration*, *201*, 56–70. https://doi.org/10.1016/J.GEXPLO.2019.03.010

Lotfy, H., & Elaal, E. A. (2015). Equatorial paleolatitude for Northeast Africa in thet Late Triassic: paleomagnetic study on the Gezira and Bir-Umhebal [229-223 Ma] ring complexes, Southeastern Desert, Egypt. *Arabian Journal of Geosciences*, 11, 446. https://doi.org/10.1007/s12517-018-3806-x

Lovecchio, J. P., Rohais, S., Joseph, P., Bolatti, N. D., & Ramos, V. A. (2020). Mesozoic rifting evolution of SW Gondwana: A poly-phased, subduction-related, extensional history responsible for basin formation along the Argentinean Atlantic margin. *Earth-Science Reviews*, *203*, 103138. https://doi.org/10.1016/J.EARSCIREV.2020.103138

Lowes., F. J. (1974). Spatial Power Spectrum of the Main Geomagnetic Field, and Extrapolation to the Core. *Geophysical Journal International, 36(3),* 717–730. https://doi.org/10.1111/j.1365-246X.1974.tb00622.x

Lucas, S. G. (2005). Pangaea. In R. C. Selley, L. R. M. Cocks, & I. R. Plimer (Eds.), *Encyclopedia of Geology* (pp. 225-228). Elsevier. https://doi.org/10.1016/B0-12-369396-9/00434-2

Lucas, S. G. (2010). Multichron. *Lethaia.* 43, 282. https://doi.org/10.1111/j.1502-3931.2009.00207.x

Lucas, S. G., & Tanner, L. H. (2014). The Triassic Timescale 2013. In R. Rocha, J. Pais, J. C. Kullberg, S. Finney (Eds.), *STRATI 2013* (pp. 19-22). Springer. https://doi.org/10.1007/978-3-319-04364-7_4

Lund, S. P., & Keigwin, L. (1994). Measurement of the degree of smoothing in sediment paleomagnetic secular variation records: an example from late Quaternary deep-sea sediments of the Bermuda Rise, western North Atlantic Ocean. *Earth and Planetary Science Letters*, 122, 317-330. https://doi.org/10.1016/0012-821X(94)90005-1

Luppo, T., López de Luchi, M. G., Rapalini, A. E., Martínez Dopico, C. I., & Fanning, C. M. (2018). Geochronologic evidence of a large magmatic province in northern Patagonia encompassing the Permian-Triassic boundary. *Journal of South American Earth Sciences*, *82*, 346–355. https://doi.org/10.1016/J.JSAMES.2018.01.003

Luppo, T., Martínez Dopico, C. I., Rapalini, A. E., López de Luchi, M. G., Miguez, M., & Fanning, C. M. (2019). Paleomagnetism of Permo–Triassic volcanic units in northern Patagonia: are we tracking the final stages of collision of Patagonia? *International Journal of Earth Sciences*, *108*(2), 621–647. https://doi.org/10.1007/s00531-018-01672-9

Lustrino, M., Abbas, H., Agostini, S., Caggiati, M., Carminati, E., & Gianolla, P. (2019). Origin of Triassic magmatism of the Southern Alps (Italy): Constraints from geochemistry and Sr-Nd-Pb isotopic ratios. *Gondwana Research*, *75*, 218–238. https://doi.org/10.1016/J.GR.2019.04.011

Lyons, J. J., Coe, R. S., & Zhao, X. (2002). Paleomagnetism of the early Triassic Semeitau igneous series, eastern Kazakstan. *Journal of Geophysical Research*, 107, B72139. https//doi.org/10.1029/2001JB000521

Maher, B. A. (1988). Magnetic properties of some synthetic sub-micron magnetites. *Geophysical Journal*, *94*, 83–96. https://doi.org/10.1111/j.1365-246X.1988.tb03429.x

Manzoni, M. (1970). Paleomagnetic data of middle and upper Triassic age from the Dolomites (Eastern Alps, Italy). *Tectonophysics*, *10*(4), 411–424. https://doi.org/10.1016/0040-1951(70)90119-8

Marescotti, P., Vanko, D. A., & Cabella, R. (2000). From oxidizing to reducing alteration: Mineralogical variations in pillow basalts from the east flank, Juan de Fuca Ridge. *Proceedings of the Ocean Drilling Program: Scientific Results*, *168*, 119–135. https://doi.org/10.2973/odp.proc.sr.168.006.2000

Maron, M., Muttoni, G., Rigo, M., Gianolla, P., & Kent, D. (2019). New magnetobiostratigraphic results from the Ladinian of the Dolomites and implications for the Triassic geomagnetic polarity timescale. *Palaeogeography, Palaeoclimatology, Palaeoecology*, 517, 52-73. https://doi.org/10.1016/j.palaeo.2018.11.024

Martínez Dopico, C. I., López de Luchi, M. G., Rapalini, A. E., Fanning, C. M., & Antonio, P. Y. J. (2019). Geochemistry and geochronology of the shallow-level La Esperanza magmatic system (Permian-Triassic), Northern Patagonia. *Journal of South American Earth Sciences*, *96*. https://doi.org/10.1016/j.jsames.2019.102347

Martínez Dopico, C. I., Tohver, E., López de Luchi, M. G., Wemmer, K., Rapalini, A. E., & Cawood, P. A. (2017). Jurassic cooling ages in Paleozoic to early Mesozoic granitoids of northeastern Patagonia: 40Ar/39Ar, 40K–40Ar mica and U–Pb zircon evidence. *International Journal of Earth Sciences*, *106*(7), 2343–2357. https://doi.org/10.1007/S00531-016-1430-0/FIGURES/4

Matuyama, M. (1929). On the direction of magnetization of basalts in Japan, Tyosen and Manchuria. *Proceedings of the Imperial Academy*, *5*, 203–205.

McElhinny, M. W., & Larson, R. L. (2003). Jurassic dipole low defined from land and sea data. *Eos, Transactions, American Geophysical Union*, 84, 362-366. https://doi.org/10.1029/2003EO370003

McElhinny, M. W., & McFadden, P. L. (1997). Palaeosecular variation over the past 5 Myr based on a new generalized database. *Geophysical Journal International*, 131(2), 240–252. https://doi.org/10.1111/j.1365-246X.1997.tb01219.x

McElhinny, M. W., & McFadden, P. L. (2000). Paleomagnetism: Continents and Oceans (2nd ed., 386 pp.). San Diego, CA: Academic Press.

McFadden, P. L., & Lowes, F. J. (1981). The discrimination of mean directions drawn from Fisher distributions. Geophysical JournalInternational, 67(1), 19–33. https://doi.org/10.1111/j.1365-246x.1981.tb02729.x

McFadden, P. L., & McElhinny, M. W. (1988). The combined analysis of remagnetization circles and direct observations in palaeomagnetism. *Earth and Planetary Science Letters*, 87, 161-172. https://doi.org/10.1016/0012-821X(88)90072-6

McFadden, P. L., & Merrill, R. T. (1984). Lower mantle convection and geomagnetism. *Journal of Geophysical Research*, *89*(B5), 3354–3362. https://doi.org/10.1029/JB089IB05P03354

McFadden, P. L., Merrill, R. T., & McElhinny, M. W. (1988). Dipole/quadrupole family modeling of paleosecular variation. *Journal of Geophysical Research*, 93(B10), 11,583–11,588. https://doi.org/10.1029/JB093iB10p11583

McFadden, P. L., Merrill, R. T., McElhinny, M. W., & Lee, S. (1991). Reversals of the Earth's magnetic field and temporal variations of the dynamo families. *Journal of Geophysical Research*, 96(B3), 3923–3933. https://doi.org/10.1029/90JB02275

McKay, M. P., Coble, M. A., Hessler, A. M., Weislogel, A. L., & Fildani, A. (2016). Petrogenesis and provenance of distal volcanic tuffs from the Permian-Triassic Karoo Basin, South Africa: A window into a dissected magmatic province. *Geosphere*, *12*(1), 1–14. https://doi.org/10.1130/GES01215.1

McNamara, A. K. (2019). A review of large low shear velocity provinces and ultra low velocity zones. *Tectonophysics*, *760*, 199–220. https://doi.org/10.1016/j.tecto.2018.04.015

McPheron, R. L. (2022). Earth's magnetic field, geomagnetism, terrestrial magnetism. Retrieved August 20, 2022, from https://www.britannica.com/science/geomagnetic-field

Meduri, D. G., Biggin, A. J., Davies, C. J., Bono, R. K., Sprain, C. J., & Wicht, J. (2021). Numerical Dynamo Simulations Reproduce Paleomagnetic Field Behavior. *Geophysical Research Letters*, *48*(5), e2020GL090544. https://doi.org/10.1029/2020GL090544

Meert, J. G., Pivarunas, A. F., Evans, D. A. D., Pisarevsky, S. A., Pesonen, L. J., Li, Z. X., et al. (2020). The magnificent seven: A proposal for modest revision of the Van der Voo (1990) quality index. *Tectonophysics*, *790*. https://doi.org/10.1016/J.TECTO.2020.228549

Merrill, R. T., & McFadden, P. L. (2003). The geomagnetic axial dipole field assumption. *Physics of the Earth and Planetary Interiors*, *139*(3–4), 171–185. https://doi.org/10.1016/J.PEPI.2003.07.016

Merrill, R. T., McElhinny, M. W., & McFadden, P. L. (1998). Chapter 3 Foundations of paleomagnetism. In *International geophysics* (pp. 69–114). https://doi.org/10. 1016/S0074-6142(96)80004-0

Mietto, P., Manfrin, S., Preto, N., Rigo, M., Roghi, G., Furin, S., et al. (2012). The Global Boundary Stratotype Section and Point (GSSP) of the Carnian Stage (Late Triassic) at Prati di Stuores/Stuores Wiesen Section (Southern Alps, NE Italy). *Episodes Journal of International Geoscience*, *35*(3), 414–430. https://doi.org/10.18814/EPIIUGS/2012/V35I3/003

Milana, J. P., & Alcober, O. A. (1994). Modelo tectosedimentario de la cuenca triásica de Ischigualasto (San Juan, Argentina). *Revista de la Asociacion Geologica Argentina, 49(3-4)*, 217-235.

Mišković, A., Spikings, R. A., Chew, D. M., Košler, J., Ulianov, A., & Schaltegger, U. (2009). Tectonomagmatic evolution of Western Amazonia: Geochemical characterization and zircon U-Pb geochronologic constraints from the Peruvian Eastern Cordilleran granitoids. *GSA Bulletin*, *121*(9–10), 1298–1324. https://doi.org/10.1130/B26488.1

Mochizuki, N., Maruuchi, T., Yamamoto, Y., & Shibuya, H. (2013). Multi-level consistency tests in paleointensity determinations from the welded tuffs of the Aso pyroclastic-flow deposits. *Physics of the Earth and Planetary Interiors*, *223*, 40–54. https://doi.org/10.1016/J.PEPI.2013.05.001

Mochizuki, N., Tsunakawa, H., Oishi, Y., Wakai, S., Wakabayashi, K., & Yamamoto, Y. (2004). Palaeointensity study of the Oshima 1986 lava in Japan: implications for the reliability of the Thellier and LTD-DHT Shaw methods. *Physics of the Earth and Planetary Interiors, 146,* 395–416. https://doi:10.1016/j.pepi.2004.02.007

Monti, M., & Franzese, J. R. (2019). Triassic continental oblique rifting controlled by Paleozoic structural grain: The Puesto Viejo Basin, western Argentina. *Journal of South American Earth Sciences*, *95*, 102240. https://doi.org/10.1016/J.JSAMES.2019.102240

Morad, S., Sirat, M., El-Ghali, M. A. K., & Mansurbeg, H. (2011). Chloritization in Proterozoic granite from the Äspö Laboratory, southeastern Sweden: record of hydrothermal alterations and implications for nuclear waste storage. *Clay Minerals*, *46*(3), 495–513. https://doi.org/10.1180/claymin.2011.046.3.495

Morrison, G. W. (1980). Characteristics and tectonic setting of the shoshonite rock association. *Lithos*, *13*(1), 97–108. https://doi.org/10.1016/0024-4937(80)90067-5

Moskowitz, B. M., Jackson, M., & Chandler, V. (2015). Geophysical Properties of the Near-Surface Earth: Magnetic Properties. In G. Schubert (Eds.) *Treatise on Geophysics: Second Edition*, *11*, 139–174. https://doi.org/10.1016/B978-0-444-53802-4.00191-3

Moskowitz, B. M., Jackson, M., & Kissel, C. B. (1998). Low-temperature magnetic behavior of titanomagnetites. *Earth and planetary Science Letters, 157, 141*–149. https://doi.org/10.1016/S0012-821X(98)00033-8

Mundil, R., Brack, P., Meier, M., Rieber, H., & Oberli, F. (1996). High resolution U-Pb dating of Middle Triassic volcaniclastics: Time-scale calibration and verification of tuning parameters for carbonate sedimentation. *Earth and Planetary Science Letters*, *141*(1–4), 137–151. https://doi.org/10.1016/0012-821X(96)00057-X

Mundil, R., Pálfy, J., Renne, P. R., & Brack, P. (2010). The Triassic timescale: New constraints and a review of geochronological data. *Geological Society Special Publication*. https://doi.org/10.1144/SP334.3

Nagata, T., Arai, Y., & Momose, K. (1963). Secular Variation of the Geomagnetic Total Force during the Last 5000 Years. *Journal of Geophysical Research, 68(18),* 5277– 5281. https://doi.org/10.1029/j.2156-2202.1963.tb00005.x

Nagy, L., Williams, W., Muxworthy, A. R., & Shcherbakov, V. P. (2017). Stability of equidimensional pseudo–single-domain magnetite over billion-year timescales. *Earth, Atmosphere, and planetary Sciences, 114(39),* 10356–10360. https://doi.org/10.1073/pnas.1708344114

Nardini, N., Casetta, F., Ickert, R. B., Mark, D. F., Ntaflos, T., Zanetti, A., & Coltorti, M. (2022). From the Middle Triassic Cima Pape complex (Dolomites; Southern Alps) to the feeding systems beneath active volcanoes: Clues from clinopyroxene textural and compositional zoning. *Journal of Volcanology and Geothermal Research*, *422*. https://doi.org/10.1016/J.JVOLGEORES.2021.107459

Néel, L. (1949). Théorie du traînage magnétique des ferromagnétiques en grains fins avec application aux terres 5 cuites. *Annales de géophysique, 5,* 99-136.

Néel, L. (1955). Some theoretical aspects of rock-magnetism. *Advances in Physics, 4(14),* 191-243, https://doi.org/10.1080/00018735500101204

Nimmo, F. (2015). Energetics of the Core. In G. Schubert (Eds.) *Treatise on Geophysics: Second Edition*, *8*, 27–55. https://doi.org/10.1016/B978-0-444-53802-4.00139-1

O'Rourke, J. G., Gillmann, C., & Tackley, P. (2018). Prospects for an ancient dynamo and modern crustal remanent magnetism on Venus. *Earth and Planetary Science Letters*, *502*, 46–56. https://doi.org/10.1016/J.EPSL.2018.08.055

Ogg, J. G. (2012). Geomagnetic Polarity Time Scale. In F. M. Gradstein, J. G. Ogg, M. G. Schmitz, & G. M. Ogg (Eds.), *The Geologic Time Scale* (pp. 85–113). Boston, MA: Elsevier. https://doi.org/10.1016/B978-0-444-59425-9.00005-6

Ogg, J. G., Ogg, G. M., & Gradstein, M. (2016). Triassic. In J. G. Ogg, G. M. Ogg, & M. Gradstein (Eds), *A Concise Geologic Time Scale* (pp. 133-149). Boston, MA: Elsevier. https://doi.org/10.1016/C2009-0-64442-1

Ohmoto, H. (2003). Nonredox Transformations of Magnetite-Hematite in Hydrothermal Systems. *Economic Geology*, *98*(1), 157–161. https://doi.org/10.2113/GSECONGEO.98.1.157

Oishi, Y., Tsunakawa, H., Mochizuki, N., Yamamoto, Y., Wakabayashi, K-I., & Shibuya, H. (2005). Validity of the LTD-DHT Shaw and Thellier palaeointensity methods: a case study of the Kilauea 1970 lava. *Physics of the Earth and Planetary Interiors, 149,* 243–257. https://doi:10.1016/j.pepi.2004.10.009

Olson, P. (2016). Mantle control of the geodynamo: Consequences of top-down regulation. *Geochemistry, Geophysics, Geosystems*, *17*(5), 1935–1956. https://doi.org/10.1002/2016GC006334

Olson, P., & Amit, H. (2015). Mantle superplumes induce geomagnetic superchrons. *Frontiers in Earth Science*, *3*, 38. https://doi.org/10.3389/FEART.2015.00038/BIBTEX

Olson, P., Deguen, R., Hinnov, L. A., & Zhong, S. (2013). Controls on geomagnetic reversals and core evolution by mantle convection in the Phanerozoic. *Physics of the Earth and Planetary Interiors*, *214*, 87–103. https://doi.org/10.1016/J.PEPI.2012.10.003

Olson, P., Driscoll, P., & Amit, H. (2009). Dipole collapse and reversal precursors in a numerical dynamo. *Physics of the earth and Planetary Interiors,* 173, 21-140. https://doi.org/10.1016/j.pepi.2008.11.010

Opdyke, N. D., & Channell, J. E. T. (1996). *Magnetic Stratigraphy*, 64. London, UK: Academic Press. https://doi.org/10.1016/S0074-6142(06)80003-3

Opdyke, N. D., Roberts, J., Claoué-Long, J., Irving, E., & Jones, P. J. (2000). Base of the Kiaman: Its definition and global stratigraphic sequence. *GSA Bulletin*, 112, 1315-1341. https://doi.org/10.1130/0016-7606(2000)112<1315:BOTKID>2.0.CO;2

Opdyke, N. D., Kent, D. V., Foster, D. A., & Huang, K. (2015). Paleomagnetism of Miocene volcanics on Sao Tome: Paleosecular variation at the Equator and a comparison to its latitudinal dependence over the last 5 Myr. *Geochemistry, Geophysics, Geosystems*, *16,* 3870– 3882. https://doi.org/10.1002/2015GC005901

Otake, T., Wesolowski, D. J., Anovitz, L. M., Allard, L. F., & Ohmoto, H. (2010). Mechanisms of iron oxide transformations in hydrothermal systems. *Geochimica et Cosmochimica Acta*, *74*(21), 6141–6156. https://doi.org/10.1016/J.GCA.2010.07.024

Ottone, E. G., Monti, M., Marsicano, C. A., de la Fuente, M. S., Naipauer, M., Armstrong, R., & Mancuso, A. C. (2014). A new Late Triassic age for the Puesto Viejo Group (San Rafael depocenter, Argentina): SHRIMP U–Pb zircon dating and biostratigraphic correlations across

southern Gondwana. *Journal of South American Earth Sciences*, *56*, 186–199. https://doi.org/10.1016/J.JSAMES.2014.08.008

Özdemir, Ö. (2007). Magnetization, Thermoremanent. In D., Gubbins & E. Herrero-Bervera (Eds.), *Encyclopedia of Geomagnetism and Paleomagnetism* (pp. 609–616). Dordrecht: Springer.

Pal, P. C. (1991). The Correlation of Long-Term Trends in the Palaeointensity and Reversal Frequency Variations. *Journal of Geomagnetism and Geoelectricity*, *43*, 409–428. https://doi.org/10.5636/jgg.43.409

Palencia-Ortas, A., Ruiz-Martinez, V. C., Villalaín, J. J., Osete, M. L., Vegas, R., Touil, A., et al. (2011). A new 200 Ma paleomagnetic pole for Africa, and paleo-secular variation scatter from Central Atlantic Magmatic Province (CAMP) intrusives in Morocco (Ighrem and Foum Zguid dykes). *Geophysical Journal International*, 185, 1220-1234. https//doi.org/10.1111/j.1365-246X.2011.05017.x

Palmer, H. C., MacDonald, W. D., Grommé, C. S., & Ellwood, B. B. (1996). Magnetic properties and emplacement of the Bishop Tuff, California. *Bulletin of Volcanology, 58(2-3),* 101–116. https://doi.org/10.1007/s004450050129

Pankhurst, R. J., Rapela, C. W., Fanning, C. M., & Márquez, M. (2006). Gondwanide continental collision and the origin of Patagonia. *Earth-Science Reviews, 76,* 235 – 257.

Parker, R. L. (1994). *Geophysical inverse theory*, Princeton Series in Geophysics. Princeton, NJ: Princeton University Press.

Pastor-Galán, D., Nance, R. D., Murphy, J. B., & Spencer, C. J. (2019). Supercontinents: myths, mysteries, and milestones. https://doi.org/10.1144/SP470.16

Paterson, G. A., Davies, C. J., & Shaar, R. (2019). Editorial: The evolving geomagnetic field. *Frontiers in Earth Science*. Frontiers Media S.A. https://doi.org/10.3389/feart.2019.00077

Paterson, G. A., Heslop, D., & Pan, Y. (2016). The pseudo-Thellier palaeointensity method: New calibration and uncertainty estimates. *Geophysical Journal International*, *207*(3), 1596–1608. https://doi.org/10.1093/gji/ggw349

Paterson, G. A., Heslop, D., Muxworthy, A. R., Paterson, G. A., Heslop, D., Muxworthy, A. R., et al. (2010). Deriving confidence in paleointensity estimates. *Geochemistry, Geophysics, Geosystems*, *11*(7), 7–18. https://doi.org/10.1029/2010GC003071

Paterson, G. A., Muxworthy, A. R., Yamamoto, Y., & Pan, Y. (2017). Bulk magnetic domain stability controls paleointensity fidelity. *Proceedings of the National Academy of Sciences of the United States of America*, *114*(50), 13120–13125. https://doi.org/10.1073/PNAS.1714047114

Paterson, G. A., Tauxe, L., Biggin, A. J., Shaar, R., & Jonestrask, L. C. (2014). On improving the selection of Thellier-type paleointensity data. *Geochemistry, Geophysics, Geosystems*, *15*(4), 1180–1192. https://doi.org/10.1002/2013GC005135

Paterson, G. A., Zhao, X., Jackson, M., & Heslop, D. (2018). Measuring, Processing, and Analyzing Hysteresis Data. *Geochemistry, Geophysics, Geosystems*, *19*(7), 1925–1945. https://doi.org/10.1029/2018GC007620

Pavlov, V. E., & Gallet, Y. (2020). Developing the Cambrian and Ordovician Magnetic Polarity Time Scale: Current Data and Attempt of Synthesis. *Izvestiya, Physics of the Solid Earth*, *56*(4), 437–460. https://doi.org/10.1134/S1069351320040072/FIGURES/10

Pavlov, V. E., Courtillot, V., Bazhenov, M. L., & Veselovsky, R. V. (2007). Paleomagnetism of the Siberian Traps: New data and a new over 250 Ma pole for Siberia. *Tectonophysics*, 443, 72-92. https/doi.org//10.1016/j.tecto.2007.07.005

Pavlov, V. E., Fluteau, F., Latyshev, A. V., Fetisova, A. M., Elkins-Tanton, L. T., Black, B. A., et al. (2019). Geomagnetic secular variations at the Permian-Triassic boundary and pulsed magmatism during eruption of Siberian Traps. *Geochemistry, Geophysics, Geosystems*, 20, 773-791. https://doi.org/10.1029/2018GC007950

Pearson, K. (1900). X. On the Criterion that a Given System of Deviations from the Probable in the Case of a Correlated System of Variables is Such that it Can Be Reasonably Supposed to have Arisen from Random Sampling. *The London, Edinburgh, and Dublin Philosophical Magazine and Journal of Science, 50,* 157-175, https://doi.org/10.1080/14786440009463897

Perkins, M. E., & Nash, B. P. (2002). Explosive silicic volcanism of the Yellowstone hotspot: The ash fall tuff record the par-titioning of explosive hotspot volcanism into stages likely reflects variation in the style. *GSA Bulletin*, *114(3),* 367–381. https://doi.org/10.1130/0016-7606(2002)114%3C0367:ESVOTY%3E2.0.CO;2

Perrin, M. (1998). Paleointensity determination, magnetic domain structure, and selection criteria. *Journal of Geophysical Research: Solid Earth*, *103*(B12), 30591–30600. https://doi.org/10.1029/98JB01466

Perrin, M., & Shcherbakov, V. (1997). Paleointensity of the Earth's Magnetic Field for the Past 400 Ma: Evidence for a Dipole Structure during the Mesozoic Low. *Journal of Geomagnetism and Geoelectricity*, *49*(4), 601–614. https://doi.org/10.5636/JGG.49.601

Perrin, Mereille, Schnepp, E., & Shcherbakov, V. (1998). Paleointensity database updated. *Eos, Transactions American Geophysical Union*, *79*(16), 198–198. https://doi.org/10.1029/98EO00145

Prévot, M., Derder, M. E. M., McWilliams, M., & Thompson, J. (1990). Intensity of the Earth's magnetic field: Evidence for a Mesozoic dipole low. *Earth and Planetary Science Letters*, *97*(1–2), 129–139. https://doi.org/10.1016/0012-821X(90)90104-6

Purcell, E. M., & Morin, D. J. (2013). *Electricity and Magnetism (3rd ed.)*. Cambridge: Cambridge University Press. https://doi.org/10.1017/CBO9781139012973

Quidelleur, X., & Courtillot, V. (1996). On low-degree spherical harmonic models of paleosecular variation. *Physics of the Earth and Planetary Interiors, 95,* 55–77. http://dx.doi.org/10.1016/0031-9201(95)03115-4

Radi, H. A., & Rasmussen, J. O. (2013). Sources of Magnetic Field. *Undergraduate Lecture Notes in Physics*, 889–932. https://doi.org/10.1007/978-3-642-23026-4_26

Raftery, A. E. (1995). Bayesian Model Selection in Social Research. *Sociological Methodology*, *25*, 111–163. https://doi.org/10.2307/271063

Ramos, V. A. (1988). Tectonics of the Late Proterozoic – Early Paleozoic: a collisional history of Southern South America. *Episodes, 11(3),* 168–174.

Ramos, V. A. (2004). Cuyania, an Exotic Block to Gondwana: Review of a Historical Success and the Present Problems. *Gondwana Research*, *7*(4), 1009–1026. https://doi.org/10.1016/S1342-937X(05)71081-9

Ramos, V. A., & Kay, S. M. (1991). Triassic rifting and associated basalts in the Cuyo basin, central Argentina. *Special Paper of the Geological Society of America*, *265*, 79–91. https://doi.org/10.1130/SPE265-P79

Rapalini, A. E. (1998). Syntectonic magnetization of the mid-Palaeozoic Sierra Grande Formation: further constraints on the tectonic evolution of Patagonia. *Journal of the Geological Society 155 (1),* 105–114. https://doi.org/10.1144/gsjgs.155.1.0105

Reitsma, M. (2012). Reconstructing the Late Paleozoic : Early Mesozoic plutonic and sedimentary record of south-east Peru : Orphaned back-arcs along the western margin of Gondwana. [Doctoral thesis, Université de Genève]. Archive ouverte UNIGE. https://doi.org/10.13097/archive-ouverte/unige:23095

Reitsma, M., Schaltegger, U., Spikings, R., Winkler, W., & Carlotto, V. (2010). Constraining the age of the Mitu Group, south-east Peru: U-Pb ages of detrital and igneous zircons. *European Geoscience Union General Assembly, 12.*

Riehle, J. R., Miller, T. F., & Bailey, R. A. (1995). Cooling, degassing and compaction of rhyolitic ash flow tuffs: a computational model. *Bulletin of Volcanology,* 57, 319–336. https://doi.org/10.1007/BF00301291

Riisager, P., & Riisager, J. (2001). Detecting multidomain magnetic grains in Thellier palaeointensity experiments. *Physics of the Earth and Planetary Interiors, 125(1-4),* 111–117. https://doi.org/10.1016/S0031-9201(01)00236-9

Roberts, A. P., Almeida, T. P., Church, N. S., Harrison, R. J., Heslop, D., Li, Y., et al. (2017). Resolving the Origin of Pseudo-Single Domain Magnetic Behavior. *Journal of Geophysical Research: Solid Earth*, *122*(12), 9534–9558. https://doi.org/10.1002/2017JB014860

Rolph, T. C., & Shaw, J. (1985). A new method of palaeofield magnitude correction for thermally altered samples and its application to Lower Carboniferous lavas. *Geophysical Journal of the Royal Astronomical Society, 80(3),* 773–781. https://doi. org/10.1111/j.1365-246X.1985.tb05124.x

Roquet, J., & Thellier, É. (1946). Sur des lois numériques simples, relatives à l'aimantation thermorémanente du sesquioxyde de fer rhomboédrique. *Comptes rendus de l'Académie des Sciences, 222,* 1288–1290.

Rowe, M. C., Kent, A. J. R., & Nielsen, R. L. (2009). Subduction Influence on Oxygen Fugacity and Trace and Volatile Elements in Basalts Across the Cascade Volcanic Arc. *Journal of Petrology, 50(1),* 61–91. https://doi.org/10.1093/petrology/egn072

Ruiz-Martinez, V. C., Torsvik, T. H., van Hinsbergen, D. J. J., & Gaina, C. (2012). Earth at 200 Ma: Global palaeogeography refined from CAMP palaeomagnetic data. *Earth and Planetary Science Letters*, 331-332, 67-79. https://doi.org/10.1016/j.epsl.2012.03.008

Sanchez, S., Wicht, J., Bärenzung, J., & Holschneider, M. (2019). Sequential assimilation of geomagnetic observations: Perspectives for the reconstruction and prediction of core dynamics. *Geophysical Journal International, 217(2),* 1434– 1450. https://doi.org/10.1093/gji/ggz090

Sbarbori, E., Tauxe, L., Goguitchaichvili, A., Urrutia-Fucugauchi, J., & Bohrson, W. A. (2009). Paleomagnetic behavior of volcanic rocks from Isla Socorro, Mexico. *Earth, Planets and Space*, *61*(1), 191–204. https://doi.org/10.1186/BF03352899/METRICS

Schabes, M. E., & Bertram, H. N. (1988). Magnetization processes in ferromagnetic cubes. *Journal of Applied Physics*, *64*(3), 1347. https://doi.org/10.1063/1.341858

Schlinger, C. M., Veblen, D. R., & Rosenbaum, J. G. (1991). Magnetism and magnetic mineralogy of ash flow tuffs from Yucca Mountain, Nevada. *Journal of Geophysical Research, 96,* 6035–6052. https://doi:10.1029/90JB02653

Schmidt, P. W. (1993). Palaeomagnetic cleaning strategies. *Physics of the Earth and Planetary Interiors*, *76*(1–2), 169–178. https://doi.org/10.1016/0031-9201(93)90066-I

Schneider, D. A., & Kent D. V. (1990). The time-averaged paleomagnetic field. *Reviews of Geophysics, 28(1),* 71-96. https://doi.org/10.1029/RG028i001p00071#

Schubert, G., Zhang, K., Kivelsont, M. G., & Anderson, J. D. (1996). The magnetic field and internal structure of Ganymede. *Nature, 384,* 544–545. https://doi.org/10.1038/384544a0

Schwarz, E. J., & Symons, D. T. A. (1969). Geomagnetic intensity between 100 million and 2500 million years ago. *Physics of the Earth and Planetary Interiors*, *2*(1), 11–18. https://doi.org/10.1016/0031-9201(69)90014-4

Selkin, P. A., & Tauxe, L. (2000). Long-term variations in palaeointensity. *Philosophical Transactions of the Royal Society of London. Series A: Mathematical, Physical and Engineering Sciences*, *358*(1768), 1065–1088. https://doi.org/10.1098/RSTA.2000.0574

Selkin, P. A., Gee, J. S., & Tauxe, L. (2007). Nonlinear thermoremanence acquisition and implications for paleointensity data. *Earth and Planetary Science Letters, 256(1–2),* 81–89.

Sen, G., & Stern, R. J. (2021). Subduction Zone Magmas, *2*, 33–51. https://doi.org/10.1016/B978-0-08-102908-4.00086-2

Senanyake, W.E, & McElhinny, M. W. (1983). A paleointensity method for use with highly oxidised basalts, and application to some Permian volcanics. *Journal of Geophysics, 52*, 85-96.

Shaar, R., & Tauxe, L. (2015). Instability of thermoremanence and the problem of estimating the ancient geomagnetic field strength from non-single-domain recorders. *Proceedings of the National Academy of Sciences,* 12(36), 11187-11192. https://doi.org/10.1073/pnas.1507986112

Sharps. R., McWilliams, M., Li, Y., Cox, A., Zhang, Z., Zhai, Y., et al. (1989). Lower Permian paleomagnetism of the Tarim block, northwestern China. *Earth and Planetary Science Letters*, 92, 275-291. https://doi.org/10.1016/0012-821X(89)90052-6

Shashkanov, V. A., & Metallova, V. V. (1972). Violation of Thellier's law for partial thermoremanent magnetisation. *Izvestiya, Physics of the Solid Earth, 8*, 180–184.

Shaw, J. (1974). A New Method of Determining the Magnitude of the Palaeomagnetic Field: Application to five historic lavas and five archaeological samples. *Geophysical Journal International*, *39*(1), 133–141. https://doi.org/10.1111/J.1365-246X.1974.TB05443.X

Shaw, J., Walton, D., Yang, S., Rolph, T. C., & Share, J. A. (1996). Microwave archaeointensities from Peruvian ceramics. *Geophysical Journal International, 124(1),* 241– 244. https://doi.org/10.1111/j.1365-246X.1996.tb06367.x

Shcherbakov, V. P., Gribov, S. K., Lhuillier, F., Aphinogenova, N. A., & Tsel'movich, V. A. (2019). On the Reliability of Absolute Palaeointensity Determinations on Basaltic Rocks Bearing a Thermochemical Remanence. *Journal of Geophysical Research: Solid Earth*, *124*(8), 7616–7632. https://doi.org/10.1029/2019JB017873

Shcherbakova, V. V., Zhidkov, G. V., Shcherbakov, V. P., Latyshev, A. V., & Fetisova, A. M. (2015). Verifying the Mesozoic Dipole Low Hypothesis by the Siberian Trap Data. *Physics of the Solid Earth.* 51, 362-382. https://doi.org/10.1134/S1069351315030155

Shipunov, S. V., Muraviev, A. A., & Bazhenov, M. L. (1998). A new conglomerate test in palaeomagnetism. *Geophysical Journal International*, *133*(3), 721–725. https://doi.org/10.1046/j.1365-246X.1998.00516.x

Shufeng, Y., Hanlin, C., Li, Z., Li, Y., Xing, Y. U., Li, D., & Lifeng, & M. (2013). SCIENCE CHINA Progress of Projects Supported by NSFC Early Permian Tarim Large Igneous Province in northwest China. *Science China: Earth Sciences*, *56*, 2015–2026. https://doi.org/10.1007/s11430-013-4653-y

Sloman, L. E. (1989). Triassic shoshonites from the Dolomites, northern Italy: alkaline arc rocks in a strike-slip setting. *Journal of Geophysical Research*, *94*(B4), 4655–4666. https://doi.org/10.1029/JB094iB04p04655

Smart, J. S. (1955). The Néel Theory of Ferrimagnetism. *Citation: American Journal of Physics*, *23*, 356. https://doi.org/10.1119/1.1934006

Smirnov, A. V., Kulakov, E. V., Foucher, M. S., & Bristol, K. E. (2017). Intrinsic paleointensity bias and the long-term history of the geodynamo. *Science Advances*, *3*(2). https://doi.org/10.1126/SCIADV.1602306

Soffel, H. C., & Harzer, F. (1991). An Upper Carboniferous-Lower Permian (280 Ma) palaeomagnetic pole from the western margin of the Bohemian Massif. *Geophysical journal International*, 105, 547-551. https://doi.org/10.1111/j.1365-246X.1991.tb06733.x

Solodovnikov, G. M. (1992a). Paleointensity of the Geomagnetic Field in the Lower Early Permian. *Izvestiya, Earth Physics, 28(8),* 718–722.

Solodovnikov, G. M. (1992b). Geomagnetic Intensity in the Middle Carboniferous of Uzbekistan. *Izvestiya, Earth Physics, 28(6),* 511–515.

Solodovnikov, G. M. (1992c). Paleostrength of Geomagnetic Field in Middle-Late Carboniferous. *Izvestiya, Earth Physics, 28(4),* 327–331.

Song, P., Ding, L., Lippert, P. C., Li, Z., Liyum, Z., & Xie, J. (2020). Paleomagnetism of Middle Triassic lavas from northern Qiangtang (Tibet): Constraints on the closure of the Paleo-Tethys Ocean. *Journal of Geophysical Research: Solid Earth*, 125. https://doi.org/10.1029/2019JB017804

Spikings, R., Reitsma, M. J., Boekhout, F., Mišković, A., Ulianov, A., Chiaradia, M., et al. (2016). Characterisation of Triassic rifting in Peru and implications for the early disassembly of western Pangaea. *Gondwana Research*, *35*, 124–143. https://doi.org/10.1016/J.GR.2016.02.008

Spohn, T., Sohl, F., & Breuer, D. (1998). Mars. *The Astronomy and Astrophysics Review, 8*, 181–236.

Sprain, C. J., Biggin, A. J., Davies, C. J., Bono, R. K., & Meduri, D. G. (2019). An assessment of long duration geodynamo simulations using new paleomagnetic modeling criteria (QPM). *Earth and Planetary Science Letters, 526,* 115758. https://doi.org/10.1016/j.epsl.2019.115758

Sprain, C. J., Feinberg, J. M., Geissman, J. W., Strauss, B., & Brown, M. C. (2015). Paleointensity during periods of rapid reversal: A case study from the Middle Jurassic Shamrock batholith, western Nevada. *GSA Bulletin*, *128(1–2),* 223–238. https://doi.org/10.1130/B31283.1

Stampfli, G. M., Hochard, C., Vérard, C., Wilhem, C., & von Raumer, J. (2013). The formation of Pangea. *Tectonophysics*, *593*, 1–19. https://doi.org/10.1016/J.TECTO.2013.02.037

Stokking, L. B., & Tauxe, L. (1987). Acquisition of chemical remanent magnetization by synthetic iron oxide. *Nature, 327*, 610–612.

Storck, J.-C., Wotzlaw, J.-F., Karakas, Ö., Brack, P., Gerdes, A., & Ulmer, P. (2020). Hafnium isotopic record of mantle-crust interaction in an evolving continental magmatic system. *Earth and Planetary Science Letters*, *535*, 116100. https://doi.org/10.1016/J.EPSL.2020.116100

Storck, J.-C., Brack, P., Wotzlaw, J.-F., & Ulmer, P. (2019). Timing and evolution of Middle Triassic magmatism in the Southern Alps (northern Italy), *176*, 253–268. https://doi.org/10.6084/m9.figshare.c.4287506

Takai, A., Shibuya, H., Yoshihara, A., & Hamano, Y. (2002). Paleointensity measurements of pyroclastic flow deposits co-born with widespread tephras in Kyushu Island, Japan. *Physics of the Earth and Planetary Interiors, 133,* 159–179.

Tanaka, K., Kono, M., & Uchimura, H. (1995). Some global features of palaeointensity in geological time. *Geophysical Journal International, 120,* 97-102. https://doi.org/10.1016/0012-821X(90)90104-6

Tarduno, J. A., & Cottrell, R. D. (2005). Dipole strength and variation of the time-averaged reversing and nonreversing geodynamo based on Thellier analyses of single plagioclase crystals. *Journal of Geophysical Research*, 110, B11101. https://doi.org/10.1029/2005JB003970

Tarduno, J. A., Cottrell, R. D., & Smirnov, A. V. (2001). High geomagnetic intensity during the mid-cretaceous from Thellier analyses of single plagioclase crystals. *Science*, *291*(5509), 1779–1783. https://doi.org/10.1126/SCIENCE.1057519

Tarduno, J. A., Cottrell, R. D., & Smirnov, A. V. (2007). Paleointensity: Absolute Determinations Using Single Plagioclase Crystals. *Encyclopedia of Geomagnetism and Paleomagnetism*, 749–753. https://doi.org/10.1007/978-1-4020-4423-6_251

Tauxe, L, & Staudigel, H. (2004). Strength of the geomagnetic field in the Cretaceous Normal Superchron: New data from submarine basaltic glass of the Troodos Ophiolite. *Geochemistry, Geophysics, Geosystems*, *5*(2). https://doi.org/10.1029/2003GC000635

Tauxe, L. (1998). Paleomagnetic Principles and Practice (pp. 35–75). Kluwer Academic Publishers.

Tauxe, L. (2005). Inclination flattening and the geocentric axial dipole hypothesis. *Earth and Planetary Science Letters*, *233*(3–4), 247–261. https://doi.org/10.1016/J.EPSL.2005.01.027

Tauxe, L., & Kent, D, V. (2004). A simplified statistical model for the geomagnetic field and the detection of shallow bias in paleomagnetic inclinations: was the ancient magnetic field dipolar? In J. E. T. Channel, D. V. Kent, W. Lowrie, J. G. Meert (Eds), *Timescales of the Paleomagnetic Field, Geophysical Monograph Series* (Vol. 145, pp. 101-115). Washington, DC: American Geophysical Union. https://doi.org/ 10.1002/9781118665855

Tauxe, L., Banerjee. S. K., Butler. R. F., & van der Voo, R. (2018). Essentials of Paleomagnetism, 5th Web Edition. https://earthref.org/MagIC/books/Tauxe/Essentials/

Tauxe, L., Pick, T., & Kok, Y. S. (1995). Relative paleointensity in sediments: A Pseudo-Thellier Approach. *Geophysical Research Letters*, *22*(21), 2885–2888. https://doi.org/10.1029/95GL03166

Tauxe, L., Santos, C. N., Cych, B., Zhao, X., Roberts, A. P., Nagy, L., & Williams, W. (2020). Understanding Nonideal Paleointensity Recording in Igneous Rocks: Insights from Aging Experiments on Lava Samples and the Causes and Consequences of "Fragile" Curvature in Arai Plots. *Geochemistry, Geophysics, Geosystems*, *22*(1), e2020GC009423. https://doi.org/10.1029/2020GC009423

Thallner, D., Biggin, A. J., McCausland, P. J. A., & Fu, R. R. (2021). New Paleointensities From the Skinner Cove Formation, Newfoundland, Suggest a Changing State of the Geomagnetic Field at the Ediacaran-Cambrian Transition. *Journal of Geophysical Research: Solid Earth*, *126*(9), e2021JB022292. https://doi.org/10.1029/2021JB022292

Thellier, É. (1937a). Aimantation des terres cuites: application à la recherche de l'intensité du champ magnétique dans le passé. *Comptes rendus de l'Académie des Sciences, 204,* 184–186.

Thellier, É. (1937b). Recherche de l'intensité du champ magnétique terrestre dans le passé: premiers résultats. *Les Presses universitaires de France, 15,* 179–184.

Thellier, É. (1937c). Sur la disparition de l'aimantation permanente des terres cuites, par réchauffement en champ magnétique nul. *Comptes rendus de l'Académie des Sciences, 205,* 334–336.

Thellier, É. (1938). Sur l'aimantation des terres cuites et ses applications géophysiques. [Doctoral thesis, Université de Paris]. Les Presses universitaires de France.

Thellier, É. (1941a). Sur la vérification d'une méthode permettant de déterminer l'intensité du champ magnétique terrestre dans le passé. *Comptes rendus de l'Académie des Sciences, 212,* 281–283.

Thellier, É. (1941b). Sur les propriétés de l'aimantation thermorémanente des terres cuites. *Comptes rendus de l'Académie des Sciences, 213,* 1019–1022.

Thellier, É. (1946). Sur la thermorémanence et la théorie du métamagnétisme. *Comptes rendus de l'Académie des Sciences, 223,* 319–321.

Thellier, E., & Thellier, O. (1959). Sur l'intensité du champ magnétique terrestre dans le passé historique et géologique. *Annales de Geophysique,* 15, 285.

Thomas, D. N., Rolph, T. C., & Frie, D. F. (1997). Permo-Carboniferous (Kiaman) palaeointensity results from the western Bohemian Massif, Germany. *Geophysical Journal International*, *130*, 257–265. https://doi.org/10.1111/j.1365-246X.1997.tb01004.x

Thomas, D. N., Rolph, T. C., & Shaw, J. (1995). Palaeointensity results from the Permo-Carboniferous (Kiaman) reversed superchron: the Great Whin and Midland Valley sills of the northern United Kingdom. *Geophysical Journal International*, *123*, 798–816. https://doi.org/10.1111/j.1365-246X.1995.tb06891.x

Thomas, D. N., Rolph, T. C., Shaw, J., Gonzalez De Sherwood, S., & Zhuang, Z. (1998). Palaeointensity studies of a late Permian lava sucession from Guizhou Province, south China: implications for post-Kiaman dipole field behaviour. *Geophysical Journal International*, *134*(3), 856–866. https://doi.org/10.1046/J.1365-246X.1998.00634.X/2/134-3-856-FIG009.JPEG

Tomezzoli, R. N., Saint Pierre T., & Valenzuela, C. (2009). New palaeomagnetic results from Late Paleozoic volcanic units along the Western Gondwana margin in La Pampa, Argentina. *Earth, Planets and Space*, 61, 183-189. https//doi.org/ 10.1186/BF03352898

Torsvik, T. H., & Domeier, M. (2017). Correspondence: Numerical modelling of the PERM anomaly and the Emeishan large igneous province. *Nature Communications 2017 8:1*, *8*(1), 1–3. https://doi.org/10.1038/s41467-017-00125-2

Torsvik, T. H., & M. Cocks, L. R. (2016). Earth History and Palaeogeography. *Earth History and Palaeogeography*, 1–332. https://doi.org/10.1017/9781316225523

Torsvik, T. H., Smethurst, M. A., Burke, K., & Steinberger, B. (2006). Large igneous provinces generated from the margins of the large low-velocity provinces in the deep mantle. *Geophysical Journal International*, *167*(3), 1447–1460. https://doi.org/10.1111/J.1365-246X.2006.03158.X/2/167-3-1447-FIG012.JPEG

Torsvik, T. H., van der Voo, R., Doubrovine, P. V., Burke, K., Steinberger, B., Ashwal, L. D., Trønnes, R. G., Webb, S. J., Bull, A. L., et al. (2014). Deep mantle structure as a reference frame for movements in and on the Earth. *Atmospheric, and Planetary Sciences*, *111*. https://doi.org/10.1073/pnas.1318135111

Torsvik, T.H., Van der Voo, R., Preeden, U., Mac Niocaill, C., Steinberger, B., Doubrovine, P.V., et al. (2012). Phanerozoic polar wander, palaeogeography and dynamics. *Earth-Science Reviews, 114,* 325-368.

Tsunakawa, H., & Shaw, J. (1994). The Shaw method of palaeointensity determinations and its application to recent volcanic rocks. *Geophysical Journal International*, *118*, 781–787. https://doi.org/10.1111/j.1365-246X.1994.tb03999.x

Uliana, M. A., Biddle, K. T., & Cerdan, J. (1989). Mesozoic Extension and the Formation of Argentine Sedimentary Basins. *Extensional Tectonics and Stratigraphy of the North Atlantic Margins*, 599–614. https://doi.org/10.1306/M46497C39

Usui, Y., & Tian, W. (2017). Paleomagnetic directional groups and paleointensity from the flood basalt in the Tarim large igneous province: Implications for eruption frequency 1. Geomagnetism. *Earth, Planets and Space*, *69*(1), 1–12. https://doi.org/10.1186/S40623-016-0595-X/FIGURES/8

Valencio. D. A., Mendía, J. E., & Vilas, J. F. (1975). Palaeomagnetism and K-Ar ages of Triassic igneous rocks ro the Ischigualasto-Ischichuca Basin and Puesto Viejo formation, Argentina. *Earth and Planetary Science Letters*, 26, 319-330. https://doi.org/10.1016/0012-821X(75)90007-2

van der Boon, A., Biggin, A. J., Thallner, D., Hounslow, M. W., Bono, R., Nawrocki, J., et al. (2022). A persistent non-uniformitarian paleomagnetic field in the Devonian? *Earth-Science Reviews*, *231*, 104073. https://doi.org/10.1016/J.EARSCIREV.2022.104073

Van der Voo, R. (1990). The reliability of paleomagnetic data. *Tectonophysics*, 184(1), 1–9. https://doi.org/10.1016/0040-1951(90)90116-P

van Hinsbergen, D. J. J., de Groot, L. V., van Schaik, S. J., Spakman, W., Bijl, P. K., Sluijs, A., et al. (2015). A Paleolatitude Calculator for Paleoclimate Studies (model version 2.1). *PLoS ONE*. https://doi.org/10.1371/journal.pone.0126946

Vandamme, D. (1994). A new method to determine paleosecular variation. *Physics of the Earth and Planetary Interiors*, 85(1–2), 131–142. https://doi.org/10.1016/0031-9201(94)90012-4

Vaniman, D. (2006). Chapter 2.2 Tuff mineralogy. *Special Paper of the Geological Society of America*, *408*, 11–15. https://doi.org/10.1130/2006.2408(2.2)

Vaughan, P. M., & Pankhurst, R. J. (2008). Tectonic overview of the West Gondwana margin. *Gondwana Research, 13(2),* 150–162. https://doi.org/10.1016/j.gr.2007.07.004

Veevers, J. J. (1989). Middle/Late Triassic (230 +5 Ma) singularity in the stratigraphic and magmatic history of the Pangean heat anomaly. https://doi.org/10.1130/0091-7613(1989)017<0784:MLTMSI>2.3.CO;2

Veikkolainen, T., & Pesonen, L. J. (2014). Palaeosecular variation field reversals and the stability of the geodynamo in the Precambrian. *Geophysical Journal International*, 199, 1515-1526. https://doi.org/10.1093/gji/ggu348

Vigliotti, L. Alvarez, W., & McWilliams, M. (1990). No relative rotation detected between Corsica and Sardinia. *Earth and Planetary Science Letters*, 98, 313-318. https://doi.org/10.1016/0012-821X(90)90033-T

Walderhaug, H. J., Eide, E. A., Scott, R. A., Inger, S., & Golionko, E. G. (2005). Palaeomagnetism and $^{40}Ar/^{39}Ar$ geochronology from the South Taimyr igneous complex, Arctic Russia: a Middle-Late Triassic magmatic pulse after Siberian flood-basalt volcanism. *Geophysical Journal International*, 163, 501-517. https//doi.org/10.1111/j.1365-246X.2005.02741.x

Walker, G. P. L. (1992). Morphometric study of pillow-size spectrum among pillow lavas, *Bulletin of Volcanology, 54*, 459–474.

Wanless, R. K., Stevens, R. D., Lachance, G. R., & Rimsaite, J. Y. H. (1966). Age Determinations and Geological Studies K-Ar Isotopic Ages, Report 6, *Geological survey of Canada.*

Watkins, N. D. (1973). Brunhes epoch geomagnetic secular variation on Reunion Island. *Journal of Geophysical Research*, *78*(32), 7763–7768. https://doi.org/10.1029/jb078i032p07763

Watson, G. S. (1956). A Test for Randomness of Directions. *Geophysical Supplements to the Monthly Notices of the Royal Astronomical Society*, *7*(4), 160–161. https://doi.org/10.1111/J.1365-246X.1956.TB05561.X

Watson, G. S., & Beran, R. J. (1967). Testing a Sequence of Unit Vectors for Serial Correlation. *Journal of Geophysical Research,* 72, 5655-5659. https://doi.org/10.1029/JZ072i022p05655

Wei, B., Yang, X., Cheng, X., Domeier, M., Wu, H., Kravchinsky, V. A., et al. (2020). An Absolute Paleogeographic Positioning of the Early Permian Tarim Large Igneous Province. *Journal of Geophysical Research: Solid Earth*, *125*(5), e2019JB019111. https://doi.org/10.1029/2019JB019111

Wignall, P. B. (2015). The killing seas: the great Permo-Triassic mass extinction. In *The Worst of Times: How Life on Earth Survived Eighty Million Years of Extinctions* (pp. 39-88). Princeton University Press. https://doi.org/10.2307/j.ctvc77862.8

Williams, W., & Dunlop, D. (1989). Three-dimensional micromagnetic modelling of ferromagnetic domain structure. *Nature, 337*, 634–637. https://doi.org/10.1038/337634a0

Wilson, R. L. (1961). Palaeomagnetism in Northern Ireland Part I The Thermal Demagnetization of Natural Magnetic Moments in Rocks. *Geophysical Journal International, 5(1),* 45–58. https://doi.org/10.1111/j.1365-246X.1961.tb02928.x

Wilson, R. L., & Watkins, N. D. (1967). Correlation of Petrology and Natural Magnetic Polarity in Columbia Plateau Basalts, *Geophysical Journal International, 12,* 405–424. https://doi.org/10.1111/j.1365-246X.1967.tb03150.x

Wilson, R. L., Dagley, P., & McCormack, A. G. (1972). Palaeomagnetic Evidence about the Source of the Geomagnetic Field. *Geophysical Journal of the Royal Astronomical Society*, *28*(2), 213–224. https://doi.org/10.1111/j.1365-246X.1972.tb06124.x

Wright, H. M. N., Lesti, C., Cas, R. A. F., Porreca, M., Viramonte, J. G., Folkes, C. B., & Giordano, G. (2011). Columnar jointing in vapor-phase-altered, non-welded Cerro Galán Ignimbrite, Paycuqui, Argentina. *Bulletin of Volcanology, 73,* 1567-1582. https://doi.org/10.1007/s00445-011-0524-6

Wu, L., Kravchinsky, V. A., Gu, Y. J., & Potter, D. K. (2017). Absolute reconstruction of the closing of the Mongol-Okhotsk Ocean in the Mesozoic elucidates the genesis of the slab geometry underneath Eurasia. *Journal of Geophysical Research: Solid Earth*, *122*(7), 4831–4851. https://doi.org/10.1002/2017JB014261

Wynne, P. J., Irving, E., & Osadetz, k. (1983). Paleomagnetism of the Esayoo formation (Permian) of northern Ellesmere Island: possible clue to the solution of the Nares Strait dilemma. *Tectonophysics*, 100, 241-256. https//doi.org/ 10.1016/0040-1951(83)90190-7

Xiang, N., Landschoot, C. (2019). Bayesian Inference for Acoustic Direction of Arrival Analysis Using Spherical Harmonics. *Entropy*, 21, 579. https://doi.org/10.3390/e21060579

Xu, W., Van der Voo, R., Peacor, D. R., & Beaubouef, R. T. (1997). Alteration and dissolution of fine-grained magnetite and its effects on magnetization of the ocean floor. *Earth and Planetary Science Letters*, *151*(3–4), 279–288. https://doi.org/10.1016/S0012-821X(97)81854-7

Yamamoto, Y., & Yamaoka, R. (2018). Paleointensity study on the holocene surface lavas on the island of Hawaii using the Tsunakawa–Shaw method. *Frontiers in Earth Science*, *6*, 48. https://doi.org/10.3389/FEART.2018.00048/BIBTEX

Yamamoto, Y., Shibuya, H., Tanaka, H., & Hoshizumi, H. (2010). Geomagnetic paleointensity deduced for the last 300 kyr from Unzen Volcano, Japan, and the dipolar nature of the Iceland Basin excursion. *Earth and Planetary Science Letters*, *293*(3–4), 236–249. https://doi.org/10.1016/J.EPSL.2010.02.024

Yamamoto, Y., Tsunakawa, H., & Shibuya, H. (2003). Palaeointensity study of the Hawaiian 1960 lava: implications for possible causes of erroneously high intensities. *Geophysical Journal International*, *153*, 263–276. https://doi.org/10.1046/j.1365-246X.2003.01909.x

Yamamoto, Y., Tsunakawa, H., Shaw, J., & Kono, M. (2007). Paleomagnetism of the Datong monogenetic volcanoes in China: paleodirection and paleointensity during the middle to early Brunhes Chron. *Earth, Planets and Space, 59,* 727–746. https://doi.org/10.1186/BF03352736

Yang, S., Chen, H., Li, Z., Li, Y., Yu, X., Li, D., & Meng, L. (2013). Early Permian Tarim Large Igneous Province in northwest *China Science China Earth Sciences, 56,* 2015–2026. https://doi.org/10.1007/s11430-013-4653-y

Yoshimura, Y., Yamazaki, T., Yamamoto, Y., Ahn, H. S., Kidane, T., & Otofuji, Y. ichiro. (2020). Geomagnetic Paleointensity Around 30 Ma Estimated from Afro-Arabian Large Igneous Province. *Geochemistry, Geophysics, Geosystems*, *21*(12), e2020GC009341. https://doi.org/10.1029/2020GC009341

Young, H. D., & Sears, F. W. (1992). *University physics*, *8*. Reading: Addison-Wesley Publishing Company.

Yu, Y. (2010). Paleointensity determination using anhysteretic remanence and saturation isothermal remanence. *Geochemistry, Geophysics Geosystems, 11.* doi:10.1029/2009GC002804

Yu, Y., Dunlop, D. J., & Özdemir, Ö. (2003). Are ARM and TRM analogs? Thellier analysis of ARM and pseudo-Thellier analysis of TRM. *Earth and Planetary Science Letters*, *205*(3–4), 325–336. https://doi.org/10.1016/S0012-821X(02)01060-9

Yuan, K., Van der Voo, R., Bazhenov, M. L., Bakhmutov, V., Alkehin, V., & Hendriks, B. W. H. (2011). Permian and Triassic palaeolatitudes of the Ukrainian shield with implications for Pangaea reconstructions. *Geophysical Journal International*, 184, 595-610. https//doi.org/10.1111/j.1365-246X.2010.04889.x

Yuguchi, T., Izumino, Y., & Sasao, E. (2021c). Genesis and development processes of fractures in granite: Petrographic indicators of hydrothermal alteration. *PLoS ONE, 16(5).* https://doi.org/10.1371/journal.pone.0251198

Yuguchi, T., Matsuki, T., Izumino, Y., Sasao, E., & Nishiyama, T. (2021a). Mass transfer associated with chloritization in the hydrothermal alteration process of granitic pluton. *American Mineralogist*, *106*(7), 1128–1142. https://doi.org/10.2138/am-2020-7353

Yuguchi, T., Yagi, K., Sasao, E., & Nishiyama, T. (2021b). K-Ar geochronology for hydrothermal K-feldspar within plagioclase in a granitic pluton: constraints on timing and thermal condition for hydrothermal alteration. *Heliyon*, *7*(4). https://doi.org/10.1016/J.HELIYON.2021.E06750

Zanetti, A., Mazzucchelli, M., Sinigoi, S., Giovanardi, T., Peressini, G., & Fanning, M. (2013). SHRIMP U–Pb Zircon Triassic Intrusion Age of the Finero Mafic Complex (Ivrea–Verbano Zone, Western Alps) and its Geodynamic Implications. *Journal of Petrology, 54(11),* 2235–2265. https://doi.org/10.1093/petrology/egt046

Zhang, N., & Zhong, S. J. (2011). Heat fluxes at the Earth's surface and core–mantle boundary since Pangea formation and their implications for the geomagnetic superchrons. *Earth and Planetary Science Letters, 306,* 205–216. https://doi.org/10.1016/j.epsl.2011.04.001

Zhang, Y., Ogg, J. G., Franz, M., Bachmann, G. H., Szurlies, M., Röhling, H., et al. (2020). Carnian (Late Triassic) magnetostratigraphy from the Germanic Basin allowing global correlation of the Mid-Carnian Episode. *Earth and Planetary Science Letters*, 541. https://doi.org/10.1016/j.epsl.2020.116275

Zhao, G., Morvan, F., & Wan, X. (2015). Micromagnetic Calculation for Exchange-Coupled Nanocomposite Permanent Magnets. *Reviews in Nanoscience and Nanotechnology*, *3*(4), 227–258. https://doi.org/10.1166/RNN.2014.1058

Zhao, J., Brugger, J., & Pring, A. (2019). Mechanism and kinetics of hydrothermal replacement of magnetite by hematite. *Geoscience Frontiers*, *10*(1), 29–41. https://doi.org/10.1016/J.GSF.2018.05.015

Zhao, J., Huang, B., Yan, Y., & Zhang, D. (2015). Late Triassic paleomagnetic result from the Baoshan Terrane, West Yunnan of China: Implication for orientation of the East Paleotethys suture zone and timing of the Sibumasu-Indochina collision. *Journal of Asian Earth Sciences*, 111, 350-364. http://dx.doi.org/10.1016/j.jseaes.2015.06.033

Zhou, W., Van der Voo, R., Peacor, D. R., Wang, D., & Zhang, Y. (2001). Low-temperature oxidation in MORB of titanomagnetite to titanomaghemite: A gradual process with implications for marine magnetic anomaly amplitudes. *Journal of Geophysical Research: Solid Earth*, *106*(B4), 6409–6421. https://doi.org/10.1029/2000JB900447

Zijderveld, J. D. A. (1967). A. C. Demagnetization of Rocks: Analysis of Results. In D. W. Collinson, K. M. Creer, S. K. Runcorn (Eds.) *Developments in Solid Earth Geophysics 3*, 254–286. https://doi.org/10.1016/B978-1-4832-2894-5.50049-5